Energy Efficiency of High Pressure Pneumatic Systems

José A. Trujillo

Department of Fluid Mechanics

Escuela Técnica Superior de Ingenierías Industrial y Aeronáutica de Terrassa
Polytechnic University of Catalonia

Thesis directed by
Professor Esteban Codina Macià
Professor Pedro Javier Gámez Montero

A thesis submitted for the degree of
PhilosophiæDoctor (PhD)
September 2015

1. Reviewer: .....

2. Reviewer: .....

3. Reviewer: .....

4. Reviewer: .....

5. Reviewer: .....

Day of the defense: .....

Signature from head of PhD committee:

Abstract

The energy efficiency assessment of high-pressure pneumatic circuits is the aim of this dissertation. From a historical perspective the past and current activities with regards to the energy saving conservation in pneumatic technology were examined, and it could be concluded that high pressure pneumatic circuits have been repeatedly used for years in several industrial applications but to date no studies on that specific field are known.

After a systematic review of studies concerning energy saving in pneumatic applications, a complete dynamic model for a high-pressure air blowing machine, employed in the production of plastic bottles, was developed. A synthetic version of the real pneumatic system was considered and consisted of a valve manifold, two tanks, one that simulated the mould cavity where the plastic preform is commonly blown and the other, was intended to recycle air. The one-dimensional models were derived for the pneumatic valve, pipes and vessels. The dynamic modelling of the valve took into account the flow non-linearities through the various geometrical restrictions as well as the pressure and temperature evolution at the inner chambers. Because of the existence of flow discontinuities in the pipes, different solving methods were applied, taking as starting point the Method of Characteristics and continued delving into finite volume methods such as Riemann-solver-based schemes.

On the experimental phase a single blowing station unit was designed and built up. The pressure and temperature characteristics at different positions of the pneumatic circuit were measured in detail. In addition, the fluid flow through the valve manifold could be characterised by the sonic conductance and critical pressure ratio, which were determined by the isothermal discharge method.

Effort was also expended to study the behaviour of the pressure waves generated along the tubes. The pressure wave propagation was computationally charted, with the intention of assessing how this parameter affected the recycling process.

The examination of the experimental results proved the efficiency of the recycling process and demonstrated to be in close agreement with the mathematical model. The parameters governing the maximum amount of air to be recycled at each working cycle were identified, and the influence of the pipe geometry was discussed. Finally the author provides recommendations for future research and makes suggestions regarding the valve design to enhance the efficiency of the system.

To my parents

and

Ana

Acknowledgements

This dissertation would not have been possible without the guidance and the help of several individuals who in one way or another contributed and extended their valuable assistance in the preparation and completion of this study. I attribute the level of my PhD degree to their encouragement and experience, without which this work would not have been completed or written.

First and foremost I must thank Dr. Esteban Codina who has supported me throughout my thesis with his knowledge whilst allowing me the room to work in my own way. I also offer my sincerest gratitude to Naotake Oneyama who initiated me on the energy saving technology during my stay at SMC Corporation Ltd and acted as my mentor in the early stages of this research. I would also like to thank to my co-supervisor Dr Javier Gámez who assisted me during the difficult times when writing this thesis, he gave me the moral support and the freedom I needed to move on.

I honestly appreciate the invaluable assistance of Drs Gustavo Rausch and Javier Freire, who accompanied me in the laboratory through the obstacles I faced when calibrating the measuring units and provided me with advise and tools I have used to produce my results. Thanks for your patience and comprehension.

In my daily work I must thank Francisco Ramirez, a fine technician who inconditionally offered me his support as well as, Enrique Pérez, an excellent colleague, who gave me an outstanding guidance when designing the experimental prototypes.

All of them have been supportive since the days I began working with this research. Ever since, they have supported me not only by providing a research assistantship over almost six years, but also academically and emotionally through the rough road to finish this thesis.

The Department of Fluid Mechanics has provided the support and equipment I have needed to produce and complete my thesis and the LABSON has funded my studies.

I owe a huge debt of gratitude and sincere thanks to my girlfriend, Ana, who has often had to bear the brunt of my frustration and rages against the world. Thank you for your love, understanding and encouragement particularly during the last-leg of this long journey. Thank you for generously giving me the time to complete this thesis and for continuously supporting me along the way.

Last but not least, my most sincere thanks as always, to my parents for their strong encouragement, unconditional love and belief in me. Thank you for supporting me every step of the way and for constantly being there for me - I am greatly indebted to you. Dad, I could not thank you enough for all that you have done for me and the support you offered me when setting up the test bench. I dedicate this thesis to you with all my love and gratitude.

Contents

List of Figures

LIST OF FIGURES

LIST OF FIGURES

LIST OF FIGURES

List of Tables

Glossary

Roman Symbols

$\breve{A}$ Pipe area $[m^2]$

$\ddot{z}$ Spool valve acceleration $[\frac{m}{s^2}]$

$Ð_p$ Pipe diameter $[m]$

$\dot{q}$ Rate of heat transfer per unit mass of fluid and per unit time $\left[\frac{J}{s \cdot kg}\right]$

$\dot{z}$ Spool valve velocity $[\frac{m}{s}]$

$\dot{m}$ Mass flow rate $[\frac{kg}{s}]$

A Non-dimensional velocity of sound $[-]$

a Velocity of sound $\left[\frac{m}{s}\right]$

A_A Non-dimensional isentropic velocity of sound $[-]$

b Critical pressure ratio $[-]$

C Sonic conductance of a component under test $\left[\frac{m^4 \cdot s}{kg}\right]$

C_d Discharge coefficient $[-]$

c_f Viscous friction damping coefficient for moving parts in the valve $[\frac{kg}{s}]$

c_p Specific heat at constant pressure $\left[\frac{J}{kg^\circ K}\right]$

c_v Specific heat at constant volume $\left[\frac{J}{kg^\circ K}\right]$

e_0 Stagnation internal energy $[\frac{J}{kg}]$

f Friction coefficient in the pipe $[-]$

F_f Flow forces acting on the spool valve $[N]$

F_s Static forces acting on the entire control surface $[N]$

g Gravity acceleration $\left[\frac{m}{s^2}\right]$

Gr Grassof number $[-]$

Gz Graetz number $[-]$

h Fluid enthalpy per unit mass $[\frac{J}{kg}]$

k Spring constant $\left[\frac{N}{m}\right]$

L Non-dimensional length $[-]$

l Characteristics length of the system $[m]$

m Fluid mass $[kg]$

m_v Mass of moving parts in the valve manifold $[kg]$

Nu Nusselt number $[-]$

p Fluid pressure $[Pa]$

P_r Prandtl number $(P_r = \frac{\mu c_p}{\lambda})$[-]

r Pipe radius $[m]$

Re Reynolds number $[-]$

S_i Cross-sectional area of a restriction within the valve manifold $[m^2]$

T Gas temperature $[^\circ K]$

t Time $[s]$

T_w Wall temperature $[^\circ K]$

u Gas velocity in x-direction $[\frac{m}{s}]$

V Gas volume $[m^3]$

v Velocity of jet at vena contracta $\left[\frac{m}{s}\right]$

X Non-dimensional cartesian coordinate $[-]$

x Cartesian coordinate $[m]$

z Spool valve displacement $[m]$

Greek Symbols

α Heat transfer coefficient $\left[\frac{W}{m^{2\circ}C}\right]$

β Invariant Riemann variable $[-]$

γ Ratio of specific heats $[-]$

λ Invariant Riemann variable $[-]$

λ_g Thermal conductivity $\left[\frac{W}{m^{\circ}K}\right]$

μ Fluid dynamic viscosity $\left[\frac{kg}{ms}\right]$

Φ Non-flow exergy $[\frac{J}{kg}]$

ϕ Area ratio $[-]$

τ Non-dimensional time $[-]$

Θ Transfer exergy $[W]$

θ Jet angle $[deg]$

ϱ Mass density $\left[\frac{kg}{m^3}\right]$

ζ Stream exergy $[\frac{J}{kg}]$

Subscripts

0 Stagnation conditions

c Air conditions in the chamber

CS	Control surface
CV	Control volume
e	External fluid properties
g	Fluid properties
i	Internal fluid properties
in	Entry fluid flow to the spool valve control volume
out	Exit fluid flow from the spool valve control volume
p	Fluid properties at the pipe
ref	Reference conditions
t	Fluid properties at the vena contracta
v_i	Index referring to each spool valve of the valve manifold
w	Material properties

Chapter 1

Literature review

"The more a thing is perfect,
the more it feels pleasure and pain."
Dante Alighieri, *The Divine Comedy*

Pneumatics found entry into industry soon after 1950. Since then compressed air systems have been implemented in many different types of manufacturing processes. Without doubt, pneumatic systems represented an instrument that brought innovative methods for improving the existing industrial processes. However, it was not until the beginning of the seventies that the use of compressed air in factories began to be regarded as an expensive way to generate energy. In fact, energy conservation started to be seriously questioned after experiencing the first oil crisis in 1973. The rising oil demands and the way in which fossil fuel conditioned the demanding economic growth, contributed to engage energy conservation. The trend of the industry, however, far from developing less energy-demanding processes, followed an energy consumption model that forced governments to review the industrial landscape at the beginning of the nineties. The main reasons at that time were the global warming, CO_2 emissions and green house effect, which unfortunately have become very common words in our daily life, and are partly caused by the non-regulated use of the energetic resources. Taking as reference the compressed air industry, it must be taken into account that the main responsible for electricity consumption is the air compressor, representing up to 90% of the total cost. In fact, the compressed air systems typically consume 10% to

20% of the total electricity in manufacturing factories. Therefore, one of the aspects that measure the efficiency of the system is the adequate air usage according to the production demands.

The quantitative aspect of how energy consumption may be controlled in pneumatic systems was already mentioned by Quillman [1978] (255), who pointed out the need of reducing the operating pressure of pneumatic components as well as adapting the pressure according to the production demands without altering productivity. Despite evidence of an increased awareness of this matter, an energy saving approach was not always embraced by the users. One of the reasons behind that attitude may be the fact that the cost involved in implementing a recovery circuit was excessive when compared to the cost for purchasing and using compressed air. In addition, there was not known circuit which was efficient and required a minimum amount of maintenance. However with the rapid increase in the costs of equipment, labor, and also the inadequate air capacity in plants, mainly because of the growing use of pneumatics as a motive force, the need of applying energy saving measures started to be questioned. As a matter of fact air leakage, amongst other parameters, has been commonly taken as one of the main energy loss factors inherent to pneumatic systems. Additionally many publications, normally provided by pneumatic makers, have contributed to raise awareness amongst users by emphasising the consequences of not applying a regular maintenance in industrial pneumatic applications. Then, may we believe that energy conservation is somehow associated to the lack of knowledge by the pneumatic users? The answer to this question is certainly not clear, but a high percentatge of the wrong use of compressed air is directly linked to this factor. On that respect several publications proposed countermeasures to tackle not only air leakage in pneumatic systems, but were also focused on a significant aspect of compressed air circuits when being assessed from energy saving point of view, which is the sizing method. The first documents which put into question the energy conservation in pneumatic systems were published at the beginning of the seventies. Most of them focused on the regulation and sizing of pneumatic components [1971] (191). The authors already noticed how critical was the designing stage in order to optimitize a pneumatic circuit. At that time, the flow dynamic specifications of the valves were defined by a flow coefficient C_v, a dimensionless number that described the conductance of an orifice device, which eased the selection

of the right component according to the operating requirements [1975] (106), [1976] (94), [1977] (97), [1981] (107). Those first contributions introduced a framework for evaluating pneumatic components technology not only as part of a system but also as individual units to be improved from technical point of view.

At the end of the eighties, the rising global environmental issues created a growing level of alarm over the increasing effects of climate change. Governments promoted the need of applying urgent countermeasures to minimize the CO_2 emissions that culminated in the establishment of the Kyoto protocol in 1995, which entered into force in 2005. That first agreement stimulated researchers to review the energy saving activities carried out in numerous industrial fields and pneumatic technology represented also a part of the target. The following sections describe the steps taken in order to implement and develop energy conservation activities in the pneumatic industry over the last fifty years as well as the enormous possibilities that pneumatics offers to energy conservation.

1.1 Pneumatic technology

During the decade of the sixties industry began experiencing a significant evolution thanks to pneumatic technology. At that time the major considerations in the design and selection of pneumatic components were reliability, productivity and cost, in addition, and also but of lesser priority, was the necessity to conserve energy. The seventies contributed to increase awareness of the limited energy resources and led several pneumatic makers to define the designing rules to be applied in order to minimize the air consumption. Moreover the continued economic growth propelled the need for developing more compact and reliable pneumatic components, which allowed using less amount of compressed air.

1.1.1 Exhaust air recovery system

It is well known that in a meter-out circuit the air is unnecessarily released to the atmosphere after the stroke is completed, though the pressure in the cylinder exhaust chamber maintains a comparatively high value during the stroke (fig.1.1). Therefore proposals to recover exhaust air while maintaining pressure for recycling were put forward at the end of the seventies.

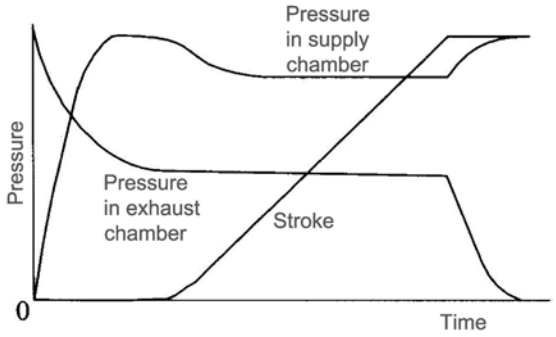

Figure 1.1: Response of double acting cylinder

In the year 1966 Schneider (272) proposed the recovery of the air usually exhausted during the return stroke of a pneumatic cylinder to atmosphere. The accumulated air could be transferred to another work cylinder, with the advantage that both were operated independently (fig.1.2).

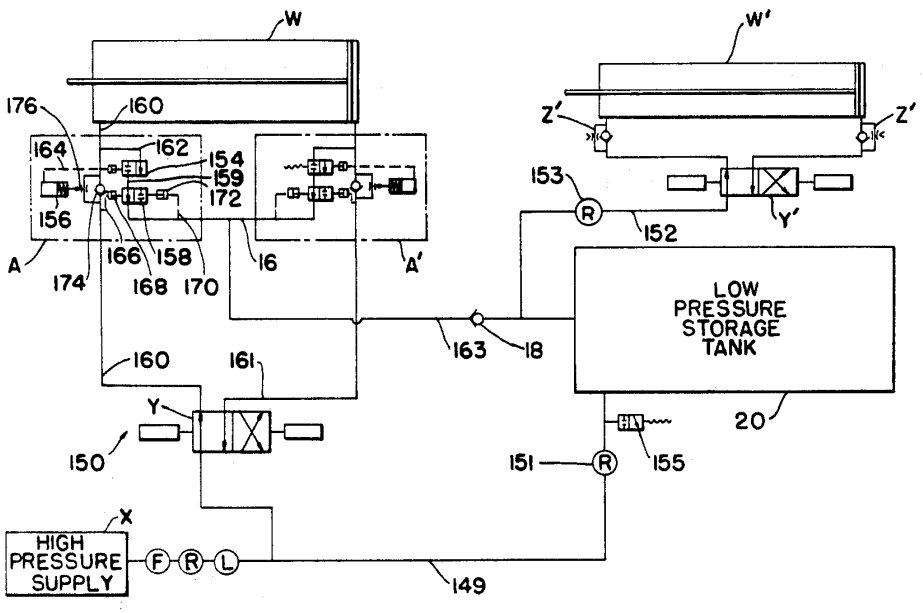

Figure 1.2: Recovery air from a cylinder to a storage tank - US patent 3400636

In the year 1986 Sanville (268) suggested the use of a secondary reservoir in an open-loop system to collect exhaust air rather than vent it to atmosphere, and then reuse

the stored air on the return stroke.

Figure 1.3 shows a patent published by SMC Corporation in 1979 (348) (see also [1981] (343)) that described a passive recovery system where the exhaust air was recovered and recycled as low-pressure secondary air supply. When the solenoid valve was not energised high pressure air from the head chamber of the cylinder was recovered to an accumulator by a recovery valve until the pressure in the head chamber falled to almost that inside the tank, afterwards the recovery valve switched, releasing the remaining air to the atmosphere. In this way, the recovered low-pressure air could be used for the return stroke of the cylinder. In addition, compressed air recovered to the tank was suitable to be used as:

- Air source for systems that used low pressure air as working medium such as signal air system or cylinder drive system, that did not require output.
- Air source for cooling.
- Air source for increasing pressure by compressor and recirculating to the cylinder drive section.

A selector valve was connected between the driving chamber and an accumulator for collecting exhaust air. The channel from the applicable selector valve to the accumulator was equipped with a pilot collecting valve that switches the position of the channel from the above selector valve depending on the magnitude of the acting force by the pilot air pressure and on the magnitude of the preset acting force of the set device. The applicable pilot collecting valve switches the applicable channel to the collecting position that communicates with the accumulator in a case where the acting force of the pilot air pressure is great, and to the exhausting position that is open to the atmosphere in a case where the above force is small. This actuator drive unit is characterized by its ability to recover the above actuator with the high-pressure air from the high-pressure air supply or with the air that is collected/accumulated in the accumulator by branching the applicable pilot channel of the collecting valve from the channel between the above selector valve and the above pressure chamber on the drive unit side.

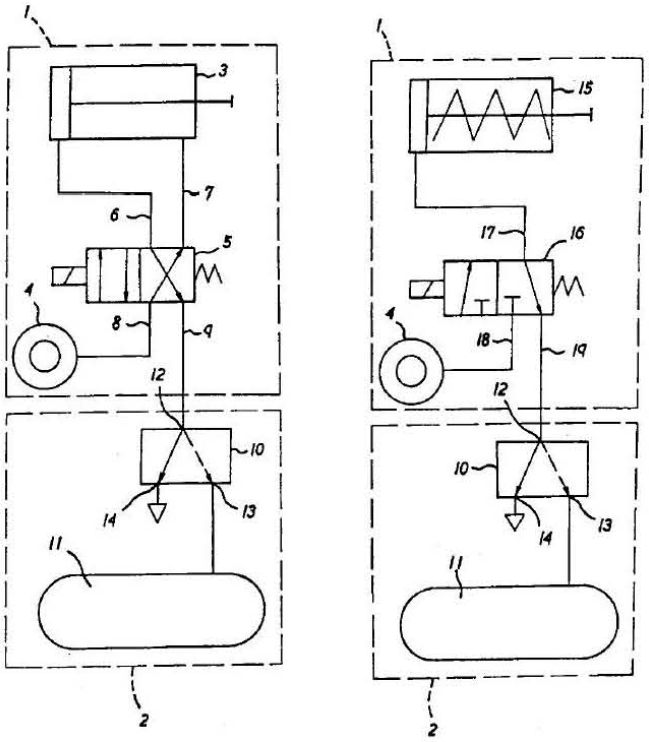

Figure 1.3: Exhaust air recovery circuit

Rexnord Inc. [1982] (304) addressed the utilization of the pressurized fluid for the return stroke, which was previously used for the working stroke. The proposal, however, due to the number of valves required to establish a connection between the cylinder and the reservoir, made the system less efficient from structural and operational point of view. Similarly Hoerbirger Ventilwerke AG [1983] (111) proposed a year later a device for automatically returning a pneumatically operated actuating cylinder. During the working stroke the reservoir stored air from the rod chamber as well as from the pressure regulator, which was utilized for returning the piston to the original position. The designs presented by those patents evolved during the following years until POS-LINE AB (Fig.1.4) developed a jacketed reciprocatable pneumatic actuator [1994] (129), [1996] (130), [1997] (131), [1997] (326), that incorporated the technical advantages proposed by Rexnord Inc some years ago, but with the difference that a cross channel, which interconnected the working and return chamber, avoided using a number of valves that directly affected the cycle time. However the concept still presented several drawbacks,

such as, high backpressure generated in the return chamber when a great amount of kinetic energy was supplied to heavy objects, the great number of movable parts that comprised the unit, and the limited strength of the piston rod since it was hollow. Despite the inconveniences the double power differential cylinder saved at least 30-50% of compressed air and was suitable for pressing, clamping and lifting work that required specified output for the operating stroke, but did not require large output for return.

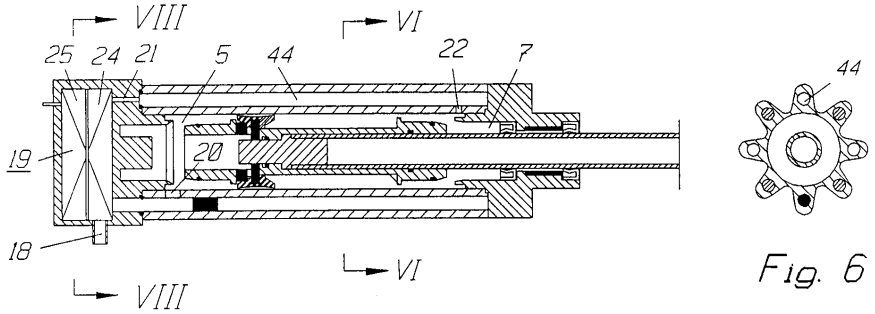

Figure 1.4: POS-LINE AB pneumatic cylinder saving concept

In the year 1994, Quaglia (250), (see also [1995] (253), [1995] (254), [1994] (251), [1994] (252)), proposed a non-conventional pneumatic cylinder that incorporated multiple cylinder chambers embedded into a single actuator with the intent of recycling compressed air. The new actuator could operate without consuming compressed air during the retraction stroke, reaching up to 50% savings when compared with a common double-acting actuator. The prototype designed by Quaglia proved the efficiency of the concept which was patented by POS-LINE AB a year later, however the idea of accumulating the air used during the working stroke of the piston should be awarded to Varouxis (324), who patented a pneumatic cylinder with self-contained piston return in 1969 (Fig.1.5).

1.1.2 Supply-stop driving system

Based on the fact that at the end of the piston stroke the pressure of the driving fluild rises up unnecessarily to reach the value of the fluid supply circuit, Levenez et al. [1985] (202) proposed a device to stop the flow of pressurized fluid before the end or at the end of the piston stroke (Fig.1.6). As shown in Fig.1.1, after the cylinder piston rod reaches the stroke end, pressure in the supply side chamber increases further

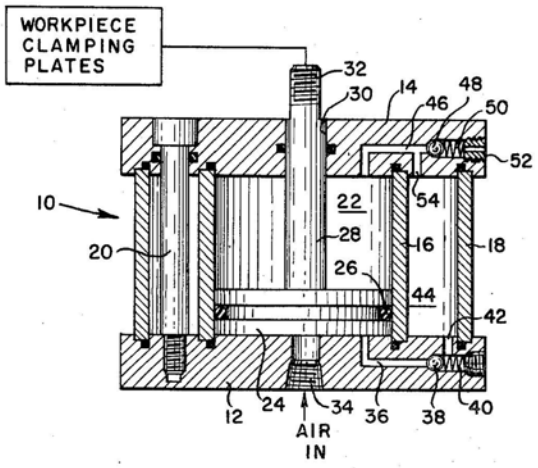

Figure 1.5: Air cylinder with self-contained pneumatic piston return

to the supply pressure and pressure in the exhaust chamber drops to the atmospheric pressure. Fig.1.7 shows the cylinder behaviour when stopping the air supply halfway through the cylinder stroke. As the remaining stroke is completed by expansion of sealed air, air filled at the stroke end will become low-pressure air, thus the amount of air released in the next cycle will be reduced.

The idea of using the air expansion was also exploited by Otis (237) (see also [1992] (238)) in 1991, who analyzed the air consumption of a pneumatic cylinder that used the air expansion during the working stroke motion of the piston-rod. By means of a linkage mechanism up to 55% air savings could be accomplished under certain operating conditions. Arigana et al. [2000] (12) utilized metering circuits to analyse the airflow requirements for open-loop point-to-point motions. They proved that the air consumption in meter-in circuits could be reduced by 40% by cutting off the air supply when the piston reached the stroke end (Fig.1.8).

1.1.3 Energy assessment of pneumatic systems

Since the second half of the nineties onwards a growing research activity began within the pneumatic field. Governments and other entities were concerned about the climate change and the serious consequences for the environment. Pneumatics, was also considered as a subject to be discussed from energy saving point of view and a proof of that are

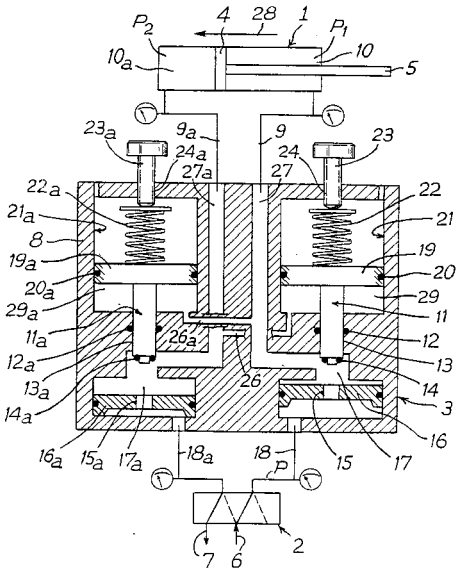

Figure 1.6: Compressed fluid saving device - Patent # US4608910

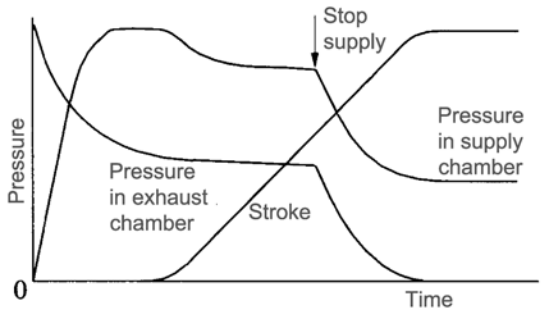

Figure 1.7: Response of cylinder supply stop driving

the numerous publications that can be found in the literature. A publication that must be taken as reference on that respect is the book published by Oneyama [2003] (234). In the book the author collected the activities carried out by the Japanese industry from 1996 to 1999 in order to meet the emissions targets declared by the Kyoto protocol. As a matter of fact 19% of the cases were related to pneumatic activities, and were typically focused on blow, piping, leakage and air source. Moreover the book described in sufficient detail the findings and achievements reached on all areas of pneumatic

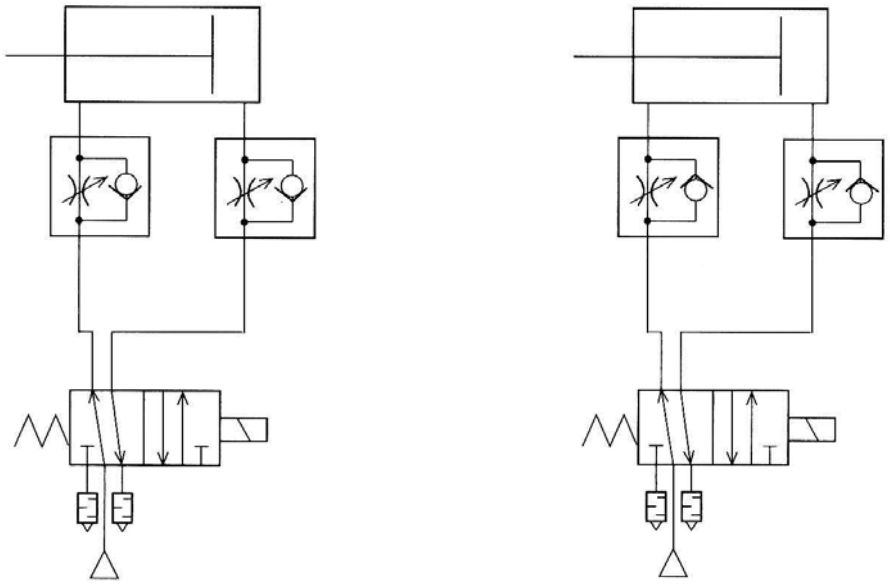

(a) (b)

Figure 1.8: Speed control circuit: (a) Meter-out circuit (b) Meter-in circuit

technology.

In a parallel approach Tokashiki et al. [1996] (309) studied the influence of the pipes on the dynamic characteristics of a pneumatic cylinder. Those mathematical models were incorporated years later on a simulating sofware. As part of that investigation, Senoo et al. [2003] (276) and Huping et al. [2003] (150) presented the pneumatic devices selection softwares developed by SMC Corporation Ltd, which applied the principles established at the beginning of the seventies and later recalled by Fleischer [1991] (108) at the beginning of the nineties, which are equipment selection, thoughtful system layout and proper equipment and piping installation.

The same year Kagawa et al. [2000] (175) determined the exergy of pneumatic air actuating systems under different operating conditions. The article presented a method to calculate the energy that may be available after overcoming the work done against friction and other transformations. The assessment, applied to both meter-in and meter-out circuits, concluded that the meter-in configuration allowed highest exergy saving when convergence velocity was not predominant. Some years later, Cai [2006] (54) (see

also [2002] (176)) introduced the term of "air power", which must be understood as the combination of transmission and expansion power that is available in compressed air, and presented a device able to measure the air power in industrial applications. Similarly, Sai et al. [2000] (266) digged into the main actors causing energy loss in compressed air systems and, as Cai previously did, used the concept of exergy to define the effective energy that can be extracted from air to do mechanical work. In a similar way, Parkinen and Zenger [2008] (241) introduced the concept of CA-index, which compared the theoretical minimum power to the real consumed power of a compressed air system. A qualitative advantage of the method, proposed by the authors, is the fact that allowed for assessment of the dynamic characteristics of a whole compressed air line under different operating conditions. The article recovered a subject that has been iteratively addressed by compressor makers during the last few years, which is the relevant role that the compressor plays in the complete pneumatic system.

Following the activity initiated some years before on the efficiency of pneumatic actuators, and taking into account that while meter-in circuits controlled the amount of supplied energy meter-out circuits did not, Mutoh et al. [2008] (229) (see also [2000] (305)), examined in 2008 the effect of tube volume and driving load in meter-out circuits. The authors concluded that by increasing the tube volume as well as the exhaust pressure could be accomplished.

Based on the groundswell of interest in identifying, comparing and testing the energy consumption of pneumatic circuits the performance of pneumatic and electric actuators, under the same operating conditions, was also investigated. Cai [2002] (52), [2006] (53) proved that the energy consumption of pneumatic actuators, specially at a vertical actuation with long cycle time, was lower than the energy required by an electrical actuator.

1.1.4 Efficiency of servo-pneumatic actuator systems

Following a different line of investigation, Wang et al. [2000] (330) reported the use of input shaping to choose a command profile for point-to-point motions that would result in energy savings for closed loop pneumatic servo-actuators, and showed that some velocity profiles could reduce energy demand relative to other profiles. The same author years later [2011] (329) presented an optimal control theory for servo-pneumatic

actuator systems. The result of the investigation concluded that savings between 3 to 5% could be obtained when implementing the energy efficient velocity profile. Al-Dakkan et al. [2003] (5) proposed controlling the positioning of a pneumatic actuation with three-way valves instead of using a standard single four-way valve. By doing that, each valve area could be controlled independently, and also allowed minimizing the airflow for a given load and trajectory. Experiments demonstrated that the power consumption of such pneumatic servo-system could be reduced up to 45%.

Pu et al. [1997] (249) described a pneumatic arrangement that incorporated a standard four-way spool valve controlled pneumatic servo-actuator, with an additional two-way valve between the two sides of the cylinder. The strategy was to devise a control path between the drive and exhaust chambers of the cylinder directly. The advantage of this technique from energy efficiency point of view was already identified by Shen and Goldfarb [2007] (283) who presented a closed-loop servo-control of pneumatic actuation with improvements respect to the concept provided by Pu some years ago. This paper presented a crossflow energy saving approach that enabled significant energy saving for a pneumatic actuator in the context of servo actuation. The experimental results showed that up to 52% relative to a standard four-way valve configuration could be achieved.

Tapio and Mäkinen [2003] (303) carried out a qualitative study on energy consumption of high performance pneumatic positioning servo systems when being compared to simple pneumatic positioning systems. Ke et al. [2004] (183) conducted an energy efficiency analysis of servo-pneumatic actuator systems and presented a method of energy efficient optimal control. The velocity profile proposed by the authors achieved better results than the commonly used trapezoidal velocity profile.

Yang et al. [2008] (346) scrutinized the energy efficiency of a scroll-type air motor and determined that when compared with conventional pneumatic actuating systems, scroll-type air motors were able to convert more available energy of compressed air. The main aspect that made a difference respect to pneumatic actuators is the capacity of producing not only transmission power but also expansion power.

Blagojevic et al. [2008] (34), [2011] (35) developed an experimental model to provide energy efficiency by using energy recovery. This is the result of by-passing the chambers

actuator, which enables the air from the previous driving not to be vented irreversible to the atmosphere but to be used, in part or entirely, for the retracting motion of the actuator. The same authors investigated the effect of restoring energy on both, conventional and servo pneumatic systems. For the first concept savings of 38.8% could be accomplished and for the second configuration the savings reached an average value of 28.6% under certain operating conditions.

1.1.5 High pressure pneumatic applications

Despite the many contributions linked to energy conservation in pneumatic systems, none of the publications reviewed so far reports the efficiency on high pressure pneumatic applications. In order to bring some light to this issue, it is crucial to get into the patents published during the last twenty years. Amongst various industrial applications [1992] (15) that require of high pressure air, such as metal extrusion, oil industry, or coal blasting industry, PET (Polyethylene terephthalate) blowing machine manufacturers have contributed significantly to enhance energy efficiency to that specific field of pneumatic systems. In the case of heavy-duty blowing machines, whose production output often lies in the range of 2,000 bottles per hour to 20,000 bottles per hour and which customarily produce containers with volumes in the range of 0.5 to 3 liters, large amounts of compressed air are needed. The compressors used in this type of industrial activities require a considerable amount of energy due to the extensive air-compression required. Therefore taking into account the energy cost associated to the high pressure compressor operation some companies started to develop solutions to minimize the energy consumption.

In the food industry and, to be more precise, in the beverage industry, there has been an increasing tendency to fill beverages or foods into hollow bodies made of thermoplastic material (PET bottles). Those containers require an elevated temperature-resistance due to the multiple applications in which those bodies may be used. The process that allows achieving this characteristic property is known as air blowing process. The container in its original state is called preform and is blown with compressed air until obtaining the desired shape. The operation of supplying compressed air is divided into a preblowing phase in which gas is supplied at a low pressure level, and a subsequent main blowing phase, in which gas is supplied at a higher pressure level. The first stage

of the blowing process uses compressed air with a pressure in the range of 10 to 25 bars, and during the second stage, pressure in the range of 25 to 40 bar is supplied to the preform. Prior to this, the preform is stretched inside the blow mold by a stretch rod after thermal conditioning. The final blowing pressure is high enough that the plastic molded blank is pressed against the wall of the blow mold. This pressure is maintained for a certain time in order to give the specific contours.

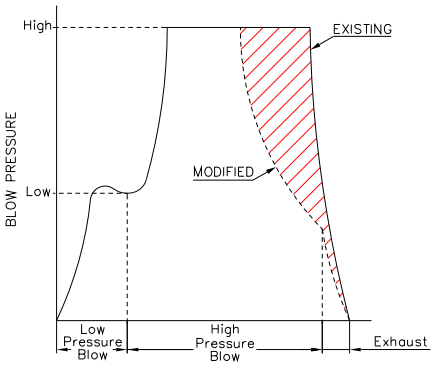

Figure 1.9: Blowing process time - The Continental Group Patent # US4488863A

Despite the origins of the air blowing technology dated back to the 1950s, our historical review starts in 1981 with a patent published by Air Products and Chemicals Inc. (112). The invention related to a process for the production of blow molded articles in which the blowing gas, that contained not only air but also fluorine (used to improve the impermeability of the container), was recovered and treated to be used in subsequent molding operations. A year later Bosch GmbH Robert suggested recovering the compressed air used in the molding operation to feed other pneumatic applications.

In fact a similar proposal was provided by The Continental Group Inc. (334) in 1984, which was subsequently taken as reference by other blow molding bottle manufacturers. It is known that in this type of industrial processes, after an initial stretching of the preform, the blow molding is completed by the introduction of high pressure air. Once the PET container reaches the final shape within the cavity, the blowing gas is vented to atmosphere. Based on this working principle, The Continental Group Inc proposed to make a self-sustained low pressure supply by connecting the low pressure line to the exhaust for a limited period of time (Fig.1.9). The storage device containing the

pre-blowing air was equipped with a pressure regulating valve so the excess pressure could escape to the outside. The solution, however, presented two major disadvantages: the structural complexity and the regulation of the pre-blowing pressure was not very accurate.

Some years later Krupp Corpoplast Maschinenbau GmbH (336), (337) [1995] presented an invention that recovered part of the air used for molding a container made of thermosplastic material. The high-pressure blowing air was supplied to the low-pressure air supply during a transitional phase by employing a reversing mechanism. To limit the pressure fluctuations in the low-pressure air supply a pressure monitoring system was set-up. The stored air could be subsequently transferred to secondary pneumatic circuits or also, could even be utilized for returning the stretching rod to the original position. However the mentioned proposal had disadvantages. The recirculation of blowing air led to an increase in the pre-blowing pressure air line. Also the recirculated air was consumed in neighboring blowing stations, which was the reason why a pressure equilibrium was established. However, the pressure equilibrium depended on the recirculation time, in other words, the duration of the transitional phase, which was lasted as much as possible with the aim of minimizing cost, although that resulted in a high pre-blowing pressure and consequently a reduced bottle quality.

An invention that has been cited by several blowing machine manufacturers is the patent of Procontrol AG [1996] (287), which proposed to produce the high pressure air adiabatically while the low pressure air was generated isothermically, so enabling the entire blowing process to be carried out with the smallest possible amount of energy.

Over the same period and based on the same principle, A.K. Tech Lab Inc. [1997] (152) proposed recovering the exhaust air into a tank that later supplied air to operate secondary pneumatic circuits. In order to compensate the difference between the recovered air and the one consumed by the installation, a compressor provided sufficient air to balance the pressure in the tank (Fig.1.10). Also, it must be taken into account the proposal of Asahi Kasei Kogoyo Kabushiki Kaisha [1993] (138), which added a recovery container from which the compressed gas could be aspirated by a multistage compressor.

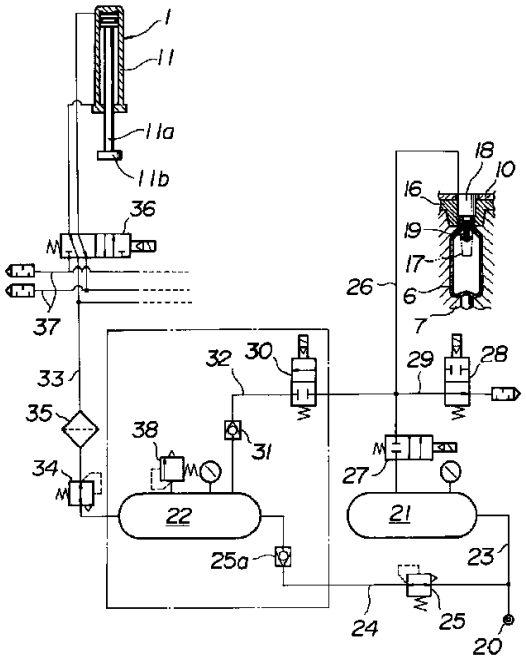

Figure 1.10: Blowing air recovery proposal - A.K. Tech Lab Patent # JPH0985812

Following the ideas established by some of the manufacturers mentioned before, Yoshino Kogyosho Co. Ltd. (270) presented an invention in 1998 that had not been raised before that time. In that particular invention the blowing air from the mold was recycled to a high-pressure accumulator until reaching a pressure level in the mold that switched into another valve that allowed recovering the remaining air to a low-pressure accumulator. This recycling principle allowed feeding the parison not only during the pre-blowing phase but also during an intermediate stage at a higher pressure, minimizing, therefore, the supplied high pressure air volume.

In certain improved implementations, a supplementary flow of gas under pressure is injected before the intermediate or final container can be extracted from the mold. That additional injection of gas is normally applied in procedures in which the containers are blow molded in very hot molds. It was proved that this operation helped to obtain containers with better mechanical properties, however contributed negatively towards reducing the already high consumption of high pressure air. Regarding this specific application, Sidel (51) [1999] proposed a solution in which part of the air used for

desgassing was transferred to another mold to perform the high-pressure blow molding phase. The invention, then, reduced the consumption of high-pressure air, specially if we take into account that each mold was able to produce two containers and the machines had a capacity of producing 50,000 bottles per hour.

Based on the existing art Technoplan (171) published in 2003 an invention which targeted the optimization of the above-mentioned methods. A relevant improvement was the fact that the recovered gas (17 bar) was expanded before being used in the low-pressure air phase, which meant that it did not have influence on the low pressure air at the time of its use. On the other hand, several proposals were given to re-use the recovered air, such as, to actuate the preform-stretching rams, actuate consumables of the packaging-production machine, or even returning the recycled gas to the compressed air network. The method allowed around 20 to 45% of air recovery and a reduction of electrical power consumption of 15 to 45%.

An interesting method for saving energy is the solution proposed by Newtec International Group (136) in 2004. The patent described the effect of limiting the high pressure air consumption by reducing the internal volume of the bottle. The invention, shown in figure 1.11, consisted of a stretch rod covered with an elastomer liner into which a incompressible fluid was introduced during the pre-blowing phase. The remaining volume was achieved with high pressure air that represented only 5% of the total volume.

Another aspect that has been addressed by the beverage industry is the production of heat-resistance hollow bodies. In this case the internal wall of the mold, against which the bottle being created is pressed, must be heated up. The bottle, then, is held against the warmed walls in order to subject the plastic to a partial crystallization. However excessive crystallization of the plastic brings out discoloration. Therefore to guarantee the desired stability of the shape preventing discoloration is necessary to cool down the container (also called in this particular case hot-fillable plastic bottle). The cooling process or also known as rinsing, was accompanied by a compressed air recycling process (Krones AG patent (137)) [2005]. However the air-recovery mechanism developed for the mentioned application had definite drawbacks, and one of them was the fact that it could not achieve a regular pre-blow flow rate due to the pressure variations in the volume allocated to the preblow stage arising by the feeds during the recovery phase.

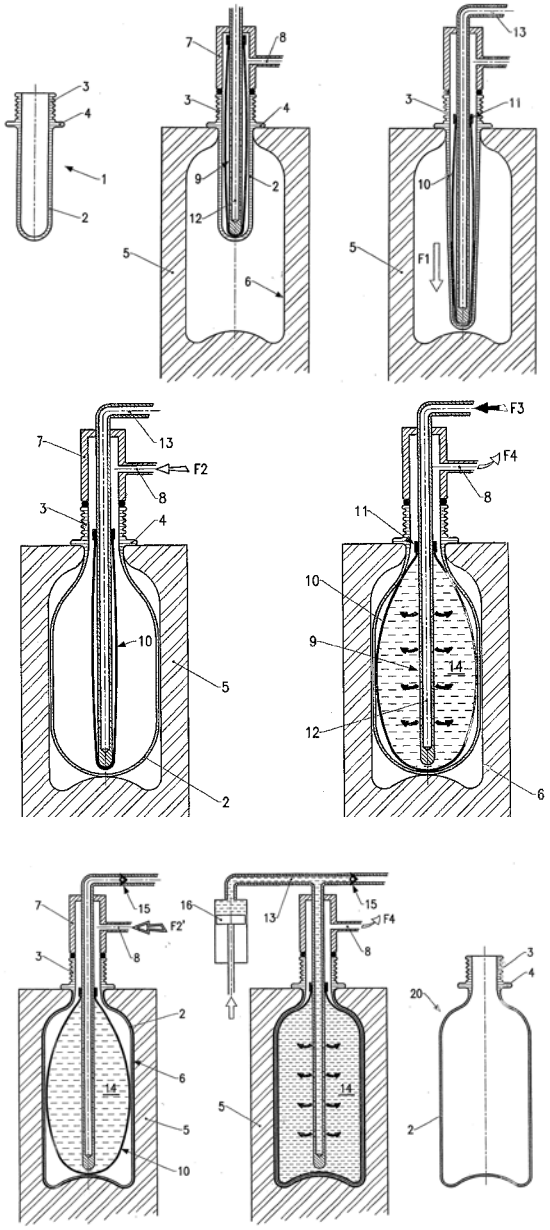

Figure 1.11: Newtec International Group Patent # WO2004098862

As a result, a constant quality of the blow-molded container could not be ensured. In fact, Krones AG [2004] (105), reviewed the method proposed by Krupp Corpoplast Maschinenbau GmbH [1994] (336) some years later to optimize the pressure monitoring

during the recovery phase in order to conserve the bottle quality as well as obtain the maximum recirculation factor and optimized the recirculation method, which ensured the maximum recirculation factor without affecting the bottle quality by controlling the pressure in the low-pressure storage unit. Depending on the existing pressure in the low-pressure air supply the transational phase was suitably shortened or lengthened.

In the year 2006 SIG Technology AG (209) published a patent that described an arrangement to recover the air used during the blowing phase (fig.1.11). One of the advantages of the proposed pneumatic design was the fact that part of the air could be recovered and used to feed the intake of the high-pressure compressor so the unit was not supplied with air at ambient pressure. Another alternative was to convey compressed air to the plant air system when a maximum permissible upper pressure level was reached in the low-pressure supply system. Both options helped to reduce the operating capacity of the plant air compressors.

In the year 2007 Technoplan Engineering (172) proposed a different approach to recycle pressure after the stretch blow molding process. As previously reviewed, all the contributions made by the numerous manufacturers were able to recycle the air at the end of each cycle, and part of that air, after being regulated, could be used for the pre-blowing stage during the following cycle, or alternatively could be dedicated to actuate pneumatic components of the existing compressed air circuit. However despite the efficiency of the process there was still no option for using the recovered air during the high-pressure blowing stage. Therefore to optimize the air recovery process and based on the state of the art at the time, Technoplan developed a blowing machine with three air blowing phases instead of two. The recovery phase, then, could be used not only for the pre-blowing step but also for the intermediate blowing step (Fig.1.13). An alternative published by EBAC Ltd (96) in 2007, discussed the possibility of recovering the air stored in the mould cavity at the end of the blowing stage in a sequential manner. The compressed air, then, could be selectively stored in accumulators with different capacities, to be subsequently re-used during the blowing phase following a stepwise procedure.

In the year 2008 Acqua Minerale San Benedetto (352) focused on a particular aspect of the recycling process that had not been addressed in the past. As it was known

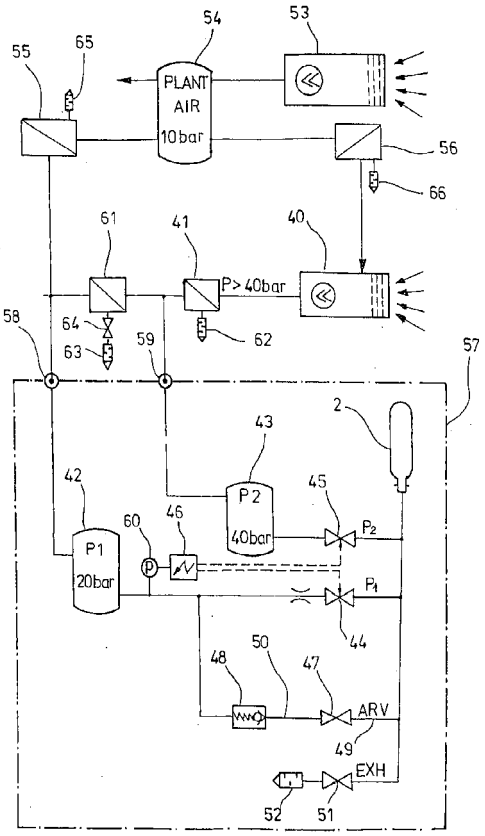

Figure 1.12: SIG Technology Patent # WO2006029584

the compressor consumed more energy to compress high-pressure than lower-pressure, therefore the recovery of the exhaust air could not only be used for driving secondary pneumatic circuits but also to produce a new container. By following this approach, the recovered air, which remained at an intermediate pressure, could be blown into the cavity after finishing the low-pressure step. Then the volume of high-pressure gas required in the second step of the blowing process was signficantly reduced (Fig.1.14).

As mentioned before, the air recovery method discussed in [2004] (136) and [2007] (87) was not able to ensure the required pressure potential to avoid pressure fluctuations during the pre-blowing process, which directly affected the quality of the end product. Similarly the recovery system implemented in [2003] (171) presented the same disadvantage, since the volume allocated to the preblow stage was only fed secondarily. During

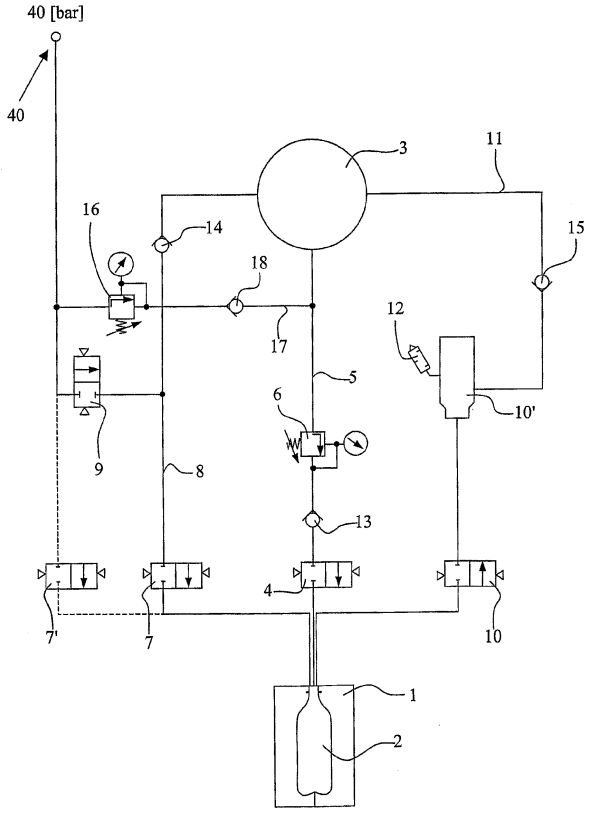

(a)

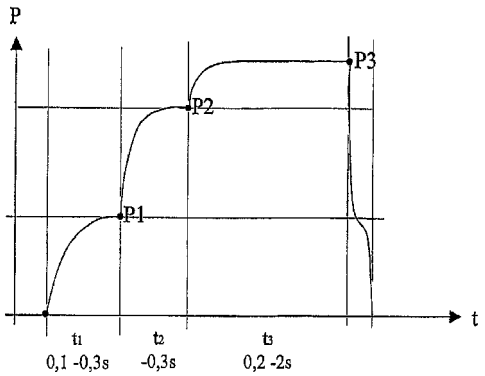

(b)

Figure 1.13: Technoplan Engineering Patent US 20040173949 A1. (a) Blow-molding machine scheme. (b) Blow-molding curve according to the method of the invention

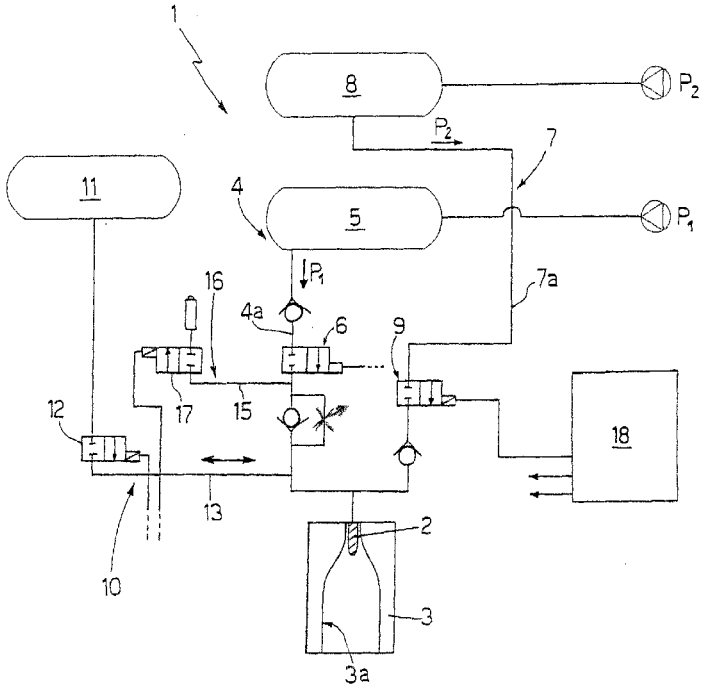

Figure 1.14: San Benedetto Acqua Minerale Patent # EP1905569

the same period Krones (87) [2008] published a patent in which the lowest pressure stage during the recovery phase mold was used to feed the volume allocated for the preblow stage (see fig.1.15). As a result, Krones proposed in 2011 (48) feeding the volume for the pre-blow stage before a volume of a higher blow stage is supplied. By doing so the probability of pressure variations could be considerably reduced (see fig.1.16). In fact, the operating principle suggested by Krones had been already documented by SIPA (353) in 2009.

Nissei ASB Machine Co. Ltd. (189) [2012] proposed an improvement of the invention published by AK Tech Lab Inc. [1995] (152) some years before. The authors determined that the amount of recycled air depended on the pressure of the recovery tank and also that the recycling ratio directly influenced the quality of the molded articles (see also [2004] (137)).

It is worth adding at this point, that in order to accomplish a correct air-flow at each blowing station, the sizing of the valve manifold is obviously a key parameter to take

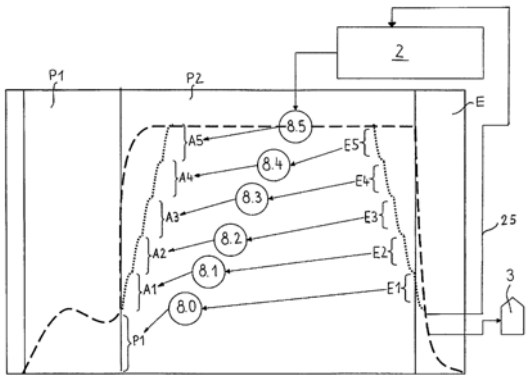

Figure 1.15: Krones AG Patent # EP1974892A2

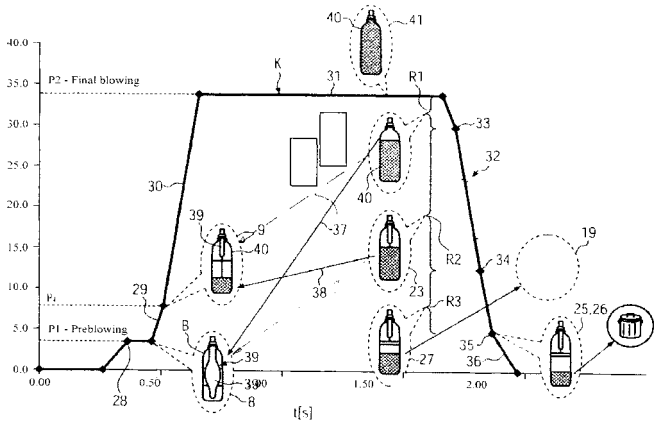

Figure 1.16: Krones AG Patent # US2011057343A1

into account. The need of developing compact designs in order to reduce the connecting tubes arranged between the valves and the blow nozzle, and thus the always present dead volume, encouraged numerous manufacturers to optimize the existing pneumatic designs (refer to [2009] (40), [2006] (186), [2005] (264), [2007] (265), [2003] (325)).

Chapter 2

Aims of the project

"Never to accept anything for true which
I did not clearly know to be such".
Descartes *Discourse on the Method* (1637)

2.1 Research objectives

Based on the previous review it appeared reasonable to attempt to gain a deeper understanding of the recycling techniques used in conjunction with certain manufacturing processes actually work and how they could be improved. On the other hand due to the vast range of pneumatic products and particular use given to them it is also necessary to focus on a specific application. Then, one of the aims of this study is to analyze the efficiency of pneumatic systems, and more specifically the high pressure systems, which allow for higher recycling ratio when compared to low pressure pneumatic applications.

Therefore taking as a reference the production process of polyethylene terephthalate containers, our first goal is to develop a mathematical model. The model determines the variation of the physical properties over a series of cycles, being able to predict the amount of recycled air that may be processed under certain operating conditions. The numerical analysis also takes into account the influence of the internal construction of the pneumatic valve manifold, a key device that will be analysed in detail, as well as the length and cross-sectional area changes along the pipes, heat transfer through pipes

and vessels, viscous forces and entropy variation.

A first approach to the problem reveals that the existence of pressure waves in pneumatic systems is related to the non-steady characteristics of the process. The periodic opening and closing of the valves and the continuous cylinder operation are two of the main sources of the mentioned non-stationarity. Furthermore, the existence of variable cross section along the pipes generate mass and energy discontinuities, which should be considered when analyzing such type of compressible flows. As a result, the models used to characterize such processes must take into account the influence of the previously mentioned singularities. Hence our preliminary goal will be to identify which solving method will adequately adressed the specificity of such physical disturbances along the flow.

The flow discontinuities, associated to the manufacturing process under discussion, suggest the need of identifying the effect of pressure waves from a recycling rate point of view, thus figuring out the most efficient pneumatic configuration. Despite the fact 3D modelling has been quite predominant since the last two decades, the one-dimensional unsteady codes still play a significant role during the designing phase. Therefore several methods are applied in this dissertation to solve the non-linear hyperbolic equations governing the flow through the connecting pipes, that go from the Method of Characteristics to more advanced solving techniques based on Riemann solvers. Thus, our second goal, will be to experimentally analyse the pressure perturbation along the pipes with the intention of predicting the optimal configuration from an energy efficiency point of view.

A third goal, that is predominant for this study, is the design and construction of a valve manifold which is a key device for this specific production process. The trends of the industry and more in particular manufacturers have been mainly focused on minimising the inherent dead volume, while this research has been centered on identifying the dynamic characteristics of the unit and how it affects to the effectiveness of the process.

The final aim is to develop an experimental test bench, which is able to reproduce the air blowing process, and measure the local temperature and pressure of the gas inside the corresponding vessels and connecting pipes.

2.2 Scope of the study

The computer model to be developed would predict the performance of the air blowing pneumatic system, such as the pressure and temperature histories in various locations as well as the heat transferred through the pipe and vessel walls to the surroundings. Depending on the adopted configuration it will be possible to determine the amount of recycled air and, therefore, the efficiency of the pneumatic lay-out. A series of experimental tests, that reproduces the operating conditions under which the PET bottle production is usually working, will be conducted and the results will be correlated with the computer simulations.

2.3 Structure of thesis

The thesis document has been organized as described below:

- **Chapter 1** surveys the literature in relation to: 1) the energy saving methods historically applied to low pressure pneumatic applications as well as the research efforts aimed at gaining a better knowledge of different pneumatic configurations; 2) utilisation of high pressure air on certain industrial applications and measures adopted by the producers in order to minimize the air consumption. As reference, the PET bottle manufacturing process is used to assess the air consumption under certain operating conditions, and the subsequent chapters introduce the mathematical models employed to solve the governing equations at the connecting pipes, valve manifold, and air vessels respectively, that, as a whole, constitute the main components being part of the pneumatic circuit to be analysed.

- **Chapter 2** presents the main topics on which this study is based.

- **Chapter 3** contains the thermodynamic and gas dynamic analysis of unsteady gas flow in a quasi-one-dimensional duct as well as the governing equations together with the assumptions applied at the boundary conditions. Different solving methods are discussed. The pipes communicate the main supply lines and the valve manifold, and at the same time, the valve manifold and the blowing and recyling vessels.

- **Chapter 4** describes the mathematical model implemented to solve the unsteady 0D governing equations inside the valve manifold, which is commonly used in the PET bottle manufacturing process. Numerical simulations to determine the discharge coefficient were also conducted and the results are compared with the experimental values discussed in Chapter 6.

- **Chapter 5** contains the heat transfer model applied to the so-called blowing and recycling vessels. The exergetic analysis of an air reservoir is conducted and the results are used as reference to estimate the energy lost on the pneumatic circuit under study.

- **Chapter 6** presents the steps followed to design the valve manifold and its complexity, as well as the experimental results of a one-station air blowing unit under different configurations. The pressure and temperature characteristics are discussed, and the influence of the pipe geometry is associated to the air recycling ratio.

- **Chapter 7** introduces the comparison between the experimental and predicted results and discusses the accuracy of the different mathematical methods implemented in the Fortran code. A final conclusion is also given.

Chapter 3

Mathematical model for the fluid transmission lines

"There is nothing so reprehensible and unimportant in nature that it would not immediately swell up like a balloon at the slightest puff of this power of knowing."
Friedrich Nietzsche, *Über Wahrheit und Lüge im außermoralischen Sinn* sec.1 (1873)

In the past five decades the continuous research on the characterization of gas flow through combustion engines has contributed to develop a good knowledge of the physical process. A wide number of mathematical methods were succesfully tested and validated by numerous experimental studies, amongst them it must be hightlighted the Method of Characteristics. Both the graphical and the numerical version of the method offered to the researchers the possibility to have a fair understanding of the propagation of pressure waves through the pipes. The method was developed by Riemann, who originally proposed this approach for the solution of the non-linear wave equations. Benson et al. [1963] (31), [1982] (29), succeded in solving the energy terms from the wave propagation terms and also in deriving the flow equations in characteristic form. Compatibility equations were constructed in finite difference form by introducing the assumption that the pressure and velocity were continuous in the solution field. The condition allowed for the presence of contact discontinuities but not shock waves; a further disadvantatge was that the compatiblity equations required an iterative solution

procedure.

Due to this fact, other mathematical techniques such as the two step Lax & Wendroff difference scheme, the McCormack scheme as well as those with flux correction techniques represented at a time an alternative solution with respect to the Method of Characteristics.

Unfortunately due to the non-steady nature of the process, it is difficult to ensure an accurate calculation of the physical properties within the fluid as it passes through the pipes. Additionally the compressibility of the flow plays an important role, specially at high pressure. The combination of the two mentioned parameters must also be accompanied by the existence of high amplitude waves which may generate shock waves as well as thermal discontinuities usually associated to the difference in temperature between supplied and exhausted air respectively. Altogether, combined with the fact that the mathematical methods, historically used to solve the hyperbolic equations governing the flow, were oscillatory in presence of discontinuities, resulted in the generation of spurious oscillations that directly altered the numerical calculation. Due to this fact, several contributions were put forward in order to minimize the negative effect of the mentioned oscillations with satisfactory results, such as, the use of artificial viscosity and flux correction techniques.

In order to cope with the discontinuities the Euler equations have to be expressed in a conservative form (finite-volume method), which are equivalent to the integral conservation laws of mass, momentum and energy, and automatically satisfy the jump conditions across the discontinuities, i.e., the Rankine-Hugoniot conditions in gas dynamics.

Therefore based on the methods succesfully applied in the modelling of internal combustion engines and, in general, machines driven by compressible fluids, the author considered that those numerical techniques (Method of Characteristics, Lax & Wendroff, McCormack, ...) could be suitable to reproduce the industrial process under discussion. Nevertheless, it must be taken into account that some of the above-mentioned techniques have been replaced by more powerful calculation methods which are founded on the proposal originally made by Godunov (119) (1959), which are the so-called Riemann solver-based methods. Therefore this study will not only implement the schemes

that have been proved to be numerically inconsistent in the presence of pressure or thermal discontinuities but also those techniques which have been able to overcome the mentioned numerical difficulties.

Despite the fact numerous and succesful advances have been accomplished in multi-dimensional computational methods during last years, the use of zero-dimensional thermodynamics and one-dimensional fluid dynamic solvers are still widely used for modelling unsteady flows in intake and exhaust pipes of internal combustion engines, the reason being is the reduction of computing time when compared with three-dimensional CFD analysis and, as in our case, it has been thought to be sufficiently accurate to analyze the physical process. As a matter of fact the method of characteristics, despite being controversial, is still used to determine the boundary conditions at the ends of the computational domain.

3.1 Implementation of the Method of Characteristics

Based on the previous introduction the Method of Characteristics offers a reasonable stability when having control of the pressure discontinuities and the boundary conditions are well developed. However, it must be bear in mind that has only first order accuracy. So taking this principle as a basis this section, therefore, describes the construction of a mathematical algorithm, using the Method of Characteristics, for the solution of the equations defining the unsteady, compressible flow of a perfect gas. The equations defining the compressible flow of a fluid are as follows [1963] (31), [1953] (281), [1954] (282), [1992] (340):

$$\frac{\partial \varrho}{\partial t} + \frac{\partial(\varrho u)}{\partial x} + \varrho u \frac{d(\ln \breve{A})}{\partial x} = 0 \tag{3.1}$$

$$\frac{\partial(\varrho u)}{\partial t} + \frac{\partial(\varrho u^2 + p)}{\partial x} + \varrho u^2 \frac{d(\ln \breve{A})}{dx} + \varrho \frac{4f}{\breve{D}_p} \frac{u^2}{2} \frac{u}{|u|} = 0 \tag{3.2}$$

$$\frac{\partial(\varrho e_0)}{\partial t} + \frac{\partial}{\partial x}\left[\varrho u \left(e_0 + \frac{p}{\varrho}\right)\right] + \varrho u \left(e_0 + \frac{p}{\varrho}\right) \frac{d}{dx}(\ln \breve{A}) - \varrho \dot{q} = 0 \tag{3.3}$$

where,

$e_0 = e + u^2/2$ (stagnation internal energy)

$\dot{q} = \alpha \pi \breve{D}_p \Delta x (T_w - T)$ (heat transfer energy per unit mass per unit time)

$\breve{A}$ (cross-sectional area)

The equations above are often converted to those given below for a solution by the Method of Characteristics:

$$\frac{\partial}{\partial t}(\varrho \breve{A} dx) + \frac{\partial}{\partial x}(\varrho u \breve{A}) = 0 \tag{3.4}$$

$$\frac{\partial u}{\partial t} + u\frac{\partial u}{\partial x} + \frac{1}{\varrho}\frac{\partial p}{\partial x} + \frac{4f}{\breve{D}_p}\frac{u^2}{2}\frac{u}{|u|} = 0 \tag{3.5}$$

$$\frac{\partial}{\partial t}\left[\left(\frac{u^2}{2} + e\right)\varrho \breve{A} dx\right] + \frac{\partial}{\partial x}\left[\varrho \breve{A} u\left(\frac{u^2}{2} + e + \frac{p}{\varrho}\right)\right] dx = \dot{q}\varrho \breve{A} dx \tag{3.6}$$

To solve these partial differential equations requires either a finite difference technique or a method of manipulating them into ordinary differential equations. It is the latter approach which was developed first by Riemann and is referred to as the Method of Characteristics. The governing equations are usually converted to ordinary differential equations using the assumption that the fluid is a perfect gas obeying the relationships:

$$\frac{p}{\varrho} = RT \tag{3.7}$$

$$e = c_v T \tag{3.8}$$

At this point it must be pointed out that the assumption of considering a perfect gas it supported on the fact that the mass-flow deffect at the pressures applied during the experimental tests, which vary between 20 to 25 bar, at a maximum fluid temperature that oscillates between 80°C to -20°C, is of 0.5% respect to the ideal condition. On the other hand the compressibility factor for air according to the Beattie-Bridgeman correlation for the mentioned range of temperatures differ between 0.98 and 1.00 at a pressure of 25 bar and a temperature of 80°C, condition that only occurs at the time that the air is supplied to the air chamber. During the discharge period the air cools down to values below 0°C at a pressure of approximately 1 bar, being the compressibility factor of 0.999. Therefore to consider the gas as perfect for the range of pressures and temperatures of the application under study is sufficiently accurate.

Based on the previous statement equation (3.6) may be modified to get

$$\frac{\partial}{\partial t}\left[\left(\frac{u^2}{2} + c_v T\right)\varrho \breve{A} dx\right] + \frac{\partial}{\partial x}\left[\varrho \breve{A} u\left(\frac{u^2}{2} + c_p T\right)\right] dx = \dot{q}\varrho \breve{A} dx \tag{3.9}$$

Employing the continuity equation (3.4), (3.9) may be written

$$\frac{d}{dt}\left(c_v T + \frac{u^2}{2}\right) = \dot{q} - \frac{u}{\varrho}\frac{\partial p}{\partial x} - \frac{p}{\varrho \breve{A}}\frac{\partial(\breve{A}u)}{\partial x} \tag{3.10}$$

where

$$\frac{d}{dt} = \frac{\partial}{\partial t} + u\frac{\partial}{\partial x} \tag{3.11}$$

The following expression

$$\frac{d}{dt}\left(\frac{u^2}{2}\right) = u\frac{\partial u}{\partial t} + u^2\frac{\partial u}{\partial x} \tag{3.12}$$

may be combined with equation (3.5) to give

$$-\frac{u}{\varrho}\frac{\partial \varrho}{\partial x} = \frac{d}{dt}\left(\frac{u^2}{2}\right) + u\frac{4f}{\mathcal{D}_p}\frac{u^2}{2}\frac{u}{|u|} \tag{3.13}$$

Then inserting equation (3.13) into equation (3.10) yields

$$\frac{d}{dt}(c_v T) = \dot{q} + u\frac{4f}{\mathcal{D}_p}\frac{u^2}{2}\frac{u}{|u|} - \frac{p}{\varrho \breve{A}}\frac{\partial(\breve{A}u)}{\partial x} \tag{3.14}$$

From the perfect gas law,

$$\frac{d}{dt}(c_v T) = \frac{d}{dt}\left(\frac{1}{\gamma - 1}\frac{p}{\varrho}\right) \tag{3.15}$$

and after differentiation, we obtain

$$\frac{d(c_v T)}{dt} = \frac{1}{\gamma - 1}\frac{1}{\varrho}\left[\left(\frac{\partial p}{\partial t} + u\frac{\partial p}{\partial x}\right) - \frac{p}{\varrho}\left(\frac{\partial \varrho}{\partial t} + u\frac{\partial \varrho}{\partial x}\right)\right] \tag{3.16}$$

Then using the continuity equation (3.4) becomes

$$\frac{\partial(\breve{A}u)}{\partial x} = -\frac{\breve{A}}{\varrho}\left(\frac{\partial \varrho}{\partial t} + u\frac{\partial \varrho}{\partial x}\right) \tag{3.17}$$

and susbtituting into equations (3.14) and (3.16) results

$$\frac{1}{\gamma - 1}\frac{1}{\varrho}\left[\left(\frac{\partial p}{\partial t} + u\frac{\partial p}{\partial x}\right) - \frac{p}{\varrho}\left(\frac{\partial \varrho}{\partial t} + u\frac{\partial \varrho}{\partial x}\right)\right] - \frac{p}{\varrho^2}\left(\frac{\partial \varrho}{\partial t} + u\frac{\partial \varrho}{\partial x}\right) = \dot{q} + u\frac{4f}{\mathcal{D}_p}\frac{u^2}{2}\frac{u}{|u|} \tag{3.18}$$

Equation (3.18) may also be written as follows

$$\left(\frac{\partial p}{\partial t}+u\frac{\partial p}{\partial x}\right)-a^2\left(\frac{\partial \varrho}{\partial t}+u\frac{\partial \varrho}{\partial x}\right)-(\gamma-1)\varrho\left(\dot{q}+u\frac{4f}{\text{Đ}_p}\frac{u^2}{2}\frac{u}{|u|}\right)=0 \tag{3.19}$$

Two additional expressions may be derived from equations (3.5), (3.6) and (3.19)

$$\left[\frac{\partial p}{\partial t}+(u+a)\frac{\partial p}{\partial x}\right]+\varrho a\left[\frac{\partial u}{\partial t}+(u+a)\frac{\partial u}{\partial x}\right]- (\gamma-1)\varrho\left(\dot{q}+u\frac{4f}{\text{Đ}_p}\frac{u^2}{2}\frac{u}{|u|}\right)+a^2\frac{\varrho u}{\breve{A}}\frac{d\breve{A}}{dx}+\varrho a\frac{4f}{\text{Đ}_p}\frac{u^2}{2}\frac{u}{|u|}=0 \tag{3.20}$$

$$\left[\frac{\partial p}{\partial t}+(u-a)\frac{\partial p}{\partial x}\right]-\varrho a\left[\frac{\partial u}{\partial t}+(u-a)\frac{\partial u}{\partial x}\right]- (\gamma-1)\varrho\left(\dot{q}+u\frac{4f}{\text{Đ}_p}\frac{u^2}{2}\frac{u}{|u|}\right)+a^2\frac{\varrho u}{\breve{A}}\frac{d\breve{A}}{dx}-\varrho a\frac{4f}{\text{Đ}_p}\frac{u^2}{2}\frac{u}{|u|}=0 \tag{3.21}$$

Equations (3.20) and (3.21) can now be transformed from partial to ordinary differential equations along the characteristics lines $\left(\frac{dx}{dt}\right)_{I,II}=u\pm a$, resulting in

$$\frac{dp}{dt}\pm\varrho a\frac{du}{dt}=(\gamma-1)\varrho-\left(\dot{q}+u\frac{4f}{\text{Đ}_p}\frac{u^2}{2}\frac{u}{|u|}\right)-a^2\frac{\varrho u}{\breve{A}}\frac{d\breve{A}}{dx}\mp\varrho a\frac{4f}{\text{Đ}_p}\frac{u^2}{2}\frac{u}{|u|} \tag{3.22}$$

In effect, equation (3.22) may be re-arranged to yield,

$$(du)_\pm=\mp\frac{2}{\gamma-1}(da)_\pm+ \left[\mp\frac{au}{\breve{A}}\frac{d\breve{A}}{dx}\pm\gamma\frac{\dot{q}}{a}-\frac{4f}{\text{Đ}_p}\frac{u^2}{2}\frac{u}{|u|}\left(1\mp\frac{u}{a}\right)+\frac{a^2}{\gamma}\frac{\partial}{\partial x}\left(\ln\frac{a^{\frac{2\gamma}{\gamma-1}}}{p}\right)\right](dt)_\pm \tag{3.23}$$

A further characteristic, called path line, may be determined from equation (3.19). Along this characteristic curve the entropy or temperature gradients may have discontinuities and are described by the following expressions,

$$\left(\frac{dx}{dt}\right)_{path}=u \tag{3.24}$$

$$\left(\frac{dp}{dt}\right)_{path}=\frac{2\gamma}{\gamma-1}\frac{p}{a}\left(\frac{da}{dt}\right)_{path}-\varrho\left(u\frac{4f}{\text{Đ}_p}\frac{u^2}{2}\frac{u}{|u|}+\dot{q}\right) \tag{3.25}$$

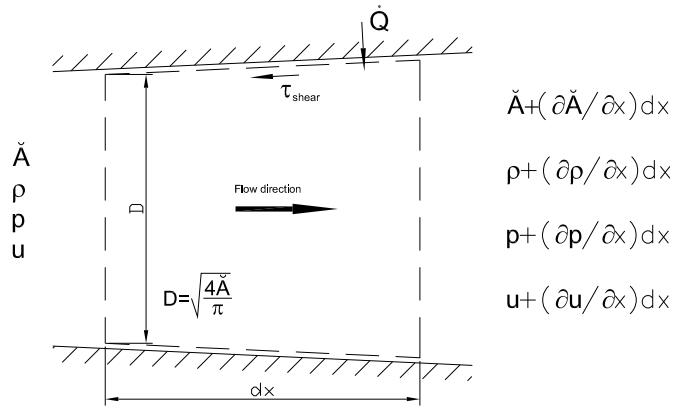

Figure 3.1: Control surface for the flow through the pipe

As a matter of fact if there is no heat transfer or pipe wall friction, equation (3.25) becomes $\partial p/\partial \varrho = a^2$, which is the speed of sound for an isentropic pressure wave. In this particular case the energy equation can be replaced by an isentropic relationship; such flow is referred to as homentropic flow.

In case of homentropic flow the two characteristic variables, also called Riemann variables, can be transformed into non-dimensional form λ and β, and be replaced in (3.23) and (3.25) respectively. It is worth to mention that these variables always remain constant in value if viewed from an observation point moving with a particular velocity.

$$\frac{a}{a_0} + \frac{\gamma - 1}{2}\frac{u}{a_0} = \lambda \tag{3.26}$$

$$\frac{a}{a_0} - \frac{\gamma - 1}{2}\frac{u}{a_0} = \beta \tag{3.27}$$

Then the non-dimensional non-homentropic form of the compatibility equations will be for the characteristic line λ,

$$\begin{aligned}\lambda_{P\prime} \;=\; & \lambda_R - \frac{(\lambda_R + \beta_R)(\lambda_R - \beta_R)}{2}\left(\frac{1}{Đ_p}\right)\left(\frac{dĐ_p}{dX}\right)\Delta\tau + \left(\frac{\lambda_R + \beta_R}{2}\right) \\ & \left(\frac{A_{A_{P\prime}} - A_{A_R}}{A_{A_R}}\right) - \frac{f_R L_{ref}}{Đ_{p_R}}\frac{(\lambda_R - \beta_R)^2}{\gamma - 1}\frac{\lambda_R - \beta_R}{|\lambda_R - \beta_R|}\left(1 - 2\frac{\lambda_R - \beta_R}{\lambda_R + \beta_R}\right)\Delta\tau + \\ & \frac{(\gamma - 1)^2}{2}\dot{q}\frac{L_{ref}}{{a_0}^3}\frac{2}{(\lambda_R + \beta_R)}\Delta\tau\end{aligned} \tag{3.28}$$

and analogously for the characteristic line β,

$$\begin{aligned}\beta_{P'} &= \beta_S - \frac{(\lambda_S+\beta_S)(\lambda_S-\beta_S)}{2}\left(\frac{1}{\mathcal{D}_p}\right)\left(\frac{d\mathcal{D}_p}{dX}\right)\Delta\tau + \left(\frac{\lambda_S+\beta_S}{2}\right)\\ &\left(\frac{A_{A_{P'}}-A_{A_S}}{A_{A_S}}\right) - \frac{f_S L_{ref}}{\mathcal{D}_{pS}}\frac{(\lambda_S-\beta_S)^2}{\gamma-1}\frac{\lambda_S-\beta_S}{|\lambda_S-\beta_S|}\left(1+2\frac{\lambda_S-\beta_S}{\lambda_S+\beta_S}\right)\Delta\tau +\\ &\frac{(\gamma-1)^2}{2}\dot{q}\frac{L_{ref}}{{a_0}^3}\frac{2}{(\lambda_S+\beta_S)}\Delta\tau \end{aligned} \tag{3.29}$$

and finally for the path line λ_0,

$$dA_A = \frac{\gamma-1}{2}L_{ref}\frac{A_{A_M}}{{A_M}^2}\left(\frac{\dot{q}}{{a_0}^3}+\frac{2f}{\mathcal{D}_p}\left|\frac{\lambda_M-\beta_M}{\gamma-1}\right|^3\right)\Delta\tau \tag{3.30}$$

3.1.1 Numerical solution to the governing equations

The resolution method adopted to solve the characteristic equations will be now discussed. First, the subsonic flow is considered, being the linear interpolation between nodes $i-1$ and i,

$$\lambda_R = \lambda_i - \frac{\partial X}{\Delta X}(\lambda_i - \lambda_{i-1}) \tag{3.31}$$

$$\beta_R = \beta_i - \frac{\partial X}{\Delta X}(\beta_i - \beta_{i-1}) \tag{3.32}$$

$$\frac{\partial X}{\Delta X} = \frac{\frac{\gamma+1}{2(\gamma-1)}\lambda_i - \frac{3-\gamma}{2(\gamma-1)}\beta_i}{\frac{\Delta X}{\Delta\tau}+\frac{\gamma+1}{2(\gamma-1)}(\lambda_i-\lambda_{i-1})-\frac{3-\gamma}{2(\gamma-1)}(\beta_i-\beta_{i-1})} \tag{3.33}$$

Following the same procedure the Rieman invariants between nodes i and $i+1$ can be determined as follows,

$$\lambda_S = \lambda_i - \frac{\partial X}{\Delta X}(\lambda_i - \lambda_{i+1}) \tag{3.34}$$

$$\beta_S = \beta_i - \frac{\partial X}{\Delta X}(\beta_i - \beta_{i+1}) \tag{3.35}$$

$$\frac{\partial X}{\Delta X} = \frac{\frac{\gamma+1}{2(\gamma-1)}\beta_i - \frac{3-\gamma}{2(\gamma-1)}\lambda_i}{\frac{\Delta X}{\Delta\tau}+\frac{\gamma+1}{2(\gamma-1)}(\beta_i-\beta_{i+1})-\frac{3-\gamma}{2(\gamma-1)}(\lambda_i-\lambda_{i+1})} \tag{3.36}$$

In case of supersonic flow two different cases must be evaluated:

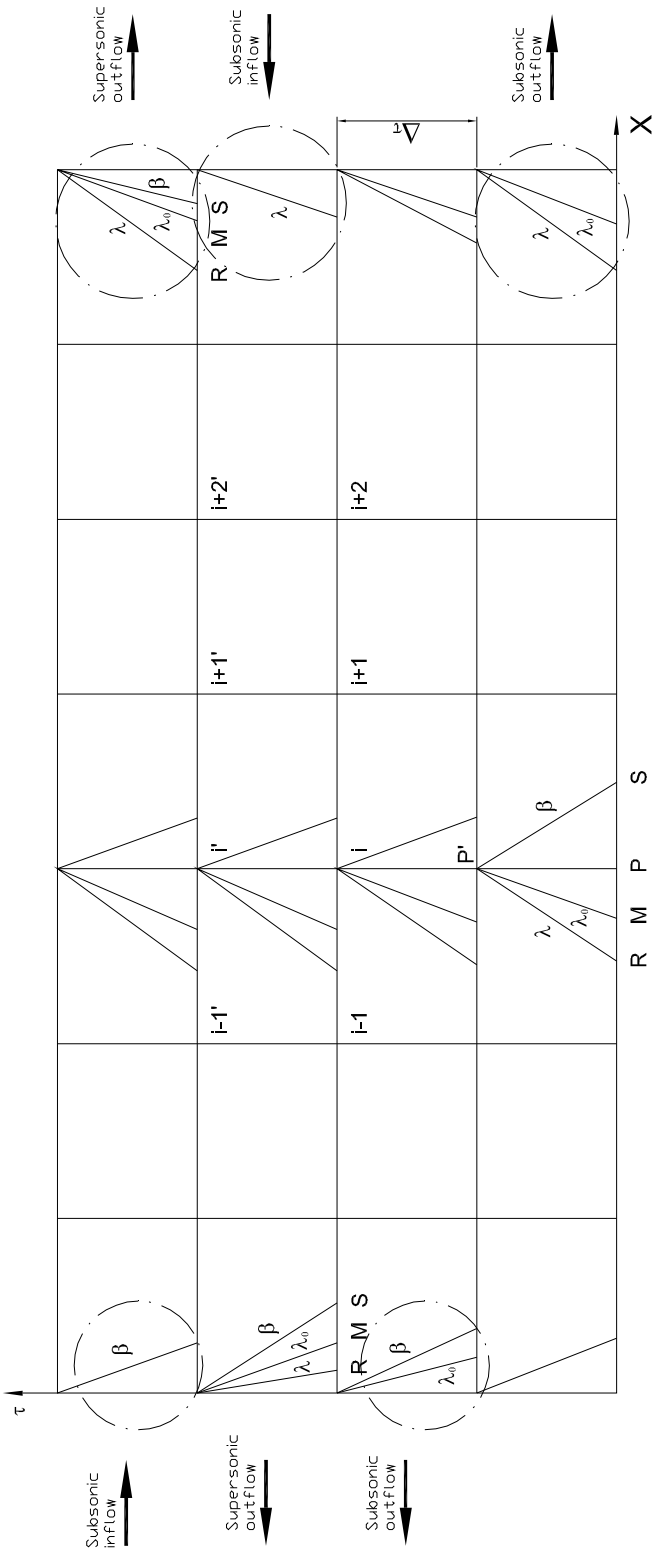

Figure 3.2: Grid notation for non-homentropic flow

- Positive supersonic flow

$$\frac{\partial X}{\Delta X} = \frac{\frac{3-\gamma}{2(\gamma-1)}\beta_i - \frac{\gamma+1}{2(\gamma-1)}\lambda_i}{\frac{\Delta X}{\Delta \tau} + \frac{3-\gamma}{2(\gamma-1)}(\lambda_i - \lambda_{i-1}) - \frac{\gamma+1}{2(\gamma-1)}(\beta_i - \beta_{i-1})} \tag{3.37}$$

$$\beta_S = \beta_i - \frac{\partial X}{\Delta X}(\beta_i - \beta_{i-1}) \tag{3.38}$$

- Negative supersonic flow

$$\frac{\partial X}{\Delta X} = \frac{\frac{3-\gamma}{2(\gamma-1)}\beta_i - \frac{\gamma+1}{2(\gamma-1)}\lambda_i}{\frac{\Delta X}{\Delta \tau} + \frac{3-\gamma}{2(\gamma-1)}(\beta_i - \beta_{i+1}) - \frac{\gamma+1}{2(\gamma-1)}(\lambda_i - \lambda_{i+1})} \tag{3.39}$$

$$\beta_R = \lambda_i - \frac{\partial X}{\Delta X}(\lambda_i - \lambda_{i+1}) \tag{3.40}$$

It must be noticed that in order to evaluate the Riemann variables at each node the time step must lie in the zone of dependence of the previous time step. This condition is represented by the relation (3.41), which is also known as the Courant-Friedrichs-Lewy (CFL) stability condition.

$$\frac{dt}{dx} = \left(\frac{1}{|u| + a}\right)_{min} \tag{3.41}$$

As previously mentioned the values of the Riemann variables are supposed to be varying linearly along the mesh length. This assumption, however, is more accurate when the mesh size becomes smaller.

3.1.2 Determination of heat transfer at the pipes

The investigation assumes that no combustion takes place and heat transfer in the pipe section is mainly caused by conduction and convection. In order to calculate the heat transfer coefficients in the internal and external surface of the pipes the following semi-empirical correlations are applied,

- Nusselt number for the inner surface of the pipe

$$Nu_i = \begin{cases} 1.86\,(Re_i Pr_i)^{0.33}\left(\frac{\mu_i}{\mu_{w_i}}\right)^{0.14}\left(\frac{\mathcal{D}_{p_i}}{l}\right)^{0.33} & \text{if } Re_i < 2000, Gz_i > 10 \\ 0.023\left(\frac{\varrho_i u_i \mathcal{D}_{p_i}}{\mu_i}\right)^{0.8}\left(\frac{c_{p_i}\mu_i}{\lambda_{g_i}}\right)^{0.4} & \text{if } Re_i > 2000 \end{cases} \tag{3.42}$$

- Nusselt number for the outer surface of the pipe

$$Nu_e = \begin{cases} 0.47\,(Gr_e \cdot Pr_e)^{0.25} & \text{if } 10^4 < Gr_e \cdot Pr_e < 10^9 \\ 0.1\,(Gr_e \cdot Pr_e)^{0.33} & \text{if } Gr_e \cdot Pr_e > 10^9 \end{cases} \tag{3.43}$$

where Gr refers to the Grashoff number, Pr represents the Prandtl number, the subindex i/e refer to the internal and external side of the pipe surfaces respectively, and Nu corresponds to the Nusselt number which is defined as follows,

$$\alpha_{i/e} = \frac{Nu_{i/e}\lambda_{g_{i/e}}}{Ð_{p_{i/e}}} \tag{3.44}$$

Regarding the heat transfer through the pipe walls Benson amongst others relied on the Reynolds-Colburn analogy, which allows calculating the film heat transfer coefficient by the following expression,

$$\alpha_i = \varrho_i \frac{f_i}{2} c_{p_i} u_i \tag{3.45}$$

Under this approach one should assume that the wall temperature remains constant over time, but as the experiments have proven [1985] (200), [1996] (309), the heat transfer through the pipes has got an influence on the pressure characteristics of the system, thus a mathematical model of the temperatures along the pipes was developed.

Therefore if a path line is followed in the tube it may be considered as representing the motion of a infinitesimal layer of gas. The rate at which energy is being transferred per unit mass in this layer is given by $\dot{Q}$ and it is for this quantity that some assumption must be made. In evaluating $\dot{Q}$ the assumption that the heat transfer coefficient at any instant can be calculated from the instantaneous value of the velocity by means of the appropriate steady state relationship, yields

$$\dot{q}_i = \frac{4\alpha_i\,(T_{w_i} - T_{g_i})}{\varrho_i Ð_{p_i}} \tag{3.46}$$

The heat transfer per unit of mass in equation (3.28) and (3.29) is the arithmetic mean value of the values at the corresponding node i, thus

$$\begin{aligned}\lambda_{P\prime} &= \lambda_R - \frac{(\lambda_R+\beta_R)(\lambda_R-\beta_R)}{2}\left(\frac{1}{\mathcal{D}_p}\right)\left(\frac{d\mathcal{D}_p}{dX}\right)\Delta\tau + \left(\frac{\lambda_R+\beta_R}{2}\right) \\ &\left(\frac{A_{A_{P\prime}}-A_{A_R}}{A_{A_R}}\right) - \frac{f_R L_{ref}}{\mathcal{D}_R}\frac{(\lambda_R-\beta_R)^2}{\gamma-1}\frac{\lambda_R-\beta_R}{|\lambda_R-\beta_R|}\left(1-2\frac{\lambda_R-\beta_R}{\lambda_R+\beta_R}\right)\Delta\tau + \\ &\frac{(\gamma-1)^2}{2}\left(\frac{\dot{q}_{i-1}+\dot{q}_i}{2}\right)\frac{L_{ref}}{a_0^3}\frac{2}{(\lambda_R+\beta_R)}\Delta\tau \end{aligned} \tag{3.47}$$

$$\begin{aligned}\beta_{P\prime} &= \beta_S - \frac{(\lambda_S+\beta_S)(\lambda_S-\beta_S)}{2}\left(\frac{1}{\mathcal{D}_p}\right)\left(\frac{d\mathcal{D}_p}{dX}\right)\Delta\tau + \left(\frac{\lambda_S+\beta_S}{2}\right) \\ &\left(\frac{A_{A_{P\prime}}-A_{A_S}}{A_{A_S}}\right) - \frac{f_S L_{ref}}{\mathcal{D}_S}\frac{(\lambda_S-\beta_S)^2}{\gamma-1}\frac{\lambda_S-\beta_S}{|\lambda_S-\beta_S|}\left(1+2\frac{\lambda_S-\beta_S}{\lambda_S+\beta_S}\right)\Delta\tau + \\ &\frac{(\gamma-1)^2}{2}\left(\frac{\dot{q}_i+\dot{q}_{i+1}}{2}\right)\frac{L_{ref}}{a_0^3}\frac{2}{(\lambda_S+\beta_S)}\Delta\tau \end{aligned} \tag{3.48}$$

The value of $\dot{Q}$ in equation (3.30) will be assessed at point M for all grid points, therefore the compatibility equation becomes

$$dA_A = \frac{\gamma-1}{2}L_{ref}\frac{A_{A_M}}{{A_M}^2}\left(\frac{\dot{q}_M}{a_0^3}+\frac{2f}{\mathcal{D}_p}\left|\frac{\lambda_M-\beta_M}{\gamma-1}\right|^3\right)\Delta\tau \tag{3.49}$$

The heat transfer along the pipe accounts for radial and axial conduction heat and convection heat at the inner and outer of the pipes. It was assumed, however, that the radiation heat transfer was not relevant for the analysis under study.

Figure 3.3 shows the pipe discretization which allows defining the energy balance for each control volume. Therefore for any intermediate mesh point as well as for the control volumes limiting with the vessels and valve manifold, the energy balance is detailed in tables

The heat transfer between the pipe and the bonded seals as well as between the last ones and the valve manifold or vessels was neglected. On the other hand the end pipe wall exposed to the internal fluid was treated as a vertical wall where only convection heat transfer occurs.

After rearranging the above-mentioned equations an expression can be obtained for each mesh point that takes the form,

$$a_{i,j}T^{t+\Delta t}_{w_{i,j}} = b_{i,j}T^t_{w_{i+1,j}} + c_{i,j}T^t_{w_{i-1,j}} + \left(e_{i,j}T^t_{w_{i,j+1}} + f_{i,j}T^t_{w_{i,j-1}} + d_{i,j}\right) \tag{3.59}$$

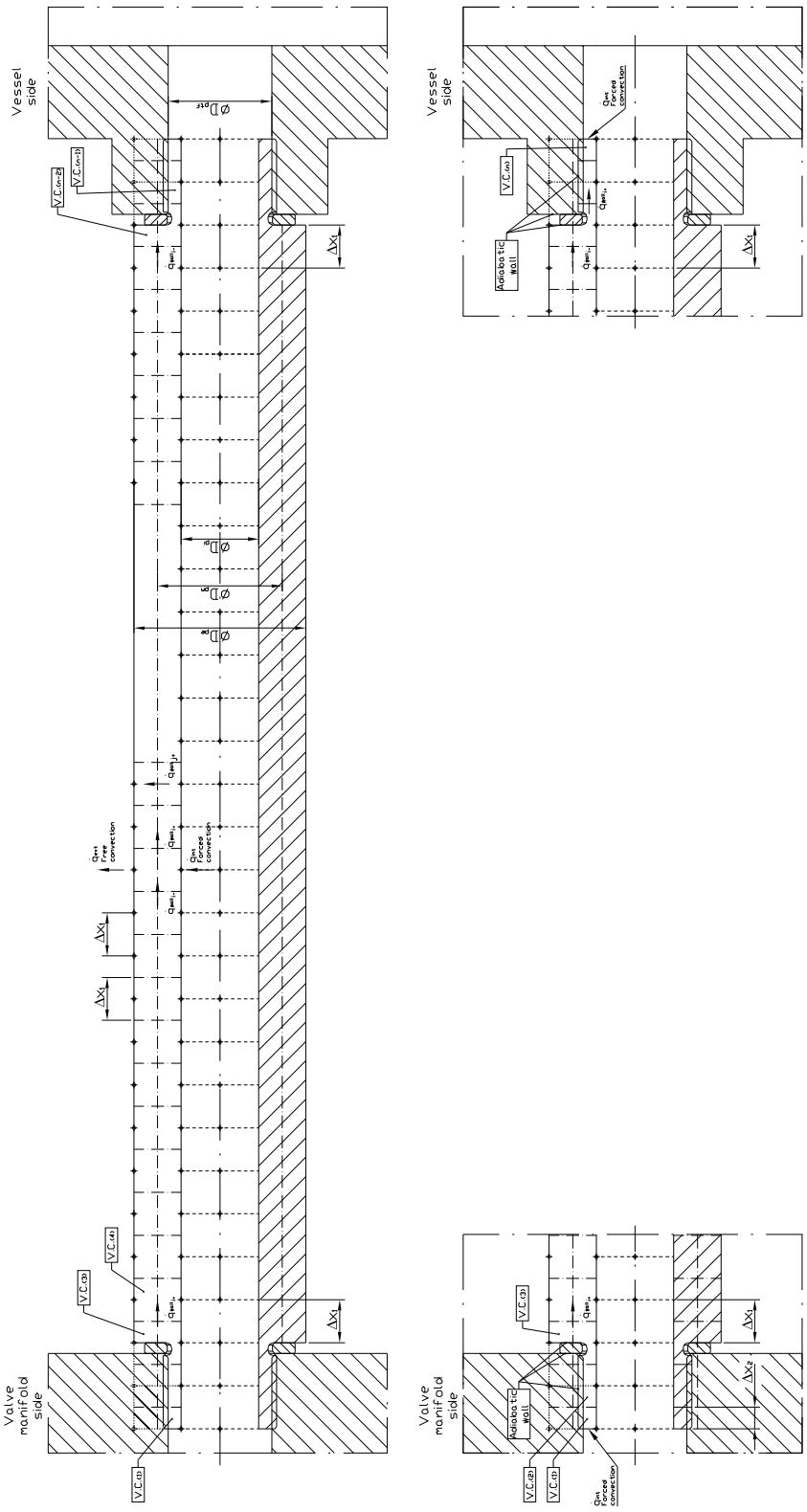

Figure 3.3: Mesh along the axial and radial direction of a non-tapered pipe

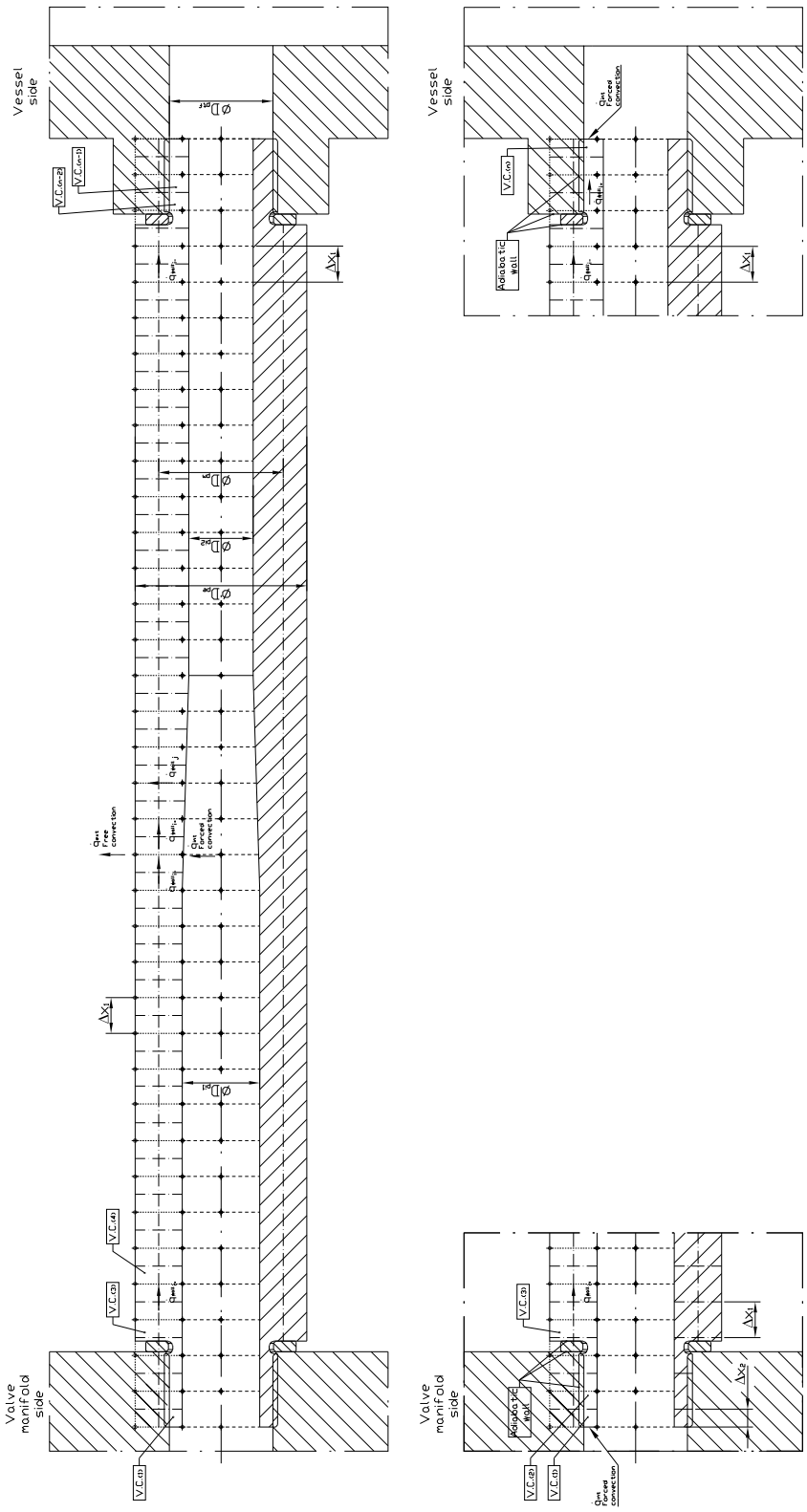

Figure 3.4: Mesh along the axial and radial direction of a pipe with gradual area changes

Table 3.1

Governing equations of heat transfer for intermediate nodes

$\boxed{V.C._{node=(i=1,j=1)}}$

$$\alpha_{i,j}^{t}\left(T_{g_i}^{t}-T_{w_{i,j}}^{t}\right)\pi \mathcal{D}_{p_i}\Delta x_2+\overline{\alpha}_{i,j}^{t}\left(T_{g_c}^{t}-T_{w_{i,j}}^{t}\right)\frac{\pi}{4}\left(\mathcal{D}_{p_{tf}}^{2}-\mathcal{D}_{p_i}^{2}\right)= \lambda_{w_{(+i)}}\left(\frac{T_{w_{i,j}}^{t}-T_{w_{i+1,j}}^{t}}{\Delta x_1}\right)\frac{\pi}{4}\left(\mathcal{D}_{p_{tf}}^{2}-\mathcal{D}_{p_i}^{2}\right)+\varrho_w C_{p_w}V_{i,j}\left(\frac{T_{w_{i,j}}^{t+\Delta t}-T_{w_{i,j}}^{t}}{\Delta t}\right) \quad (3.50)$$

$\boxed{V.C._{node=(3,j)<i,j<((n-2),j)}}$

$$\lambda_{w_{(-i)}}\left(\frac{T_{w_{i-1,j}}^{t}-T_{w_{i,j}}^{t}}{\Delta x_1}\right)\frac{\pi}{4}\left(\mathcal{D}_{p_m}^{2}-\mathcal{D}_{p_i}^{2}\right)+\alpha_{i,j}^{t}\pi \mathcal{D}_{p_i}\Delta x_1(T_{g_i}^{t}-T_{w_{i,j}}^{t})=\lambda_{w_{(+j)}}\left(\frac{T_{w_{i,j}}^{t}-T_{w_{i,j+1}}^{t}}{\Delta r_1}\right)\pi \mathcal{D}_{p_m}\Delta x_1+ \lambda_{w_{(+i)}}\left(\frac{T_{w_{i,j}}^{t}-T_{w_{i+1,j}}^{t}}{\Delta x_1}\right)\frac{\pi}{4}\left(\mathcal{D}_{p_m}^{2}-\mathcal{D}_{p_i}^{2}\right)+\varrho_w C_{p_w}V_{i,j}\left(\frac{T_{w_{i,j}}^{t+\Delta t}-T_{w_{i,j}}^{t}}{\Delta t}\right) \quad (3.51)$$

$\boxed{V.C._{node=(3,j+1)<i,j+1<((n-2),j+1)}}$

$$\lambda_{w_{(-i)}}\left(\frac{T_{w_{i-1,j+1}}^{t}-T_{w_{i,j+1}}^{t}}{\Delta x_1}\right)\frac{\pi}{4}\left(\mathcal{D}_{p_e}^{2}-\mathcal{D}_{p_m}^{2}\right)+\lambda_{w_{(-j)}}\left(\frac{T_{w_{i,j}}^{t}-T_{w_{i,j+1}}^{t}}{\Delta r_1}\right)\pi \mathcal{D}_{p_m}\Delta x_1= \alpha_{e}^{t}\pi \mathcal{D}_{p_e}\Delta x_1(T_{w_{i,j+1}}^{t}-T_{amb})+\lambda_{w_{(+i)}}\left(\frac{T_{w_{i,j+1}}^{t}-T_{w_{i+1,j+1}}^{t}}{\Delta x_1}\right)\frac{\pi}{4}\left(\mathcal{D}_{p_e}^{2}-\mathcal{D}_{p_m}^{2}\right)+\varrho_w C_{p_w}V_{i,j+1}\left(\frac{T_{w_{i,j+1}}^{t+\Delta t}-T_{w_{i,j+1}}^{t}}{\Delta t}\right) \quad (3.52)$$

Table 3.2

Governing equations of heat transfer for boundary nodes (continuous on Table 3.3)

$\boxed{V.C._{node=(3,j)}}$

$$\lambda_{w_{(-i)}}\left(\frac{T^t_{w_{i-1,j}}-T^t_{w_{i,j}}}{\Delta x_1}\right)\frac{\pi}{4}\left(\text{Đ}^2_{p_{tf}}-\text{Đ}^2_{p_i}\right)+\alpha^t_{i,j}\pi\text{Đ}_{p_i}\Delta x_1(T^t_{g_i}-T^t_{w_{i,j}})=\lambda_{w_{(+j)}}\left(\frac{T^t_{w_{i,j}}-T^t_{w_{i,j+1}}}{\Delta r_1}\right)\pi\text{Đ}_{p_m}\frac{\Delta x_1}{2}$$
$$+\lambda_{w_{(+i)}}\left(\frac{T^t_{w_{i,j}}-T^t_{w_{i+1,j}}}{\Delta x_1}\right)\frac{\pi}{4}\left(\text{Đ}^2_{p_m}-\text{Đ}^2_{p_i}\right)+\varrho_w C_{p_w}V_{i,j}\left(\frac{T^{t+\Delta t}_{w_{i,j}}-T^t_{w_{i,j}}}{\Delta t}\right) \quad (3.53)$$

$\boxed{V.C._{node=((n-2),j)}}$

$$\lambda_{w_{(-i)}}\left(\frac{T^t_{w_{i-1,j}}-T^t_{w_{i,j}}}{\Delta x_1}\right)\frac{\pi}{4}\left(\text{Đ}^2_{p_m}-\text{Đ}^2_{p_i}\right)+\alpha^t_{i,j}\pi\text{Đ}_{p_i}\Delta x_1(T^t_{g_i}-T^t_{w_{i,j}})=\lambda_{w_{(+j)}}\left(\frac{T^t_{w_{i,j}}-T^t_{w_{i,j+1}}}{\Delta r_1}\right)\pi\text{Đ}_{p_m}\frac{\Delta x_1}{2}$$
$$+\lambda_{w_{(+i)}}\left(\frac{T^t_{w_{i,j}}-T^t_{w_{i+1,j}}}{\Delta x_1}\right)\frac{\pi}{4}\left(\text{Đ}^2_{p_{tf}}-\text{Đ}^2_{p_i}\right)+\varrho_w C_{p_w}V_{i,j}\left(\frac{T^{t+\Delta t}_{w_{i,j}}-T^t_{w_{i,j}}}{\Delta t}\right) \quad (3.54)$$

$\boxed{V.C._{node=(3,j+1)}}$

$$\lambda_{w_{(-j)}}\left(\frac{T^t_{w_{i,j}}-T^t_{w_{i,j+1}}}{\Delta r_1}\right)\pi\text{Đ}_{p_m}\frac{\Delta x_1}{2}=\lambda_{w_{(+i)}}\left(\frac{T^t_{w_{i,j+1}}-T^t_{w_{i+1,j+1}}}{\Delta x_1}\right)\frac{\pi}{4}\left(\text{Đ}^2_{p_e}-\text{Đ}^2_{p_m}\right)+$$
$$\alpha^t_e\pi\text{Đ}_{p_e}\frac{\Delta x_1}{2}(T^t_{w_{i,j+1}}-T^t_{amb})+\varrho_w C_{p_w}V_{i,j+1}\left(\frac{T^{t+\Delta t}_{w_{i,j+1}}-T^t_{w_{i,j+1}}}{\Delta t}\right) \quad (3.55)$$

Table 3.3

Governing equations of heat transfer for boundary nodes

$\boxed{V.C._{node=((n-2),j+1)}}$

$$\lambda_{w_{(-i)}}\left(\frac{T^t_{w_{i-1,j+1}}-T^t_{w_{i,j+1}}}{\Delta x_1}\right)\frac{\pi}{4}\left(\mathcal{D}^2_{p_e}-\mathcal{D}^2_{p_m}\right)+\lambda_{w_{(-j)}}\left(\frac{T^t_{w_{i,j}}-T^t_{w_{i,j+1}}}{\Delta r_1}\right)\pi\mathcal{D}_{p_m}\frac{\Delta x_1}{2}=$$
$$\alpha^t_e\pi\mathcal{D}_{p_e}\frac{\Delta x_1}{2}(T^t_{w_{i,j+1}}-T^t_{amb})+\varrho_w C_{p_w}V_{i,j+1}\left(\frac{T^{t+\Delta t}_{w_{i,j+1}}-T^t_{w_{i,j+1}}}{\Delta t}\right) \quad (3.56)$$

$\boxed{V.C._{node=(i=2\ \&\ (n-1),j=1)}}$

$$\alpha^t_{i,j}\left(T^t_{g_i}-T^t_{w_{i,j}}\right)\pi\mathcal{D}_{p_i}\Delta x_1+\lambda_{w_{(-i)}}\left(\frac{T^t_{w_{i-1,j}}-T^t_{w_{i,j}}}{\Delta x_1}\right)\frac{\pi}{4}\left(\mathcal{D}^2_{p_{tf}}-\mathcal{D}^2_{p_i}\right)=$$
$$\lambda_{w_{(+i)}}\left(\frac{T^t_{w_{i,j}}-T^t_{w_{i+1,j}}}{\Delta x_1}\right)\frac{\pi}{4}\left(\mathcal{D}^2_{p_{tf}}-\mathcal{D}^2_{p_i}\right)+\varrho_w C_{p_w}V_{i,j}\left(\frac{T^{t+\Delta t}_{w_{i,j}}-T^t_{w_{i,j}}}{\Delta t}\right) \quad (3.57)$$

$\boxed{V.C._{node=(n,j=1)}}$

$$\alpha^t_{i,j}\left(T^t_{g_i}-T^t_{w_{i,j}}\right)\pi\mathcal{D}_{p_i}\Delta x_2+\overline{\alpha}^t_{i,j}\left(T^t_{g_c}-T^t_{w_{i,j}}\right)\frac{\pi}{4}\left(\mathcal{D}^2_{p_{tf}}-\mathcal{D}^2_{p_i}\right)+$$
$$\lambda_{w_{(-i)}}\left(\frac{T^t_{w_{i-1,j}}-T^t_{w_{i,j}}}{\Delta x_1}\right)\frac{\pi}{4}\left(\mathcal{D}^2_{p_{tf}}-\mathcal{D}^2_{p_i}\right)+\varrho_w C_{p_w}V_{i,j}\left(\frac{T^{t+\Delta t}_{w_{i,j}}-T^t_{w_{i,j}}}{\Delta t}\right) \quad (3.58)$$

where the coefficients are described below,

$$a_{i,j} = \frac{\lambda_{-i}}{\Delta x_1}\frac{\pi}{4}\left(Đ_{p_{tf}}^2 - Đ_{p_i}^2\right) + \frac{\lambda_{+i}}{\Delta x_1}\frac{\pi}{4}\left(Đ_{p_{tf}}^2 - Đ_{p_i}^2\right) + \alpha_i^t \pi Đ_{p_i}\Delta x_1 + \alpha_e^t \pi Đ_{p_e}\Delta x_1 + \frac{\lambda_{+j}}{\Delta r_1}\pi Đ_{p_{tf}}\Delta x_1 + \varrho_w \frac{C_{p_w}}{\Delta t}V_{i,j} \quad (3.60)$$

$$b_{i,j} = \frac{\lambda_{+i}}{\Delta x_1}\frac{\pi}{4}\left(Đ_{p_{tf}}^2 - Đ_{p_i}^2\right) \quad (3.61)$$

$$c_{i,j} = \frac{\lambda_{-i}}{\Delta x_1}\frac{\pi}{4}\left(Đ_{p_{tf}}^2 - Đ_{p_i}^2\right) \quad (3.62)$$

$$e_{i,j} = \frac{\lambda_{+j}}{\Delta r_1}\pi Đ_{p_{tf}}\Delta x_1 \quad (3.63)$$

$$f_{i,j} = \frac{\lambda_{-j}}{\Delta r_1}\pi Đ_{p_{tf}}\Delta x_1 \quad (3.64)$$

$$d_{i,j} = \alpha_i^t T_{g_i}\pi Đ_{p_i}\Delta x_1 + \alpha_e^t T_{amb}\pi Đ_e \Delta x_1 + \varrho_w \frac{C_{p_w}}{\Delta t}V_{i,j} + e_{i,j} + f_{i,j} \quad (3.65)$$

Note that the heat transfer between the pipe and the valve manifold as well as the vessel inlet, which is contact with the pipe have been disregarded, therefore depending on the location of the grid point within the pipe the internal and external convection heat transfer will be removed, and analogously will apply to the radial conduction heat transfer.

In order to solve the system of equations the Tri-Diagonal Matrix Algorithm (TDMA) algorithm is applied to the radial and axial direction respectively until reaching a prescribed accuracy. The fluid temperature is taken directly from the flow solver which is running in parallel to the heat transfer algorithm.

3.1.3 Friction coefficient at the pipes

In the same way, the friction factor in a smooth circular duct can be estimated through the expressions described below. Those equations can be applied under the assumption that the flow is regarded as subsonic.

$$f = \begin{cases} \dfrac{16}{Re} & \text{for laminar flow } (Re < 2300) \\ \dfrac{0.0791}{Re^{0.25}} & \text{for transitional flow } (2300 \leq Re \leq 4000) \\ \dfrac{0.04}{Re^{0.16}} & \text{for turbulent flow } (Re > 4000) \end{cases} \quad (3.66)$$

3.1.4 Path lines characteristics computation

The entropy level at each node will be determined by the path line characteristics. The technique, in this case, to figure out the location of each path line at time t is based on an inverse-marching method [1976] (354), [1977] (355). By following this method there will be no need for an additional interpolation to ensure that the path line slope pass through the node P' at time $t+\Delta t$. As it was necessary to preserve the identity of each path line due to the complexity of the process, this method was considered accurate enough to analyze the entropy variation along the pipes.

Referring to figure 3.2 the Riemann invariants can be calculated by linear interpolation,

$$\lambda_M = \lambda_i + (\lambda_i - \lambda_{i-1}) \left(\frac{x_M - x_{i-1}}{x_i - x_{i-1}} \right) \tag{3.67}$$

Then assuming the path line is straight over the short dimensional interval dt,

$$x_{P'} = x_M + \left(\frac{\lambda_M - \beta_M}{\gamma - 1} \right) \Delta\tau \tag{3.68}$$

from the path line compatibility equation yields

$$\delta A_{A_M} = \frac{(\gamma - 1)}{2} \frac{4A_{A_M}}{(\lambda_M + \beta_M)^2} \left(\frac{\dot{q} L_{ref}}{a^3{}_0} + \frac{2 f L_{ref}}{Đ_p} \left| \frac{\lambda_M - \beta_M}{\gamma - 1} \right|^3 \right) \tag{3.69}$$

and consequently,

$$\delta A'_{A_P} = A_{A_M} + \delta A_{A_M} \tag{3.70}$$

The entropy level at nodes R and S can be obtained by linear interpolation.

3.1.5 Pipes with variable cross-section

The area term indicated in equations (3.28) and (3.29) is developed in terms of the internal circular pipe diameter. Then,

$$\frac{1}{\breve{A}} \frac{d\breve{A}}{dX} = \frac{2}{Đ_p} \frac{dĐ_p}{dX} \tag{3.71}$$

being,

$$\frac{1}{Đ_p} \frac{dĐ_p}{dX} = \frac{2 \left(\frac{dĐ_p}{dX} \right)}{2Đ_{p_{left}} + \frac{dĐ_p}{dX}(X_R + X_P)} \tag{3.72}$$

and the average diameter

$$\overline{\mathcal{D}_p} = \mathcal{D}_{p_{left}} + \frac{d\mathcal{D}_p}{dX}\left(\frac{X_R + X_P}{2}\right) \tag{3.73}$$

On figure 3.5 is depicted the transformation from a tapered pipe to the equivalent mean diameter pipe, which is determined between the nodes R and P and P and S respectively. Note that those positions are exactly the ones associated to the λ and β characteristics at a non-dimensional time τ.

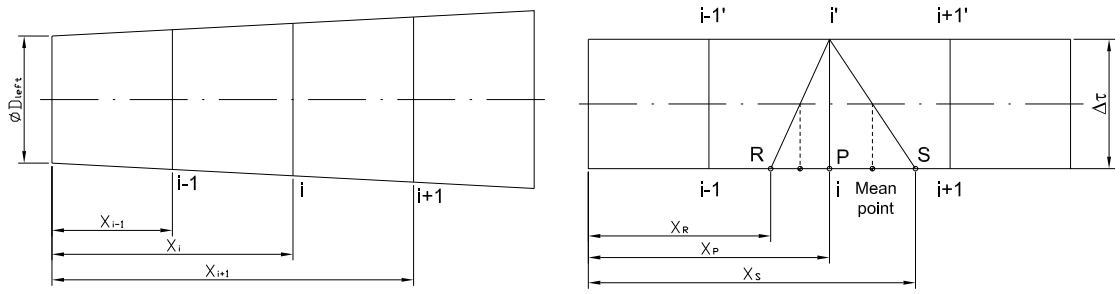

(a) Pipe section **(b)** Characteristics lines at the x-t diagram

Figure 3.5: Transformation of a tapered pipe

The influence of the pipe cross-sectional area variation along the pipe length was also analysed by considering the tapered pipe as a series of straigth pipes with an increasing or decreasing area change depending on the pipe geometry (36).

Thus, the equivalent diameter between the first two pipe sections is for the first section $\mathcal{D}_{p_{m_1}} = \sqrt{\frac{\mathcal{D}^2_{p_{left}} + \mathcal{D}^2_{p_1}}{2}}$, and for the second section results $\mathcal{D}_{p_{m_2}} = \sqrt{\frac{\mathcal{D}^2_{p_1} + \mathcal{D}^2_{p_2}}{2}}$ (refer to figure 3.6). Equally, the equivalent mean internal pipe area become $\breve{A}_{m_1} = \frac{\breve{A}_{left} + \breve{A}_1}{2}$ and $\breve{A}_{m_2} = \frac{\breve{A}_1 + \breve{A}_2}{2}$ respectively.

The process is inherently non-isentropic, therefore the calculation method applied to solve the governing equations between junctions makes use of the momentum equation. Nevertheless the Benson's constant pressure criterion is of significant help when solving the system of equations. The resulting equations to be used in case of having right-running flow sudden enlargement will be as follows,

$$\beta_{j,i} = \frac{2\beta_{1,i+1} - (1 - \frac{\breve{A}_{j,i}}{\breve{A}_{1,i+1}})\lambda_{j,i}}{1 + \frac{\breve{A}_{j,i}}{\breve{A}_{1,i+1}}} \tag{3.74}$$

$$\lambda_{1,i+1} = \frac{2\lambda_{j,i}\frac{\breve{A}_{j,i}}{\breve{A}_{1,i+1}} + \beta_{1,i+1}(1 - \frac{\breve{A}_{j,i}}{\breve{A}_{1,i+1}})}{1 + \frac{\breve{A}_{j,i}}{\breve{A}_{1,i+1}}} \tag{3.75}$$

The use of Benson's criterium is in fact conditioned by the particle Mach number at the join between sub-pipes. Therefore, taking into account that the number of nodes have been chosen to be $\frac{1}{6} < \frac{\breve{A}_{1,j+1}}{\breve{A}_{i,j}} < 6$, the existence of flow separation from the walls will be mainly associated to the flow regime. Based on this statement, the governing equations for sudden expansion between pipe sections yields,

Sudden expansion (right-running flow)

$$\varrho_{0_i}\left(\frac{\lambda_{j,i}+\beta_{j,i}}{2}\right)^{\frac{2}{\gamma-1}}\breve{A}_{j,i}a_{0_i}\left(\frac{\lambda_{j,i}-\beta_{j,i}}{\gamma-1}\right) + \varrho_{0_{i+1}}\left(\frac{\lambda_{j,i+1}+\beta_{j,i+1}}{2}\right)^{\frac{2}{\gamma-1}}\breve{A}_{j,i+1}a_{0_{i+1}}\left(\frac{\lambda_{j,i+1}-\beta_{j,i+1}}{\gamma-1}\right) = 0 \tag{3.76}$$

$$\left[\left\{a_{0_i}\left(\frac{\lambda_{j,i}-\beta_{j,i}}{\gamma-1}\right)\right\}^2 + \frac{2}{\gamma-1}a_{0_i}^2\left(\frac{\lambda_{j,i}+\beta_{j,i}}{2}\right)^2\right] - \left[\left\{a_{0_{i+1}}\left(\frac{\lambda_{j,i+1}-\beta_{j,i+1}}{\gamma-1}\right)\right\}^2 + \frac{2}{\gamma-1}a_{0_{i+1}}^2\left(\frac{\lambda_{j,i+1}+\beta_{j,i+1}}{2}\right)^2\right] = 0 \tag{3.77}$$

$$p_{ref}\left[\left(\frac{\lambda_{j,i}-\beta_{j,i}}{2}\right)^{\frac{2\gamma}{\gamma-1}} - \left(\frac{\lambda_{j,i+1}-\beta_{j,i+1}}{2}\right)^{\frac{2\gamma}{\gamma-1}}\right] - \left[\varrho_{0_i}\left(\frac{\lambda_{j,i}+\beta_{j,i}}{2}\right)^{\frac{2}{\gamma-1}}\frac{\breve{A}_{j,i}}{\breve{A}_{j,i+1}}\frac{2}{\gamma-1}a_{0_i}\left(\frac{\lambda_{j,i}-\beta_{j,i}}{\gamma-1}\right)\right] \left[a_{0_{i+1}}\left(\frac{\lambda_{j,i+1}-\beta_{j,i+1}}{\gamma-1}\right) - a_{0_i}\left(\frac{\lambda_{j,i}+\beta_{j,i}}{\gamma-1}\right)\right] = 0 \tag{3.78}$$

In the event of reaching the local acoustic velocity at the node (j,i), the reflecting characteristics is as follows,

$$\beta_{j,i} = \frac{1 + \dfrac{3-\gamma}{\gamma-1}\lambda_{j,i}}{\dfrac{\gamma+1}{\gamma-1}} \tag{3.79}$$

Differently from the expansion between sub-pipes, in a contracting pipe the flow is considered to be isentropic, therefore the $c_{0_{j,i}} = c_{0_{j,i+1}}$. The momentum equation is then neglected and gives,

Sudden contraction (right-running flow)

$$\varrho_{0_i}\left(\frac{\lambda_{j,i}+\beta_{j,i}}{2}\right)^{\frac{2}{\gamma-1}} \breve{A}_{j,i}\left(\frac{\lambda_{j,i}-\beta_{j,i}}{\gamma-1}\right) + \varrho_{0_{i+1}}\left(\frac{\lambda_{j,i+1}+\beta_{j,i+1}}{2}\right)^{\frac{2}{\gamma-1}} \breve{A}_{j,i+1}\left(\frac{\lambda_{j,i+1}-\beta_{j,i+1}}{\gamma-1}\right) = 0 \tag{3.80}$$

$$\left[\left(\frac{2}{\gamma-1}\left(\frac{\lambda_{j,i}-\beta_{j,i}}{\gamma-1}\right)\right)^2 + \frac{2}{\gamma-1}\left(\frac{\lambda_{j,i}+\beta_{j,i}}{2}\right)^2\right] - \left[\left(\frac{2}{\gamma-1}\left(\frac{\lambda_{j,i+1}-\beta_{j,i+1}}{\gamma-1}\right)\right)^2 + \frac{2}{\gamma-1}\left(\frac{\lambda_{j,i+1}+\beta_{j,i+1}}{2}\right)^2\right] = 0 \tag{3.81}$$

The sonic condition will be reached now at the node $(j, i+1)$, leading to

$$\lambda_{1,i+1} = \frac{1 + \dfrac{3-\gamma}{\gamma-1}\beta_{1,i+1}}{\dfrac{\gamma+1}{\gamma-1}} \tag{3.82}$$

3.1.6 Treatment of boundary conditions

The boundary conditions at the end pipes were described by the expressions originally derived by Benson [1955] (27), [1982] (29). As a first approximation two different types of boundary conditions were taken into account. The first type was related to the pipe ends limiting with the pressure vessels. And the second type concerned to the flow restriction through the valve manifold. In this last case, a restriction existing between the inlet and outlet pipes connecting the manifold with the vessels, was considered to be the most appropriate approach to simulate this type boundary condition, therefore the sonic conductance and critical pressure ratio experimentally determined were used to calculate the mass flow rate through the pneumatic component.

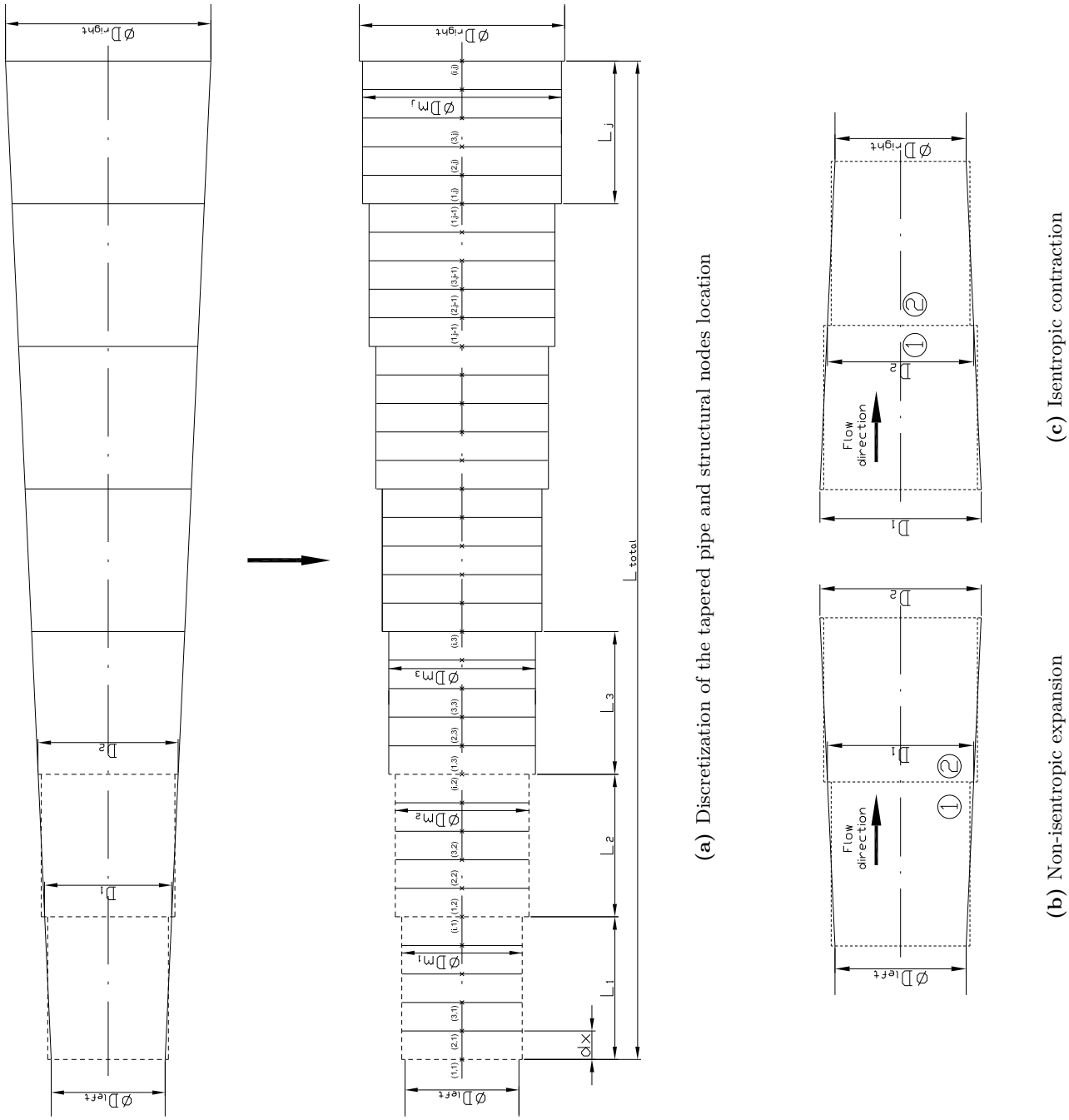

(a) Discretization of the tapered pipe and structural nodes location

(b) Non-isentropic expansion

(c) Isentropic contraction

Figure 3.6: Analysis of a pipe with variable cross-sectional area

3.1.6.1 End pipe model

The system of equations governing the fluid flow through a partially open end is shown below. It is worth to mention that even though the case under study does not include a geometric restriction at the pipe end, the real section of fluid flow at the throat was thought to be slightly smaller than the pipe area, therefore the equations below can also be applied. Two different scenarios were taken into account, at one side, flow from the cavity to the pipe (*inflow*) and, on the other side, flow from the pipe to the cavity (*outflow*). The equations governing the flow are described below:

1. Flow from the vessel to the pipe through a partially open end: In this situation the gas entering the pipe expands adiabatically but not isentropically due to the irreversibilities generated from the section, where the throat is located, into the pipe. On the other hand it was assumed that the contracting process from the outside (*cavity volume*) to the throat was isentropic. It must be noticed that this approach is based on considering the vessel at a constant static pressure.

   (a) Subsonic flow

$$\frac{a_t}{a_0} = \sqrt{\left(1 - \frac{\gamma - 1}{2}\left(\frac{u_t}{a_0}\right)^2\right)} \tag{3.83}$$

$$\left(\frac{u_p}{a_0}\right)^2 - \frac{2}{\gamma + 1}\left(\frac{1}{\phi}\frac{\left(\frac{a_t}{a_0}\right)^2}{\frac{u_t}{a_0}} + \gamma\frac{u_t}{a_0}\right)\frac{u_p}{a_0} + \frac{2}{\gamma + 1} = 0 \tag{3.84}$$

$$\left(\frac{p_p}{p_0}\right)^{\frac{\gamma-1}{2\gamma}} = \left(\frac{a_t}{a_0}\right)^{\frac{1}{\gamma}}\left[\phi\frac{u_t}{u_p}\left(1 - \frac{\gamma - 1}{2}\left\{\frac{u_p}{u_0}\right\}^2\right)\right]^{\frac{\gamma-1}{2\gamma}} \tag{3.85}$$

   (b) Sonic flow

$$\left(\frac{p_p}{p_0}\right)^{\frac{\gamma-1}{2\gamma}} = \left[\phi\left(\frac{2}{\gamma + 1}\right)^{\frac{\gamma+1}{2(\gamma-1)}}\left(\frac{1}{\frac{u_p}{a_0}} - \frac{\gamma - 1}{2}\frac{u_p}{a_0}\right)\right]^{\frac{\gamma-1}{2\gamma}} \tag{3.86}$$

(c) Sonic threshold

$$\left(\frac{u_p}{a_0}\right)^2 - \left(\frac{2}{\gamma+1}\right)^{3/2}\left(\frac{1}{\phi}+\gamma\right)\frac{u_p}{a_0} + \frac{2}{\gamma+1} = 0 \tag{3.87}$$

2. Flow from the pipe to the vessel through a partially open end: The common assumption when analyzing the outflow from the pipe to the cavity is that the turbulence generated during the expansion does not contribute to any pressure recovery which means that $p_t = p_0$ for subsonic flow. Additionally the flow from the pipe to the throat is contracting and, therefore, is taken as isentropic, being in this case represented by a contraction which goes from the pipe to the section where the throat is located.

(a) Subsonic flow

$$\left[\left(\frac{a_p}{a_0}\right)^{\frac{4}{\gamma-1}} - \phi^2\right]\left(\frac{u_p}{a_0}\right)^2 - \phi^2\frac{2}{\gamma-1}\left[\left(\frac{a_p}{a_0}\right)^2 - 1\right] = 0 \tag{3.88}$$

(b) Sonic flow

$$\phi^2 - \left[\frac{\gamma+1}{\gamma-1} - \frac{2}{\gamma-1}\left(\frac{a_p}{a_t}\right)_{cr}^2\right]\left(\frac{a_p}{a_t}\right)_{cr}^{\frac{4}{\gamma-1}} = 0 \tag{3.89}$$

$$\frac{u_p}{a_p} = \phi\left(\frac{a_t}{a_p}\right)_{cr}^{\frac{\gamma+1}{\gamma-1}} \tag{3.90}$$

Further development of the above illustrated expressions was presented by Blair and Cahoon [1972] (39), who turned the fluid velocity and sonic speed at the pipe end into non-dimensional terms represented by the Riemann variables. The resulting set of equations have been deducted in Chapter 8.

On the other hand the non-isentropic case brings to consider the influence of the entropy of the inflowing gas into the pipe. As discussed originally by Benson the corrected value of the Riemann invariant approaching the boundary must be determined through an iterative process. Therefore, prior to the evaluation of the Riemann invariant reflected at the pipe end it will be necessary to assess the entropy gradient as follows,

$$\lambda_c = \lambda_n + \left(\frac{\lambda_c + \beta_c}{2}\right)\left(\frac{A_{A_c} - A_{A_n}}{A_{A_c}}\right) \tag{3.91}$$

In our particular case two cases may be analysed, which are the open end and the partially open end boundary condition. For the first case the approach will be as described below,

$$\beta_c = \left(\frac{3-\gamma}{\gamma+1}\right)\lambda_c + \frac{2}{\gamma+1}\sqrt{(\gamma^2-1)A_0^2 + 2(1-\gamma)\lambda_c^2} \tag{3.92}$$

The value of β_c is substituted into equation (3.91) and the process will be repeated until reaching the requested accuracy for β.

3.1.6.2 Pipe restriction model - Valve analogy

The fluid flow through the reduction of cross-sectional area of a pipe has been usually analysed as a sudden restriction immediately followed by an enlargement inflow. The equations, therefore, governing the flow through the restriction are as follows,

(a) Subsonic flow:

$$\varrho_{0_1}\left[\frac{\lambda_{p_1}+\beta_{p_1}}{2}\right]^{\frac{2}{\gamma-1}} a_{0_1}\left(\frac{\lambda_{p_1}+\beta_{p_1}}{\gamma-1}\right)\breve{A}_1 - \varrho_t u_t \breve{A}_t = 0 \tag{3.93}$$

$$\varrho_t u_t \breve{A}_t - \varrho_{p_2}\left[\frac{\lambda_{p_2}+\beta_{p_2}}{2}\right]^{\frac{2}{\gamma-1}} a_{0_2}\left(\frac{\lambda_{p_2}+\beta_{p_2}}{\gamma-1}\right)\breve{A}_{p_2} = 0 \tag{3.94}$$

$$a_{0_1}^2\left[\frac{2}{\gamma-1}\left[\frac{\lambda_{p_1}+\beta_{p_1}}{2}\right]^2 + \left(\frac{\lambda_{p_1}-\beta_{p_1}}{\gamma-1}\right)^2\right] - \frac{2}{\gamma-1}a_t^2 - u_t^2 = 0 \tag{3.95}$$

$$\frac{2}{\gamma-1}a_t^2 + u_t^2 - a_{0_2}^2\left[\frac{2}{\gamma-1}\left[\frac{\lambda_{p_2}+\beta_{p_2}}{2}\right]^2 + \left(\frac{\lambda_{p_2}-\beta_{p_2}}{\gamma-1}\right)^2\right] = 0 \tag{3.96}$$

$$P_{ref}\breve{A}_{p_2}\left(\left[\left(\frac{p_t}{p_{ref}}\right)^{\frac{\gamma-1}{2\gamma}}\right]^{\frac{2}{\gamma-1}} - \left[\left(\frac{p_{p_2}}{p_{ref}}\right)^{\frac{\gamma-1}{2\gamma}}\right]^{\frac{2}{\gamma-1}}\right) +$$
$$\gamma\varrho_{0_1}\breve{A}_{p_1}\left[\frac{\lambda_{p_1}+\beta_{p_1}}{2}\right]^{\frac{2}{\gamma-1}} a_{0_1}\left(\frac{\lambda_{p_1}-\beta_{p_1}}{\gamma-1}\right)\left(u_t - a_{0_2}\left(\frac{\lambda_{p_2}-\beta_{p_2}}{\gamma-1}\right)\right) = 0 \tag{3.97}$$

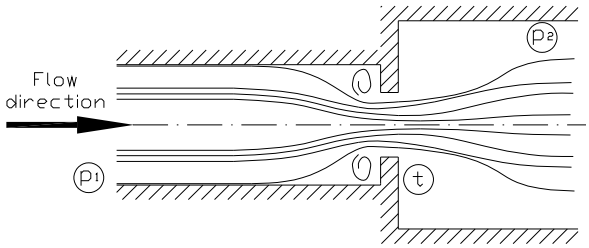

Figure 3.7: Flow restriction scheme

(b) Sonic flow: The sonic condition at the throat reduces the number of equations described for the subsonic case. In order to ensure the thermodynamic accuracy the momentum equation will be retained.

The system of equations was solved by using the Newton-Raphson method for multiple non-linear equations. The results, however, as there will be illustrated in Chapter 6 did not probe a good correlation between both experimental and mathematical values, therefore at that point it was considered that the influence of the air volume contained in the valve manifold could not be ignored and could also affect the recycling performance of the pneumatic system. On the other hand it is worth to mention that more recent publications [2010] (222) have questioned the validity of the equations above, which are based on isentropic flow assumptions. Despite the discrepancy between results when applying the mentioned premises, the theoretical model discussed before was considered to be accurate enough for the purpose of this study.

3.2 Numerical solution by finite volume method

3.2.1 The Lax Wendroff method

Based on the fact that the smooth waves forms exist for a short period of time due to the various geometries existing along the way several methods were put forward in the past with the intention to overcome such difficulties. In order to cope with the flow discontinuities the Euler equations must be expressed in a conservative form. Equations (3.1) to (3.3) can be written in vector form as:

$$\frac{\partial W}{\partial t} + \frac{\partial F(W)}{\partial x} + S(W) = 0 \tag{3.98}$$

where,

$$W(x,t) = \begin{bmatrix} \varrho \\ \varrho u \\ \varrho e_0 \end{bmatrix}$$

$$F(W) = \begin{bmatrix} \varrho u \\ \varrho u^2 + p \\ \varrho u h_0 \end{bmatrix}$$

$$S(W) = \begin{bmatrix} \varrho u \\ \varrho u^2 \\ \varrho u h_0 \end{bmatrix} \frac{d}{dx}(ln\breve{A}) + \begin{bmatrix} 0 \\ \varrho \frac{4f}{\breve{D}_p} \frac{u^2}{2} \frac{u}{|u|} \\ -\varrho \dot{Q} \end{bmatrix}$$

and $h_0 = e_0 + \dfrac{p}{\varrho}$ (stagnation enthalpy).

This approach is known as the finite-volume method, and, in essence satisfy the jump conditions across discontinuities. On the other hand the lack of a dissipative mechanism in the Euler equations after being discretized to a difference form without any modification result in numerical solutions which are non-stable. In order to overcome this inconvenient, a term of viscous diffusion is introduced to the difference scheme.

Based on the previous principle the Lax-Wendroff two-stage scheme was extensively used as a representative tool being part of the centered difference schemes. The original method is based on a the Taylor theorem,

$$W_i^{n+1} = W_i^n + \Delta t \frac{\partial W_i}{\partial t} + \frac{1}{2}\Delta t^2 \frac{\partial^2 W_i}{\partial t^2} + o(\Delta t^3) = W_i^n - \Delta t \left(\frac{\partial F_i}{\partial x} + S_i \right) - \frac{1}{2}\Delta t^2 \frac{\partial}{\partial t}\left(\frac{\partial F_i}{\partial x} \right) \quad (3.99)$$

where

$$\frac{\partial F_i}{\partial t} = \frac{\partial F_i}{\partial W}(\frac{\partial W}{\partial t} = -B(W)\left(\frac{\partial F_i}{\partial x} + S_i \right) \quad (3.100)$$

After substitution equation becomes,

$$W_i^{n+1} = W_i^n - \Delta t \left(\frac{\partial F_i}{\partial x} \right)_i + \frac{1}{2}\Delta t^2 \frac{\partial}{\partial x}\left(B(W)\frac{\partial F}{\partial x} \right)_i - \Delta t S_i \quad (3.101)$$

Here the centered spatial difference is used to obtain a second-order accuracy,

$$\left(\frac{\partial F_i}{\partial t}\right)_i = \frac{F_{i+1} - F_{i-1}}{2\Delta x} + o(\Delta x^2) \tag{3.102}$$

The artificial viscosity term is therefore

$$\frac{\partial}{\partial x}\left(B\frac{\partial F}{\partial x}\right)_i = \frac{1}{2}\Delta x^2\left[(B_{i+1} + B_i)(F_{i+1} - F_i) - (B_i + B_{i-1})(F_i - F_{i-1})\right] + o(\Delta x^2) \tag{3.103}$$

which makes the solution stable.

The two-stage version of the Lax-Wendroff method was proposed by Richtmyer. Each time step is further divided into two identical time stage lengths. The first stage uses the Lax's method, and the second stage is a mid-grid leapfrog calculation.

In the first stage,

$$W_{i-1/2}^{n+1/2} = \frac{1}{2}(W_{i-1}^n + W_i^n) - \frac{\Delta t}{2\Delta x}(F_i^n - F_{i-1}^n) - \frac{\Delta t}{4}(S_{i-1}^n + S_i^n) \tag{3.104}$$

and

$$W_{i+1/2}^{n+1/2} = \frac{1}{2}(W_i^n + W_{i+1}^n) - \frac{\Delta t}{2\Delta x}(F_{i+1}^n - F_i^n) - \frac{\Delta t}{4}(S_i^n + S_{i+1}^n) \tag{3.105}$$

and in the second stage,

$$W_i^{n+1} = W_i^n - \frac{\Delta t}{\Delta x}(F_{i+1/2}^{n+1/2} - F_{i-1/2}^{n+1/2}) - \frac{\Delta t}{2}(S_{i-1/2}^{n+1/2} + S_{i+1/2}^{n+1/2}) \tag{3.106}$$

However, since it has only first order accuracy, mass and energy discontinuity often occur in tapered pipes. On the other hand the two step Lax Wendroff scheme in its basic form has second order accuracy in time and space, but non physical overshoots were commonly generated being necessary the introduction of flux correction techniques which effectively removed the non physical overshoots. However the anti overshoot technique were not derived from the conservation equations that govern the flow, thus leading the scheme to become first order accurate.

3.2.2 The HLL approximate Riemann solver

With regards to the finite-volume technique, the Godunov upstream difference scheme, which is based on the exact solution of the Riemann problem, presented several advantages when solving the Euler equations, however due to the computing time required

to solve the non-linear Riemann problem some proposals where put forward to simplify the calculation process. This approach is known as the approximate Riemann solver, and in particular to the Harten, Lax and van Leer method. The HLL upstream difference method is an explicit scheme with first-order accuracy.

Below are the signal speeds at the mid-grid points, which are determined by using the arithmetic mean values at the corresponding grid points.

$$u_{i+1/2} = \frac{u_i + u_{i+1/2}}{2} \tag{3.107}$$

$$a_{i+1/2} = \frac{a_i + a_{i+1/2}}{2} \tag{3.108}$$

and similarly,

$$b^l_{i+1/2} = u_{i+1/2} - a_{i+1/2} \tag{3.109}$$

$$b^r_{i+1/2} = u_{i+1/2} + a_{i+1/2} \tag{3.110}$$

The flux and source terms at the mid-grid points are calculated based on the upstream scheme,

$$F_{i+1/2}(W_i, W_{i+1}) = \begin{cases} F(W_i) & \text{for } 0 \le b^l_{i+1/2} \\ \dfrac{b^r_{i+1/2}F(W_i) - b^l_{i+1/2}F(W_{i+1})}{b^r_{i+1/2} - b^l_{i+1/2}} + \\ \qquad \dfrac{b^r_{i+1/2}b^l_{i+1/2}}{b^r_{i+1/2} - b^l_{i+1/2}}(W_{i+1} - W_i) & \text{for } b^l_{i+1/2} \le 0 \le b^r_{i+1/2} \\ F(W_{i+1}) & \text{for } b^r_{i+1/2} \le 0 \end{cases} \tag{3.111}$$

$$S_i(W_{i-1/2}, W_{i+1/2}) = \begin{cases} S(W_{i-1/2}) & \text{for } 0 \le b^l_{i+1/2} \\ \dfrac{b^r_{i+1/2}S(W_{i-1/2})}{b^r_{i+1/2} - b^l_{i+1/2}} - \\ \qquad \dfrac{b^l_{i+1/2}S(W_{i+1/2})}{b^r_{i+1/2} - b^l_{i+1/2}} & \text{for } b^l_{i+1/2} \le 0 \le b^r_{i+1/2} \\ S(W_{i+1/2}) & \text{for } b^r_{i+1/2} \le 0 \end{cases} \tag{3.112}$$

The state variables at the mesh points for the new time step are determined as follows,

$$W_i^{n+1} = W_i^n - \frac{\Delta t}{\Delta x}\left[F_{i+1/2}(W) - F_{i-1/2}(W)\right] - \Delta t S(W_i) \tag{3.113}$$

In the absence of source terms the previous equations becomes,

$$W_i^{n+1} = W_i^n - \frac{\Delta t}{\Delta x}\left[F_{i+1/2}(W) - F_{i-1/2}(W)\right] \tag{3.114}$$

3.2.3 The HLLC approximate Riemann solver

The HLLC Riemann solver is a variant of the HLL scheme, with the main difference that contact and shear waves are introduced in the star region [2009] (314). Therefore the existence of a contact surface within the Star Region provides the additional star left and right regions, $*left$ and $*right$ (refer to fig.3.8). This solver is able to capture contact discontinuities, which are, as mentioned previously, common in compressible flows as the one being studied.

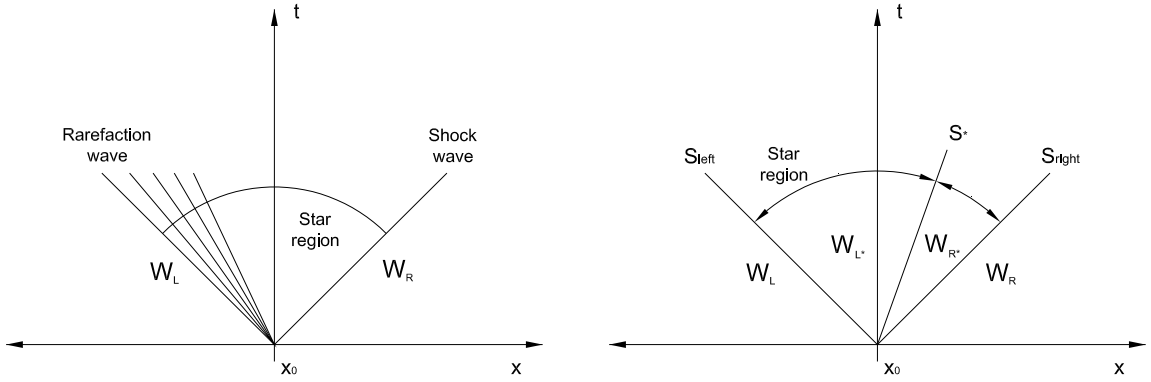

(a) Discontinuity generated at x_0 **(b)** Approximate HLLC Riemann solver

Figure 3.8: Solution in the *Star Region*

Keeping the same nomenclature to describe the wave speeds in the left, star and right regions, the solution to this is given as:

$$W_{HLLC} = \begin{cases} W_{left} & \text{if } \frac{x}{t} \leq S^{left} \\ W_{*left} & \text{if } S^{left} \leq \frac{x}{t} \leq S_* \\ W_{*right} & \text{if } S_* \leq \frac{x}{t} \leq S^{right} \\ W_{right} & \text{if } S^{right} \leq \frac{x}{t} \end{cases} \tag{3.115}$$

Applying the Rankine-Hugoniot conditions across each of the waves speeds, S_{left}, S_*, S_{right}, we get

$$F_{*left} = F_{left} + S_{left}(W_{*left} - W_{left}) \tag{3.116}$$

$$F_{*right} = F_{*left} + S_*(W_{*right} - W_{*left}) \tag{3.117}$$

$$F_{*right} = F_{right} + S_{right}(W_{*right} - W_{right}) \tag{3.118}$$

Then imposing the following conditions in the star region,

$$u_{*left} = u_{*right} = u_* = S_* \tag{3.119}$$

$$p_{*left} = p_{*right} = p_* \tag{3.120}$$

and re-arranging equations (3.116) and (3.118), the contact wave velocity can be determined,

$$S_* = \frac{p_R - p_L + \varrho_L u_L(S_L - u_L) - \varrho_R u_R(S_R - u_R)}{\varrho_L(S_L - u_L) - \varrho_R(S_R - u_R)} \tag{3.121}$$

In the same way the intermediate states can be deduced,

$$W_{*_K} = \varrho_K \left(\frac{S_K - u_K}{S_K - S_*}\right) \begin{bmatrix} 1 \\ S_* \\ \frac{E_K}{\varrho_K} + (S_* - u_K)\left[S_* + \dfrac{p_K}{\varrho_K(S_K - u_K)}\right] \end{bmatrix} \tag{3.122}$$

with the subscript K denoting $left$ and $right$ respectively. The wave speeds are defined as follows:

$$S_L = u_L - a_L q_L \tag{3.123}$$
$$S_* = u_* \tag{3.124}$$
$$S_R = u_R - a_R q_R \tag{3.125}$$

with

$$q_K = \begin{cases} 1 & \text{if } p_* \le p_K \\ \left[1 + \dfrac{\gamma+1}{2\gamma}\left(\dfrac{p_*}{p_K} - 1\right)\right]^{\frac{1}{2}} & \text{if } p_* > p_K \end{cases} \tag{3.126}$$

where the estimates for p_* and u_* are,

$$p_* = \frac{1}{2}(p_L + p_R) - \frac{1}{2}(u_R - u_L)(\tilde{\varrho}\tilde{a}) \tag{3.127}$$
$$u_* = \frac{1}{2}(u_L + u_R) - \frac{1}{2}\frac{(p_R - p_L)}{\tilde{\varrho}\tilde{a}} \tag{3.128}$$

Note that $\tilde{\varrho} = \frac{1}{2}(\varrho_{left} + \varrho_{right})$ and $\tilde{a} = \frac{1}{2}(a_{left} + a_{right})$.

The flow is supersonic if either $S_L > 0$ or $S_R < 0$, in which case the flux should be constructed using the W_L or W_R states. While if the flow is subsonic and $S_* \ge 0$, the flow moves from the left to right and W_L and W_L^* should be used to generate the flux otherwise the right state should be adopted.

Therefore, the HLLC intercell numerical flux is as follows,

$$F_{i+1/2}^{HLLC} = \begin{cases} F(W_{left}) & \text{for } 0 \leq S_{left} \\ F(W_{*left}) = F(W_{left}) + \\ \quad S_{left}(W_{*left} - W_{left}) & \text{for } S_{left} \leq 0 \leq S_{*} \\ F(W_{*right}) = F(W_{right}) + \\ \quad S_{right}(W_{*right} - W_{right}) & \text{for } S_{*} \leq 0 \leq S_{right} \\ F(W_{right}) & \text{for } S_{right} \leq 0 \end{cases} \tag{3.129}$$

3.2.4 The WAF method

The Weighted Average Flux method describes the intercell flux as follows,

$$F_{i+1/2}^{WAF} = \frac{1}{\Delta x} \int_{-\frac{\Delta x}{2}}^{\frac{\Delta x}{2}} F\left(W_{i+1/2}\left(x, t^n + \Delta t/2\right)\right) \mathrm{d}x \tag{3.130}$$

Taking that $W_{i+1/2}$ is the solution of the piecewise Riemann problem we may write

$$F_{i+1/2}^{WAF} = \frac{1}{\Delta x}\left(F_i^n + F_{i+1}^n\right) - \frac{1}{2}\sum_{k=1}^{N} c_k \Delta F_{i+1/2}^{(k)} \tag{3.131}$$

where $c_k = \frac{S_k \Delta t}{\Delta x}$ is the Courant number associated with wave k of speed S_k in the solution of the Riemann problem. Therefore when applying the equation (3.120) in equation provides a second order accurate scheme in space and time, which is accomplished without data reconstruction. Moreover, in order to avoid the oscillatory nature of the equation, a non-oscillatory TVD version is obtained as follows

$$F_{i+1/2}^{WAF} = \frac{1}{2}\left(F_i^n + F_{i+1}^n\right) - \frac{1}{2}\sum_{k=1}^{N} sign(c_k) A_k \Delta F_{i+1/2}^{(k)} \tag{3.132}$$

where A_k is a WAF flux limiter related to the conventional flux limiter B_k as shown below

$$A_k = 1 - (1 - |c_k|)B_k \tag{3.133}$$

The flux limiter $B_k(r)$ depends on the parameter $r^{(k)}$ which is actually associated to the wave k in the solution of the Riemann problem and it is defined as follows

$$r^{(k)} = \begin{cases} \dfrac{\Delta q^{(k)}_{i-1/2}}{\Delta q^{(k)}_{i+1/2}} & \text{if } c_k > 0 \\ \\ \dfrac{\Delta q^{(k)}_{i+3/2}}{\Delta q^{(k)}_{i+1/2}} & \text{if } c_k < 0 \end{cases} \tag{3.134}$$

where q states for suitable variable, and $\Delta q^{(k)}_{i+1/2}$ denotes the jump across the wave k. Finally, in combination the HLLC Riemann solver the intermediate waves can be determined.

Contrary to the approach followed with the HLL solver the source terms have not been included in the general flux scheme. In this case, the source term will be treated with an operator splitting technique that divides the Euler equations into a system of ODEs, resulting in

$$\frac{\partial W}{\partial t} + \frac{\partial F(W)}{\partial x} = 0 \tag{3.135}$$

$$\frac{\partial W}{\partial t} = S(W) \tag{3.136}$$

Equation (3.135) will be addressed as an homogeneous problem while the equation (3.136) will be solved by a first-order Euler method, which is realized through

$$W_i^{(*)} = W_i^{(t)} - \frac{\Delta t}{\Delta x}(W_i^{(t)} - W_{i-1}^{(t)}) \tag{3.137}$$

$$W_i^{(t+\Delta t)} = W_i^{(*)} - \lambda \frac{\Delta t}{\Delta x} S(W_i^{(*)}) \tag{3.138}$$

3.2.5 Ghost cell boundary conditions

The boundary conditions are imposed at the inlet and outlet of each pipe using ghost-cells, in which the first and last faces correspond to the domain limits and additional fictitious cells are outside the domain. A common approach used in many cases is to apply extrapolation techniques from the internal cell values to the unknown variables, however the procedure used to determine the variable values at the boundaries has been based on solving the governing equations through a convergent nozzle. Figure 3.9 illustrates the characteristics according to the flow direction.

According to the discretization shown in figures 3.10 and 3.11, the internal cavities of the valve manifold located immediately after the pipe ends were taken as relatively small

control volumes inside which the physical properties of the fluid could be determined under certain assumptions. Contrary to what occurs when considering the boundary conditions near a high volume reservoir the speed of the fluid cannot be disregarded, therefore the stagnation pressure will be influenced by the kinetic energy of the fluid at each specific control volume. The different cases that must be taken into account are detailed below:

1. Subsonic inflow:

$$\left(\frac{dp}{dt}\right)_p \pm \varrho_p a_p \left(\frac{du}{dt}\right)_p = (\gamma-1)\varrho\left(\dot{Q} + u\frac{4f}{Đ}\frac{u^2}{2}\frac{u}{|u|}\right) - \frac{a^2\varrho u}{\breve{A}}\frac{d\breve{A}}{dx} \mp \frac{4f}{Đ}\frac{\varrho a u^2}{2}\frac{u}{|u|} = 0 \tag{3.139}$$

$$\varrho_T u_T \frac{\breve{A}_T}{\breve{A}_P} = \varrho_P u_P \tag{3.140}$$

$$a_C^2 = a_P^2 + \frac{(\gamma-1)}{2}u_P^2 \tag{3.141}$$

$$\frac{p_C}{p_T} = \left(\frac{\varrho_C}{\varrho_T}\right)^\gamma \tag{3.142}$$

$$a_C^2 = a_T^2 + \frac{(\gamma-1)}{2}u_T^2 \tag{3.143}$$

$$p_T = p_P \tag{3.144}$$

2. Sonic inflow: In this case the equations governing the flow are the ones described above with the exception of the last equation that will be replaced by the condition $a_T = u_T$.

3. Subsonic outflow:

$$\left(\frac{dp}{dt}\right)_p \pm \varrho_p a_p \left(\frac{du}{dt}\right)_p = (\gamma-1)\varrho\left(\dot{Q} + u\frac{4f}{Đ}\frac{u^2}{2}\frac{u}{|u|}\right) - \frac{a^2\varrho u}{\breve{A}}\frac{d\breve{A}}{dx} \mp \frac{4f}{Đ}\frac{\varrho a u^2}{2}\frac{u}{|u|} = 0 \tag{3.145}$$

$$\varrho_T u_T \frac{\breve{A}_T}{\breve{A}_P} = \varrho_P u_P \tag{3.146}$$

$$\left(\frac{dp}{dt}\right)_p - a_P^2\left(\frac{d\varrho}{dt}\right)_P = (\gamma-1)\varrho\left(\dot{Q} + u\frac{4f}{Đ}\frac{u^2}{2}\frac{u}{|u|}\right) \tag{3.147}$$

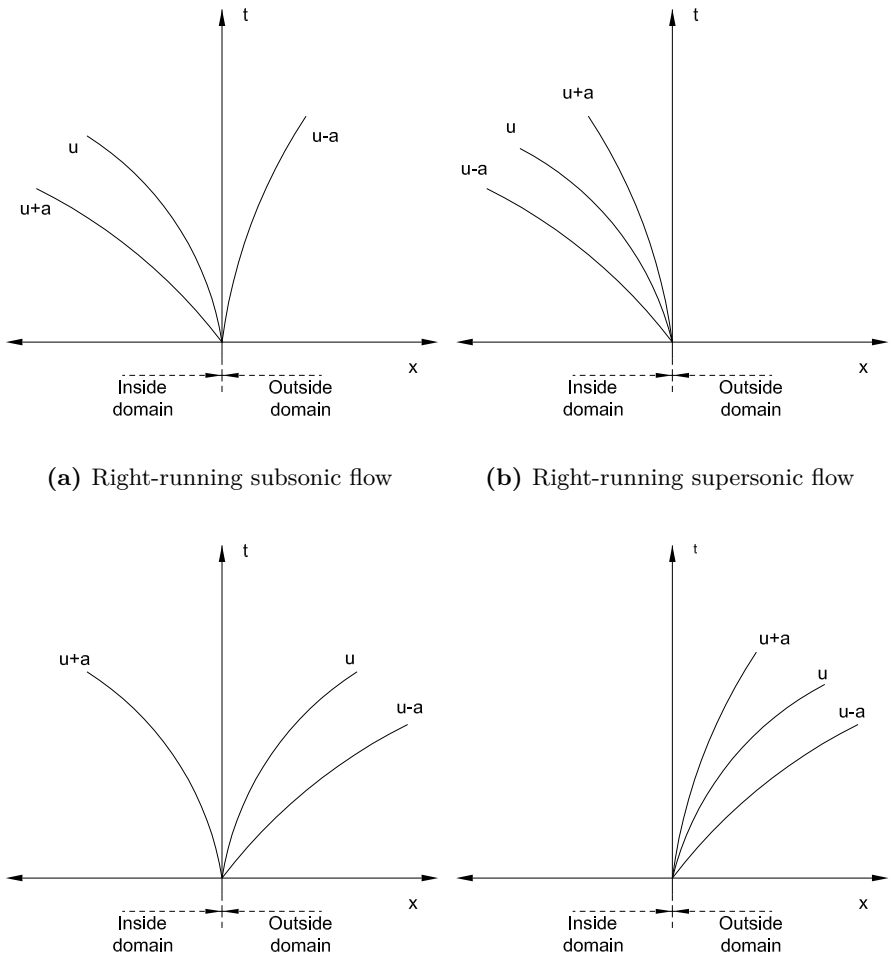

(a) Right-running subsonic flow **(b)** Right-running supersonic flow

(c) Left-running subsonic flow **(d)** Left-running supersonic flow

Figure 3.9: Direction of the characteristics according to the flow direction

$$a_C^2 = a_P^2 + \frac{(\gamma-1)}{2}u_P^2 \tag{3.148}$$

$$\frac{p_P}{p_T} = \left(\frac{\varrho_P}{\varrho_T}\right)^{\gamma} \tag{3.149}$$

$$a_P^2 + \frac{(\gamma-1)}{2}u_P^2 = a_T^2 + \frac{(\gamma-1)}{2}u_T^2 \tag{3.150}$$

$$p_T = p_C \tag{3.151}$$

4. Sonic outflow: Similarly to the sonic inflow the equations described above for the subsonic outflow can be used for the sonic case but with the exception of the last equations that must be substituted by $a_T = u_T$.

Therefore the state of gas at each boundary is obtained by solving the above equations coupled with the wave characteristics (211),(212). To determine the boundary condition at the pipe end connected with the vessel, the state in the vessel at time $t + \Delta t$ is obtained explicitly from the state at time t.

3.3 Flow characteristics through the pneumatic circuit

The methods previously discussed have been succesfully implemented in many applications, however it is not known to the author that a similar study has been reviewed by other researchers in the past. Figure 3.12 shows a schematic view of the pneumatic system employed to produce PET plastic bottles. The complexity of the air blowing production machine forces to the interconnecting pipes to take different forms depending on each specific design, however for the sake of simplicity the connections between components have been considered to be straight.

The pipe discretization has been applied to the existing connections taking into account that the mesh interval is common for all of them. This approach sometimes causes some deviations respect to the real dimension of the pipes, however those adjustments do not affect the calculation in any case.

As it will be discussed in Chapter 4 the valve manifold may be treated as a simple restriction with an effective area that varied depending on the flow path, but this approximation does not provide an adequate understanding of the physical process itself. In fact, the first attempts on representing the pressure characteristics clearly varied

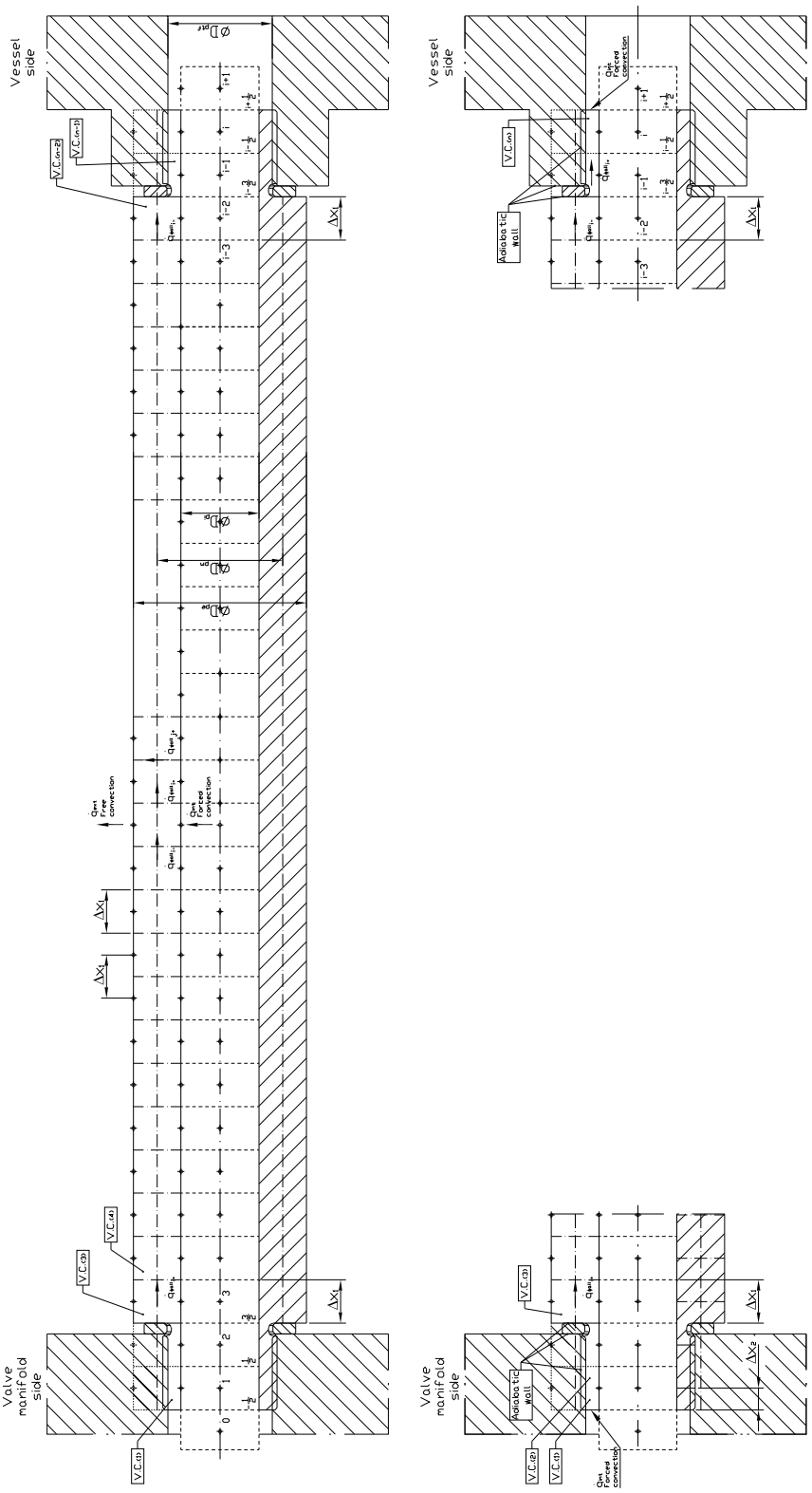

Figure 3.10: Computational grid along the axial and radial direction of a non-tapered pipe

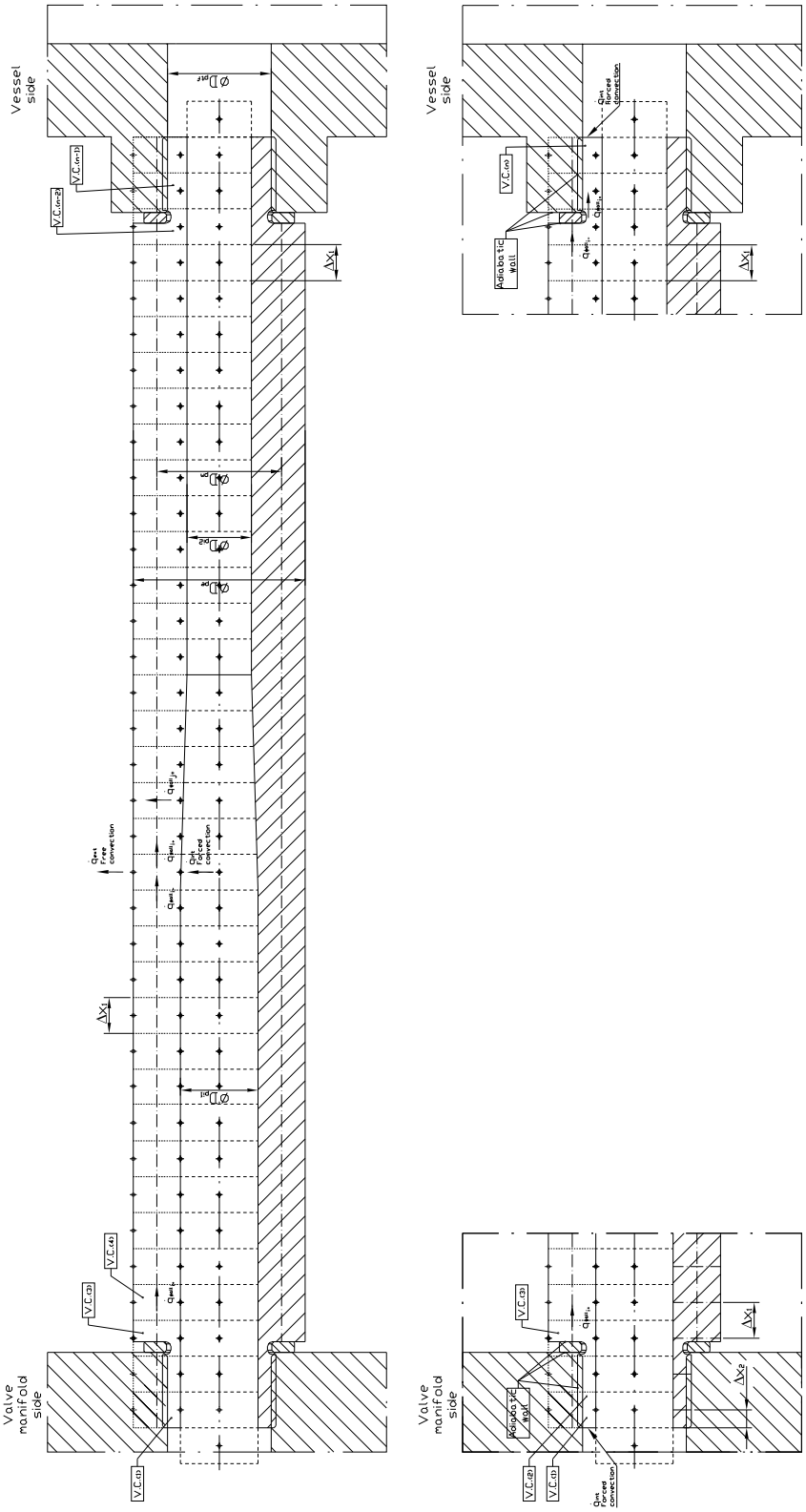

Figure 3.11: Computational grid along the axial and radial direction of a pipe with gradual area changes

respect to the experimental tests conducted in the laboratory. In must be pointed out that even though no technical article could be identified in the reviewed bibliography, the number of patents published by several manufacturers helped to compare the correct performance of the pneumatic set-up specially designed for this study. Also the pressure characteristics could be compared with the results discussed in the previous mentioned documentation. Therefore being aware of the limited available data, it was decided to validate the code by comparing the predicted and experimental results under different operating conditions and pneumatic lay-outs.

The air blowing process, as commented in Chapter 1, consists of three main stages. The first one supplied air at low pressure to the preform. What it is understood as low pressure should be considered a pressure range that varies between 10 and 15 bar respectively. The second stage provides high pressure to the perform being possible to reach up to 40 bar depending on the manufacturer. Finally the air is exhausted to the atmosphere once the shape of the bottle has been completely defined by the inner forces generated in the preform. As mentioned in Chapter 1 the numerous patents published on that respect have identified the need of recoverying part of the air instead of wasting considerable amounts of energy. Therefore it should be questioned which of the mathematical models better represent the real characteristics of the air blowing process.

Figures 3.13 to 3.15 show the pressure characteristics within the cavity and recycling vessels for different pneumatic lay-outs. The first attempts to replicate the air blowing process were mainly intended as a guide to reinforce the hypotheses and the cohesion of the theory discussed in this chapter, and highlighted a fair correlation with the documentation reviewed in Chapter 1. The simulations were conducted under the assumption that the pressure in the supply reservoirs remain constant. This point is mentioned here, but it will be covered later in Chapter 6 since the experimental condition differ from the previous statement.

The fluid flow through the pipes, that experience a gradual increase or decrease of the cross-sectional area, was analyzed with the two methods based on the Method of Characteristics. As previously discussed the first one divides the pipe into small straight sections which in turn are also subdivided into discretized pipes. The need of

determining the boundary conditions of the flow between those sections, which vary depending on the flow direction (expanding or contracting pipe), requires additional computational time. On the other hand the second approach, although divides the pipe into small straight sections, avoids the previous calculation. Both cases, were implemented under the assumption that the valve manifold behaves as a simple restriction, and helped to understand the significant influence of the valve manifold on the results. On the other hand, the second method presented spurious oscillations which were associated to shock generation. This phenomenon became more relevant when the tapered angle tended to increase and demonstrated the limitations of the mathematical model.

As a matter of fact the Method of Characteristics provides a closer correlation with the experimental model, however the assumptions applied in determining the boundary conditions at the pipe ends limiting with the valve manifold are constrained by the inner pipe diameter. Even though this aspect will be treated later in Chapters 4 and 7, the mentioned drawback could be only identified when considering the valve manifold as a combination of small chambers. This approach was taken after comparing the mathematical results, obtained when assuming the valve manifold as a restriction, with the experimental results. Basically the inner volume contained in the valve manifold was neglected when following the mentioned approach, dealing to a favourable result from energy saving point of view. Unfortunately these values were not realistic and put forward the idea of generating a mathematical model for the valve manifold to be coupled with the model already defined for the pipes.

3.4 Conclusion

A numerical one-dimensional gas dynamic algorithm for the fluid flow through the pipes connecting the valve manifold and the various reservoirs has been implemented. The model takes into account the convection and conduction heat transfer at the pipes, friction loss, variable cross-sectional of the pipe and entropy variation at each mesh node.

A brief summary of some of the most remarkable advances achieved on solving the main drawbacks inherently associated to the Method of Characteristics were also discussed. The spurious oscillations commonly caused by shock wave generation were adequately

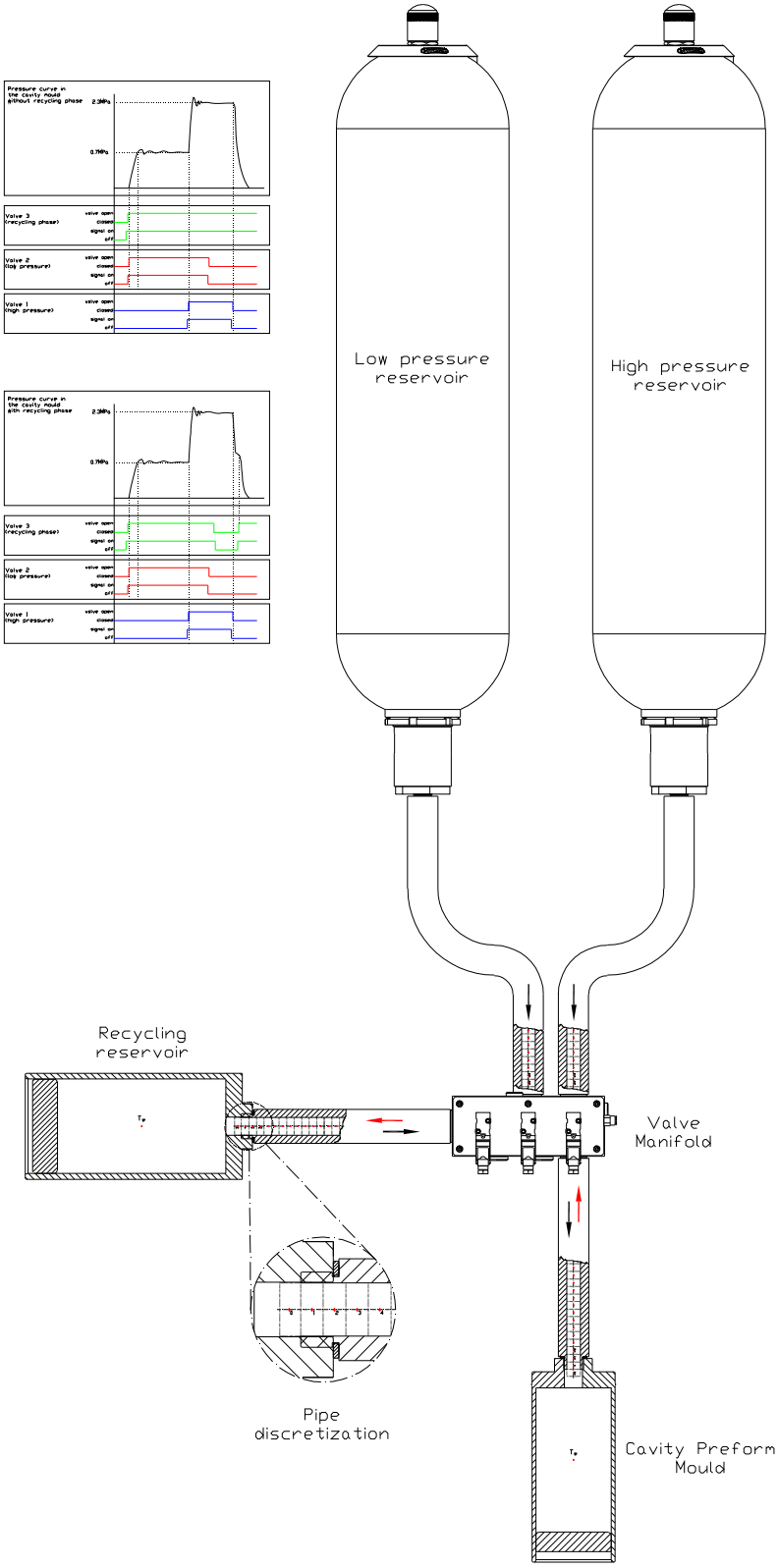

Figure 3.12: Schematic view of the pneumatic system under study including the mesh discretization for the HLL Riemann solver along the pipes

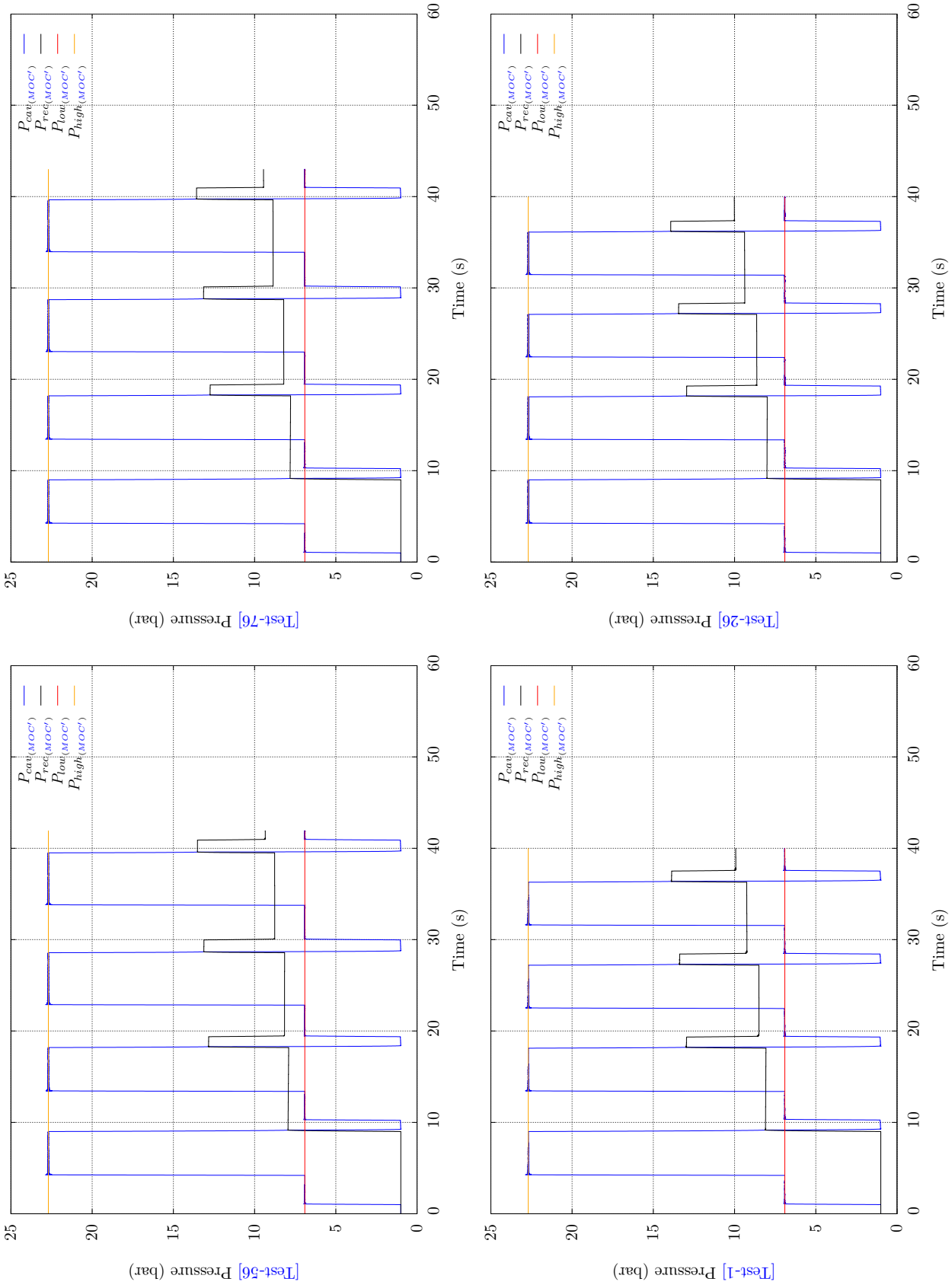

Figure 3.13: Pressure characteristics according to set-ups Test-1, Test-26, Test-56, and Test-76 (refer to Table 6.7). **MOC′**: Subscript that refers to the Method of Characteristics in combination with the valve manifold represented by a simple restriction, **cav**: Subscript that refers to the PET preform mould, **rec**: Subscript that refers to the recycling vessel, **low**: Subscript that refers to the low pressure reservoir, and **high**: Subscript that refers to the high pressure reservoir (refer to Table 6.7)

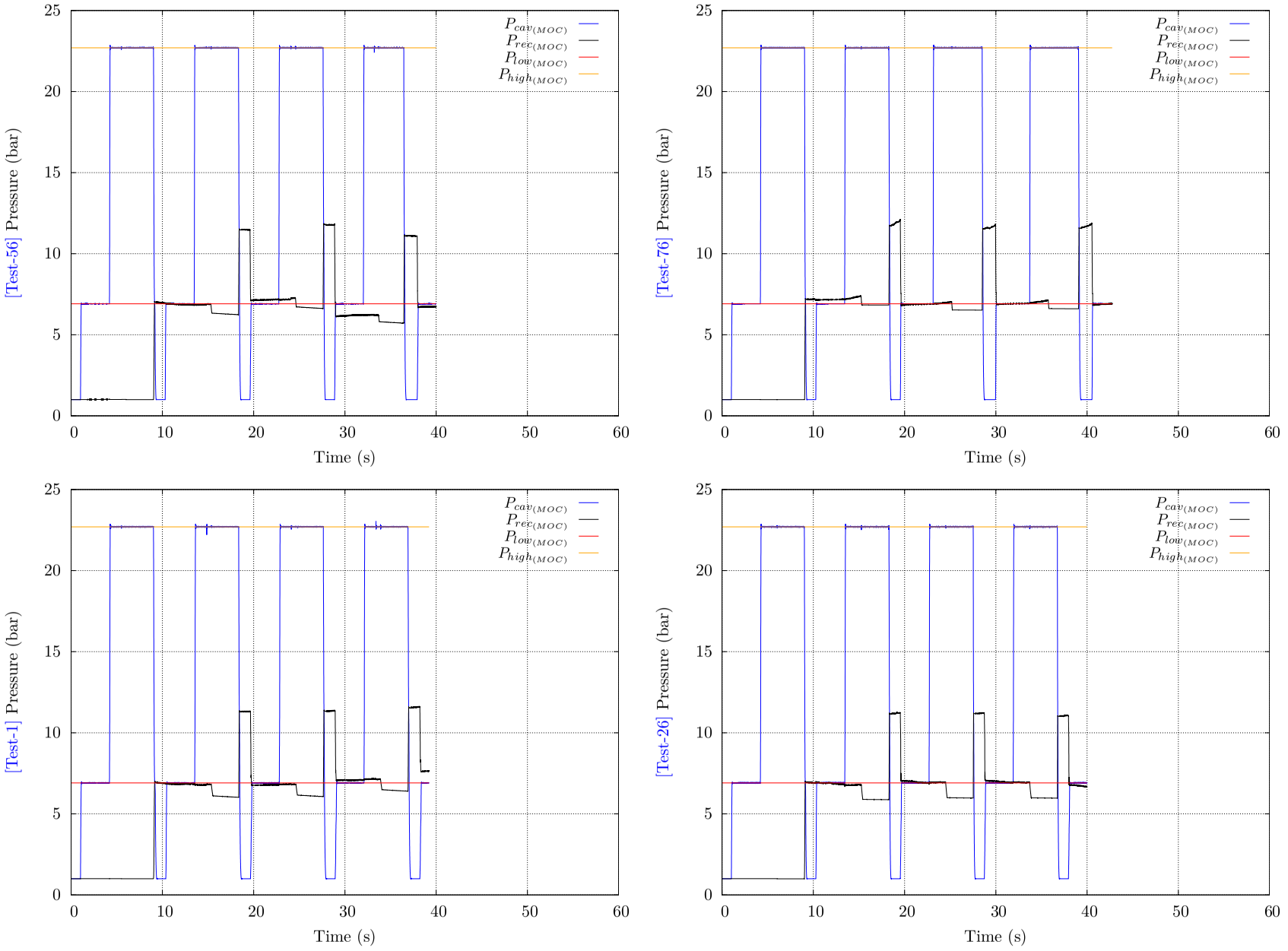

Figure 3.14: Pressure characteristics according to set-up Test-1, Test-26, Test-56, and Test-76 (refer to Table 6.7). **MOC**: Subscript that refers to the Method of Characteristics in combination with the valve manifold model, **cav**: Subscript that refers to the PET preform mould, **rec**: Subscript that refers to the recycling vessel, **low**: Subscript that refers to the low pressure reservoir, and **high**: Subscript that refers to the high pressure reservoir (refer to Table 6.7)

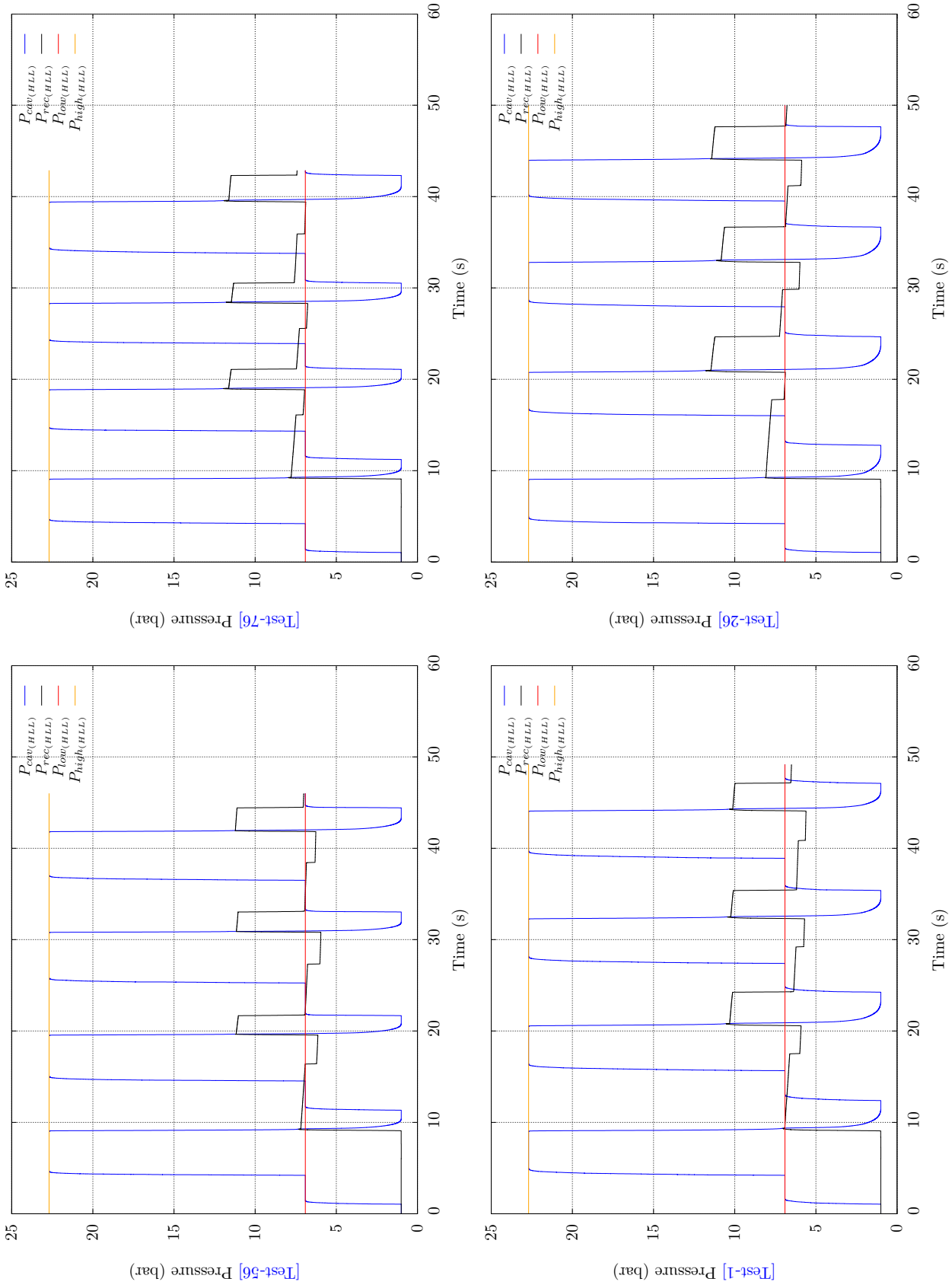

Figure 3.15: Pressure characteristics according to set-up Test-1, Test-26, Test-56, and Test-76 (refer to Table 6.7). **HLL**: Subscript that refers to the HLL Riemann solver in combination with the valve manifold model, **cav**: Subscript that refers to the PET preform mould, **rec**: Subscript that refers to the recycling vessel, **low**: Subscript that refers to the low pressure reservoir, and **high**: Subscript that refers to the high pressure reservoir (refer to Table 6.7)

addressed by the HLL Riemann solver. Therefore, based on the robustness of this last method a mathematical model, which combines the analysis of the valve manifold proposed in Chapter 4, was developed. A preliminary view of the numerical findings obtained from the Method of Characteristics and the HLL Riemann solver is presented in this chapter.

The apparent inconsistency of the results obtained from the first trials, that considered the valve manifold as a simple flow restriction, opened a new line of investigation. The implementation of the equations governing the flow through the valve manifold were also coupled with the two above-mentioned solving methods, and resulted in significant improvements in relation to the first attempts. From this point forward it was recognized the need of analyzing the valve manifold from a different perspective, since not only represents a constraint for the flow but also a volume of air that affects the maximum recycling rate to be achieved for a specific pneumatic configuration.

Chapter 4

Valve manifold modelling

"If the doors of perception were cleansed
everything would appear to man as it is, infinite"
The Marriage of Heaven and Hell, William Blake

4.1 Introduction

In order to determine the influence of the valve manifold during the blowing process, a more accurate analysis of the valve dynamics must be developed. This chapter, therefore, sets up a nonlinear time-variant deterministic model which depicts the main dynamic characteristics of the triple acting valve body.

A schematic of the pilot-operated two-stage flow control valve is shown in figure 4.1. It consists of three distinct stations which can be piloted separately. The pilot pressure acts directly on the upper chamber of each station generating a force which breaks the existing balance of forces when the spool valves are at rest. The spool valves were guided with two types of slide rings that also contribute to reduce the existing Coulomb friction, however the influence of friction force could not be totally neglected. On the other hand when the pilot air is released to the atmosphere, the spool valve returns to the original position by means of spring force with the assumption that the spring deflection is almost negligible. Regarding this last point it must be noticed that both the guiding spring design as well as the limited stroke of the spool valve reinforce this assumption.

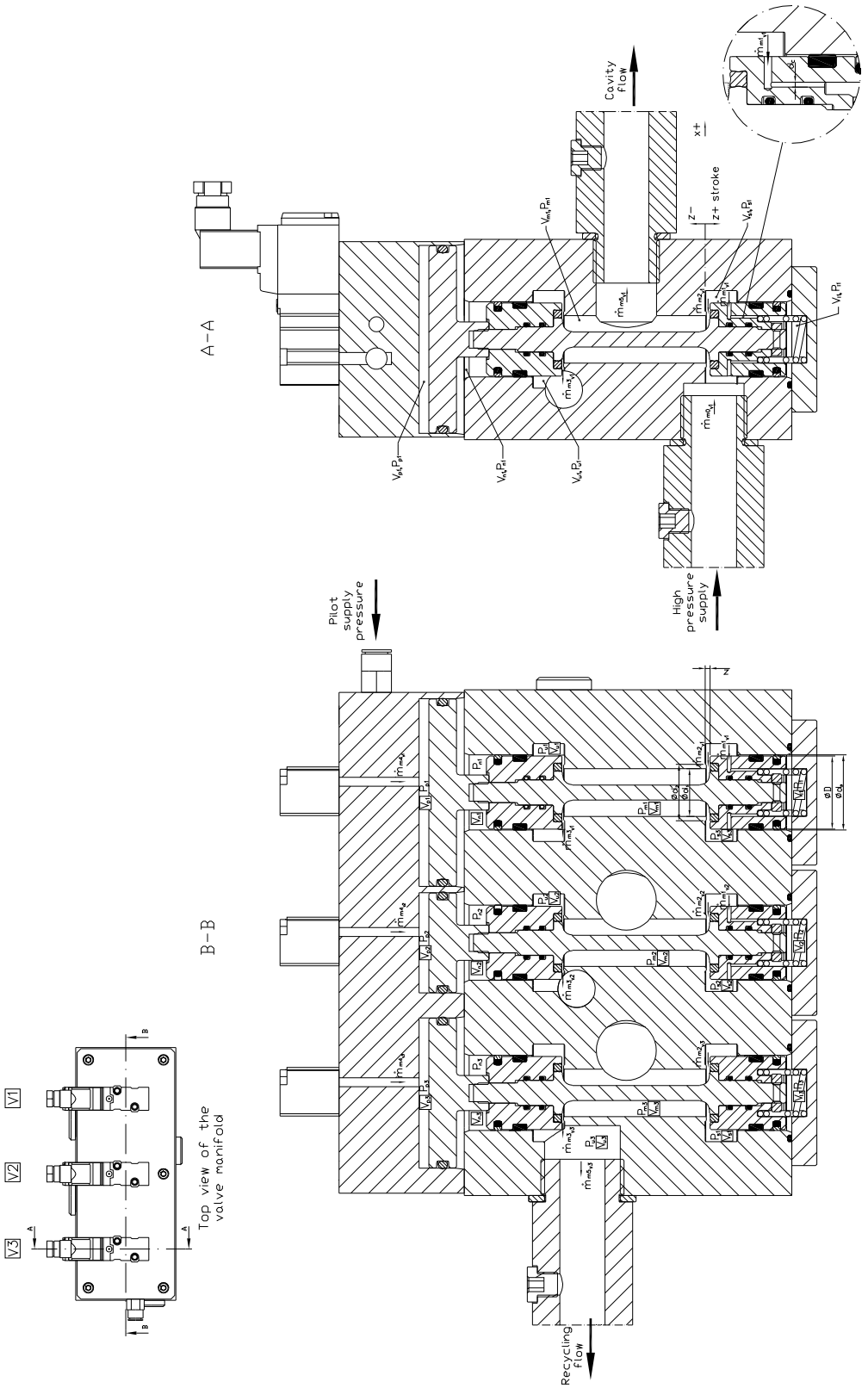

Figure 4.1: Cross-section view of the valve manifold

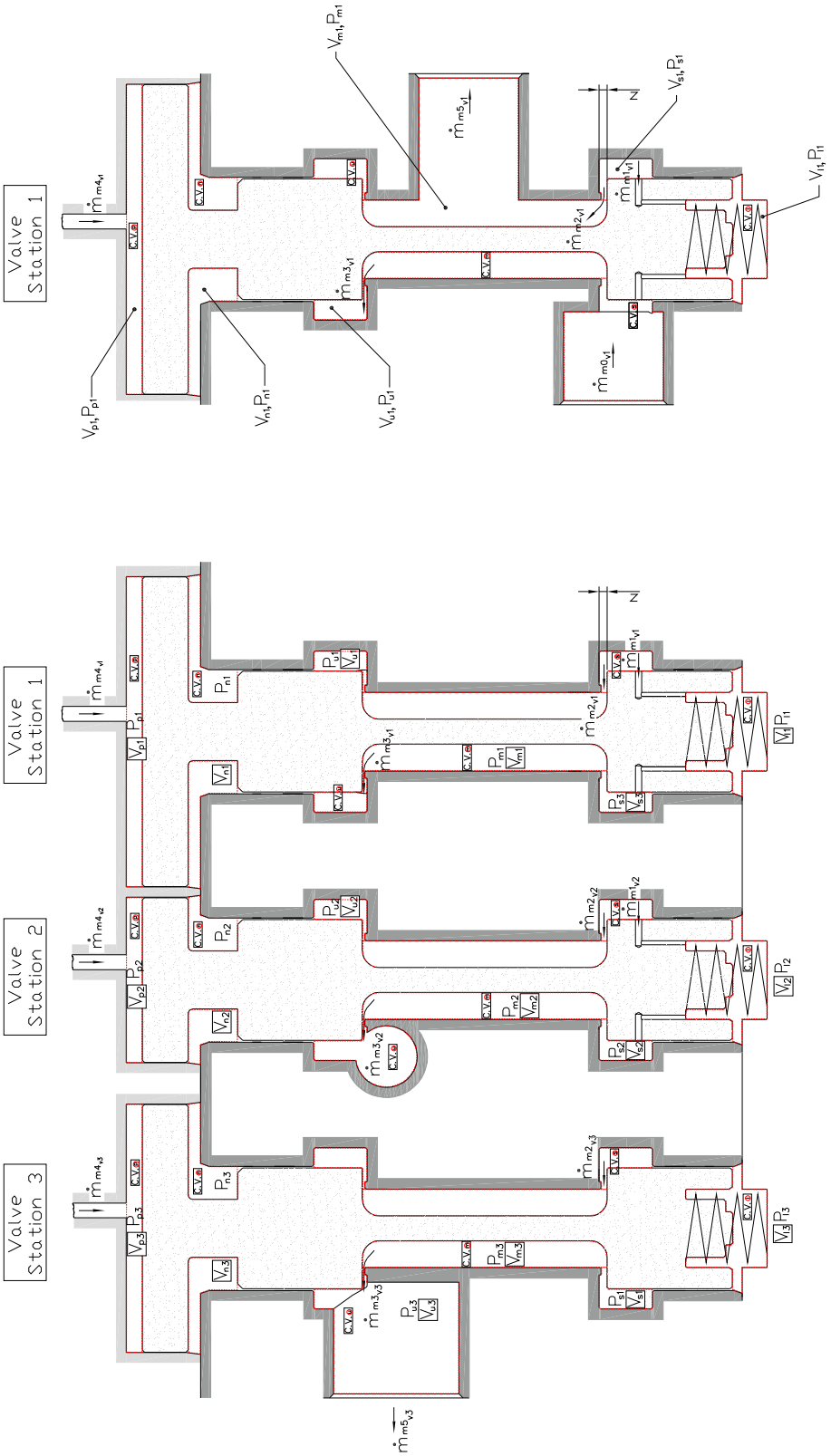

Figure 4.2: Schematic view of the main valve body and pilot ports of the pneumatic unit

4.2 Mathematical modelling

The following discussion assumes that the spool valves only moves in the axial direction. Therefore, the deviation from the central position caused by unsteady transverse flow forces was not taken into account. As it will be discussed in Chapter 6 the alignment of the spool valve respect to the valve body is a basic factor in avoiding possible eccentricities which may cause a rotating movement of the spool valve, that may consequently lead to the generation of a moment respect to its central axis.

The fluid control volume and moving parts are depicted on figure 4.2. Figure 4.3 shows the pressure forces acting on the surfaces in contact with gas, which are supposed to be evenly applied, as well as the spring force F_{spring}, which consists of the instantaneous force generated by the displacement and the nominal force existing when the valve is closed. The control volume depicted in figure 4.7 describes the nature of F_s, which is represented by the static pressure force acting on the spool valve and the flow force F_f yielded by the flow passage across the valve that originates a linear momentum change.

Therefore based on the previous assumptions the dynamics of each spool valve is given by

$$m_{v_i}(\ddot{z}_{v_i} + g) + c_f \dot{z}_{v_i} + k_{v_i}(z + z_o)_{v_i} = F_{f_{v_i}} + F_{s_{v_i}} \tag{4.1}$$

where z is the instantaneous vertical displacement referenced from the seat, k_{v_i} is the spring rate, $F_{f_{v_i}}$ and $F_{s_{v_i}}$ are the pressure forces acting on the entire control surface and the flow force respectively, and v_i is the index assigned to each spool valve.

4.2.1 Friction force

In order to determine the influence of the existing friction force the experimental set-up shown on figure 4.4 was used to measure the dry friction force exerted by the lower and upper packing against the manifold housing walls. The spool valve displacement was measured with a micrometer that was directly coupled to a dynamometer. As illustrated in figure 4.5 the difference between the spring force and the force needed to start the movement of the spool valve will determine the static friction force which increases until reaching a point where the dynamic friction becomes predominant. This experiment, however, did not take into account the influence of the O-ring allocated on the upper piston which is responsible for piloting the spool valve.

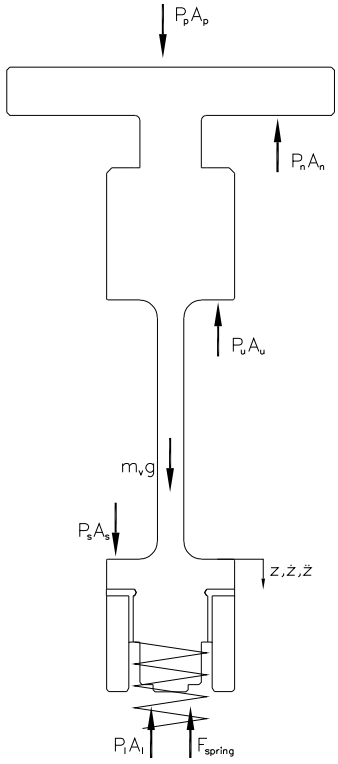

Figure 4.3: Static forces acting on the spool valve body

Based on the experimental results, the equation describing the dry friction force between the contacting surfaces can be mathematically represented as follows (289), (33),(11),(120),(256):

$$F_c = \begin{cases} F_{c_n} sgn(\dot{z}) & & \text{if } \dot{z} \neq 0 \\ \xi & \text{if } |\xi| < F_{c_0} & \text{if } \dot{z} = 0 \\ F_{c_0} sgn(\xi) & \text{if } |\xi| < F_{c_0} & \text{if } \dot{z} = 0 \end{cases}$$

where F_{c_n} is the nominal dry friction force on spool valve, F_{c_0} is the initial dry friction force on spool valve, and $\xi = \sum_{i=1}^{n} P_i A_i - F_{f_{v_i}} - F_{s_{v_i}}$ represents the balance of forces acting on the spool valve body.

4.2.2 Spool valve flow force

To reach a better understanding of the flow forces acting on the spool valve, computational fluid dynamics was implemented to the control volume illustrated on figure 4.6. The non-deformable control volume shows the boundary surfaces as well as the fluid

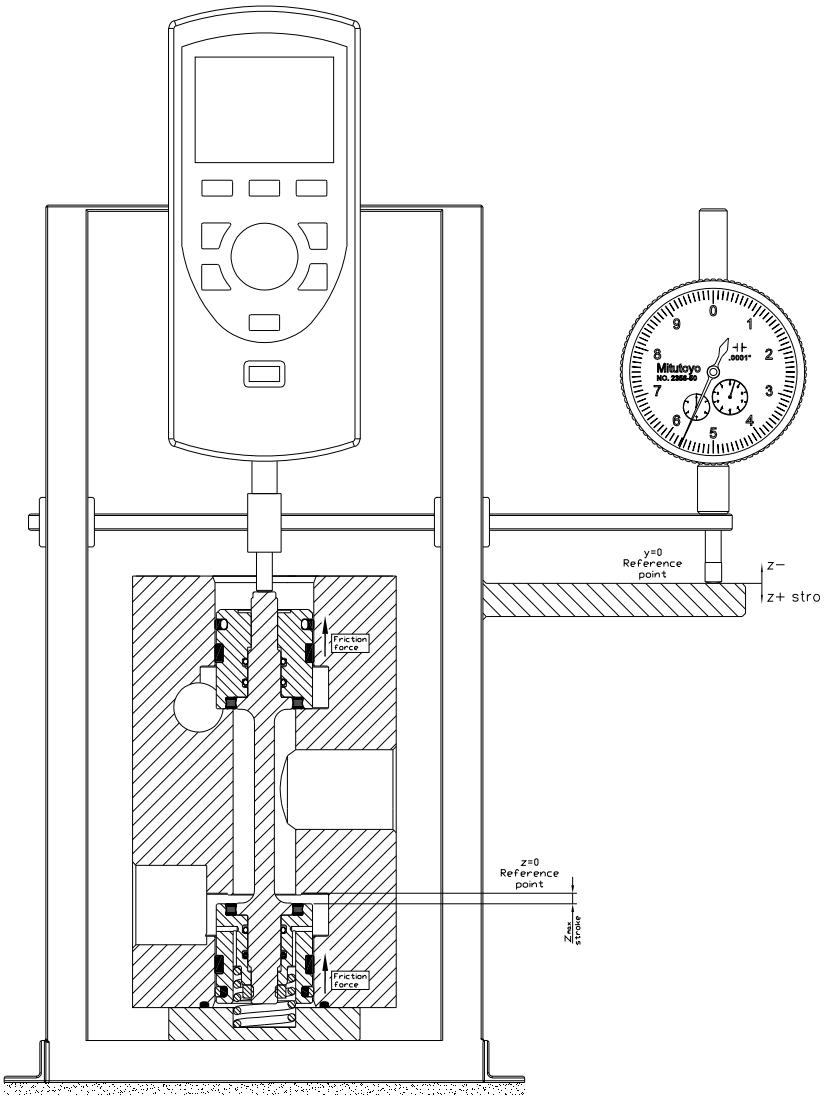

Figure 4.4: Experimental set-up to measure friction force

velocity vectors. In case that both, input and output velocity vectors only change in the x direction no momentum force will be experienced. If we apply the Navier-Stokes equations in vector form in the control volume the result will be as follows:

$$\varrho \left\{ \frac{\partial \vec{v}}{\partial t} + (\vec{v}\nabla)\vec{v} - \vec{f} \right\} = -\nabla p + \mu \nabla^2 \vec{v} \tag{4.2}$$

where ρ is the fluid density, $\vec{v}$ is the fluid velocity vector, f is the body force vector, and μ is the fluid viscosity.

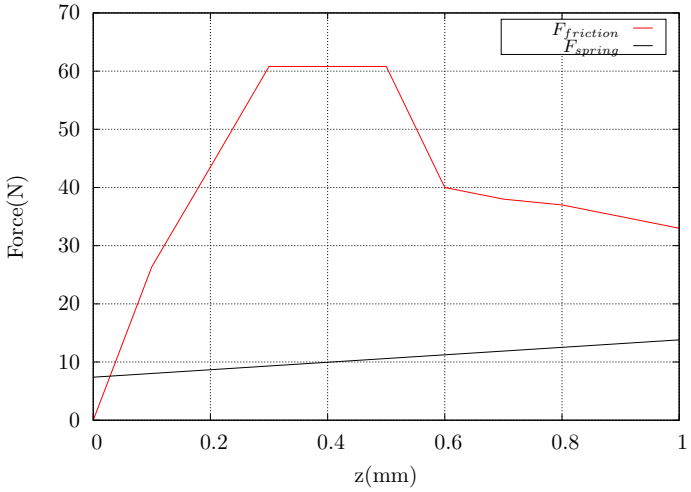

Figure 4.5: Experimental pre-slip displacement of the spool valve

When disregarding the body forces and the viscosity effect, and considering the forces acting on the z direction, equation (4.2) can be reduced to

$$\varrho \left\{ \frac{\partial \vec{v}}{\partial t} + (\vec{v}\nabla)\vec{v} \right\} = -\nabla p \tag{4.3}$$

The force-balance equation within the control volume is then determined as follows,

$$\int_{VC} \varrho \frac{\partial \vec{v}}{\partial t} dV + \int_{VC} \varrho \vec{v}_z \frac{\partial \vec{v}}{\partial z} dV = -\int_{VC} \frac{\partial \vec{p}}{\partial z} dV \tag{4.4}$$

where V is the control volume that is denoted by the dotted red line in figure 4.6. The mathematical integration of equation (4.4) gives

$$\frac{\partial}{\partial t}\left[\dot{m}(z_o + z)\right] + \dot{m}(v_{out} - v_{in}) = F_f + F_s \tag{4.5}$$

where F_s are the pressure forces acting on the inlet surface of the control volume, and F_f is the force acting on the outlet surface of the control volume. Then the following equation defines the flow force exerting on the top surface of the control volume

$$F_f = F_s - \frac{\partial}{\partial t}\left[\dot{m}(z + z_o)\right] - \dot{m}\left(v_{out} - v_{in}\right) \tag{4.6}$$

Substituting equation (4.6) into equation (4.1) and after rearranging gives

$$\begin{aligned} m_{v_i}\ddot{z}_{v_i} + c\dot{z}_{v_i} + k_{v_i}(z + z_o)_{v_i} \quad = \quad & (A_p P_p)_{v_i} + (A_s P_s)_{v_i} - (A_u P_u)_{v_i} - (A_l P_l)_{v_i} - \\ & (A_n P_n)_{v_i} + m_{v_i} g - \frac{\partial}{\partial t}\left[\dot{m}(z + z_o)\right] - \\ & \dot{m}\left(v_{out} - v_{in}\right) \end{aligned} \tag{4.7}$$

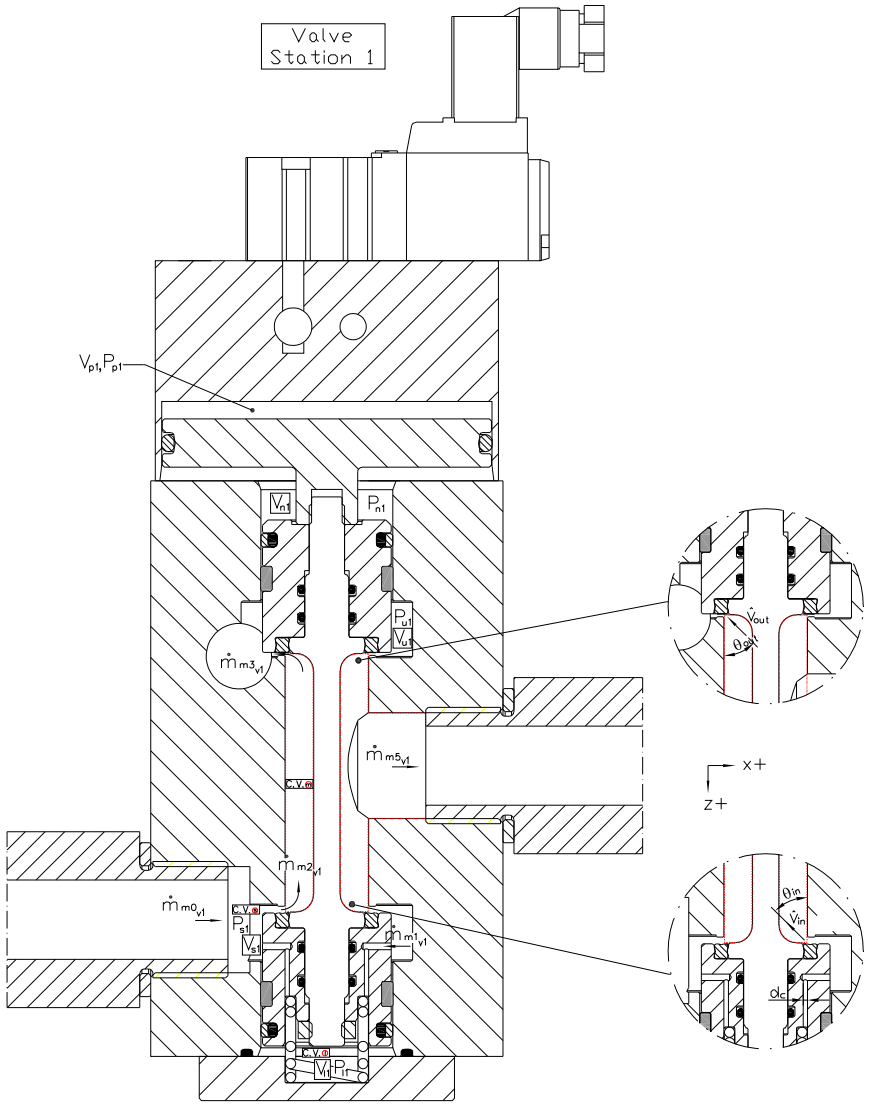

Figure 4.6: Air flow circulation through the valve opening

The steady-state form of equation (4.7) is

$$\begin{aligned} k_{v_i}(z+z_o)_{v_i} &= (A_pP_p)_{v_i} + (A_sP_s)_{v_i} - \\ &\quad (A_uP_u)_{v_i} - (A_lP_l)_{v_i} - (A_nP_n)_{v_i} + m_{v_i}g - \dot{m}\,(v_{out} - v_{in}) \end{aligned} \tag{4.8}$$

which can be manipulated in order to determine the minimum force required to shift the valve from the rest position,

$$(A_pP_p)_{v_i} \geq k_{v_i}(z+z_o)_{v_i} - ((A_sP_s)_{v_i} - (A_uP_u)_{v_i} - (A_lP_l)_{v_i} - (A_nP_n)_{v_i} + m_{v_i}g) \tag{4.9}$$

Figure 4.6 shows the velocity vector exiting or entering the control volume "m". The vector varies along the spool valve displacement exerting, therefore, a variable flow force during the stroke. The velocity vector was theoretically estimated, and was subsequently constrasted with the results obtained by computational fluid dynamics which are discussed in the next section. It must be pointed out that the influence of the flow forces generated in the internal piloting channels located at the lower packing of the spool valve was disregarded.

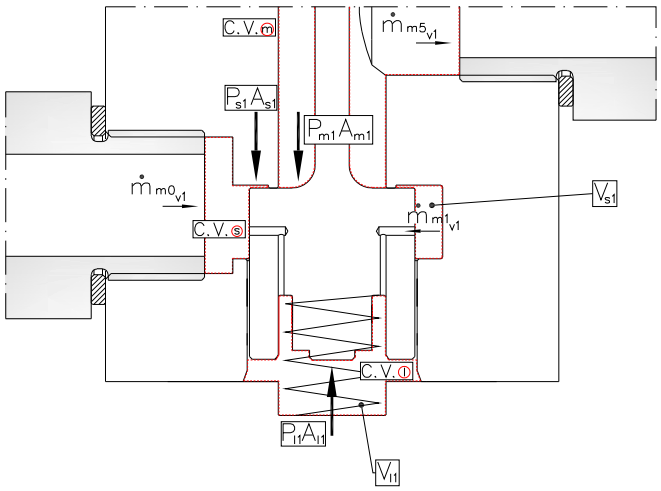

(a) Before opening

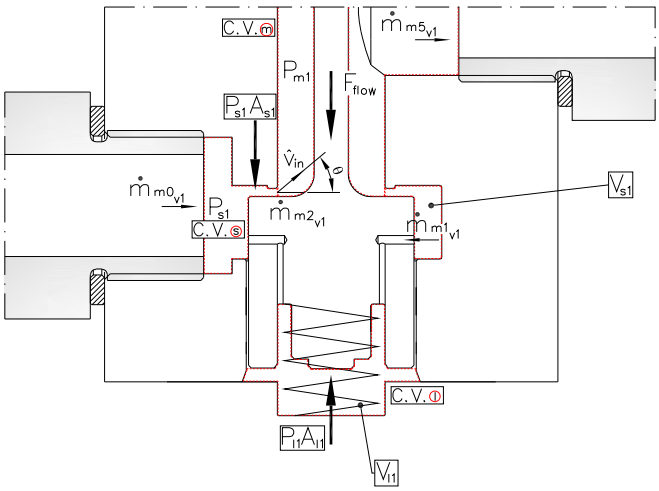

(b) After opening

Figure 4.7: Static and flow fluid forces acting on the spool valve lower packing after opening

4.2.3 CFD analysis of the valve opening

The influence of the momentum forces varies along the spool valve stroke and CFD analysis ($\kappa - \omega$ Shear Stress Transport model) (1) was used to determine the flow characteristics through the spool valve at different openings. Figures 4.11 to 4.14 shows the velocity vectors through the valve seat at different positions. It must be noticed that among the equations presented above the transient flow force has not been included in the analysis.

On the other hand, the effective area of the valve opening is usually determined experimentally. Based on the internal geometry of the valve manifold, the only way to measure the sonic conductance for an individual valve seat will be to build up a one-station valve unit which would allow testing several valve positions without being influenced by other constraints. Alternatively, CFD tools were considered to be a valid method to assess the mentioned parameter. Therefore, the discharge coefficient will be determined by applying the predicted mass flow rate instead of the experimental one. As it will be discussed in Chapter 6 the sonic conductance for the fully open position was obtained through experimental data and, it will be taken as reference to validate the simulated results.

Mass-flow rate (kg/s)	Orifice diameter (mm)			
	3	4	5	8
Simulated	0.012723	0.0224974	0.0333138	0.0866595
Theoretical	0.0132400	0.0235378	0.0367779	0.0941513
Experimental	0.0125496	0.0205102	0.0379299	0.0989923
%error $\left[\frac{(Sim.-Exp.)}{Exp.}\right]$	1.38	9.69	-12.17	-12.46
%error $\left[\frac{(Sim.-Theor.)}{Theor.}\right]$	-3.90	-4.42	-9.42	-7.95

Table 4.1: Comparison of mass-flow rate through a calibrated orifice according to the Simple Discharge Test method

The same equations used to determine the theoretical mass flow rate for a calibrated orifice were also applied to the flow going through the interconnecting ports of the valve manifold with the exception that the effective area was estimated as follows,

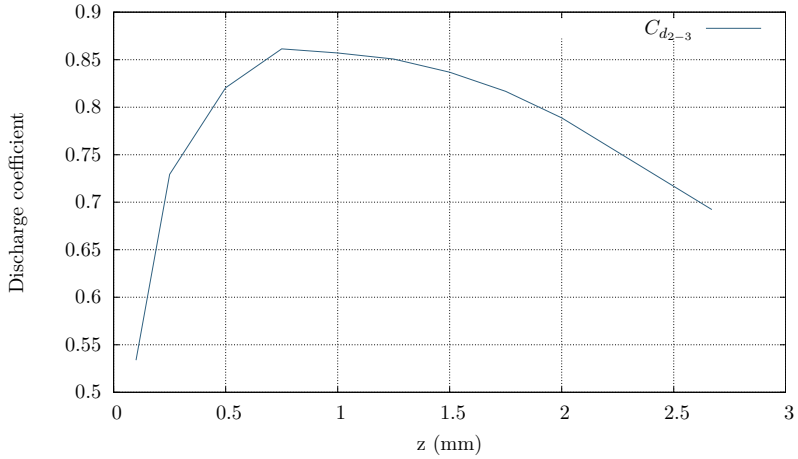

Figure 4.8: Predicted discharge coefficient between Ports 2 and 3 (refer to fig.6.25)

$$S_{eff} = \sqrt{\frac{1}{\frac{1}{S_1^2} + \frac{1}{S_2^2} + ... + \frac{1}{S_n^2}}} \tag{4.10}$$

where the subindexes 1 to n refer to the different restrictions along the flow path. Based on this principle a correlation between the discharge coefficient and the poppet valve displacement was generated for each functional flow path of the valve manifold (refer to fig.4.8 and 4.9). It must be noticed that the test conditions described by the Simple Discharge method (153),(154) were applied to the CFD analysis.

Mass-flow rate (kg/s)	Flow path			
	1-3	2-3	4-3	3-4
Simulated	0.124426	0.20667	0.103431	0.090976
Theoretical	0.136350	0.23359	0.106339	0.106339
Experimental	0.096671	0.140995	0.07851	0.078688
%error $\left[\frac{(Sim.-Exp.)}{Exp.}\right]$	28.71	46.62	31.74	15.61
%error $\left[\frac{(Sim.-Theor.)}{Theor.}\right]$	-8.74	-11.52	-2.73	-14.45

Table 4.2: Comparison of mass-flow rate through the valve manifold according to the Simple Discharge Test method (Spool valve fully open)

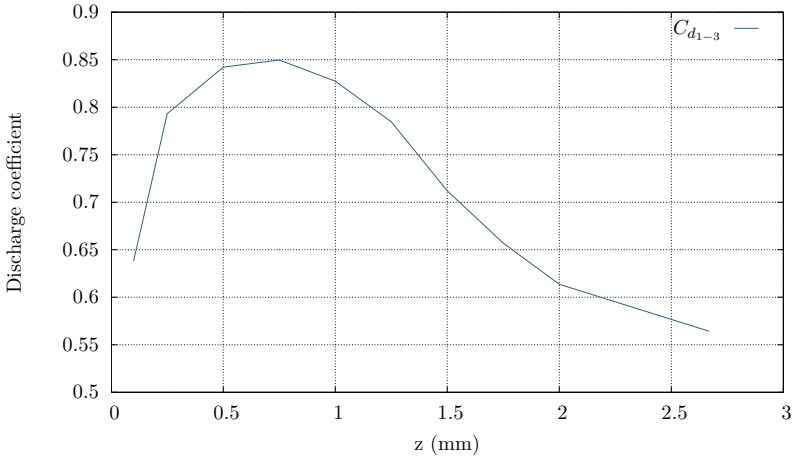

Figure 4.9: Predicted discharge coefficient between Ports 1 and 3 (refer to fig.6.25)

Based on the fact that the experimental mass-flow rate was only determined for the fully open valve position, a comparison between both predicted and empirical mass-flow rate is shown in Table 4.2. As it will be discussed in Chapter 6 the Simple Discharge method was proved to be an effective technique to estimate the sonic conductance of the valve manifold, however the results highlighted that there was a limitation in regards to the size of the tank which explains the existing deviations between the simulated and empirical results respectively.

The CFD model, in any case, demonstrated that the experimental mass flow rate was certainly underestimated and could not be used to derive the non-dimensional parameter affecting the flow through the boundary condition at the end of the pipes connected to the valve manifold. Therefore, it was thought to be appropriate for the purpose of this study the introduction of the non-dimensional parameter derived by 3D modelling in the mathematical model discussed in Chapter 3.

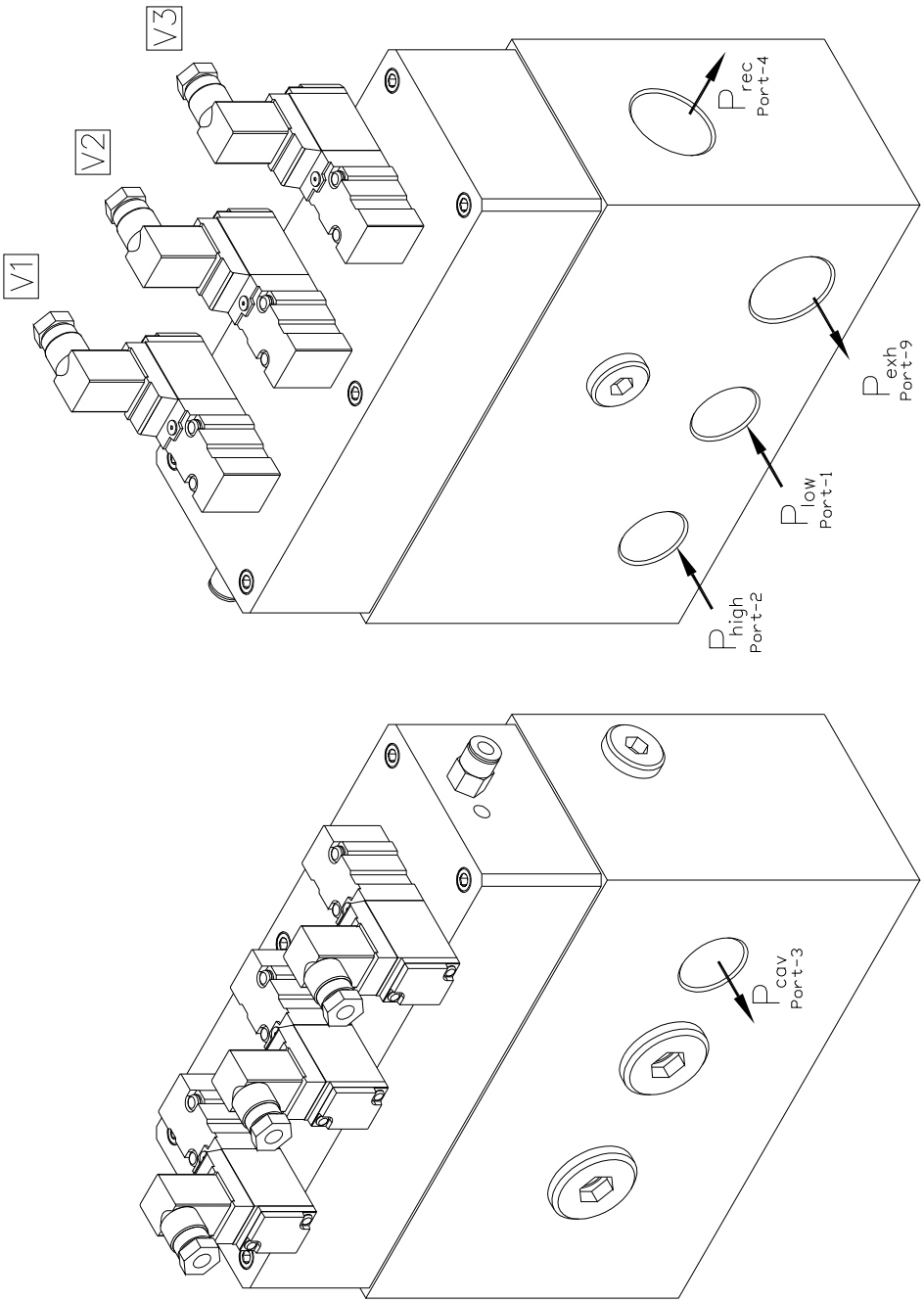

Figure 4.10: 3D view of the valve ports

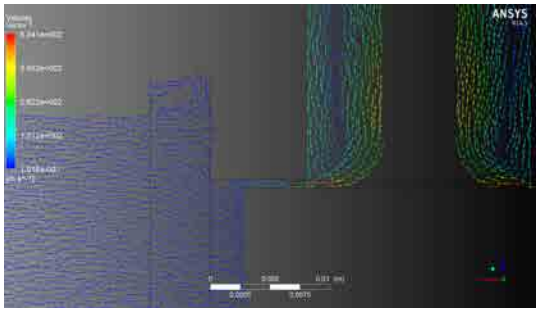

(a) z=0.25mm

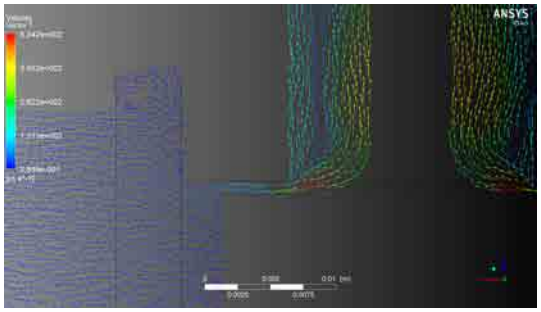

(b) z=0.5mm

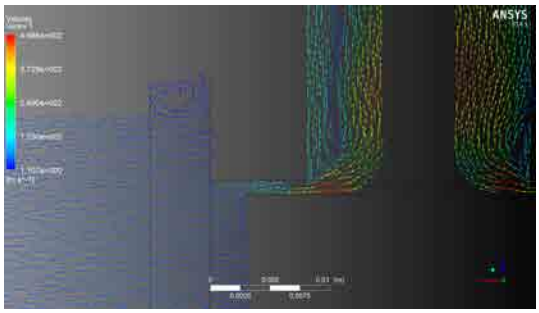

(c) z=0.75mm

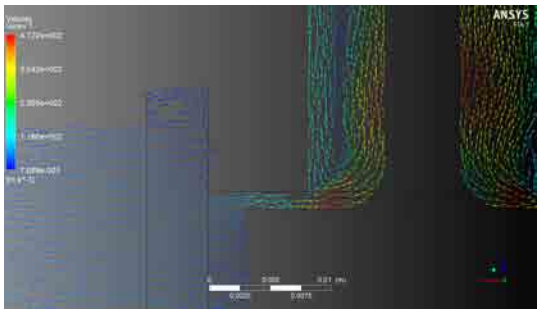

(d) z=1mm

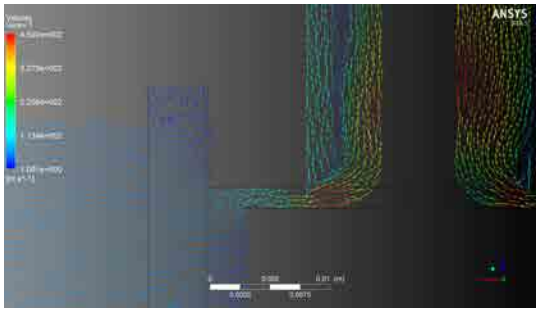

(e) z=1.25mm

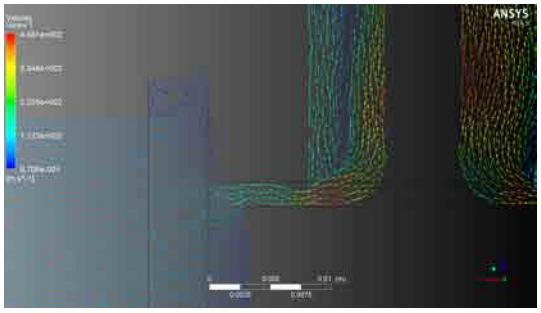

(f) z=1.5mm

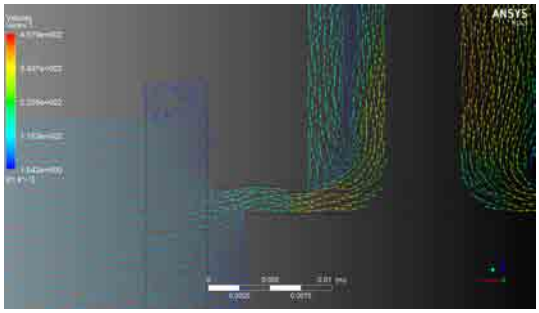

(g) z=1.75mm

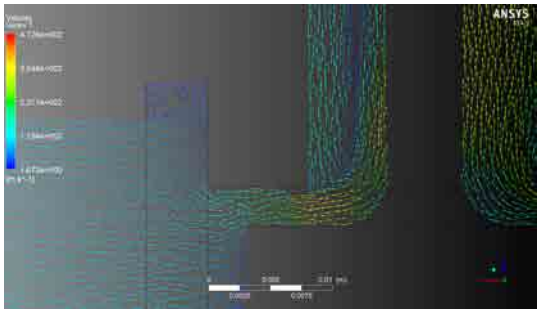

(h) z=2.67mm

Figure 4.11: Velocity vectors at various openings of the lower poppet of V_1 valve

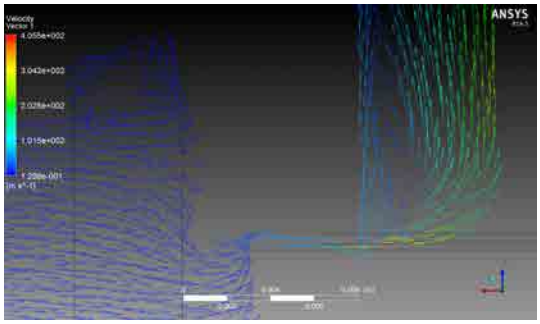

(a) z=0.25mm

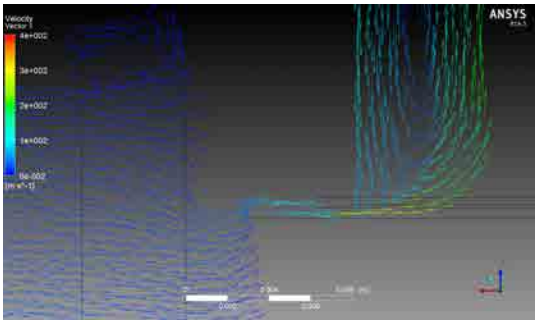

(b) z=0.5mm

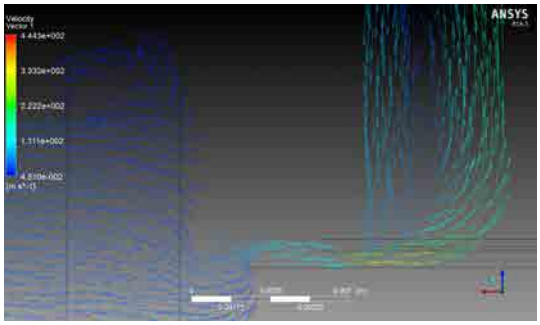

(c) z=0.75mm

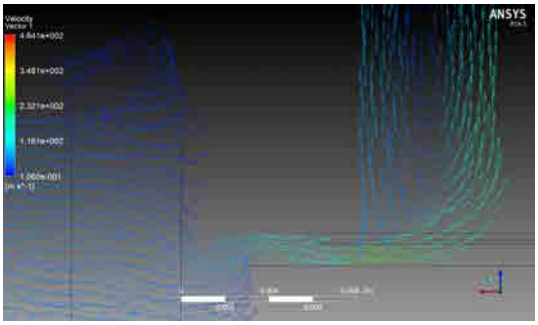

(d) z=1mm

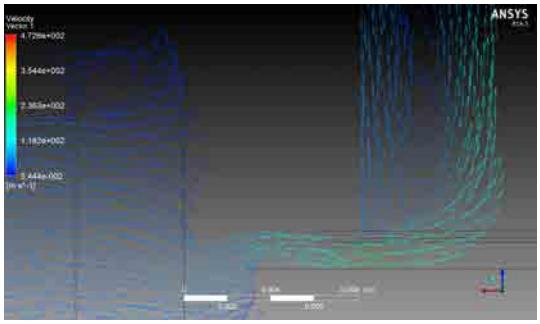

(e) z=1.25mm

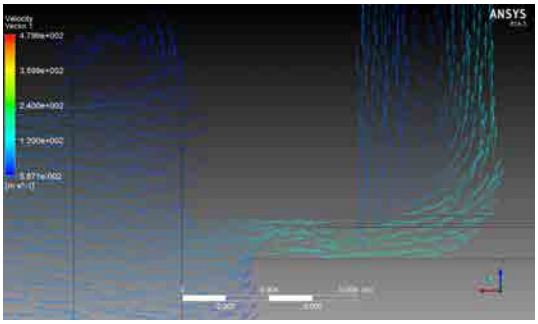

(f) z=1.5mm

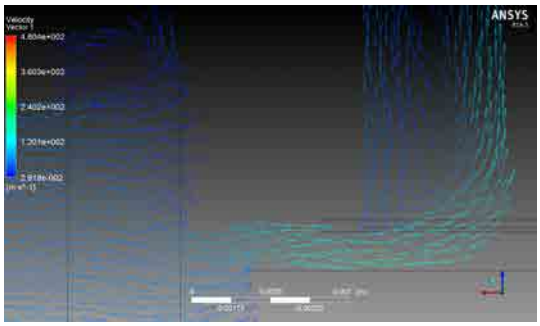

(g) z=1.75mm

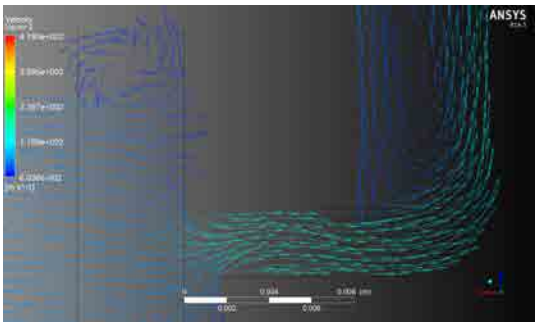

(h) z=2.67mm

Figure 4.12: Velocity vectors at various openings of the lower poppet of V_2 valve

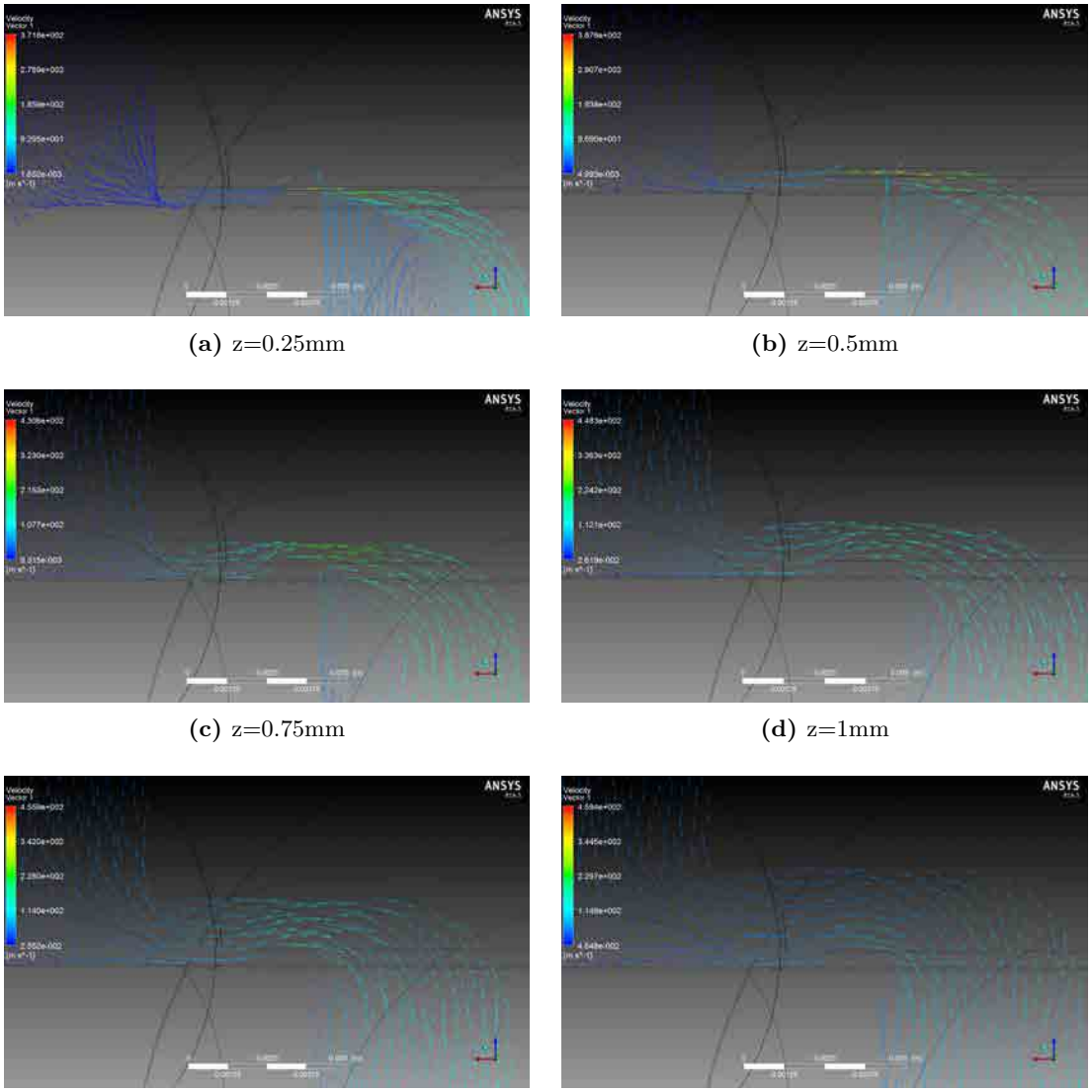

(a) z=0.25mm **(b)** z=0.5mm

(c) z=0.75mm **(d)** z=1mm

(e) z=1.25mm **(f)** z=1.5mm

Figure 4.13: Velocity vectors at various openings of the upper poppet of V_3 valve

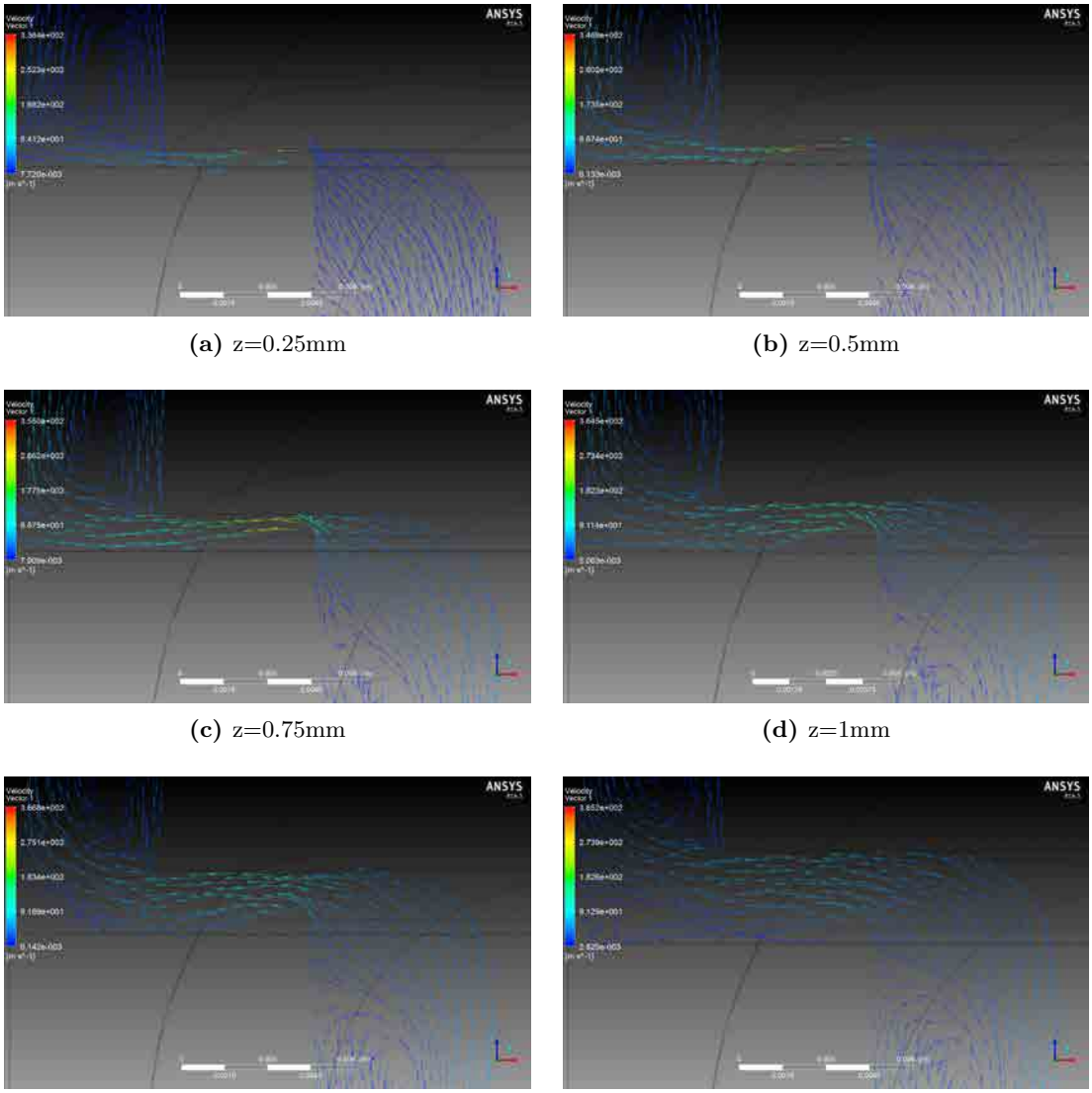

(a) z=0.25mm **(b)** z=0.5mm

(c) z=0.75mm **(d)** z=1mm

(e) z=1.25mm **(f)** z=1.5mm

Figure 4.14: Velocity vectors at various openings of the upper poppet of V_1 valve

4.2.4 Valve manifold chambers dynamics

The approach followed to derive the mathematical expressions for the pressure and temperature of the air inside each internal chamber of the flow control valve was based on the assumption that the charging and discharging processes were both adiabatic.

Considering that the gas is perfect, as well as that the pressure and temperature within

the chambers are homogeneous, the result of applying the continuity, energy and state equations at each control volume gives (262),

$$\frac{dP}{dt} = \dot{m}_{in}\frac{RT}{V}\left(\gamma\frac{T_{in}}{T} + \frac{v_{in}^2}{2c_vT}\right) - \dot{m}_{out}\frac{RT}{V}\left(\gamma\frac{T_{out}}{T} + \frac{v_{out}^2}{2c_vT}\right) - \gamma\frac{P}{V}\left(\frac{dV}{dt}\right) + \frac{\gamma-1}{V}\left(\frac{dQ}{dt}\right) \quad (4.11)$$

$$\frac{dT}{dt} = \dot{m}_{in}\frac{RT^2}{PV}\left(\gamma\frac{T_{in}}{T} + \frac{v_{in}^2}{2c_vT}\right) - \dot{m}_{out}\frac{RT^2}{PV}\left(\gamma\frac{T_{out}}{T} + \frac{v_{out}^2}{2c_vT}\right) - \frac{T}{m}\left(\dot{m}_{in} - \dot{m}_{out}\right) - (\gamma-1)\frac{T}{V}\left(\frac{dV}{dt}\right) + (\gamma-1)\frac{T}{PV}\left(\frac{dQ}{dt}\right) \quad (4.12)$$

Moreover if the flow through the pipe end is supposed to be adiabatic, the discharged mass temperature is the same as the instantaneous value of the gas temperature in the chamber (158).

In case of neglecting the kinetic energy generated at the inlet and outlet ports of the control volume as well as the heat transferred to the fluid, equations (4.11) and (4.12) become

$$\frac{dP}{dt} = \gamma\frac{R}{V}(\dot{m}_{in}T_{in} - \dot{m}_{out}T_{out}) - \gamma\frac{P}{V}\left(\frac{dV}{dt}\right) \quad (4.13)$$

$$\frac{dT}{dt} = \frac{\gamma}{m}(\dot{m}_{in}T_{in} - \dot{m}_{out}T_{out}) - \frac{T}{m}\left(\frac{dm}{dt}\right) - (\gamma-1)\frac{T}{V}\left(\frac{dV}{dt}\right) \quad (4.14)$$

The experiments conducted on dual action pneumatic actuators by Al-Ibrahim and Otis (6), (7), proved that the temperature inside the chambers laid between the theoretical adiabatic and isothermal curves. Based on those results equation (4.13) and (4.14) can be written as follows,

$$\frac{dP}{dt} = \frac{RT}{V}(\alpha_{in}\dot{m}_{in} - \alpha_{out}\dot{m}_{out}) - \alpha\frac{P}{V}\frac{dV}{dt} \quad (4.15)$$

where α, α_{in}, and α_{out} vary between 1 and γ, depending on the actual heat transfer during the process. According to Al-Ibrahim and Otis (7), the charging process could be better characterized with a value of α_{in} close to γ, while for the discharging of the chamber α_{out} should be close to 1. Finally the thermal effects derived from the work done due to change in volume, can be described with a value of $\alpha = 1.2$.

Past studies (93) have demonstrated that when charging and discharging large tanks the process is nearly isothermal, however when repeating the same experiment with small tanks the charging process differed considerably from being adiabatic while the discharging process has a good correlation with the adiabatic model. The reason behind this is that the governing forced convection heat transfer through the vessel walls helps to keep a nearly constant temperature within the vessel. However, the size of the inner chambers cannot be compared with a common vessel, therefore, without additional data regarding the real nature of the charging and discharging process inside the manifold, it was decided that these results could not be extrapolated to the case under study since the volume of the chambers are relatively small in comparison with the cylinder chambers analyzed by Otis. The simulation, therefore, does not take into account the influence of the heat transfer through the manifold walls, and this assumption was based on the geometry of the valve as well as the testing time in which the experimental analysis was performed.

On ther other hand, some of the internal volumes of the valve manifold are in fact experiencing volume variation and are described by equation (4.16),

$$\begin{aligned} V_{(l)_{v_i}} &= V_{(l)o_{v_i}} + A_{(l)_{v_i}} \left(z_{o_{v_i}} \pm z_{v_i} \right) \\ V_{(s)_{v_i}} &= V_{(s)o_{v_i}} + A_{(s)_{v_i}} \left(z_{o_{v_i}} \pm z_{v_i} \right) \\ V_{(m)_{v_i}} &= V_{(m)o_{v_i}} \\ V_{(n)_{v_i}} &= V_{(n)o_{v_i}} + A_{(n)_{v_i}} \left(z_{o_{v_i}} \pm z_{v_i} \right) \\ V_{(p)_{v_i}} &= V_{(p)o_{v_i}} + A_{(p)_{v_i}} \left(z_{o_{v_i}} \pm z_{v_i} \right) \end{aligned} \tag{4.16}$$

where $V_{o_{v_i}}$ is the non-active volume, A_{v_i} is the effective area of the chamber, $z_{o_{v_i}}$ is the height of the chamber, z_{v_i} is the spool valve position, the subindex v_i corresponds to the spool valve under study and the subscripts (l), (s), (m), (n), and (p), are associated with the internal chambers of the valve manifold. Substituting (4.16) into both (4.13) and (4.14), the time derivative for both pressure and temperature for each of the chambers are presented in tables 4.3, 4.4 and 4.5. It must be noticed that the mentioned equations do not take into account the kynetic energy generated within the control volume at each time step. Moreover they may be simplified even further by disregarding the heat transfer to the fluid, thus the pressure and temperature at

each chamber will depend only on the characteristics of the charging and discharging processes.

4.2.5 Flow equations through restrictions

The mass flow through the openings can be either subsonic or sonic depending on the pressure ratio between inlet and outlet pressure. It, therefore, results

$$\dot{m}_{m2_{v_i}} = \begin{cases} C_{d_{2_{v_i}}} A_{eff} \xi_1 \dfrac{P_{(s),v_i}}{\sqrt{T_{(s),v_i}}} & \text{if } \dfrac{P_{(m),v_i}}{P_{(s),v_i}} \leq P_{cr} \\ C_{d_{2_{v_i}}} A_{eff} \xi_2 \dfrac{P_{(s),v_i}}{\sqrt{T_{(s),v_i}}} \left(\dfrac{P_{(m),v_i}}{P_{(s),v_i}}\right)^{1/\gamma} \sqrt{1 - \left(\dfrac{P_{(m),v_i}}{P_{(s),v_i}}\right)^{(\gamma-1)/\gamma}} & \text{if } \dfrac{P_{(m),v_i}}{P_{(s),v_i}} > P_{cr} \end{cases}$$

$$\dot{m}_{m3_{v_i}} = \begin{cases} C_{d_{3_{v_i}}} A_{eff} \xi_1 \dfrac{P_{(m),v_i}}{\sqrt{T_{(m),v_i}}} & \text{if } \dfrac{P_{(u),v_i}}{P_{(m),v_i}} \leq P_{cr} \\ C_{d_{3_{v_i}}} A_{eff} \xi_2 \dfrac{P_{(m),v_i}}{\sqrt{T_{(m),v_i}}} \left(\dfrac{P_{(u),v_i}}{P_{(m),v_i}}\right)^{1/\gamma} \sqrt{1 - \left(\dfrac{P_{(u),v_i}}{P_{(m),v_i}}\right)^{(\gamma-1)/\gamma}} & \text{if } \dfrac{P_{(u),v_i}}{P_{(m),v_i}} > P_{cr} \end{cases}$$

$$\dot{m}_{m4_{v_i}} = \begin{cases} C_{d_{4_{v_i}}} A_{eff} \xi_1 \dfrac{P_{(res),v_i}}{\sqrt{T_{(res),v_i}}} & \text{if } \dfrac{P_{(p),v_i}}{P_{(res),v_i}} \leq P_{cr} \\ C_{d_{4_{v_i}}} A_{eff} \xi_2 \dfrac{P_{(res),v_i}}{\sqrt{T_{(res),v_i}}} \left(\dfrac{P_{(p),v_i}}{P_{(res),v_i}}\right)^{1/\gamma} \sqrt{1 - \left(\dfrac{P_{(p),v_i}}{P_{(res),v_i}}\right)^{(\gamma-1)/\gamma}} & \text{if } \dfrac{P_{(p),v_i}}{P_{(res),v_i}} > P_{cr} \end{cases}$$

where $C_{d_{v_i}}$ is a non-dimensional discharge coefficient referring to the corresponding spool valve seat which is obtained from CFD analysis, and the subscript (res) refers to the reservoir that supplies air to the pilot port of the valve manifold. On the other hand the stagnation pressure and temperature of the fluid upstream and downstream of the restriction will alternately vary depending on the flow direction, and applies equally to the downstream stagnation pressure. The following are constants that depend on the specific heat ratio of the given fluid,

$$\xi_1 = \sqrt{\frac{k}{R}\left(\frac{2}{k+1}\right)^{\frac{k+1}{k-1}}}; \qquad \xi_2 = \sqrt{\frac{2k}{R(k-1)}}; \qquad P_{cr} = \left(\frac{2}{k+1}\right)^{\frac{k}{k-1}}$$

The air flowing through the piloting channels, incorporated in the lower packing of the spool valves, is assumed to be laminar (9), and is determined by the equation below,

$$\dot{m}_{m1_{v_i}} = \varrho_{av} \frac{\pi d_c^4}{128 \mu_{av}} \frac{\Delta P}{l_c} \tag{4.30}$$

Table 4.3

Governing equations at the control volumes (l) and (s)

$\boxed{V.C._{\cdot(l)}}$

$$\left(\frac{dP}{dt}\right)_{(l),v_i} = \frac{R}{V_{o_{(l),v_i}} + A_{(l),v_i}(z_{o_{(l),v_i}} \pm z_{(l),v_i})}\left[\dot{m}_{m1_{v_i}}\left(\gamma T_{(s),v_i} + \frac{v^2_{out_{(1)},v_i}}{2c_v}\right)\right] - \gamma\frac{P_{(l),v_i}}{V_{o_{(l),v_i}} + A_{(l),v_i}(z_{o_{(l),v_i}} \pm z_{(l),v_i})}A_{(l),v_i}\frac{dz_{(l),v_i}}{dt} + \frac{\gamma - 1}{V_{o_{(l),v_i}} + A_{(l),v_i}(z_{o_{(l),v_i}} \pm z_{(l),v_i})}\left(\frac{dQ}{dt}\right)_{(l),v_i} \tag{4.17}$$

$$\left(\frac{dT}{dt}\right)_{(l),v_i} = \frac{1}{m_{(l),v_i}}\left[\dot{m}_{m1_{v_i}}\left(\gamma T_{(s),v_i} + \frac{v^2_{out_{(1)},v_i}}{2c_v}\right)\right] - \frac{T_{(l),v_i}}{m_{(l),v_i}}\left(\frac{dm}{dt}\right)_{(l),v_i} - (\gamma - 1)\frac{T_{(l),v_i}}{V_{o_{(l),v_i}} + A_{v_{(l),i}}(z_{o_{(l),v_i}} \pm z_{v_{(l),i}})}A_{(l),v_i}\frac{dz_{(l),v_i}}{dt} + (\gamma - 1)\frac{T_{(l),v_i}}{P_{(l),v_i}\left(V_{o_{(l),v_i}} + A_{(l),v_i}(z_{o_{(l),v_i}} \pm z_{(l),v_i})\right)}\left(\frac{dQ}{dt}\right)_{(l),v_i} \tag{4.18}$$

$\boxed{V.C._{\cdot(s)}}$

$$\left(\frac{dP}{dt}\right)_{(s),v_i} = \frac{R}{V_{o_{(s),v_i}} + A_{(s),v_i}(z_{o_{(s),v_i}} \pm z_{(s),v_i})}\left[\dot{m}_{m0_{v_i}}\left(\gamma T_{(0),v_i} + \frac{v^2_{in_{(0)},v_i}}{2c_v}\right) - \dot{m}_{m1_{v_i}}\left(\gamma T_{(s),v_i} + \frac{v^2_{out_{(1)},v_i}}{2c_v}\right) - \dot{m}_{m2_{v_i}}\left(\gamma T_{(s),v_i} + \frac{v^2_{out_{(2)},v_i}}{2c_v}\right)\right] - \gamma\frac{P_{(s),v_i}}{V_{o_{(s),v_i}} + A_{(s),v_i}(z_{o_{(s),v_i}} \pm z_{(s),v_i})}A_{(s),v_i}\frac{dz_{(s),v_i}}{dt} + \frac{\gamma - 1}{V_{o_{(s),v_i}} + A_{(s),v_i}(z_{o_{(s),v_i}} \pm z_{(s),v_i})}\left(\frac{dQ}{dt}\right)_{(s),v_i} \tag{4.19}$$

$$\left(\frac{dT}{dt}\right)_{(s),v_i} = \frac{1}{m_{(s),v_i}}\left[\dot{m}_{m0_{v_i}}\left(\gamma T_{(0),v_i} + \frac{v^2_{in_{(0)},v_i}}{2c_v}\right) - \dot{m}_{m1_{v_i}}\left(\gamma T_{(s),v_i} + \frac{v^2_{out_{(1)},v_i}}{2c_v}\right) - \dot{m}_{m2_{v_i}}\left(\gamma T_{(s),v_i} + \frac{v^2_{out_{(2)},v_i}}{2c_v}\right)\right] - \frac{T_{(s),v_i}}{m_{(s),v_i}}\left(\frac{dm}{dt}\right)_{(s),v_i} - (\gamma - 1)\frac{T_{(s),v_i}}{V_{o_{(s),v_i}} + A_{v_{(s),i}}(z_{o_{v_{(s),i}}} \pm z_{v_{(s),i}})}A_{(s),i}\frac{dz_{v_{(s),i}}}{dt} + (\gamma - 1)\frac{T_{(s),v_i}}{P_{(s),v_i}\left(V_{o_{(s),v_i}} + A_{v_{(s),i}}(z_{o_{v_{(s),i}}} \pm z_{v_{(s),i}})\right)}\left(\frac{dQ}{dt}\right)_{(s),v_i} \tag{4.20}$$

Table 4.4

Governing equations at the control volumes (m) and (u)

$\boxed{V.C._{(m)}}$

$$\left(\frac{dP}{dt}\right)_{(m),v_i} = \frac{R}{V_{o_{(m),v_i}}}\left[\dot{m}_{m2_{v_i}}\left(\gamma T_{(s),v_i}+\frac{v^2_{in_{(2)},v_i}}{2c_v}\right)-\dot{m}_{m3_{v_i}}\left(\gamma T_{(m),v_i}+\frac{v^2_{out_{(3)},v_i}}{2c_v}\right)\right]-\frac{\gamma-1}{V_{o_{(m),v_i}}}\left(\frac{dQ}{dt}\right)_{(m),v_i} \tag{4.21}$$

$$\begin{aligned}\left(\frac{dT}{dt}\right)_{(m),v_i} = {} & \frac{1}{m_{(m),v_i}}\left[\dot{m}_{m2_{v_i}}\left(\gamma T_{(s),v_i}+\frac{v^2_{in_{(2)},v_i}}{2c_v}\right)-\dot{m}_{m3_{v_i}}\left(\gamma T_{(m),v_i}+\frac{v^2_{out_{(3)},v_i}}{2c_v}\right)\right]-\frac{T_{(m),v_i}}{m_{(m),v_i}}\left(\frac{dm}{dt}\right)_{(m),v_i}- \\ & (\gamma-1)\frac{T_{(s),v_i}}{V_{o_{(s),v_i}}+A_{v_{(s),i}}(z_{o_{v_{(s),i}}}\pm z_{v_{(s),i}})}A_{v_{(s),i}}\frac{dz_{v_{(s),i}}}{dt}+ \\ & (\gamma-1)\frac{T_{(s),v_i}}{P_{(s),v_i}\left(V_{o_{(s),v_i}}+A_{v_{(s),i}}(z_{o_{v_{(s),i}}}\pm z_{v_{(s),i}})\right)}\left(\frac{dQ}{dt}\right)_{(s),v_i}\end{aligned} \tag{4.22}$$

$\boxed{V.C._{(u)}}$

$$\left(\frac{dP}{dt}\right)_{(u),v_i} = \frac{R}{V_{o_{(u),v_i}}+A_{(u),v_i}(z_{o_{(u),v_i}}\pm z_{(u),v_i})}\left[\dot{m}_{m3_{v_i}}\left(\gamma T_{(m),v_i}+\frac{v^2_{in_{(3)},v_i}}{2c_v}\right)-\dot{m}_{m5_{v_3}}\left(\gamma T_{(u),v_i}+\frac{v^2_{out_{(5)},v_i}}{2c_v}\right)\right]- \tag{4.23}$$
$$\gamma\frac{P_{(u),v_i}}{V_{o_{(u),v_i}}+A_{(u),v_i}(z_{o_{(u),v_i}}\pm z_{(u),v_i})}A_{(u),v_i}\frac{dz_{(u),v_i}}{dt}+\frac{\gamma-1}{V_{o_{(u),v_i}}+A_{(u),v_i}(z_{o_{(u),v_i}}\pm z_{(u),v_i})}\left(\frac{dQ}{dt}\right)_{(u),v_i}$$

$$\begin{aligned}\left(\frac{dT}{dt}\right)_{(u),v_i} = {} & \frac{1}{m_{(u),v_i}}\left[\dot{m}_{m3_{v_i}}\left(\gamma T_{(m),v_i}+\frac{v^2_{in_{(3)},v_i}}{2c_v}\right)-\dot{m}_{m5_{v_3}}\left(\gamma T_{(u),v_i}+\frac{v^2_{out_{(5)},v_i}}{2c_v}\right)\right]-\frac{T_{(u),v_i}}{m_{(u),v_i}}\left(\frac{dm}{dt}\right)_{(u),v_i}- \\ & (\gamma-1)\frac{T_{(u),v_i}}{V_{o_{(u),v_i}}+A_{v_{(u),i}}(z_{o_{(u),v_i}}\pm z_{(u),v_i})}A_{v_{(u),i}}\frac{dz_{(u),v_i}}{dt}+ \\ & (\gamma-1)\frac{T_{(u),v_i}}{P_{(u),v_i}\left(V_{o_{(u),v_i}}+A_{v_{(u),i}}(z_{o_{(u),v_i}}\pm z_{(u),v_i})\right)}\left(\frac{dQ}{dt}\right)_{(u),v_i}\end{aligned} \tag{4.24}$$

Table 4.5

Governing equations at the control volumes (n) and (p)

$\boxed{V.C._{(n)}}$

$$\left(\frac{dP}{dt}\right)_{(n),v_i} = -\gamma \frac{P_{(n),v_i}}{V_{o_{(n),v_i}} + A_{(n),v_i}(z_{o_{(n),v_i}} \pm z_{(n),v_i})} A_{(n),v_i} \frac{dz_{(n),v_i}}{dt} + \frac{\gamma - 1}{V_{o_{(n),v_i}} + A_{(n),v_i}(z_{o_{(n),v_i}} \pm z_{(n),v_i})} \left(\frac{dQ}{dt}\right)_{(n),v_i} \tag{4.25}$$

$$\left(\frac{dT}{dt}\right)_{(n),v_i} = -(\gamma - 1) \frac{T_{(n),v_i}}{V_{o_{(n),v_i}} + A_{v_{(n),i}}(z_{o_{(n),v_i}} \pm z_{(n),v_i})} A_{v_{(n),i}} \frac{dz_{(n),v_i}}{dt} + \tag{4.26}$$

$$(\gamma - 1) \frac{T_{(n),v_i}}{P_{(n),v_i}\left(V_{o_{(n),v_i}} + A_{v_{(n),i}}(z_{o_{(n),v_i}} \pm z_{(n),v_i})\right)} \left(\frac{dQ}{dt}\right)_{(n),v_i}$$

$\boxed{V.C._{(p)}}$

$$\left(\frac{dP}{dt}\right)_{(p),v_i} = \frac{R}{V_{o_{(p),v_i}} + A_{(p),v_i}(z_{o_{(p),v_i}} \pm z_{(p),v_i})} \dot{m}_{m4_{v_i}} \left(\gamma T_{(p),v_i} + \frac{v^2_{in_{(4)},v_i}}{2c_v}\right) -$$

$$\gamma \frac{P_{(p),v_i}}{V_{o_{(p),v_i}} + A_{(p),v_i}(z_{o_{(p),v_i}} \pm z_{(p),v_i})} A_{(p),v_i} \frac{dz_{(p),v_i}}{dt} + \frac{\gamma - 1}{V_{o_{(p),v_i}} + A_{(p),v_i}(z_{o_{(p),v_i}} \pm z_{(p),v_i})} \left(\frac{dQ}{dt}\right)_{(p),v_i} \tag{4.27}$$

$$\left(\frac{dT}{dt}\right)_{(p),v_i} = \frac{1}{m_{(p),v_i}} \left[\dot{m}_{m3_{v_i}} \left(\gamma T_{(p),v_i} + \frac{v^2_{in_{(4)},v_i}}{2c_v}\right)\right] - (\gamma - 1) \frac{T_{(p),v_i}}{V_{o_{(p),v_i}} + A_{v_{(p),i}}(z_{o_{(p),v_i}} \pm z_{(p),v_i})} A_{v_{(p),i}} \frac{dz_{(p),v_i}}{dt} + \tag{4.28}$$

$$(\gamma - 1) \frac{T_{(p),v_i}}{P_{(p),v_i}\left(V_{o_{(p),v_i}} + A_{v_{(p),i}}(z_{o_{(p),v_i}} \pm z_{(p),v_i})\right)} \left(\frac{dQ}{dt}\right)_{(p),v_i} \tag{4.29}$$

where d_c and l_c are the internal diameter and length of the piloting channels, μ_{av} and ϱ_{av} are the average value of the dynamic viscosity and density of the fluid, and ΔP is the pressure drop between internal volumes.

The flow entering and exiting each valve port $\dot{m}_{0/5_{v_i}}$ will be figured out by the results obtained at the boundary conditions applied to the pipe ends.

On the other hand the flow through any narrow annular clearance, where a sealing component is located, was ignored. This assumption was experimentally supported by ensuring that no internal leakage occurred when operating the unit.

4.3 Resolution algorithm

The system of equations consists of a combination of algebraic and differential equations that require the use of a variable Backward Differentiation Formula (BDF) method, which is also known as Gear's method. The total number of unknown variables raises to 38, and the mentioned method was chosen as the most appropriate one to efficiently handle stiff systems of equations.

The physical constraints that condition the valve displacement are

$$z = 0; \qquad \dot{z} = max(0, \dot{z}); \qquad if \quad z < 0$$

and

$$z = z_{max}; \qquad \dot{z} = min(0, \dot{z}); \qquad if \quad z > z_{max}$$

Figure 4.15 shows the numerical method followed at each time step. Basically the input values taken from the previous time step will be used as starting values for the next calculation. This applies to the pressure and temperature at the internal chambers of the valve manifold, that will subsequently be used to determine the flow condition as well as the mass flow rate going passing through at the different inner restrictions. Moreover, depending on the input signal provided to each pilot valve, the subroutine will estimate the acting force on the corresponding spool valve that will be compared with piloting force exerted on the upper piston of the spool valve. Automatically the calculation method will help to determine the position and speed of the spool valve until reaching the stroke end, and therefore the physical constraints previously mentioned

will be applied until a different input signal (open/close) will be transmitted to the piloting valves.

4.4 0D Simulation results within the valve manifold

In order to validate the mathematical model detailed on the previous sections of this chapter, the inner chambers of the valve manifold were introduced as boundary conditions of the pipe ends. By doing so, both the system of equations that defines the dynamics of the spool valves and the solver applied to determine the fluid properties at the pipes were solved in parallel. The simulated results could then be correlated with the experimental measurements presented in Chapter 11. As a matter of fact, a precise experimental method would imply a complicate test set-up that would help to monitore the pressure and temperature characteristics within each chamber. However, being aware of the objectives of this research the above-mentioned analysis was considered to be sufficient to verify the numerical algorithm. Figure 4.19 and 4.23 depictes the predicted results when applying two different solving methods for a particular test set-up.

This approach, however, presents some drawbacks. The limited size of the inner volumes, where inflow or outflow from the pipe takes place, is usually causing strong pressure fluctuations during the high pressure blowing phase, which tend to be mitigated by reducing the internal pipe diameter. This phenomenon is in fact logical since the hypothesis usually applied to the flow from the pipe to a vessel or from the vessel to the pipe assumes a very little influence of the kynetic energy within the vessel. As a consequence, the assumptions applied when deriving the equations discussed in Chapter 8 must be reconsidered, specially when applying the Method of Characteristics. On the contrary, the high resolution methods ensure a more stable pressure characteristics since the boundary conditions take into account the kynetic energy generated into the inner chambers of the valve manifold.

Therefore the use of different resolution methods for the fluid flow governing equations at the pipes in combination with the mathematical model for the valve manifold was proven to be very consistent. The introducion of the valve manifold not only as a flow

restriction highlighted the impact on the total air consumption and also revealed the design boundaries when trying to minimize the existing dead volume.

4.5 Conclusion

Chapter 4 investigates the validatity of the mathematical model developed to estimate the influence of the valve manifold along the recycling process. In order to understand the robustness of the model, the system of equations governing the pressure and temperature within the pneumatic unit were coupled with two different numerical methods that solve the unsteady fluid flow at the pipes. The simulation results obtained for a particular experiment denotes a consistent pattern. Nevertheless, the boundary conditions applied between the end pipes and the valve manifold show the strong dependence of the inner pipe diameter, specially, when applying the Method of Characteristics. The pressure pulsations travelling along the pipes step up as the inner pipe diameter increases. This point is also associated to the fact that the assumptions applied to the fluid flow from the pipe to the valve manifold and from the valve manifold to the pipe are conditioned by the kinetic energy generated within the control volumes.

The mass flow rate through the valve manifold ports determined with CFD analysis displays certain deviations respect to the experimental results, which can be justified by the limitations of the experimental set-up used to determine the sonic conductance (refer to Chapter 6). The same results, however, are in good agreement with the theoretical values, which confirms that the discharge coefficient determined through finite element techniques can be introduced in the mathematical model without causing a significant error to the predicted air blowing process.

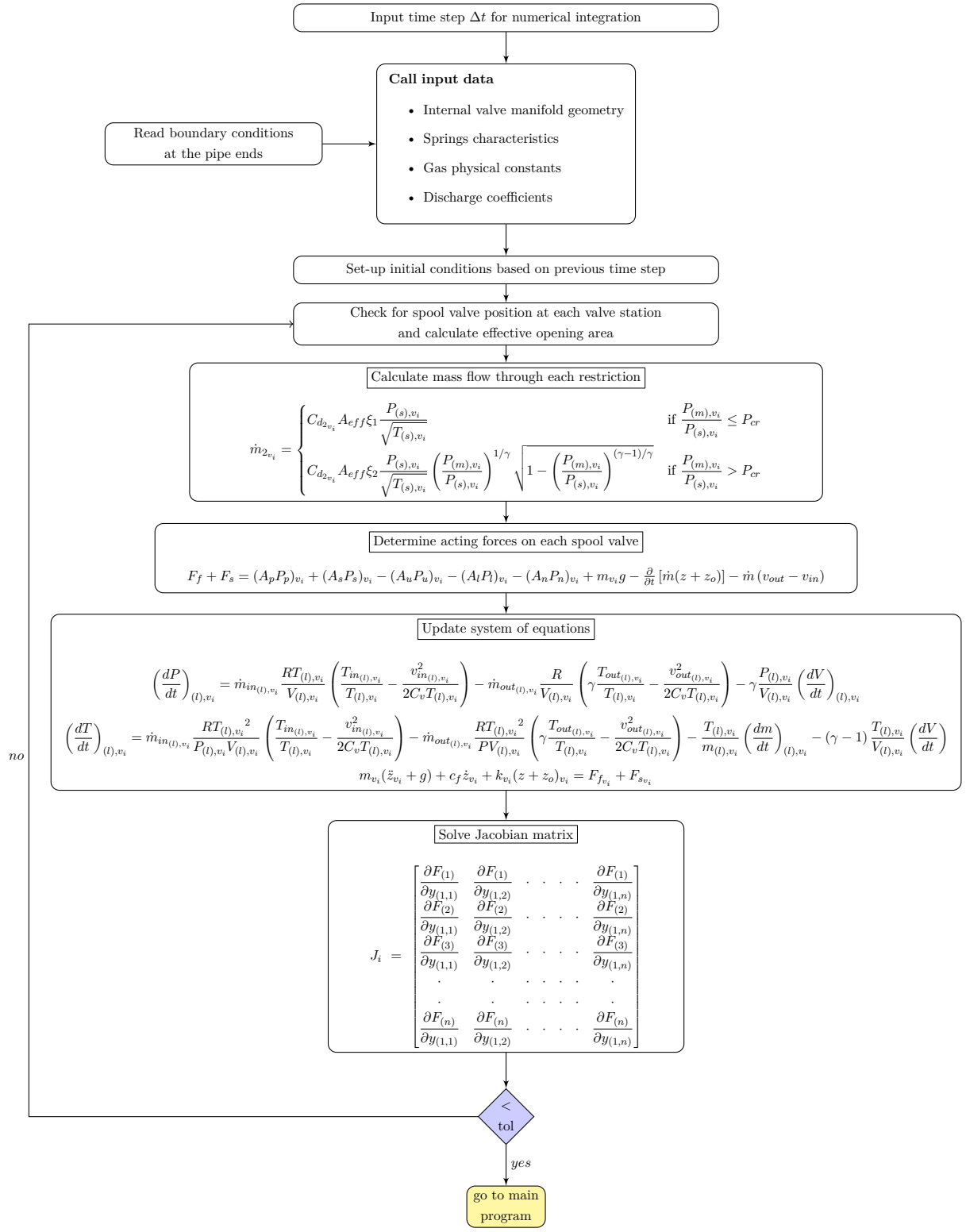

Figure 4.15: Flow chart of the FORTRAN subroutine developed to solve the system of differential equations (261)

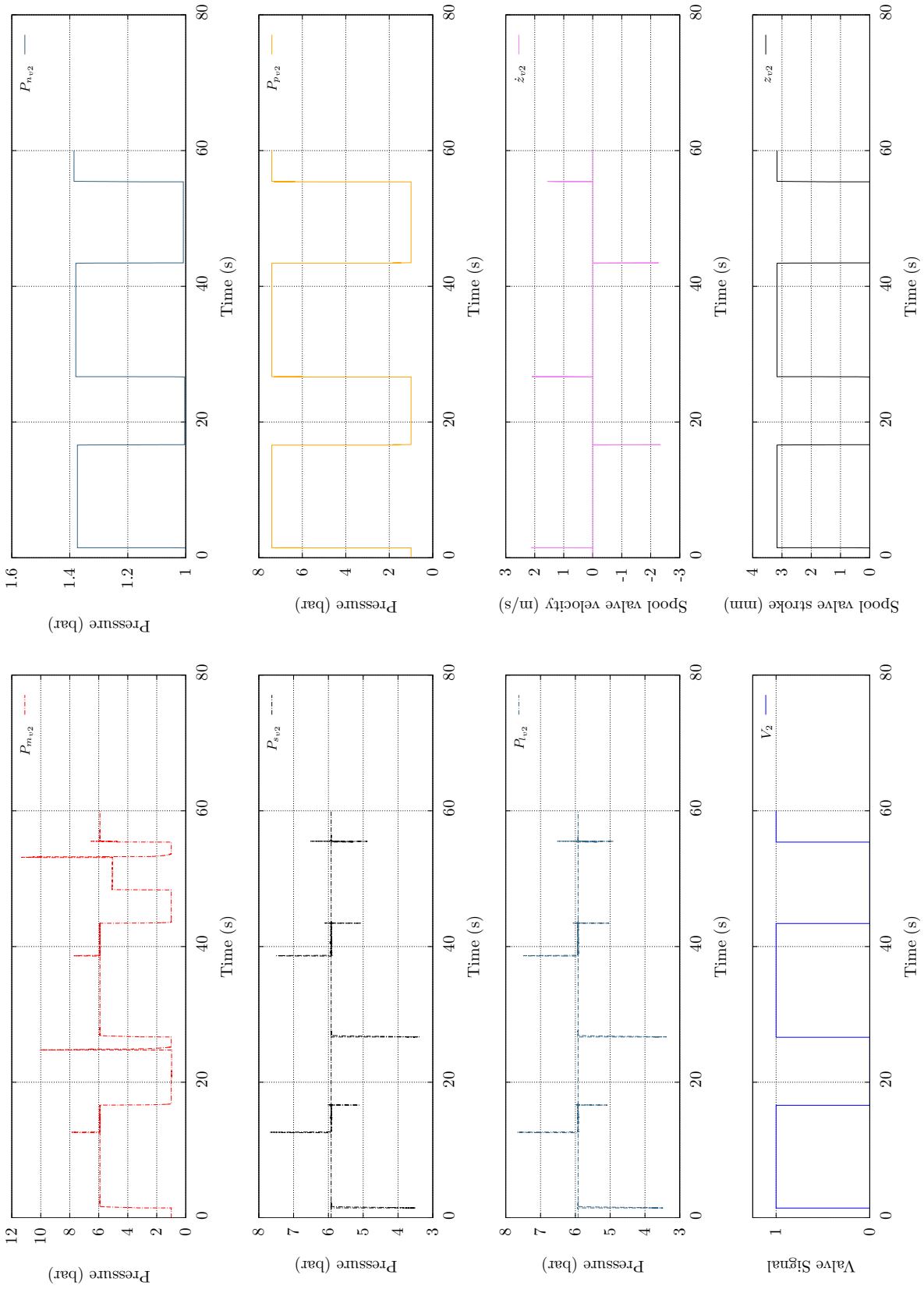

Figure 4.16: Dynamic characteristics for spool valve V_2 according to Test-56 (refer to Table 6.7)
(Transient fluid flow at the pipes solved with the Method of Characteristics)

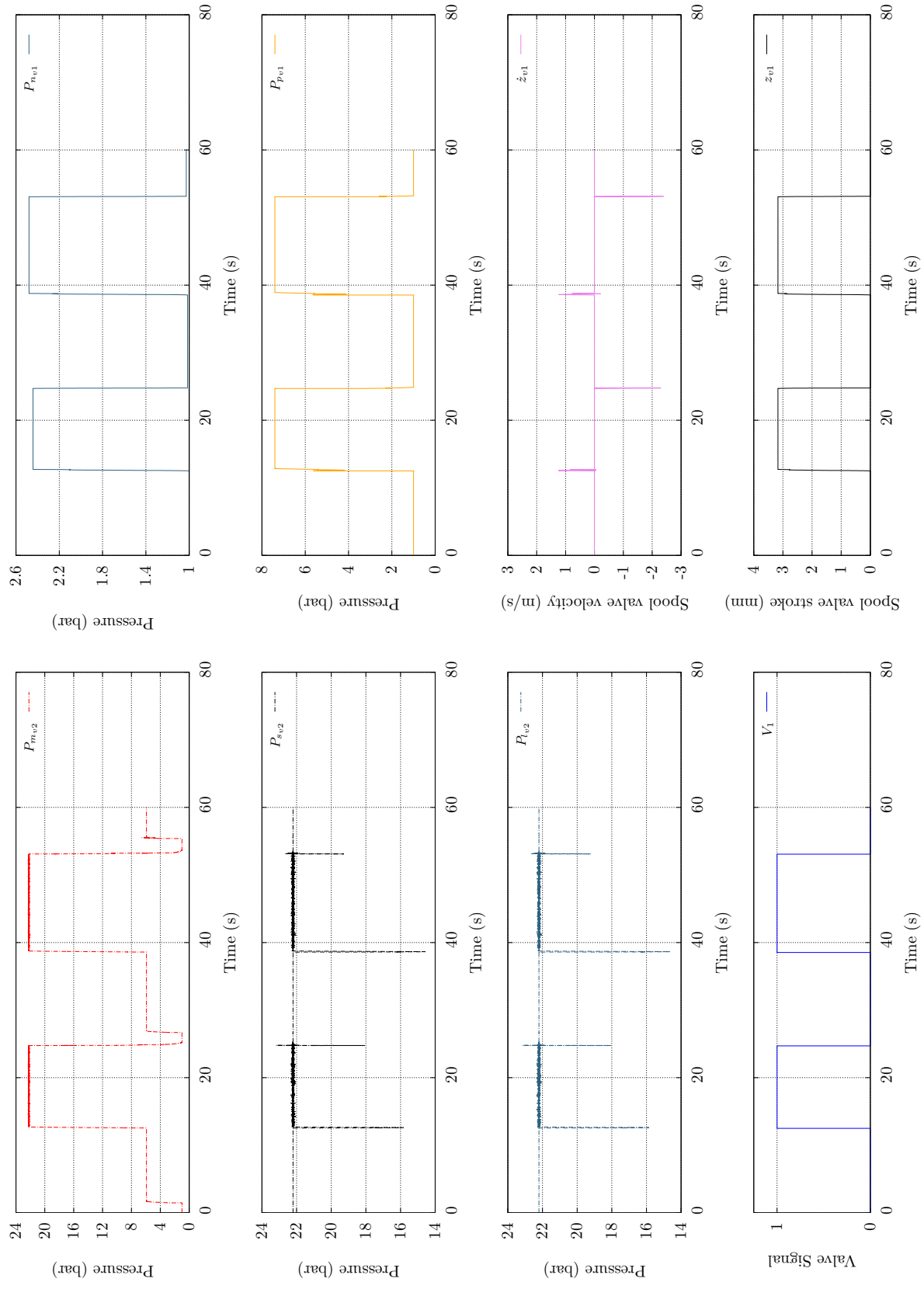

Figure 4.17: Dynamic charactertistics for spool valve V_1 according to Test-56 (refer to Table 6.7)
(Transient fluid flow at the pipes solved with the Method of Characteristics)

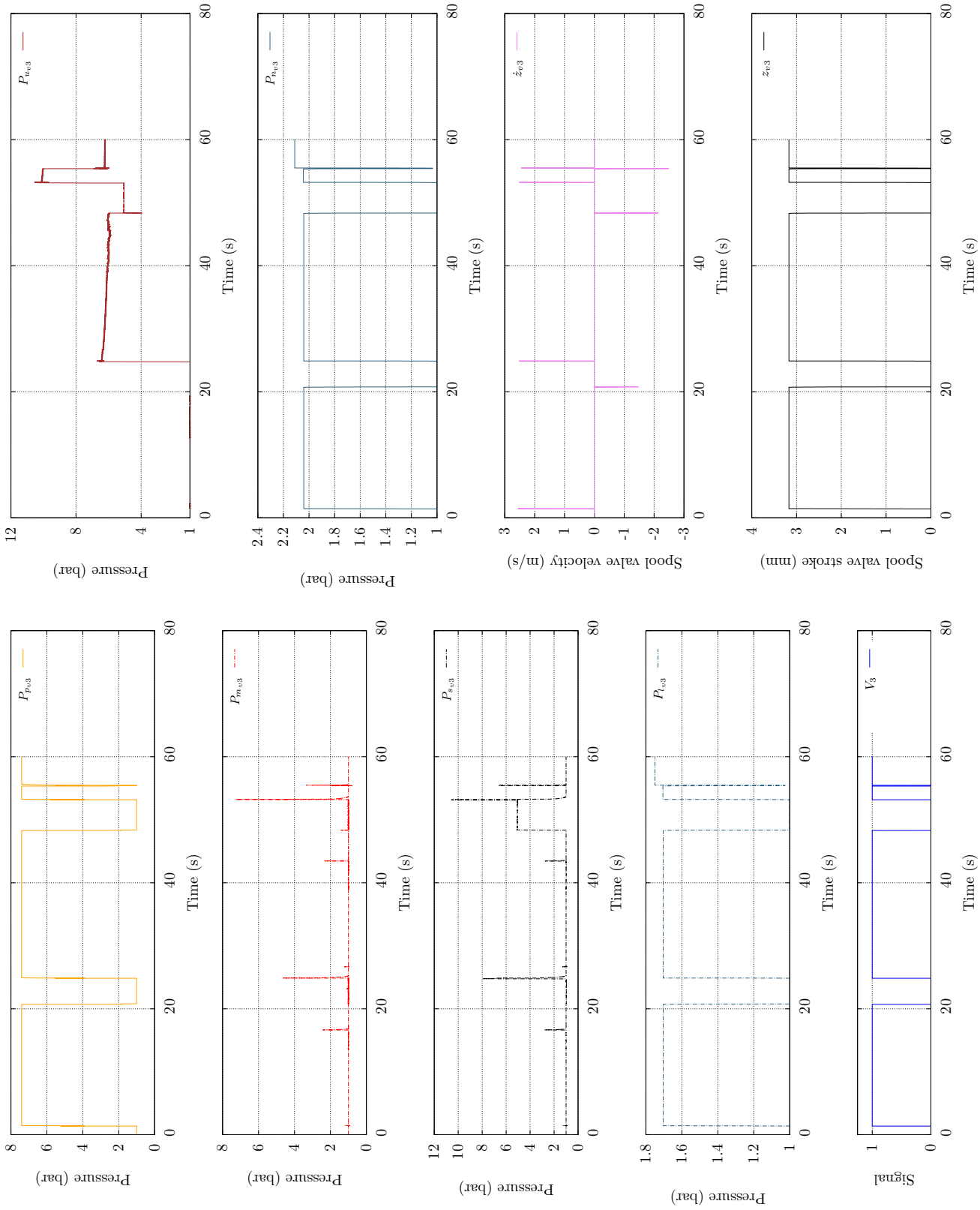

Figure 4.18: Dynamic characteristics for spool valve V_3 according to Test-56 (refer to Table 6.7)
(Transient fluid flow at the pipes solved with the Method of Characteristics)

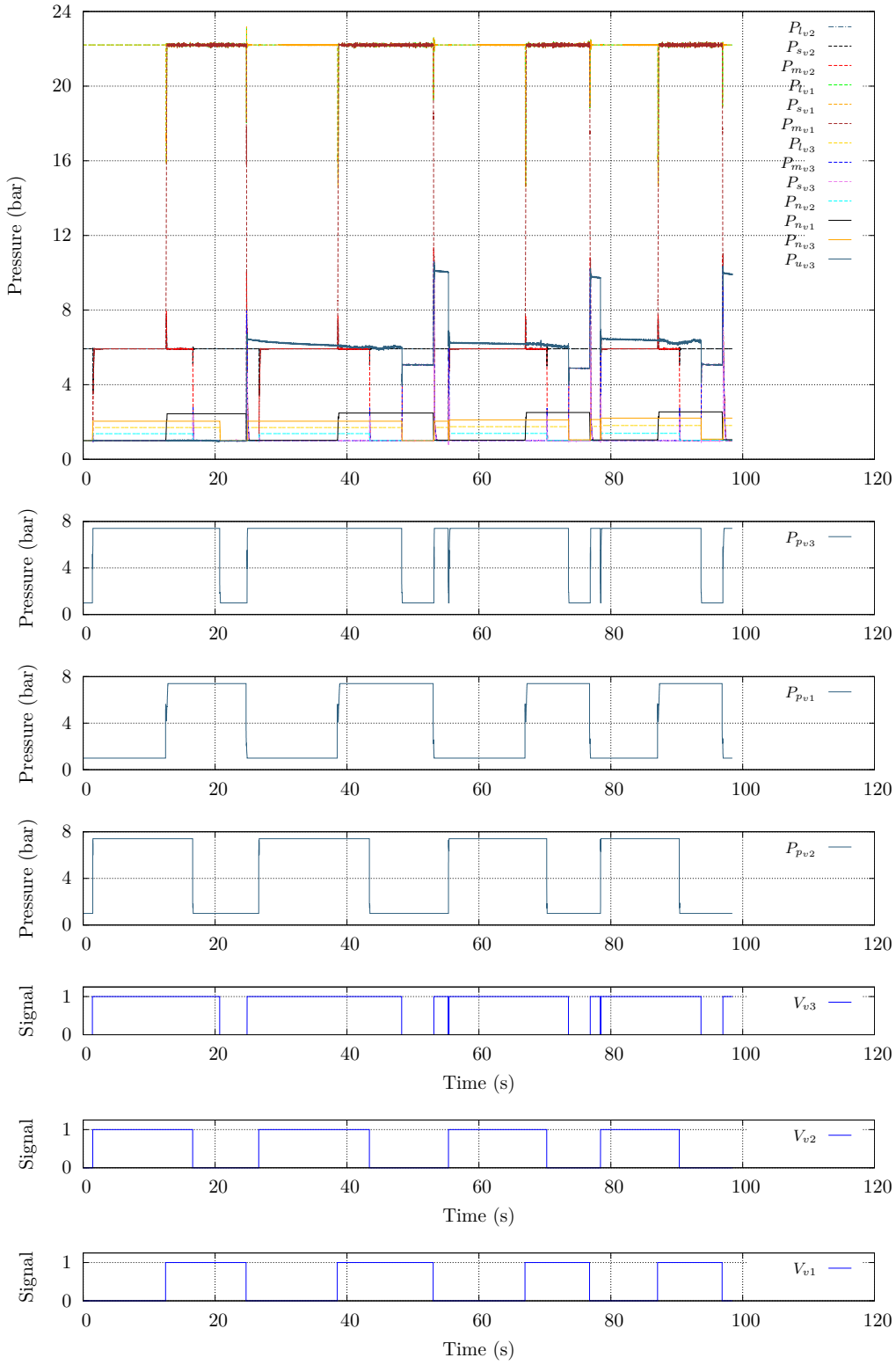

Figure 4.19: Pressure history according to Test-56 (refer to Table 6.7) (Transient fluid flow at the pipes solved with the Method of Characteristics)

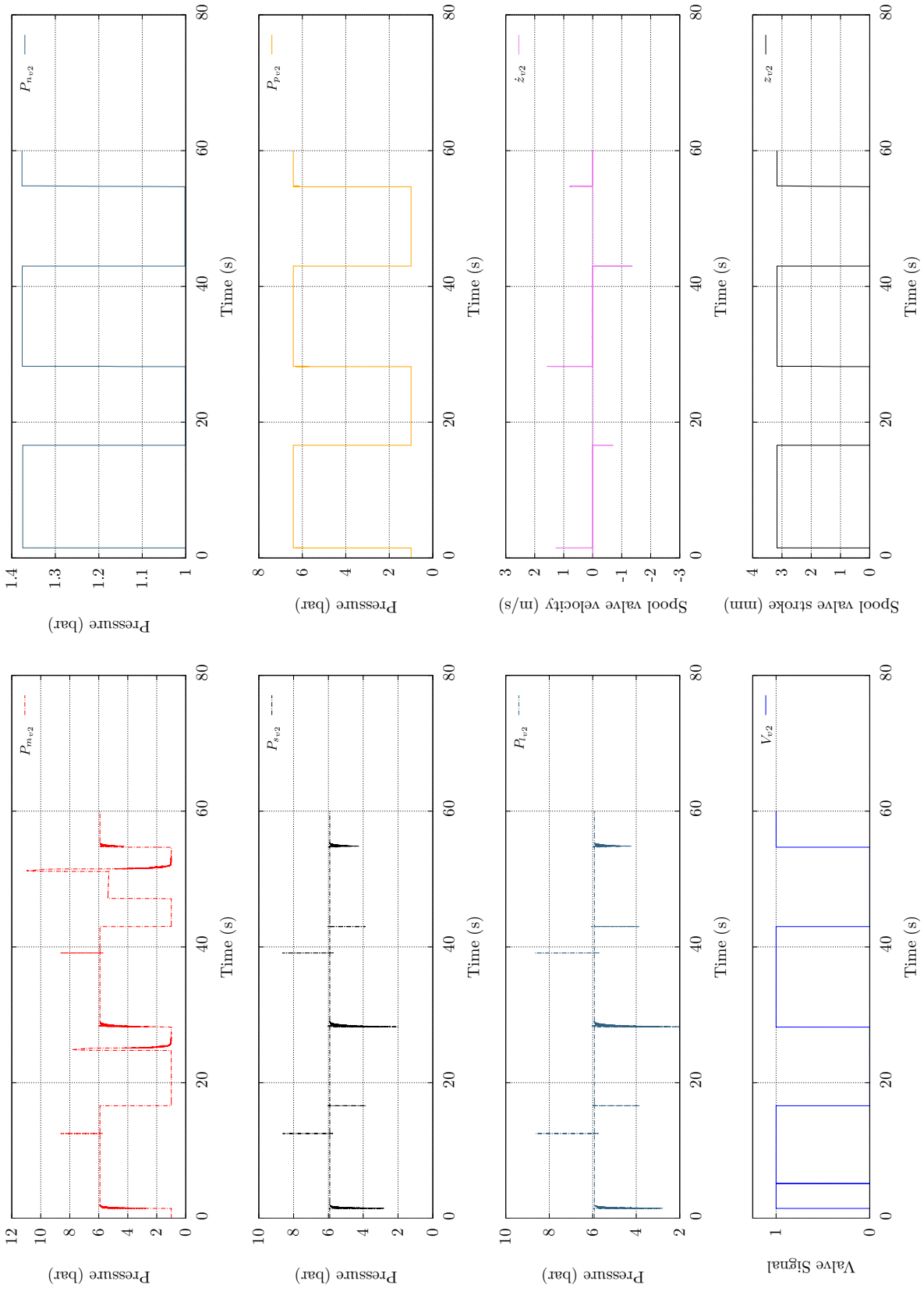

Figure 4.20: Dynamic characteristics for spool valve V_2 according to Test-56 (refer to Table 6.7)
(Transient fluid flow at the pipes solved with the HLL solver)

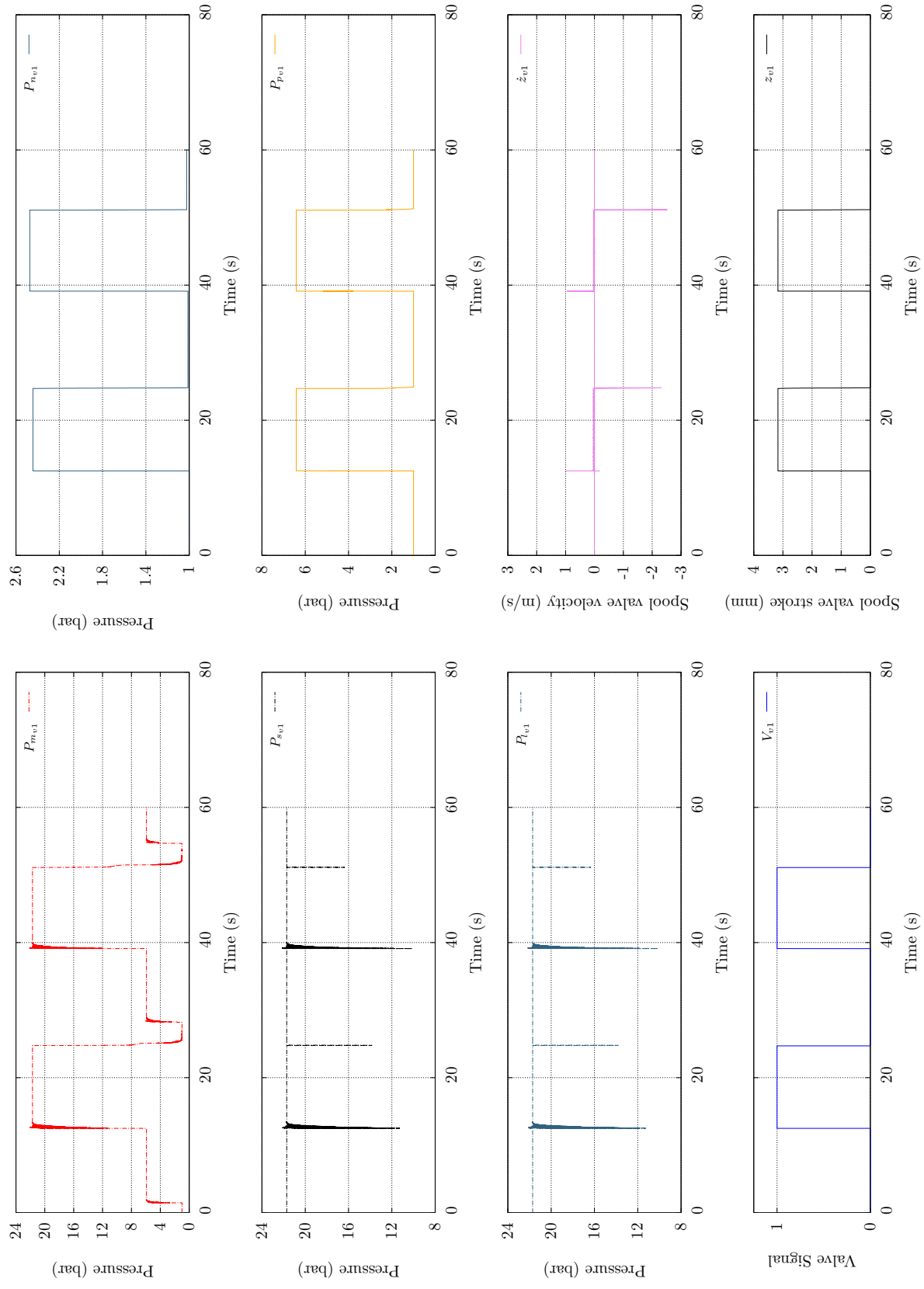

Figure 4.21: Dynamic characteristics for spool valve V_1 according to Test-56 (refer to Table 6.7)
(Transient fluid flow at the pipes solved with the HLL solver)

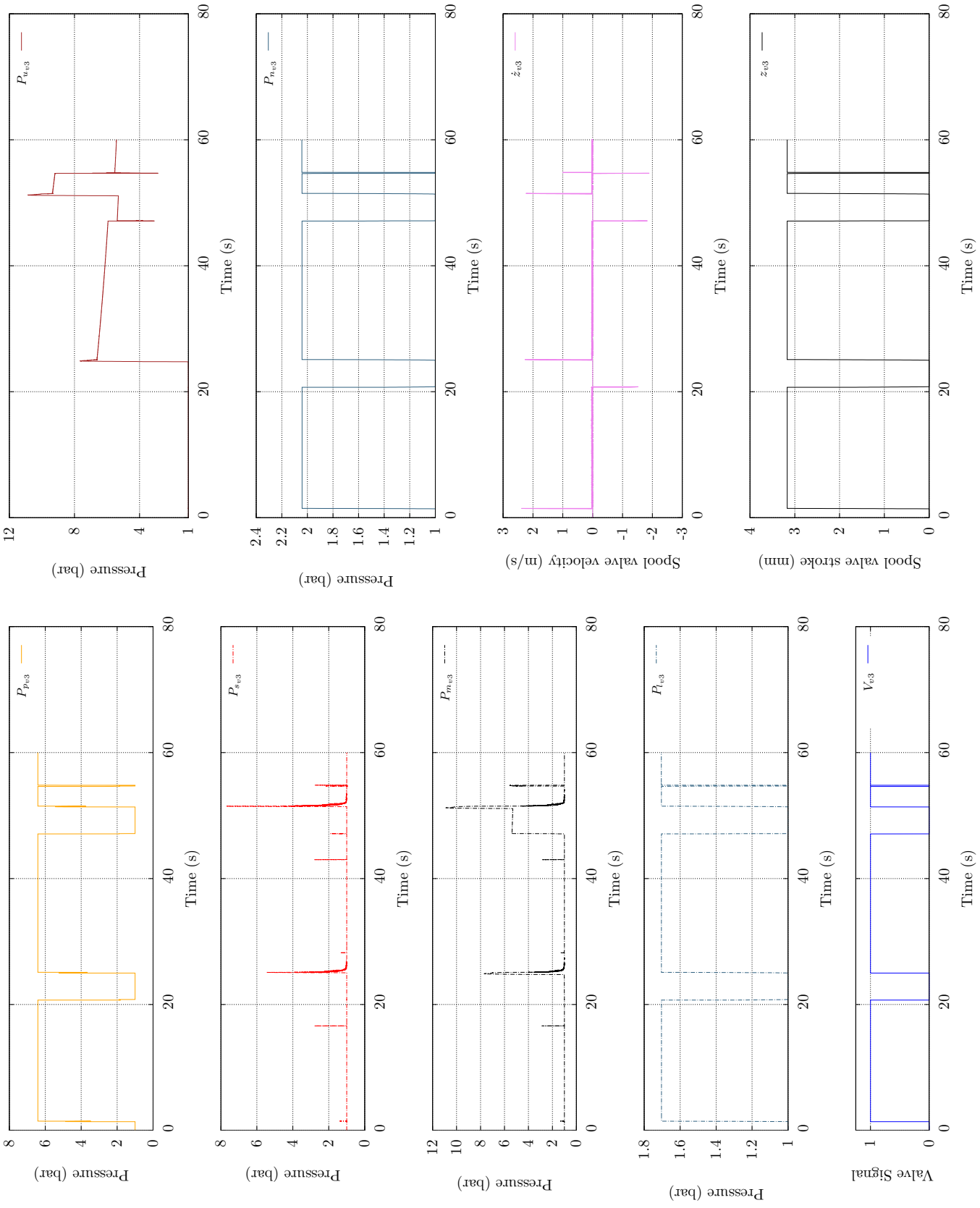

Figure 4.22: Dynamic characteristics for spool valve V_3 according to Test-56 (refer to Table 6.7)
(Transient fluid flow at the pipes solved with the HLL solver)

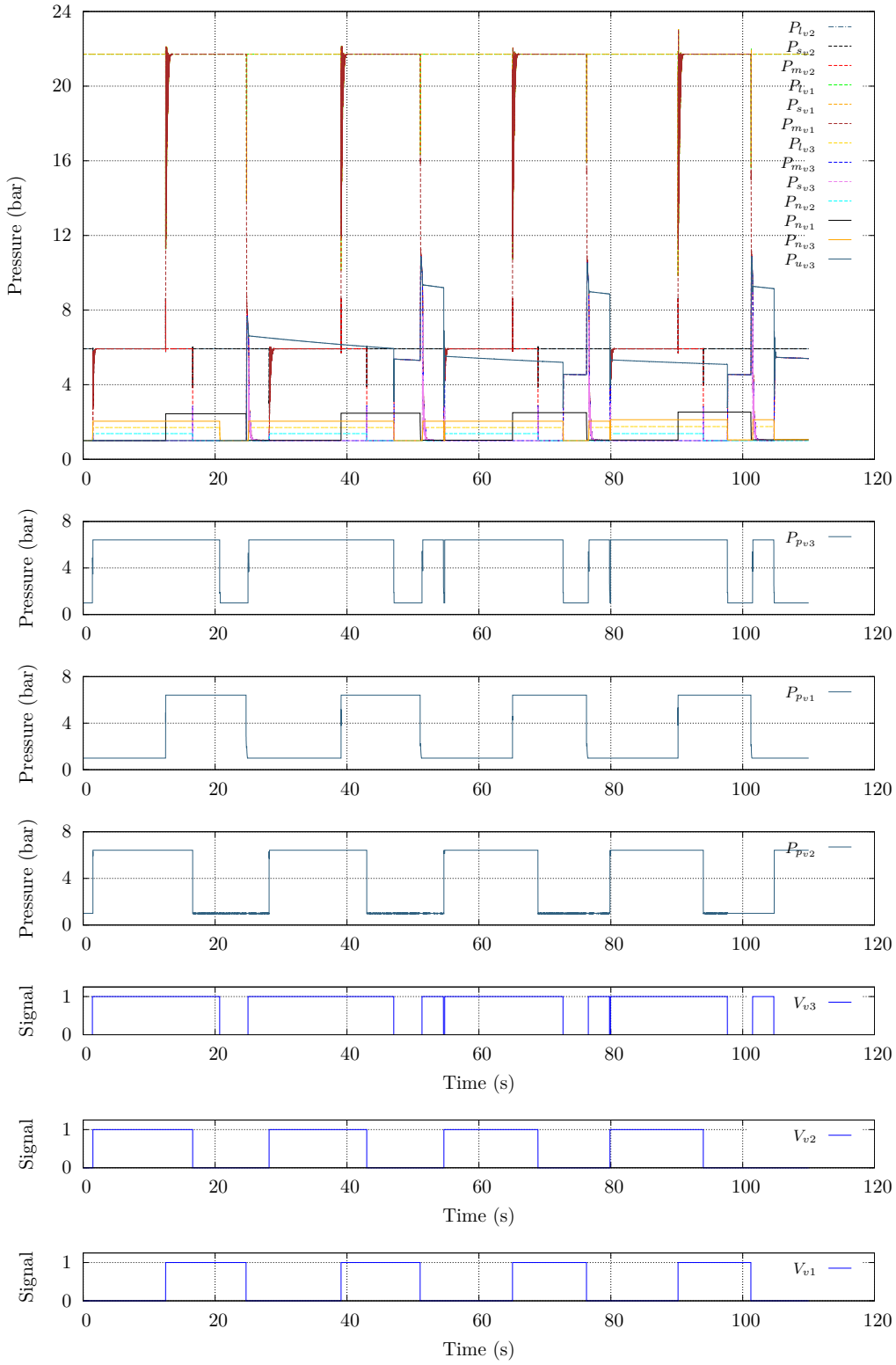

Figure 4.23: Pressure history according to Test-56 (refer to Table 6.7) (Transient fluid flow at the pipes solved with the HLL Riemann solver)

Chapter 5

Heat transfer model at the air containers

"Although to penetrate into the intimate mysteries of nature
and thence to learn the true causes of phenomena is not allowed
to us, nevertheless it can happen that a certain fictive
hypothesis may suffice for explaining many phenomena."
Leonhard Euler

In previous chapters the mathematical model to solve the flow through each component that plays a significant role within the pneumatic application under study has been discussed. This chapter, however, addresses the energy losses which directly affect the efficiency of the pneumatic circuit depicted in figure 5.1.

As a matter of fact any pneumatic system does experience irreversibilities, which cannot be avoided but reduced up to certain percentage. On the one hand, the mentioned irreversibilities are commonly associated to external friction, which is generated between the inner pipe walls and the fluid, and internal friction, which is related to viscous friction and vortex, and, on the other hand, to thermal processes.

In the past multiple experiments were conducted in with the aim of predicting the heat transfer losses in the cylinders of reciprocating machines. Those studies mainly focused on finding reliable empirical expressions to obtain a reasonable way to explain the thermal losses over a work cycle. Similarly, heat losses are particularly relevant

during the filling and emptying processes at each working cycle and, therefore, shall be specifically examined.

5.1 0D Thermodynamic volume

The performance of the recycling system is determined very largely by the efficiency of the processes of charging and discharging. The vessels have been discretized by a zero-dimensional model and are ruled by the equations already discussed in Chapter 4. The main difference, though, lies on the fact that the inner volume remains constant. It should also be noticed that the real blowing process does experience a volume change related to the expansion of the fluid inside the preform, however that physical process has not been taken into account in this study. Hence, the governing equations are as follows:

- Non-adiabatic charging:

$$\frac{dP}{dt} = \dot{m}_{in}\frac{RT}{V}\left(\gamma\frac{T_{in}}{T} - \frac{v_{in}^2}{2C_vT}\right) - (\gamma-1)\frac{\alpha_w A_w T}{PV}\left(1-\frac{T_w}{T}\right) \tag{5.1}$$

$$\frac{dT}{dt} = \dot{m}_{in}\frac{T}{m}\left(\gamma\frac{T_{in}}{T} - 1 - \frac{v_{in}^2}{2C_vT}\right) - (\gamma-1)\frac{\alpha_w A_w T^2}{PV}\left(1-\frac{T_w}{T}\right) \tag{5.2}$$

- Non-adiabatic discharging:

$$\frac{dP}{dt} = -\dot{m}_{out}\frac{RT}{V}\left(\gamma\frac{T_{out}}{T} - \frac{v_{out}^2}{2C_vT}\right) - \frac{\alpha_w A_w T}{PV}\left(1-\frac{T_w}{T}\right) \tag{5.3}$$

$$\frac{dT}{dt} = -\dot{m_{out}}\frac{RT^2}{PV}\left(\gamma\frac{T_{out}}{T} - 1 - \frac{v_{out}^2}{2C_vT}\right) - (\gamma-1)\frac{\alpha_w A_w T^2}{PV}\left(1-\frac{T_w}{T}\right) \tag{5.4}$$

the suffix *in* refers to the port where inflow occurs, as well as, suffix *out* refers to the port where outflow occurs. It must be taken into account that the equations above are only valid under the assumption that a perfect mixing of the fluid to an equilibrium state occurs, so the use of a single pressure and temperature describe the state of the gas in the vessels. To reinforce this hypothesis several experimental tests were conducted and are discussed later in this chapter.

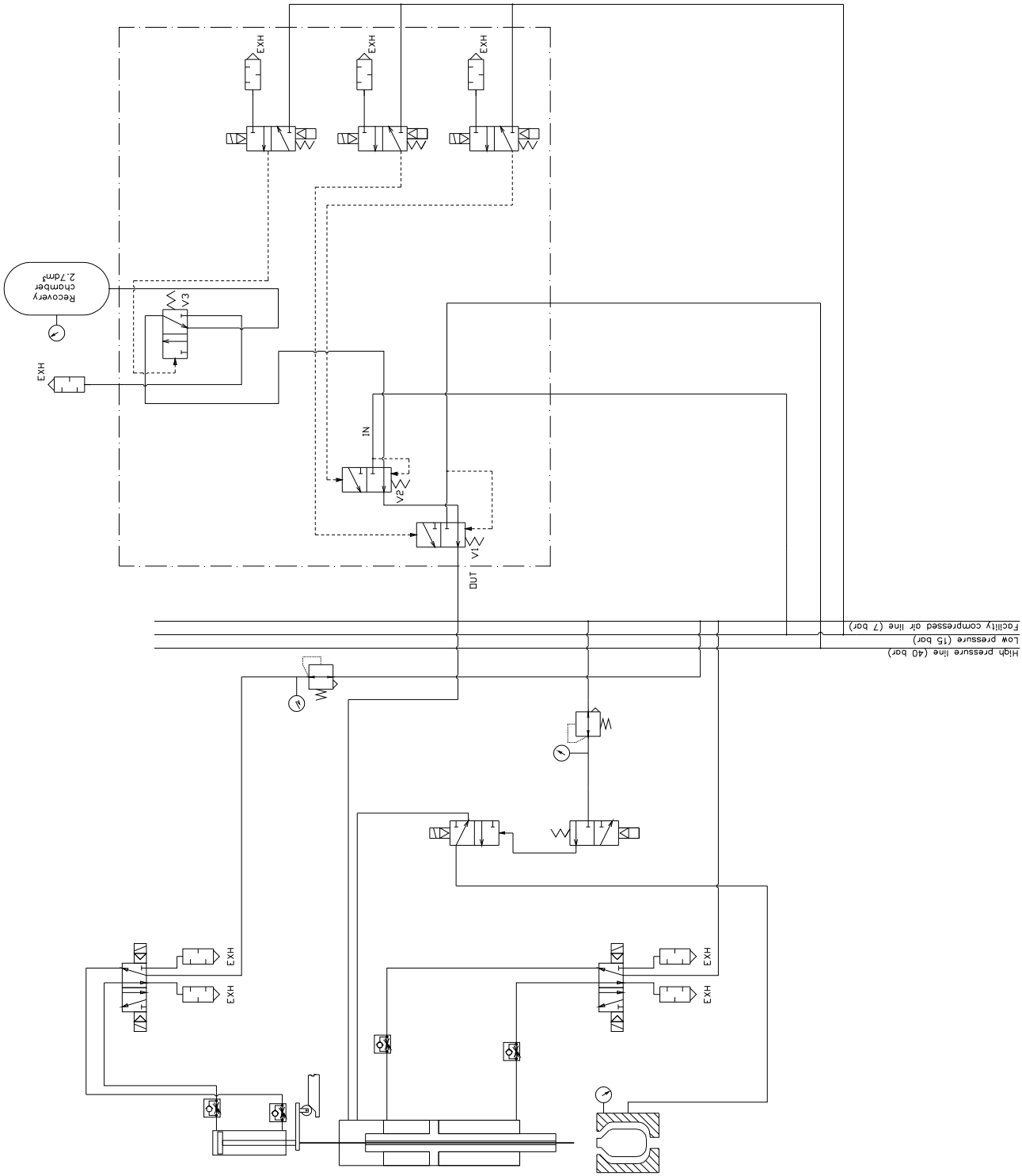

Figure 5.1: Single station PET bottle production pneumatic scheme with air recovery system

5.2 Heat transfer through the vessel walls

5.2.1 Heat transfer coefficients

Both the external and internal heat transfer coefficient at the srufaces in contact with the fluid will be assessed in accordance to the node location within the mesh. The empirical correlations to apply are shown below:

- Free convection on the outer surface of the cylindrical walls:

$$Nu_{ext} = \begin{cases} 0.47 \left[\left(\dfrac{g\beta\varrho^2 \left(T_{w_p} - T_{g_{ext}}\right) L^3}{\mu^2} \right) \left(\dfrac{\mu c_p}{\lambda} \right) \right]^{1/4} & 10^4 < Ra < 10^9 \\ 0.1 \left(\dfrac{g\beta\varrho^2 \left(T_{w_p} - T_{g_{ext}}\right) d_{p_e}^3}{\mu^2} \right)^{1/3} & Ra > 10^9 \end{cases} \tag{5.5}$$

- Free convection on the outer surface of the vertical walls:

$$Nu_{ext} = \begin{cases} 0.47 \left(GrPr\right)^{1/4} \left[1 + \left(1 + \dfrac{1}{\sqrt{Pr}} \right)^2 \right]^{-1/4} & 10^4 < Ra < 10^9 \\ 0.0246 \left(GrPr\right)^{2/5} \left[\dfrac{Pr^{1/4}}{1 + 0.494 Pr^{2/3}} \right]^{2/5} & Ra > 10^9 \end{cases} \tag{5.6}$$

- Forced convection at the wall-gas cylindrical interfaces:

$$Nu_{int} = \begin{cases} 1.86 \left(\dfrac{RePr}{L/d_{i_p}} \right)^{1/3} \left(\dfrac{\mu}{\mu_w} \right)^{0.14} & Re < 2000, Gz > 10 \\ 0.023 Re^{0.8} Pr^{0.4} & Re > 2000 \end{cases} \tag{5.7}$$

- Free convection on the inner vertical surfaces:

$$Nu_{ext} = \begin{cases} 0.47 \left(GrPr\right)^{1/4} \left[1 + \left(1 + \dfrac{1}{\sqrt{Pr}} \right)^2 \right]^{-1/4} & 10^4 < Ra < 10^9 \\ 0.0246 \left(GrPr\right)^{2/5} \left[\dfrac{Pr^{1/4}}{1 + 0.494 Pr^{2/3}} \right]^{2/5} & Ra > 10^9 \end{cases} \tag{5.8}$$

The existence of natural convection or forced convection during the discharging process is commonly modelled by a polynomial combination that measures the influence of one or the other (refer to (83),(84)). The coefficient m on equation (5.9) was chosen on the

basis of a series of trials, which indicated that a value betwen 3 and 4 was the most appropriate to ensure a good correlation with the experimental results.

$$Nu_{mixed} = \left(Nu_n^m + Nu_f^m\right)^{\frac{1}{m}} \tag{5.9}$$

5.2.2 Discretization of the vessel walls

The energy balance for the control volumes depicted in figures 5.2 and 5.3 has been addressed assuming two-dimensional conduction heat transfer in the walls and forced or natural heat convection between the wall and the fluid. The radiation heat at the outer and inner surfaces of the vessels has been disregarded. Therefore the fluid circulating through the system has been considered transparent to radiation. The equations governing the heat transfer flux through each control volume are shown in Tables 5.1 to 5.4.

For the end cover a radial distribution of the heat transfer has been considered, only the heat convection will be assessed from axial point of view. After rearranging the equations for each discretized cell (refer to Table 5.1), the following equation will be used to determine the temperature at each node of end cover mesh

$$aT_{w_i} = bT_{w_{i+1}} + cT_{w_{i-1}} + d \tag{5.10}$$

The same approach was followed with the cylindrical shell of the vessel, but in this case an axial heat condution model combined with radial heat convection was employed. An finally, the rear end cover and the inlet/outlet port of the vessel were modelled with a two-dimensional heat conduction discretization together with axial and radial heat convection. Reorganizing the equations displayed in table 5.3 and 5.4 results,

$$aT_{w_i} = bT_{w_{i+1,j}} + cT_{w_{i-1,j}} + (eT_{w_{i,j+1}} + fT_{w_{i,j-1}} + d) \tag{5.11}$$

As discussed in Chapter 3, a Gauss-Seidel method combined with an axial and/or radial TDMA will be employed to solve the system of equations. The iteration process will last until the convergence criterion is met.

Note that two methods can be used to determine the heat transfer through the vessel walls to the surroundings as well as the inner gas. The first one is based on a zero-dimensional approach for the gas inside the container and unsteady one-dimensional

heat transfer model (88), while the second one relies on a global heat transfer method which takes into account the energy balance of each individual control volume. Both of them were implemented in the Fortran code developed for this project (refer to figure 5.4).

5.2.3 Experimental pre-analysis of the temperature characteristics within a pneumatic container

Based on the fact that there was not previous data available that could be used as reference when assessing the amount of heat that is generally released through the vessel walls when a container is subjected to a continuous charging and discharging process, a series of experimental test were conducted in our laboratory. For that purpose a set of termocouples were distributed at different positions of a pneumatic double acting actuator. The temperature at the inner and outer walls of the container as well as of the inner gas supplied and released from the vessel were recorded. As shown in figure 5.6, the piston, piston rod and the rest of internal parts, were removed so the pneumatic actuator acted as a vessel.

The experimental results displayed in figures 5.7 and 5.8 (see also figures 5.11, 5.12 and 5.13) indicate that the lowest gas temperature are systematically registered by thermocouples T105, T106, T109, being thermocouple T105 the one experiencing the minimum value. On the other hand the thermocouples detecting the highest gas temperatures are the sensors T111 and T112, being T111 the one registering the greater values.

Regarding the thermocouples located at the inner walls of the container, the lowest temperatures were provided by the thermocouple T207 and T208, which demonstrate that the coldest volume of air remains at the lowest side of the container during the discharging process (also furthest point from the exhaust port). As a matter of fact a closer view to the results revealed that the inner wall temperature at positions such as T203 and T209 almost did not cool down during the discharging process. This phenomenon may be explained by the fact that the geometry of the vessel contributes to reduce the speed of the gas during the exhaust. On the contrary the highest inner wall temperatures seems to be evenly distributed along the top side inner wall, which gradually fall down when moving towards the middle part of the vessel when viewed

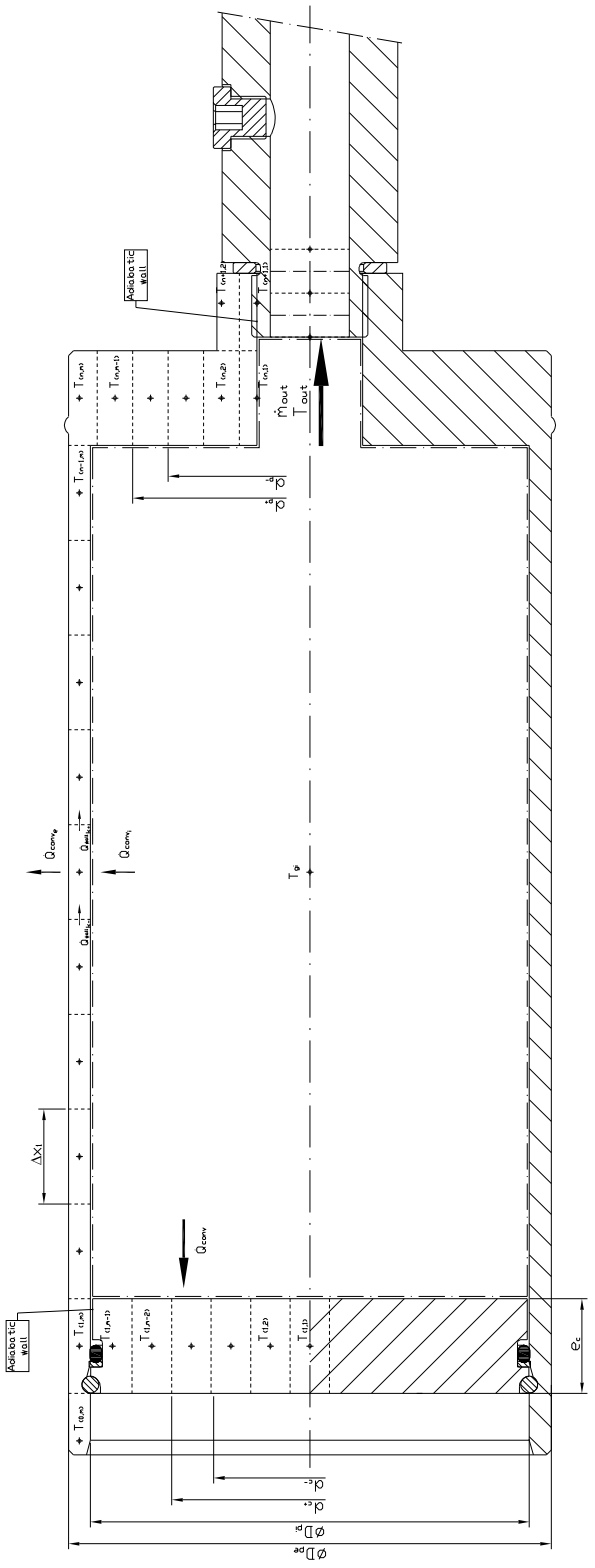

Figure 5.2: Axisymmetric distribution of the computational mesh in the cavity vessel

Table 5.1

Governing equations of heat balance through the end cover

$\boxed{V.C._{node=(1,1)}}$

$$\alpha^t_{int_{c_{(1,1)}}} \frac{\pi}{4} d^2_{c_{(+1)}} \left(T^t_{g_{int}} - T^t_{w_{(1,1)}}\right) = \lambda_{w_{c_{(+1)}}} \left(\frac{T^t_{w_{(1,1)}} - T^t_{w_{(1,2)}}}{\Delta r_1}\right) \pi d_{c_{(+1)}} e_c + \alpha^t_{e_{c_{(1,1)}}} \frac{\pi}{4} d^2_{c_{(+1)}} (T^t_{w_{(1,1)}} - T^t_{g_{ext}}) + \varrho_{w_c} C_{p_{w_c}} V_{(1,1)} \left(\frac{T^{t+\Delta t}_{w_{(1,1)}} - T^t_{w_{(1,1)}}}{\Delta t}\right) \quad (5.12)$$

$\boxed{V.C._{node=(1,2)<(1,j)<(1,m-1)}}$

$$\lambda_{w_{c_{(-j)}}} \left(\frac{T^t_{w_{(1,j-1)}} - T^t_{w_{(1,j)}}}{\Delta r_1}\right) \pi d_{c_{(-j)}} e_c + \alpha^t_{int_{c_{(1,j)}}} \frac{\pi}{4} \left(d^2_{c_{(+j)}} - d^2_{c_{(-j)}}\right) (T^t_{g_{int}} - T^t_{w_{(1,j)}}) =$$
$$\lambda_{w_{c_{(+j)}}} \left(\frac{T^t_{w_{(1,j)}} - T^t_{w_{(1,j+1)}}}{\Delta r_1}\right) \pi d_{c_{(+j)}} e_c + \alpha^t_{ext_{c_{(1,j)}}} \frac{\pi}{4} \left(d^2_{c_{(+j)}} - d^2_{c_{(-j)}}\right) (T^t_{w_{(1,j)}} - T^t_{g_{ext}}) + \varrho_{w_c} C_{p_{w_c}} V_{(1,j)} \left(\frac{T^{t+\Delta t}_{w_{(1,j)}} - T^t_{w_{(1,j)}}}{\Delta t}\right) \quad (5.13)$$

$\boxed{V.C._{node=(1,m-1)}}$

$$\lambda_{w_{c_{-(m-1)}}} \left(\frac{T^t_{w_{(1,m-2)}} - T^t_{w_{(1,m-1)}}}{\Delta r_1}\right) \pi d_{c_{-(m-1)}} e_c + \alpha^t_{int_{c_{(1,m-1)}}} \frac{\pi}{4} \left(d^2_{c_{+(m-1)}} - d^2_{c_{-(m-1)}}\right) (T^t_{g_{int}} - T^t_{w_{(1,m-1)}}) =$$
$$\alpha^t_{ext_{c_{(1,m-1)}}} \frac{\pi}{4} \left(d^2_{c_{+(m-1)}} - d^2_{c_{-(m-1)}}\right) (T^t_{w_{(1,m-1)}} - T^t_{g_{ext}}) + \varrho_{w_p} C_{p_{w_p}} V_{(1,m-1)} \left(\frac{T^{t+\Delta t}_{w_{(1,m-1)}} - T^t_{w_{(1,m-1)}}}{\Delta t}\right) \quad (5.14)$$

Table 5.2

Governing equations of heat transfer through the cylindrical shell

$\boxed{V.C._{node=(0,m)}}$

$$\bar{\alpha}^t_{ext_{(p)_{(0,m)}}} \pi d_{p_i} \frac{\Delta x_1}{2} (T^t_{w_{(0,m)}} - T^t_{g_{ext}}) + \bar{\bar{\alpha}}^t_{ext_{p_{(0,m)}}} \frac{\pi}{4} (d^2_{p_e} - d^2_{p_i})(T^t_{w_{(0,m)}} - T^t_{g_{ext}}) + \lambda_{w_{p_{+(0,m)}}} \left(\frac{T^t_{w_{(0,m)}} - T^t_{w_{(1,m)}}}{\Delta x_1} \right) \frac{\pi}{4} \left(d^2_{p_e} - d^2_{p_i} \right) +$$
$$\alpha^t_{ext_{p_{(0,m)}}} \pi d_{p_e} \Delta x_1 (T^t_{w_{(0,m)}} - T^t_{g_{ext}}) + \varrho_{w_p} C_{p_{w_p}} V_{(0,m)} \left(\frac{T^{t+\Delta t}_{w_{(0,m)}} - T^t_{w_{(0,m)}}}{\Delta t} \right) = 0 \quad (5.15)$$

$\boxed{V.C._{node=(2,m)<(i,m)<(n-1,m)}}$

$$\lambda_{w_{p_{(-i)}}} \left(\frac{T^t_{w_{(i-1,m)}} - T^t_{w_{(i,m)}}}{\Delta x_1} \right) \frac{\pi}{4} \left(d^2_{p_e} - d^2_{p_i} \right) + \alpha^t_{int_{p_{(i,m)}}} \pi d_{p_i} \Delta x_1 (T^t_{g_{int}} - T^t_{w_{(i,m)}}) =$$
$$\lambda_{w_{p_{(+i)}}} \left(\frac{T^t_{w_{(i,m)}} - T^t_{w_{(i+1,m)}}}{\Delta x_1} \right) \frac{\pi}{4} \left(d^2_{p_e} - d^2_{p_i} \right) + \alpha^t_{ext_{p_{(i,m)}}} \pi d_{p_e} \Delta x_1 (T^t_{w_{(i,m)}} - T^t_{g_{ext}}) + \varrho_{w_p} C_{p_{w_p}} V_{(i,m)} \left(\frac{T^{t+\Delta t}_{w_{(i,m)}} - T^t_{w_{(i,m)}}}{\Delta t} \right) \quad (5.16)$$

$\boxed{V.C._{node=(n,m)}}$

$$\lambda_{w_{p_{(-n)}}} \left(\frac{T^t_{w_{(n-1,m)}} - T^t_{w_{(n,m)}}}{\Delta x_1} \right) \frac{\pi}{4} \left(d^2_{p_e} - d^2_{p_i} \right) + \alpha^t_{ext_{p_{(n,m)}}} \pi d_{p_e} \Delta x_1 (T^t_{w_{(n,m)}} - T^t_{g_{ext}}) =$$
$$\lambda_{w_{(-m)}} \left(\frac{T^t_{w_{(n,m-1)}} - T^t_{w_{(n,m)}}}{\Delta r_2} \right) \pi d_{p_{(-m)}} \Delta x_1 + \alpha^t_{e_{(n,m)}} \frac{\pi}{4} \left(d^2_{p_e} - d^2_{p_i} \right) (T^t_{w_{(n,m)}} - T^t_{g_{ext}}) + \varrho_{w_p} C_{p_{w_p}} V_{(n,m)} \left(\frac{T^{t+\Delta t}_{w_{(n,m)}} - T^t_{w_{(n,m)}}}{\Delta t} \right) \quad (5.17)$$

Table 5.3

Governing equations of heat balance through the rear vessel cover

$\boxed{V.C._{node=(n,1)}}$

$$\alpha^t_{int_{p_{(n,1)}}}\pi d_{p_{input}}\Delta x_1(T^t_{g_{int}}-T^t_{w_{(n,1)}})+\alpha^t_{w_{p_{(n,1)}}}\frac{\pi}{4}\left(d^2_{p_{(+1)}}-d^2_{inlet}\right)(T^t_{g_{int}}-T^t_{w_{(n,1)}})= \lambda_{w_{p_{(+1)}}}\left(\frac{T^t_{w_{(n,1)}}-T^t_{w_{(n,2)}}}{\Delta r_2}\right)\pi d_{p_{+1}}\Delta x_1+\varrho_{w_p}C_{p_{w_p}}V_{(n,1)}\left(\frac{T^{t+\Delta t}_{w_{(n,1)}}-T^t_{w_{(n,1)}}}{\Delta t}\right) \quad (5.18)$$

$\boxed{V.C._{node=(n,2)}}$

$$\alpha^t_{int_{p_{(n,2)}}}\frac{\pi}{4}\left(d^2_{p_{(+2)}}-d^2_{p_{(-2)}}\right)(T^t_{g_{int}}-T^t_{w_{(n,2)}})+\lambda_{w_{p_{(-2)}}}\left(\frac{T^t_{w_{(n,1)}}-T^t_{w_{(n,2)}}}{\Delta r_2}\right)\pi d_{p_{(-2)}}\Delta x_1=\lambda_{w_{p_{(+2)}}}\left(\frac{T^t_{w_{(n,2)}}-T^t_{w_{(n,3)}}}{\Delta r_2}\right)\pi d_{p_{(+2)}}\Delta x_1+ \lambda_{w_{p_{(+n)}}}\left(\frac{T^t_{w_{(n,2)}}-T^t_{w_{(n+1,2)}}}{\Delta x_1}\right)\frac{\pi}{4}\left(d^2_{p_{(+2)}}-d^2_{p_{(-2)}}\right)+\varrho_{w_p}C_{p_{w_p}}V_{(n,2)}\left(\frac{T^{t+\Delta t}_{w_{(n,2)}}-T^t_{w_{(n,2)}}}{\Delta t}\right) \quad (5.19)$$

$\boxed{V.C._{node=(n,3)}}$

$$\alpha^t_{int_{p_{(n,3)}}}\frac{\pi}{4}\left(d^2_{p_{(+3)}}-d^2_{p_{(-3)}}\right)(T^t_{g_{int}}-T^t_{w_{(n,3)}})+\lambda_{w_{p_{(-3)}}}\left(\frac{T^t_{w_{(n,2)}}-T^t_{w_{(n,3)}}}{\Delta r_2}\right)\pi d_{p_{(-3)}}\Delta x_1=\lambda_{w_{p_{(+3)}}}\left(\frac{T^t_{w_{(n,3)}}-T^t_{w_{(n,4)}}}{\Delta r_2}\right)\pi d_{p_{(+3)}}\Delta x_1+ \lambda_{w_{p_{(+n)}}}\left(\frac{T^t_{w_{(n,3)}}-T^t_{w_{(n+1,3)}}}{\Delta x_1}\right)\frac{\pi}{4}\left(d^2_{p_{(+3)}}-d^2_{p_{(-3)}}\right)+\varrho_{w_p}C_{p_{w_p}}V_{(n,3)}\left(\frac{T^{t+\Delta t}_{w_{(n,3)}}-T^t_{w_{(n,3)}}}{\Delta t}\right) \quad (5.20)$$

Table 5.4

Governing equations of heat transfer through the inlet/outlet port

$\boxed{V.C._{node=(n+1,1)}}$

$$\lambda_{w_{p_{-(n+1)}}}\left(\frac{T^t_{w_{(n,1)}}-T^t_{w_{(n+1,1)}}}{\Delta x_1}\right)\frac{\pi}{4}\left(d^2_{p_{(+1)}}-d^2_{inlet}\right)=\lambda_{w_{p_{(+1)}}}\left(\frac{T^t_{w_{(n+1,1)}}-T^t_{w_{(n+1,2)}}}{\Delta r_2}\right)$$
$$\pi d_{p_{(+1)}}\Delta x_e+\varrho_{w_p}C_{p_{w_p}}V_{(n+1,1)}\left(\frac{T^{t+\Delta t}_{w_{(n+1,1)}}-T^t_{w_{(n+1,1)}}}{\Delta t}\right)=0 \quad (5.21)$$

$\boxed{V.C._{node=(n+1,2)}}$

$$\lambda_{w_{p_{(-2)}}}\left(\frac{T^t_{w_{(n+1,1)}}-T^t_{w_{(n+1,2)}}}{\Delta r_2}\right)\pi d_{p_{(-2)}}\Delta x_e+\lambda_{w_{p_{(-2)}}}\left(\frac{T^t_{w_{(n,2)}}-T^t_{w_{(n+1,2)}}}{\Delta x_1}\right)\frac{\pi}{4}\left(d^2_{p_{(+2)}}-d^2_{p_{(-2)}}\right)=$$
$$\lambda_{w_{p_{(+2)}}}\left(\frac{T^t_{w_{(n+1,2)}}-T^t_{w_{(n+1,3)}}}{\Delta r_2}\right)\pi d_{p_{(+2)}}\Delta x_e+\varrho_{w_p}C_{p_{w_p}}V_{(n+1,2)}\left(\frac{T^{t+\Delta t}_{w_{(n+1,2)}}-T^t_{w_{(n+1,2)}}}{\Delta t}\right) \quad (5.22)$$

$\boxed{V.C._{node=(n+1,2)}}$

$$\lambda_{w_{p_{(-3)}}}\left(\frac{T^t_{w_{(n+1,2)}}-T^t_{w_{(n+1,3)}}}{\Delta r_2}\right)\pi d_{p_{(-3)}}\Delta x_e+\lambda_{w_{p_{(-2)}}}\left(\frac{T^t_{w_{(n,3)}}-T^t_{w_{(n+1,3)}}}{\Delta x_1}\right)\frac{\pi}{4}\left(d^2_{ext_{inlet}}-d^2_{p_{(-3)}}\right)=$$
$$\lambda_{w_{p_{(+3)}}}\left(\frac{T^t_{w_{(n+1,2)}}-T^t_{w_{(n+1,3)}}}{\Delta r_2}\right)\pi d_{p_{(+2)}}\Delta x_e+\varrho_{w_p}C_{p_{w_p}}V_{(n+1,3)}\left(\frac{T^{t+\Delta t}_{w_{(n+1,3)}}-T^t_{w_{(n+1,3)}}}{\Delta t}\right) \quad (5.23)$$

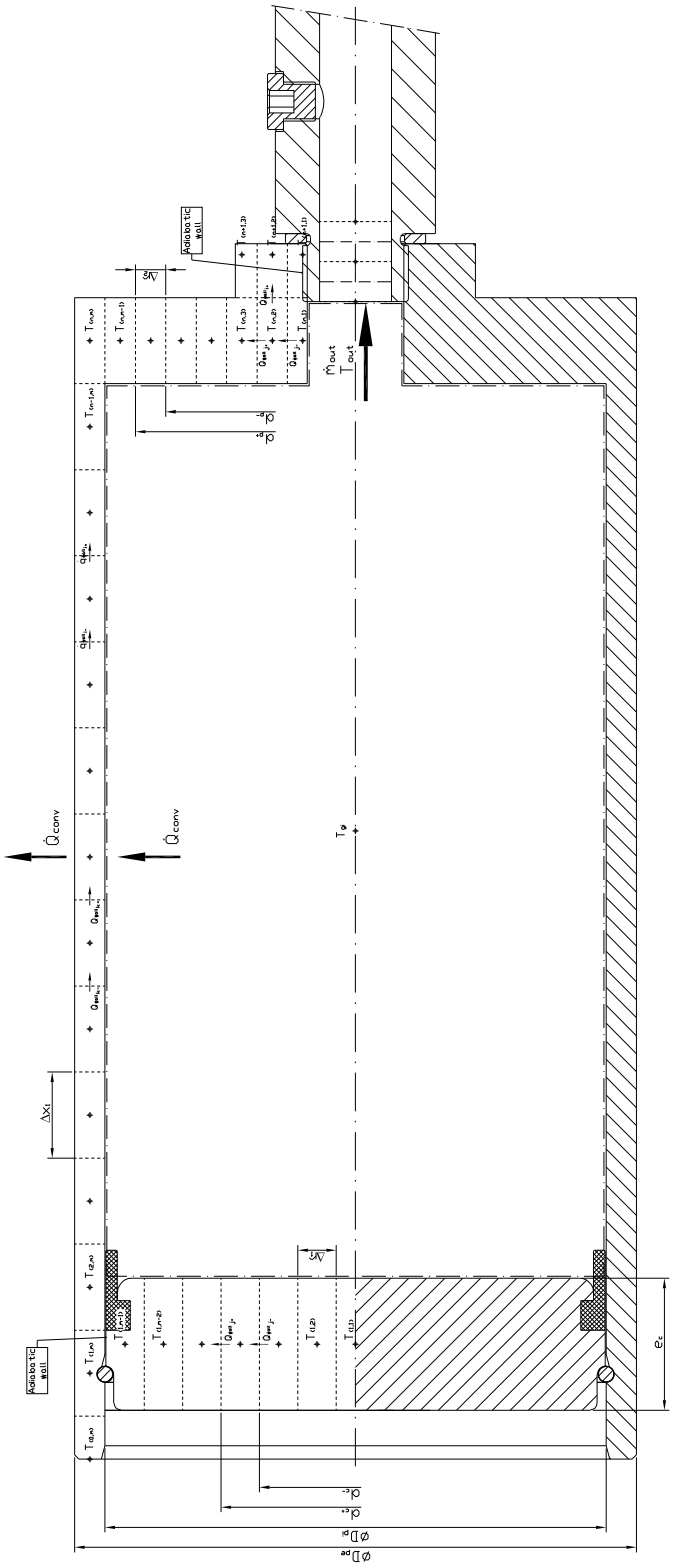

Figure 5.3: Axisymmetric distribution of the computational mesh in the recycling vessel

Figure 5.4: Flow chart of the FORTRAN subroutine developed to solve the heat transfer governing equations at the vessels

horizontally. Additionally, the temperature at the outer side of the vessel follows the inner temperature trend.

In order to determine the gas and wall temperature characteristics when the vessel is submitted to a continuous charging and discharging process, a series of tests were conducted at different operating pressures. The temperature of the points that previously registered the minimum and maximum values are depicted in figure 5.9. It should be noticed that the temperature curves must be considered as measuring a point temperature during the fill and blow out process and not the mean air temperature.

The results highlighted that for the internal gas the temperature fluctuated within the same range of values that were initially observed, while for the inner walls a smooth displacement of the averaged temperature step started raising until reaching a constant averaged value. This assymptotic behaviour of the temperature certainly remembers the expressions examined by Horlock and Woods (143) for the consecutive charging and discharging processes. The observation of the gas temperatures in the vessel over a period of 13.5 hours of continuous operation revealed that the temperatures attained after charge and discharge lied within an averaged interval of 5°C, being this variation lower or higher depending on the location of the thermocouple. This test helped to confirm that due to the nature of the physical process under study, which works over a continuous high frequency charging and discharging process, the assumption of having an even distribution of the gas temperature within the vessels is very approximated and contrarily to what the authors previously mentioned predicted, the maximum and minimum gas temperature after each charge and discharge cycle seems reasonably constant.

5.2.4 Exergy assessment of charging and discharging process

The pneumatic circuit shown in figure 5.5 may also be understood as an accumulator which delivers a certain amount of air when required by a pneumatic line that is operating in parallel. Disregarding the pneumatic circuit prior to the inlet valve, the maximum useful work (274),(266), that may be obtained from the stored gas, assuming that the process is quasi-static, is as follows,

$$\Phi = c_p T_{ref} \left\{ \frac{T}{T_{ref}} - 1 - ln\frac{T}{T_{ref}} + \frac{\gamma - 1}{\gamma} \left[ln\frac{p}{p_{ref}} + \frac{T}{T_{ref}} \left(\frac{p_{ref}}{p} - 1 \right) \right] \right\} \tag{5.24}$$

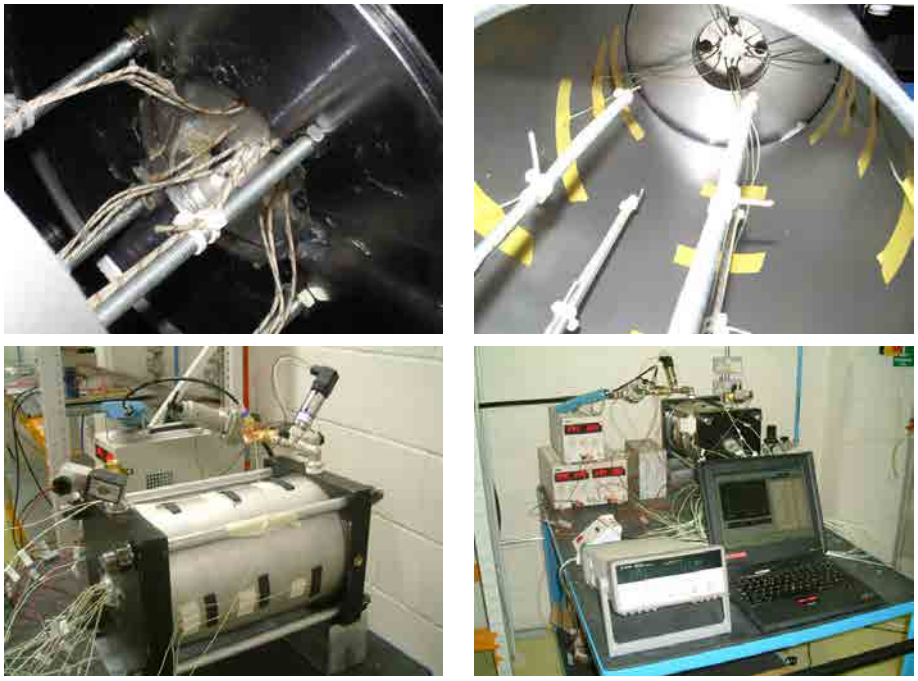

(a) Thermocouple arrangement around the inner volume of the vessel

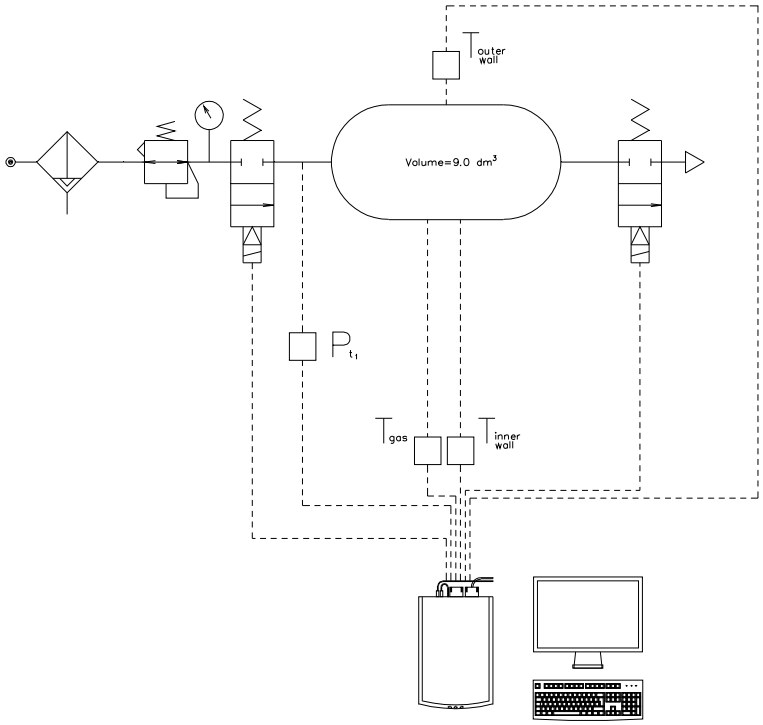

(b) Pneumatic test scheme

Figure 5.5: Lay-out of the temperature acquisition test method for a pneumatic reservoir

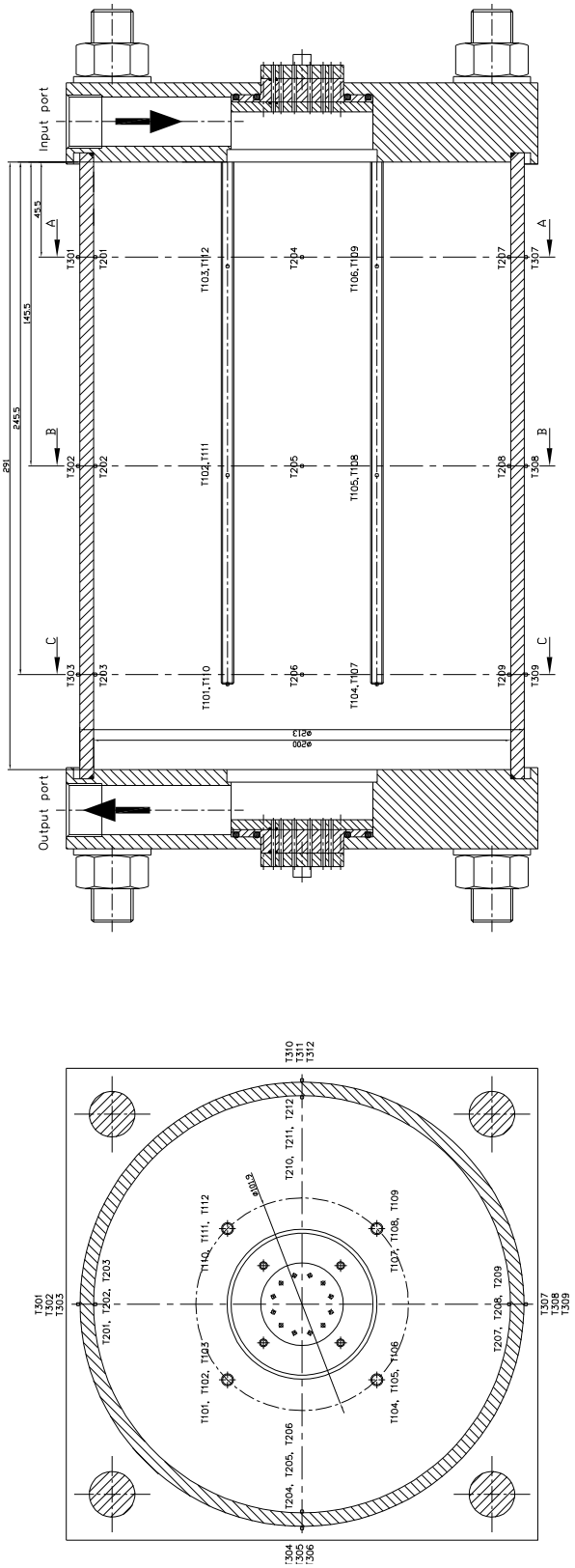

Figure 5.6: Schematic view of the thermocouples distribution at the pneumatic vessel

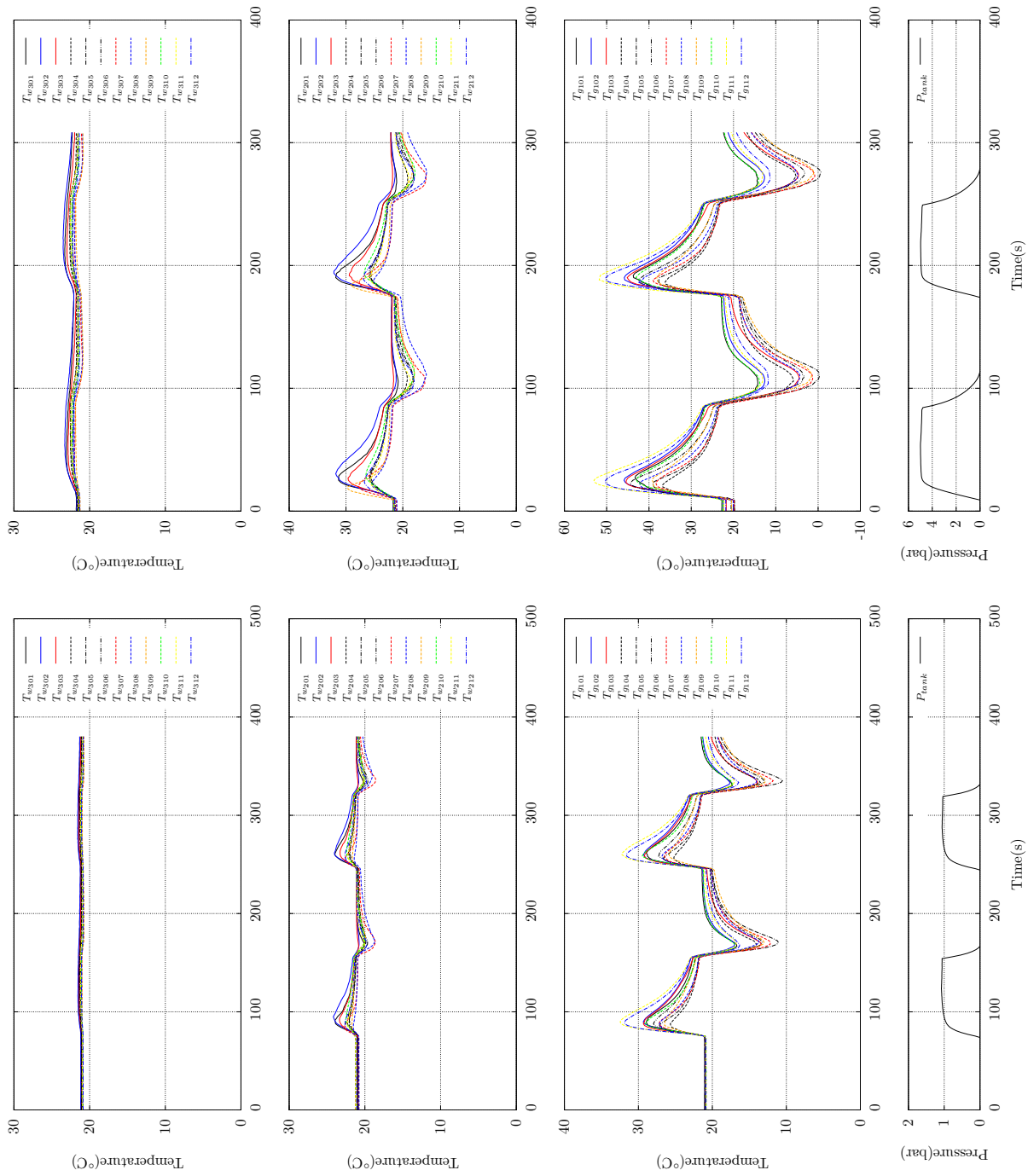

Figure 5.7: Temperature characteristics of the vessel at 1 bar (left view) and 5 bar (right view)

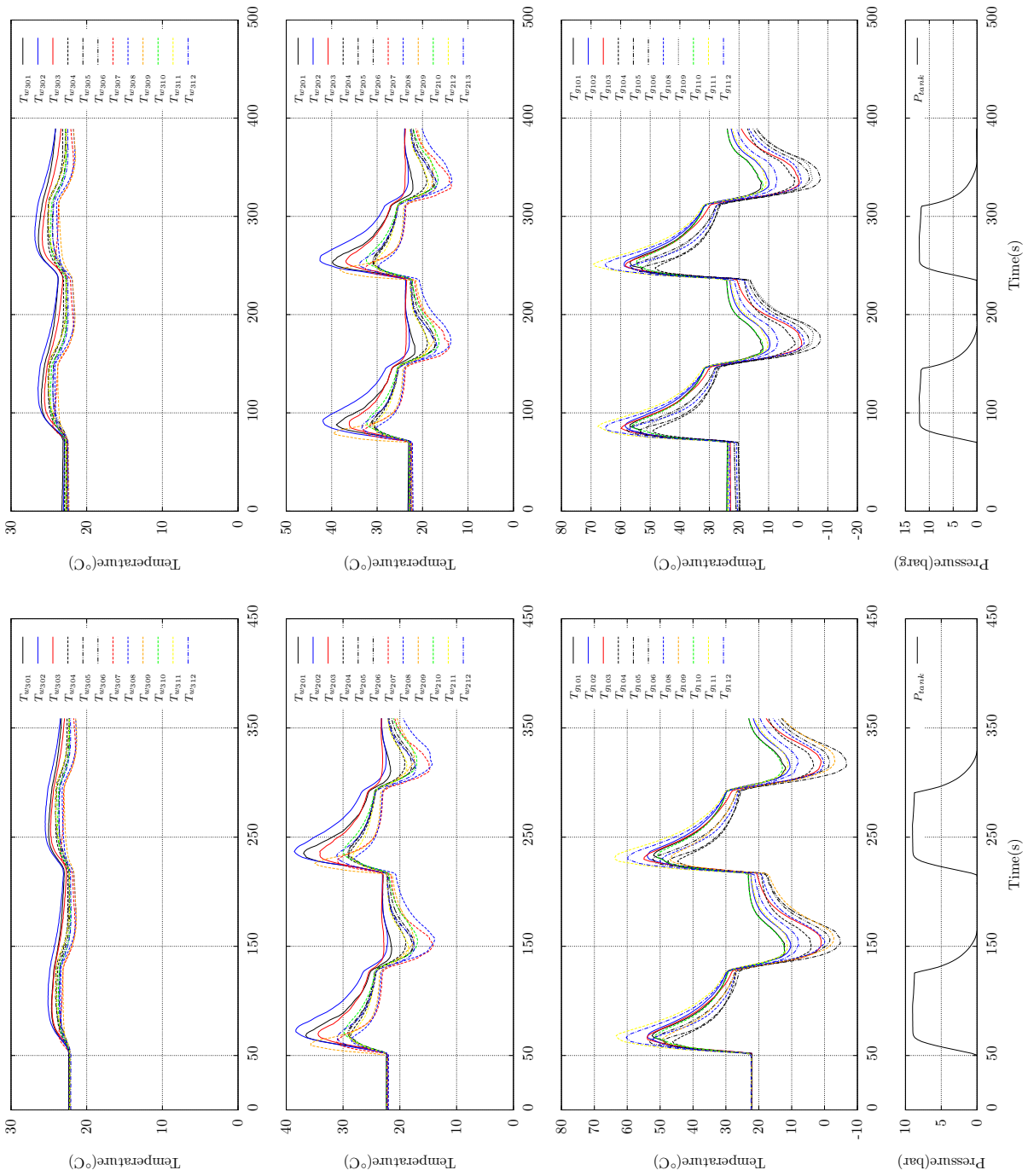

Figure 5.8: Temperature characteristics of the vessel at 9 (left view) and 12 bar (right view)

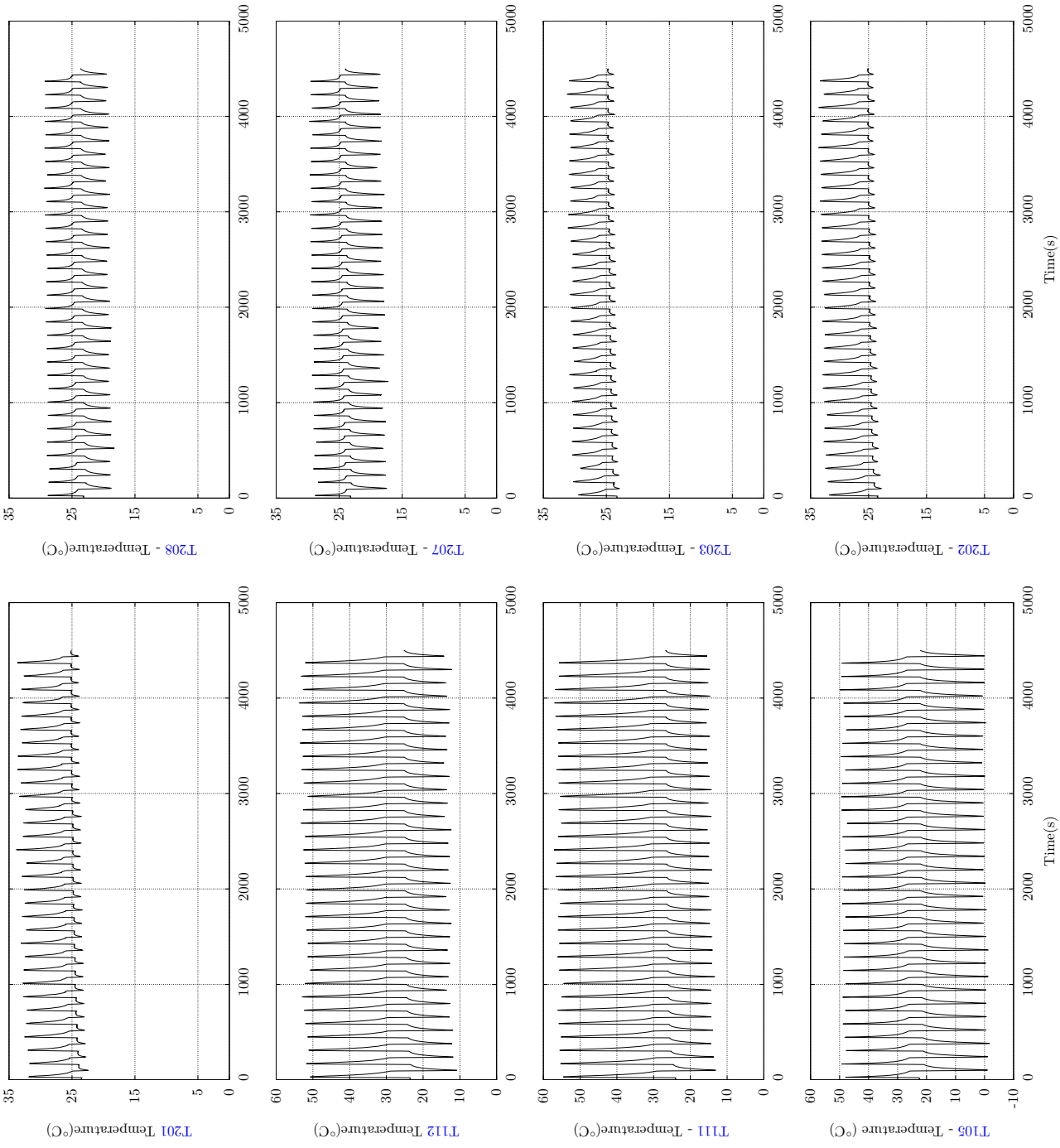

Figure 5.9: Temperature characteristics at different positions of the vessel
Operating pressure=5bar, f=0.075Hz

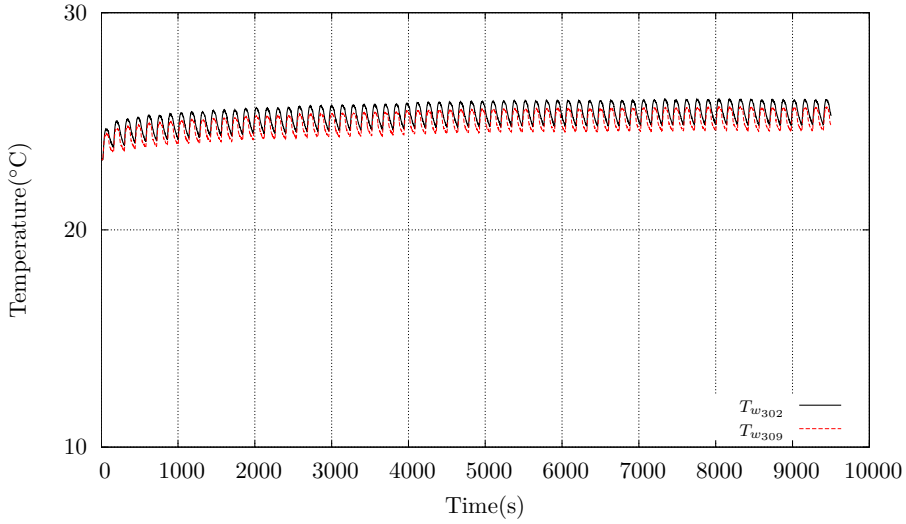

Figure 5.10: Outer wall temperature characteristics of the vessel
Operating pressure=5bar, f=0.075Hz

Under the assumption that the temperature of the gas inside the tank is the same as the temperature of the surroundings, equation 5.24 becomes

$$\Phi = c_p T_{ref} \frac{\gamma - 1}{\gamma} \left[ln \frac{p}{p_{ref}} + \frac{p_{ref}}{p} - 1 \right] \tag{5.25}$$

On the other hand, the work required to charge the vessel is defined below,

$$W_{r_{charge}} = \frac{V}{\gamma - 1} \left[p \left(\gamma \frac{T_i}{T} - 1 \right) - p_i(\gamma - 1) \right] - \alpha_w A_w \left(T - T_w \right) \Delta t \tag{5.26}$$

For an adiabatic process the previous equation becomes (134),

$$W_{r_{charge}} = \frac{V}{\gamma - 1} \left[p \left(\gamma \frac{T_i}{T} - 1 \right) - p_i(\gamma - 1) \right] \tag{5.27}$$

where the subindex i refers to the initial state of the gas in the container.

The exergy of flow energy is describes as follows,

$$W_{flow} = V \left(p - p_i \right) \tag{5.28}$$

which combined with the non-flow exergy yields the exergy of a stream of air, which in case of an ideal gas results,

$$\zeta = c_p T_{ref} \left(\frac{T}{T_{ref}} - 1 - ln \frac{T}{T_{ref}} + ln \left(\frac{p}{p_{ref}} \right)^{\frac{\gamma - 1}{\gamma}} \right) \tag{5.29}$$

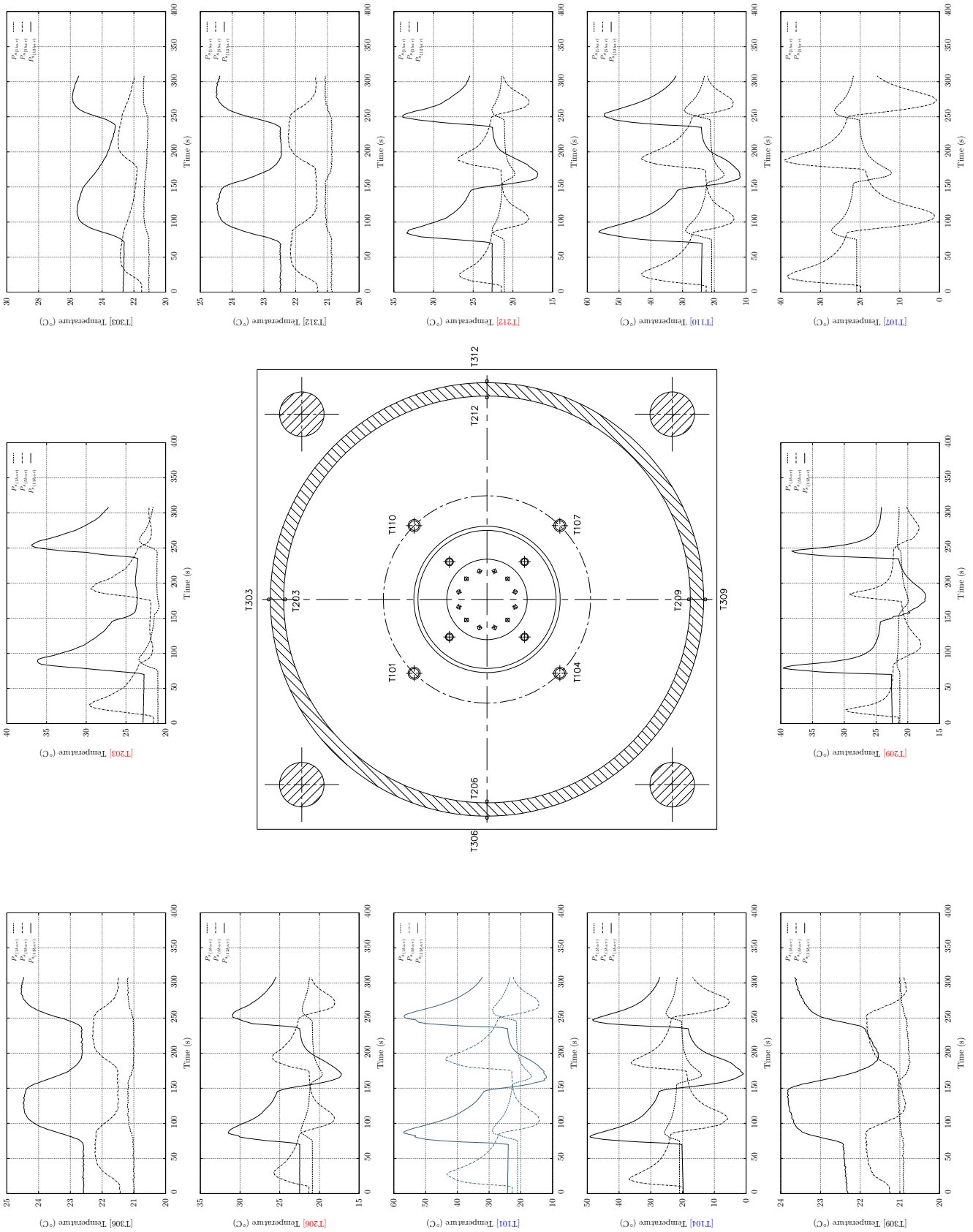

Figure 5.11: Temperature distribution at Section view A-A (refer to fig.5.6)

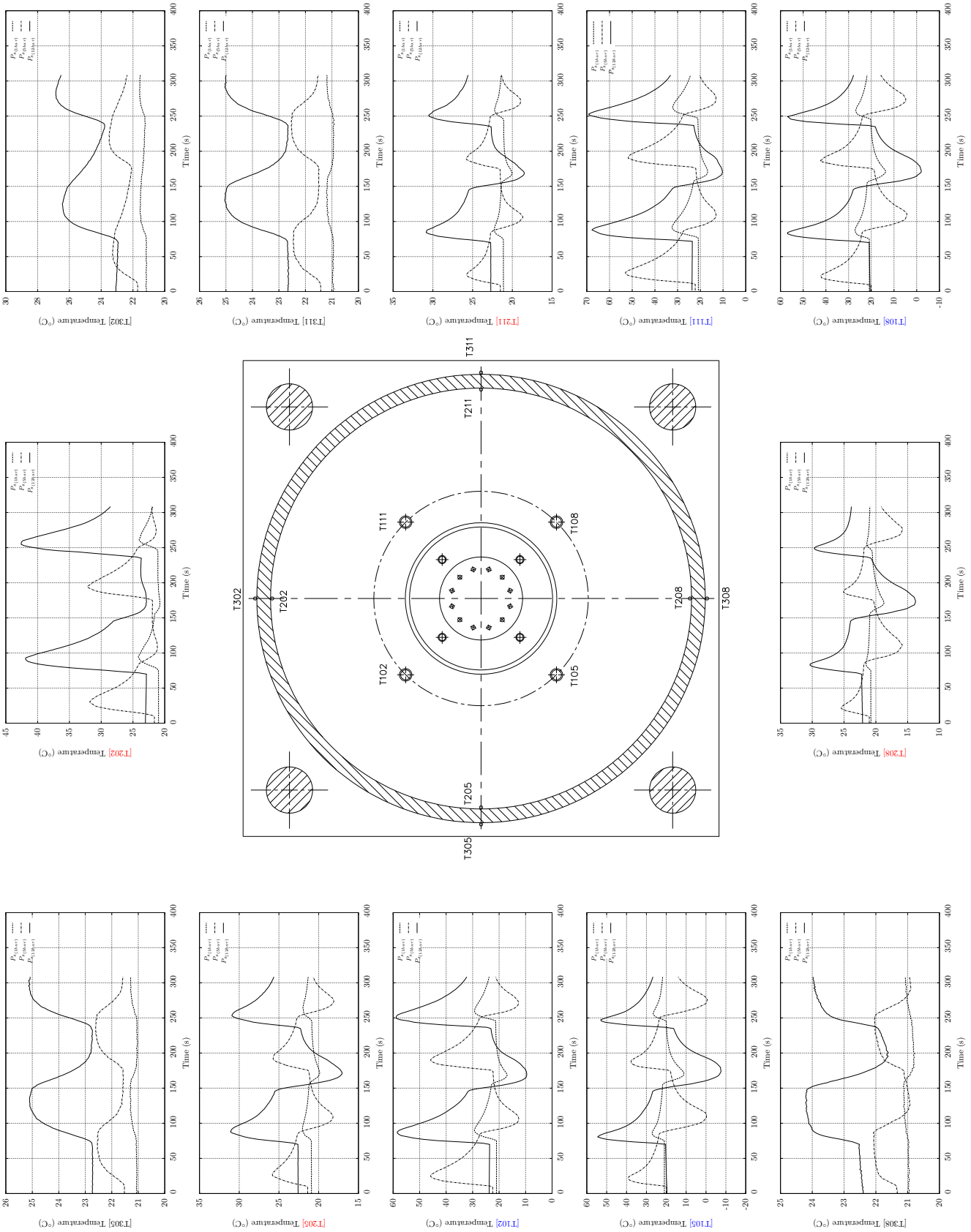

Figure 5.12: Temperature distribution at Section view B-B (refer to fig.5.6)

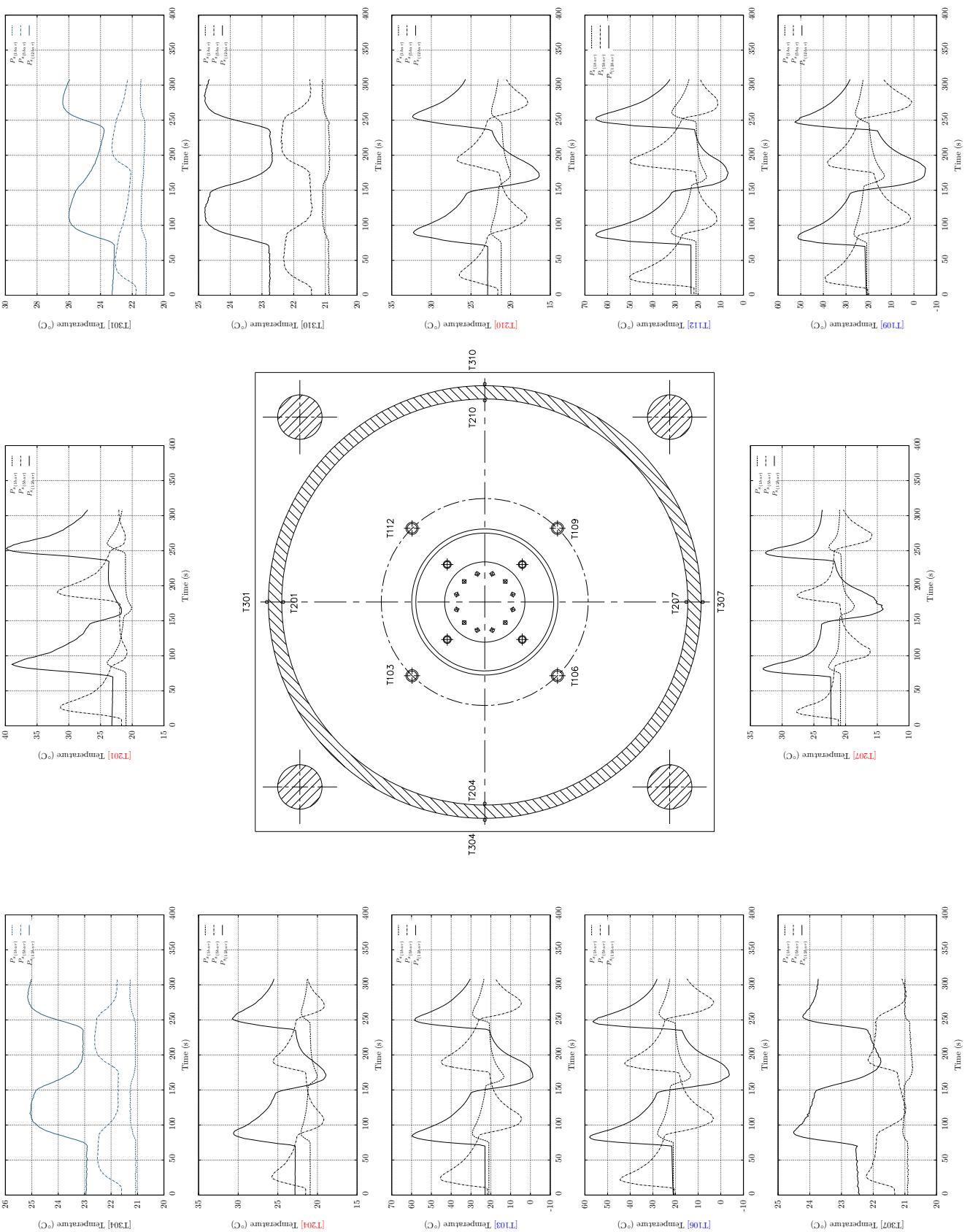

Figure 5.13: Temperature distribution at Section view C-C (refer to fig.5.6)

Assuming that potential energy effects are negligible and no chemical reaction occurs, equation (5.29) can be split into the mechanical exergy and the thermal exergy, as defined below (188),

$$\dot{\zeta}_{(M)} = \dot{m} R T_{ref} ln \frac{p}{p_{ref}} \tag{5.30}$$

$$\dot{\zeta}_{(T)} = \dot{m} c_p \left(T - T_{ref} - T_{ref} ln \frac{T}{T_{ref}} \right) \tag{5.31}$$

Also the exergy associated to heat transfer may be determined according to the following expression,

$$\dot{\Theta}_{(heat)} = \left(1 - \frac{T_0}{T} \right) \dot{Q} \tag{5.32}$$

Using the experimental results from the previous section, the heat transfer can be estimated from the inner and outer wall temperatures, considering that only radial conduction heat transfer through the cylinder tube exists, and conduction heat along the x-axis is negligible. In addition, the temperature of the gas inside the tank will be taken as an averaged value based on the measurements registered by the thermocouples.

Figure 5.14 shows the exergy consumption over a number of cycles. The most relevant aspect that has to be taken into account is the energy required to charge the vessel versus the generated useful flow energy. The ratio of both gives the efficiency of the process, which for the case under study does not exceed 40%. Based on that, if the amount of stored air is exhausted to the atmosphere, as it usually occurs in many pneumatic applications, the available accumulated energy will be completely lost, and the efficiency of the system becomes very poor. Therefore if part of the air can be recycled, the efficiency of the whole unit might be substantially improved, which is the principle applied to the air recovery line employed on the air blowing pneumatic circuit depicted in figure 5.1.

On the other hand, the stored air is also conditioned by other reversitilibites, such as, the heat transfer. From figure 5.14 it may be stated that the maximum thermal exergy is generated along the first cycles and more in particular during the discharging process. This trend, however, tends to decrease systematically since the inner wall temperature increases, making the gas to experience a lower cooling effect. This phenomenon reduces the efficiency of the process, specially during the holding period, since the energy

that the gas is able to deliver will become less than the compression work originally accumulated.

It must be noticed that flow exergy depends on the existing mass flow at the input and output ports of the container, which is conditioned by the sonic conductance of the valves. This explains why the flow exergy at the output port is higher than the flow exergy at the input port (Input valve: $C = 0.59\frac{dm^3}{sbar}$, $b = 0.48$; Output valve: $C = 3\frac{dm^3}{sbar}$, $b = 0.37$).

Next section, then, will extrapolate the results of the experiments previously conducted to enhance the efficiency of the air blowing pneumatic application.

5.3 Efficiency of the air blowing pneumatic application

Figure 5.15 describes the maximum available exergy at different operating pressures (assuming that the irreversibilities may be disregarded and the influence of temperature is negligible). Based on those premises, the non-flow exergy tends to increase while the exergy of flow almost remains constant after certain pressure. On the other hand, the experiments discussed in the previous section proved that the maximum thermal losses arise from the temperature difference between the gas and the inner walls, taking place during both compression and expansion, therefore the stored air is also experiencing a continuous energy lost associated to heat transfer.

This experiment can now be extrapolated to the pneumatic circuit depicted in figure 5.1. In order to enhance as much as possible the efficiency of the recycling process the vessel should be isolated to reduce the heat transfer and then maintain the non-flowing exergy after charge. On the other hand, the air transferred from the recycling tank to the blowing chamber and viceversa is conditioned by the maximum flow exergy that may be obtained from the fluid, which is affected by the irreversibilites that are commonly found in a compressed air line, such as heat transfer and viscous friction (52),(53),(54). Therefore, to minimize those factors the pipes should be shortened and the valve manifold should be designed to ensure a minimum dead volume.

As a matter of fact, a standard PET bottle production line may reach a capacity which usually goes over 20,000 bottles per hour, (in some cases this rate exceeds 70,000 bottles

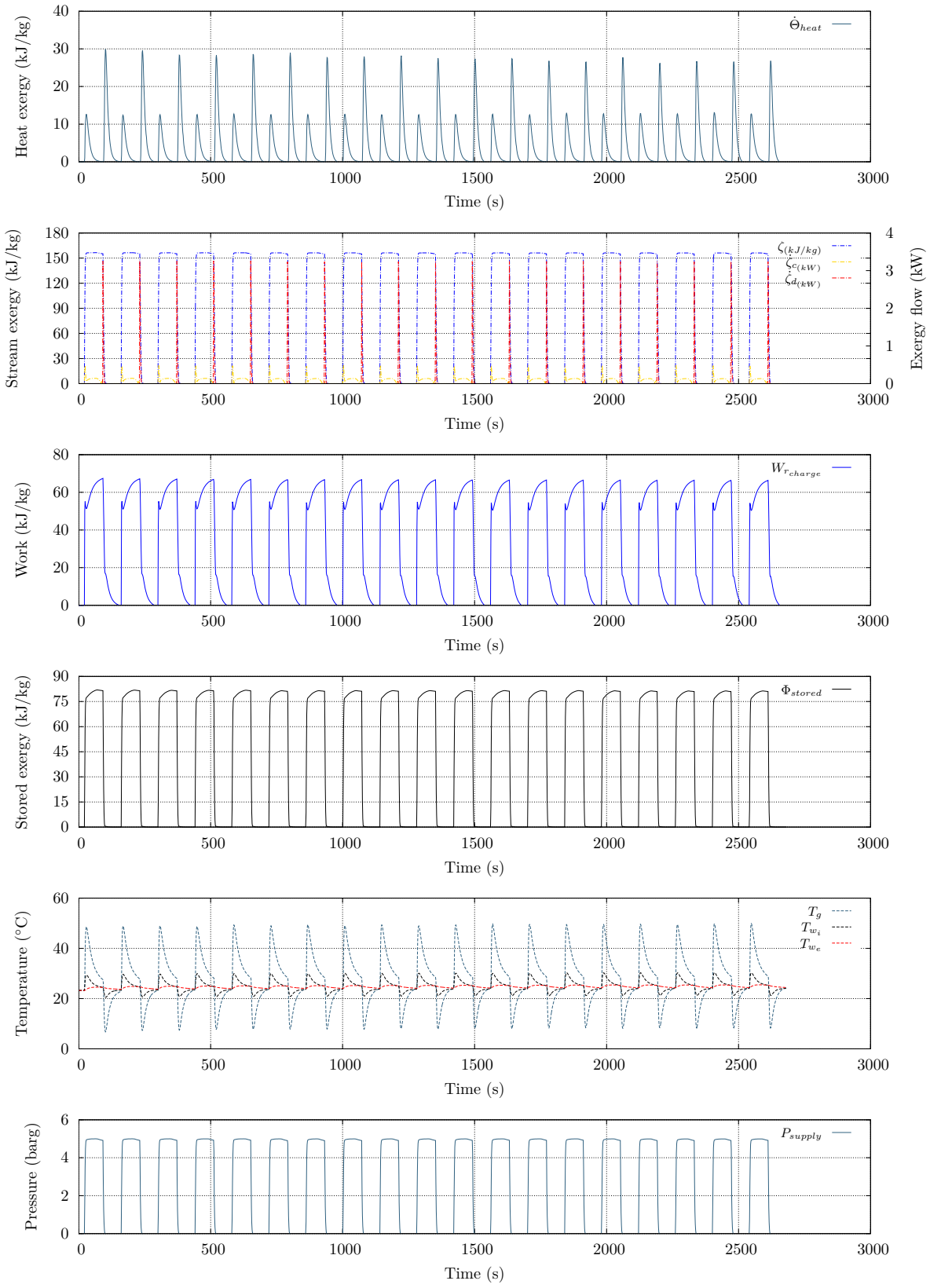

Figure 5.14: Exergy assessment of the charging ("c") and discharging ("d") process

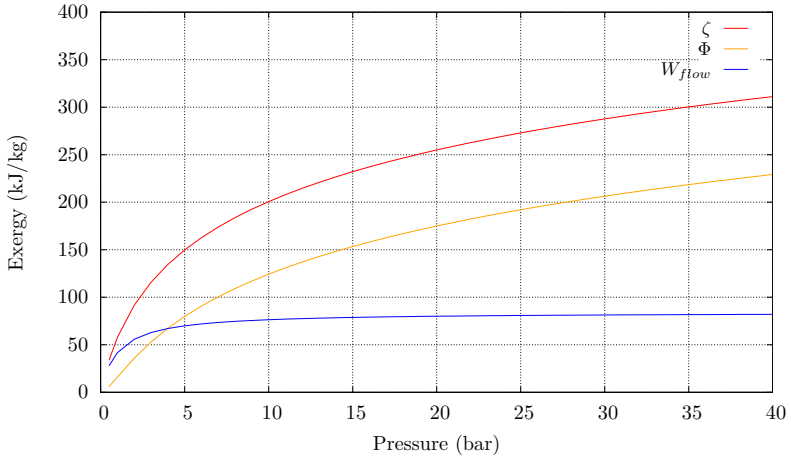

Figure 5.15: Exergy rate of a standard pneumatic system

per hour, which depends on the blowing machine concept and the volume of the item to be produced), that for a 1 dm^3 item represents a total of $20m^3$, with a pre-blowing phase between 7 to 10 bar and a final blowing phase of 40 bar, which may be converted into a maximum theoretical energy consumption of $40 \cdot 10^2 \frac{N}{m^2} \cdot \frac{20}{3600} \frac{m^3}{s} = 22.2kW/h$. Based on that, it seems apropriate to establish countermeasures to diminish the amount of air supplied to the pneumatic circuit, for instance, by re-using part of the flow energy generated during the blowing process.

Figure 5.16 describes the air consumption for a one-station blowing unit, which is the experimental case to be discussed in Chapter 6. The operating principle reveals that a first blowing phase will be provided to the cavity where the perform is moulded. Once this stage is finalized, the valve manifold will change its state to communicate the high pressure line with the cavity. Afterwards V_2 (piped to the low pressure line (refer to figure 5.6) closes and two scenarios may occur, one, the exhaust valve (V_3) is closed, which will contribute to recover the air into the recycling vessel, and, two, the exhaust valve is open, which will cause the air to be exhausted to the atmosphere. The amount of air released due to the operating sequence together with the leakage, may be reduced but not totally avoided. Therefore a reasonable approach, which has been followed by several manufacturers, is to recover the air from the high pressure stage into a vessel, that will be used later to feed the cavity vessel during the low pressure phase, or to run

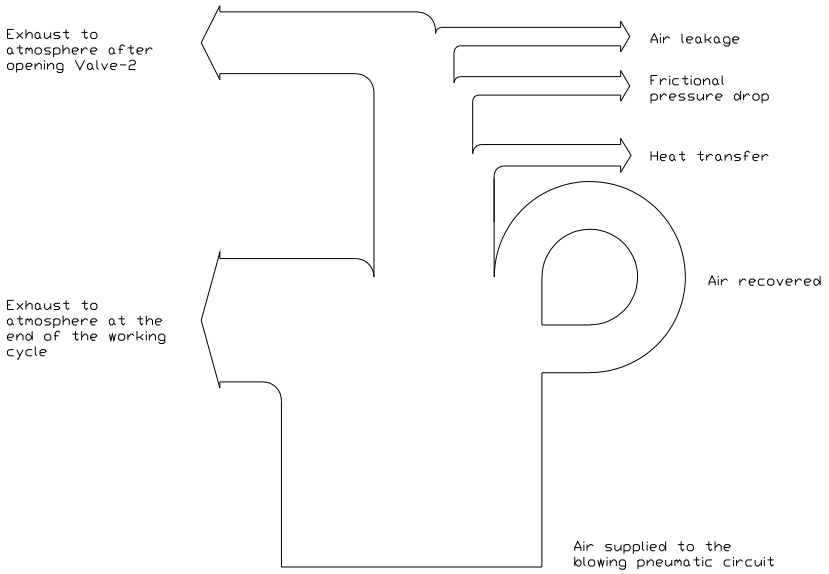

Figure 5.16: Single station PET bottle production air consumption flow chart

secondary pneumatic lines which are installed in the blowing machine. By doing so, the amount of energy that may be saved from the low pressure compressor would be of $10 \cdot 10^2 \frac{N}{m^2} \cdot \frac{20}{3600} \frac{m^3}{s} = 5.6 kW/h$ (assuming a pre-blowing phase working at 10 bar).

Another approach would be to recover part of the air used during the high-pressure blowing stage and use it afterwards during the secondary blowing phase. Then based on a production rate of 20,000 bottles per hour, assuming a recovery rate of 15 bar that would ensure a supply of 10 bar constant pressure during the pre-blowing phase (pressure losses must be taken into account), will represent a supply of 30 bar pressure during the second step of the blowing process. Hence, the theoretical energy consumption will be of $30 \cdot 10^2 \frac{N}{m^2} \cdot \frac{20}{3600} \frac{m^3}{s} = 16.7 kW/h$. The efficiency is expressed as follows,

$$\eta = \frac{Energy\ recovered}{Energy\ supplied} = \frac{8.3}{22.2} = 0.37 \tag{5.33}$$

However, the main drawback of this proposal is that the only way to increase the recovery rate is to provide higher pressure level during the secondary phase or, conversely, delay the recovery process until reaching the specific pressure level in the recovery tank. This last point can only be accomplished after a certain number of operating cycles,

in other words, one recovery cycle will not be enough to reach a certain pressure level and therefore, the pneumatic system will become less efficient.

This is in fact the experiment that will be analysed in detail in the next chapter. The air-blowing unit designed to validate the mathematical model provides up to 6 bar for the first step, while during the second step the pressure level is approximately of 22 bar. With the existing design (volume of cavity equal to $0.0015m^3$) the recovery rate is of 10 bar, that is sufficient to feed the cavity vessel during the pre-blowing phase. Therefore based on a production of 20,000 bottles per hour the efficiency rate will be of 0.45.

5.4 Conclusion

A numerical two-dimensional heat transfer model of the vessel has been proposed. The difficulty on assessing the predominance of either forced or free convective heat transfer through the inner walls of the vessel was approximated by a combination of non-dimensional coefficients which could not entirely reproduce the experimental measurements displayed in Chapter 11. Therefore, in order to understand the complexity of the heat transfer under a continuous charging and discharging operation, experiments were conducted on a pneumatic vessel. The experimental results provided a better understanding of the temperature characteristics over a number of operating cycles.

The exergy analysis of the mentioned process exhibits a significant predominance of the exergy consumption when exhausting the air to the atmosphere as well as the exergy lost associated to heat transfer, which is particularly high during the discharging stage. The temperature increase within the inner volume during the charging process contributes to a continuous temperature raises of the inner wall which minimize the cooling effect during the discharge. Even though this phenomenon helps to minimize the heat transfer through the vessel walls cannot be considered relevant from energy saving point of view. This experimental case, therefore, was taken as reference to study the air blowing process, and it was concluded that the efficiency of the air blowing pneumatic system could be enhanced not only by recovering the exhausted air at the end of the cycle but also by examining the possibility of employing isothermal containers that will ensure higher recovery rates.

Chapter 6

Experimental apparatus and procedure

> Rejoice, young man, during your childhood, and let your heart be pleasant during the days of young manhood. And follow the impulses of your heart and the desires of your eyes. Yet know that God will bring you to judgment for all these things.
> Ecclesiastes 11:9

The accuracy of the mathematical models was verified by means of experimental tests. The experimental set-up tried to reproduce the same industrial conditions under which the blow molding machines are usually operating. One of the main difficulties on the way to achieving a correct testing method was to guarantee a specific pressure level in the supply reservoirs. More specifically, the lack of a high-pressure compressor unit made difficult to ensure a consistent pressure level for the whole test procedure. Even though a sub-tank was connected between the compressed air bottle and the valve manifold for both pressure lines, the existence of pressure fluctuations could not be avoided, at it was particularly critical during the high-pressure stage. Additionally in order to simplify the pneumatic lay-out only one blowing station was built-up and monitored.

As depicted in figure 6.1 the air blowing system consisted of one cavity were the preform is supposed to be blown as well as the recovery chamber. The real circuit includes additional pneumatic components which are out of the scope of this research.

As previously discussed, the valve manifold plays a significant role in the air recovery process, therefore the use of existing solutions to set-up the experimental test were originally discussed, however as part of the research activity a valve manifold was designed and built taking into account the technical requirements of the blow molding industry. Thus, instead of supplying air at 15 bar during the pre-blowing phase, the air network could ensure a constant pressure between 5.5 to 6.5 bar, and analogously the air pressure, which could oscillate between 22 and 25 bar, was supplied to the cavity during the blowing phase. Despite the fact that those operating conditions differed from the ranges usually applied by PET blowing machines manufacturers, the experimental results helped to validate the simulations, and could be also extrapolated to the pressures currently used in the industry.

6.1 Valve manifold design

A cross-section view of the valve manifold is shown in Figure 6.2. The unit was connected to a low pressure tank as well as to a high pressure tank. The low pressure tank (25 dm^3) was supplied directly from the compressed air network while the high pressure tank (70 dm^3) was fed with a compressed air bottle. Each valve station was operated by the action of a 3/2-way solenoid valve. The valve opening time varied for each station, as it can be noticed that only stations 1 and 2 are internally piloted. In a closed position, the valve was sealed by an O-ring embedded between the piston and the rod. The valve was pressurized through ports 1 and 2 respectively, being the first one the high-pressure air supply, and the second one the low-pressure air supply.

Valve opening was accomplished by first energizing the 3/2-way port solenoid valve. As soon as the air in the upper chamber was pressurized and the force generated was sufficiently high to overcome the forces acting in the opposite direction, the seat moved down. Once the seat was displaced over the protrusion that ensured the sealing condition, the air flowed into the inner chamber of the manifold and the valve rapidly reached the full stroke. Similarly, when the pilot pressure acting in the upper chamber was released to the atmosphere, the spring force together with the force generated by the air pressurized in the lower chamber contributed to return the valve to the original position.

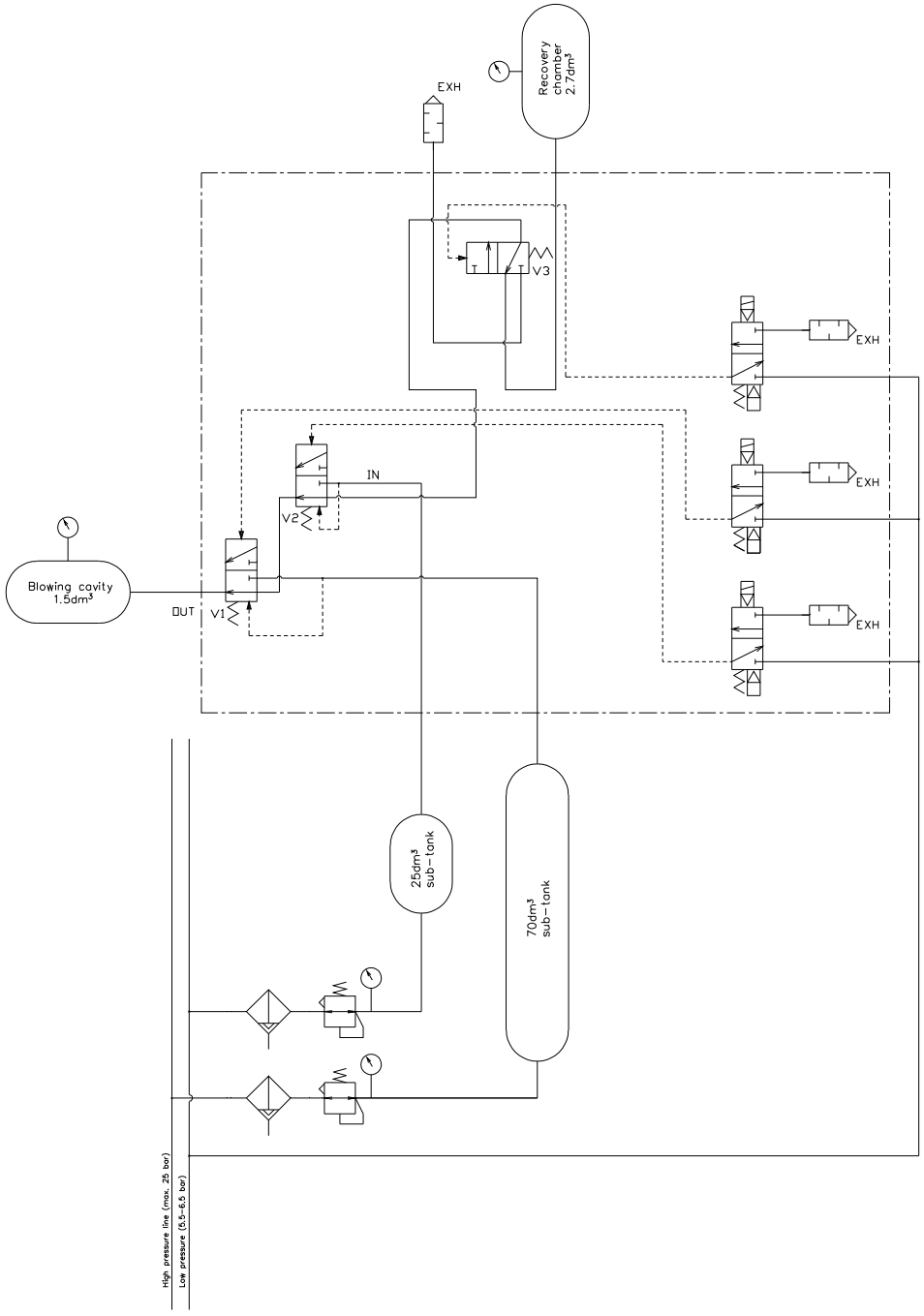

Figure 6.1: Pneumatic scheme of the valve manifold

A critical aspect of the design that required special attention was the sealing at the

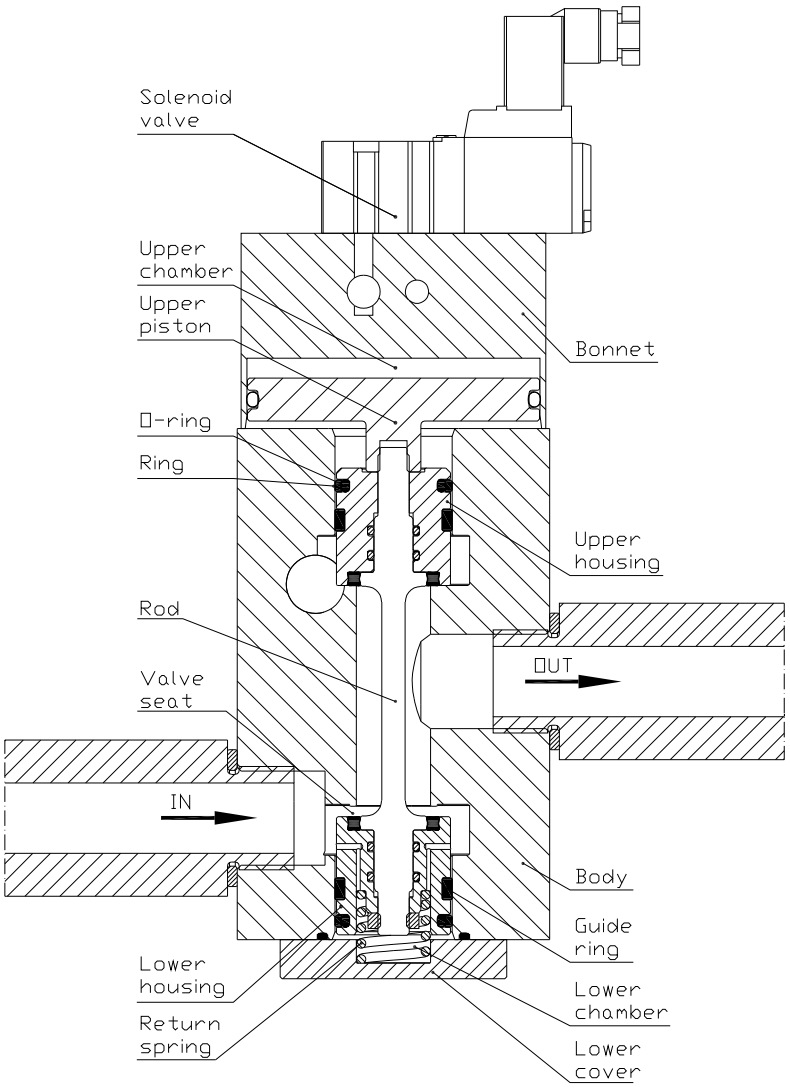

Figure 6.2: Valve manifold section view

poppet area. The main problem was to withstand the flow force acting in the O-ring as well as the compression force exerted by the body at the closing position. Even though the geometry of both spool valve and packing were intended to securely mantain the seal in place, the retention force was overtaken by a pulling force that expelled the O-ring from the groove shaped by those two parts (see figure 6.3).

As a matter of fact a clamping design would have minimized the existing difficulty, however there were not available products in the market that could be used for that particular design. Therefore, to overcome this issue a moulding tool was machined with the same geometry of the spool valve and packing once assembled (refer to fig.6.4). Liquid polyurethane was poured onto the groove and after going through a curing process of approximately 24 hours the O-ring was obtained. During this period the mould was compressed to avoid any displacement which affect the final shape of the O-ring.

Figure 6.3: O-ring damaged due to excessive compression force on the upper packing of spool valve V_1

The prototype was tested to assess the correct functionality, however despite the fact the seal remained in the designing position, the hardness of this component was extremely high, and was, therefore, not sufficiently elastic to ensure the right sealing. A countermeasure for such problems, was to lathe-cut raw polyurethane, which despite providing the requisite elasticity, did not allow obtaining the correct dimensions. As a matter of fact, the main disadvantatge of this production process is the influence of the cutting-tool on the quality of the finished workpiece. This alternative, although having good elastic performance, did not show the appropriate resilience. Therefore after trying different materials and production processes, a special four lipped profile NBR O-ring, called Quad-Ring (commercialized by Trelleborg Sealing Solutions), was probed to be the more efficient solution to ensure the poppet sealing. The O-ring was fixed to the packing with a polyurethane adhesive, however the functionality was limited and the O-ring had to be replaced after operating the valve for a number of cycles.

Figure 6.4: View of the tool used to produce polyurethane ring moulded gaskets

The illustrations exhibit how both upper and lower pistons were guided respect to the manifold body with slide rings. The rings, made of a self-lubricating thermoplastic bearing material, helped to minimize the friction force. On the other hand the sealing between the poppet chamber and the pilot chambers was accomplished with double acting O-rings, which were embraced with a special graphite guide, that allowed generating a lubricating film during operation. As a matter of fact the first propotypes were built with double acting hydraulic seals, which are usually used with mineral oil. Compressed air acts in the opposite way to mineral oil, enhancing the friction and wear, so the material normally used on this type of seals did not achieve the expected low-friction condition. It is also worth to mention that the main valves were made up from three pieces in order to improve machining accuracy and ease the assembly process.

Another aspect that must be pointed out are the laterals forces acting on the poppet valve. These forces, mainly caused by flow momentum forces, could be counterbalanced by the stabilization force generated by the two mentioned sliding guides. At the same time the spring force which tend to close the poppet valve was considered to act in the vertical direction only. To support this assumption special attention was paid to

Spring characteristics Material: SUS 302	Samples		
	k_{s1}	k_{s2}	k_{s3}
Free length (mm)	36.4	36.3	36.2
Wire diameter (mm)	2.22	2.23	2.21
Outer diameter (mm)	18.55	18.60	18.44
Mean diameter (mm)	16.33	16.37	16.23
Spring index $(-)$	7.36	7.34	7.34
Wahl factor $(-)$	1.201	1.202	1.202
Maximum compression (mm)	17.85	17.75	17.65
Maximum operating load (N)	250.26	239.98	239.33
Spring constant (N/mm)	14.02	13.52	13.56
Shear stress (N/mm^2)	1142.80	1084.38	1101.59
Active coils $(-)$	3	3	3
Critical axial load (N)	37.46	37.76	37.27
Slenderness ratio $(-)$	2.229	2.217	2.230

Table 6.1: Calculations of the compression helical springs

the manufacturing process of the compression springs. The stainless steel squared and ground end compression springs were designed to fit into the pockets accommodated in the lower packing and cover, so the guiding during the opening stroke could be guaranteed.

Furthermore in order to avoid side deflection a sleeve-shaped concept was given to the lower packing so the spring was enclosed on the upper side while being guided by the pocket integrated in the lower cover (refer to fig.6.5). The springs charateristics are shown in Table 6.1.

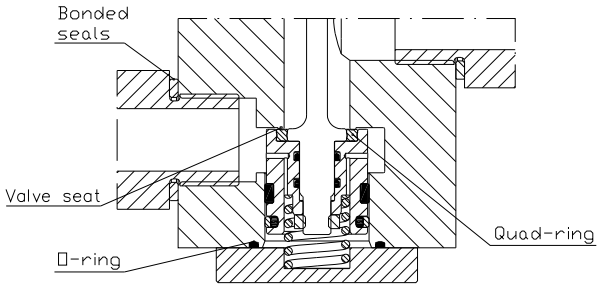

Figure 6.5: Lower packing concept for the spool valves V_1 and V_2

6.2 Thermocouple design and set-up

Internal flow diagnostics inside the cavities consisted of 0.3 millimeters chromel-alumel thermocouples and a flush-mounted pressure transducer. The thermocouples were used to obtain a quantitative assessment of the differences in temperature within the cavities as well as to determine the effects of heat transfer on gas discharge and charge respectively. It is worth mentioning that the experimental test were performed with K type thermocouples (Chromel-Alumel), which were proved to be accurate enough to analyse the process under study.

Also, when accurate thermocouple measurements are required, it is common practice to reference both legs to copper lead wire at the ice point so that copper leads may be connected to the emf readout instrument. This procedure avoids the generation of thermal emfs at the terminals of the readout instrument. Changes in reference junction temperature influence the output signal and practical instruments must be provided with a means to cancel this potential source of error. The emf generated is dependent on a difference in temperature, so in order to make a measurement the reference must be known. This is usually accomplished by placing the reference junction in an ice water bath at a constant 0°C.

While the pressure in the discharging and charging of air is accurately measured, the thermal environment within the chambers is irregular so several issues must be addressed prior to reach a correct thermocouple design. A thermocouple can only indicate the temperature of its own junction so any differences between the thermocouple junction temperature and gas temperature are defined to be errors. The measurement errors are associated to both steady-state and transient deviations. The first ones were assessed as follows:

- Velocity error: The gas velocity inside the vessels also affects the temperature readings. When having low values of the ratio of orifice-to-vessel cross sectional area, the gas velocity inside the vessel is small except for a region around the exit orifice. Therefore the only parameter that may be modified to reduce the velocity error is the velocity. The area ratio for the cavity chamber was 0.032 while for the recycling chamber was 0.035 (refer to figures 6.6 and 6.7). Moreover the thermocouples where located far from the vessel entrance and parallel to the

flow direction. Then the influence of the gas velocity was considered to be very low.

- Conduction error: The conduction error occurs from conduction of heat through the thermocouple to the thermocouple support. The most common way to reduce the conduction error is to increase the junction length-to-diameter ratio. The specific conditions under which the test was performed made the conduction error non-existent.

- Radiation error: When addressing the radiation error, and referring to the internal distribution of thermocouples inside the vessels, the only way to minimize the radiation error is by reducing the value of probe length-to-diameter ratio, so special attention was paid during the manufacturing process of the thermocouples to minimize the exposed surface to the internal atmosphere.

On other hand, the transient errors are difficult to compensate and in fact the only way to minimize its influence was by fabricating thermocouples with the smallest possible time constant. So as previously mentioned the characteristics of each probe was tested in order to select the most appropriate thermocouples.

Therefore, on the based of the previous considerations, the heat transfer by convection was considered to be the only one affecting the temperature readings. From the energy balance on the thermocouple junction results that the total gas temperature is $T_g = T_j + \tau_c \frac{dT_g}{dt}$, where $\tau_c = \frac{m_j c_j}{h_j A_j}$, is a time constant associated to the thermocouple characteristics, and in this case the subscript j referes to the physical properties of the thermocouple junction. If we disregard the transient temperature effect, the second term of the equation may be neglected.

Additionally the effect of one thermocouple on the measurement taken by an adjacent thermocouple was also taken into account when distributing the probes within the inner volume of the chambers. As it can be seen in figures 6.8 and 6.9 the probes have been strategically positioned to minimize this effect.

Another aspect to be noted was the influence of the chamber wall temperature on the thermocouple measurement. This last point could not be assessed since the inner wall temperature was not measured.

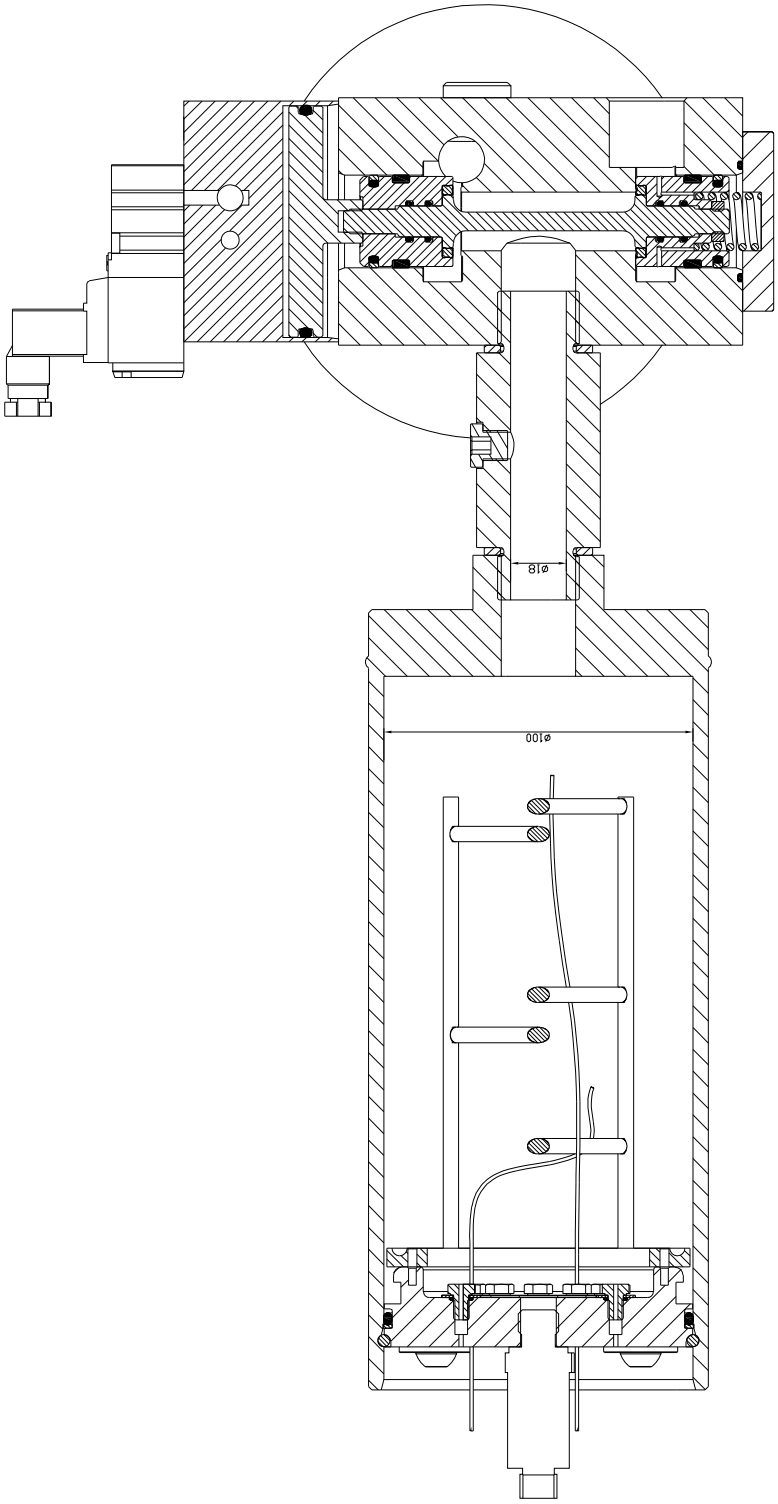

Figure 6.6: Section view of the blowing cavity piped to valve manifold

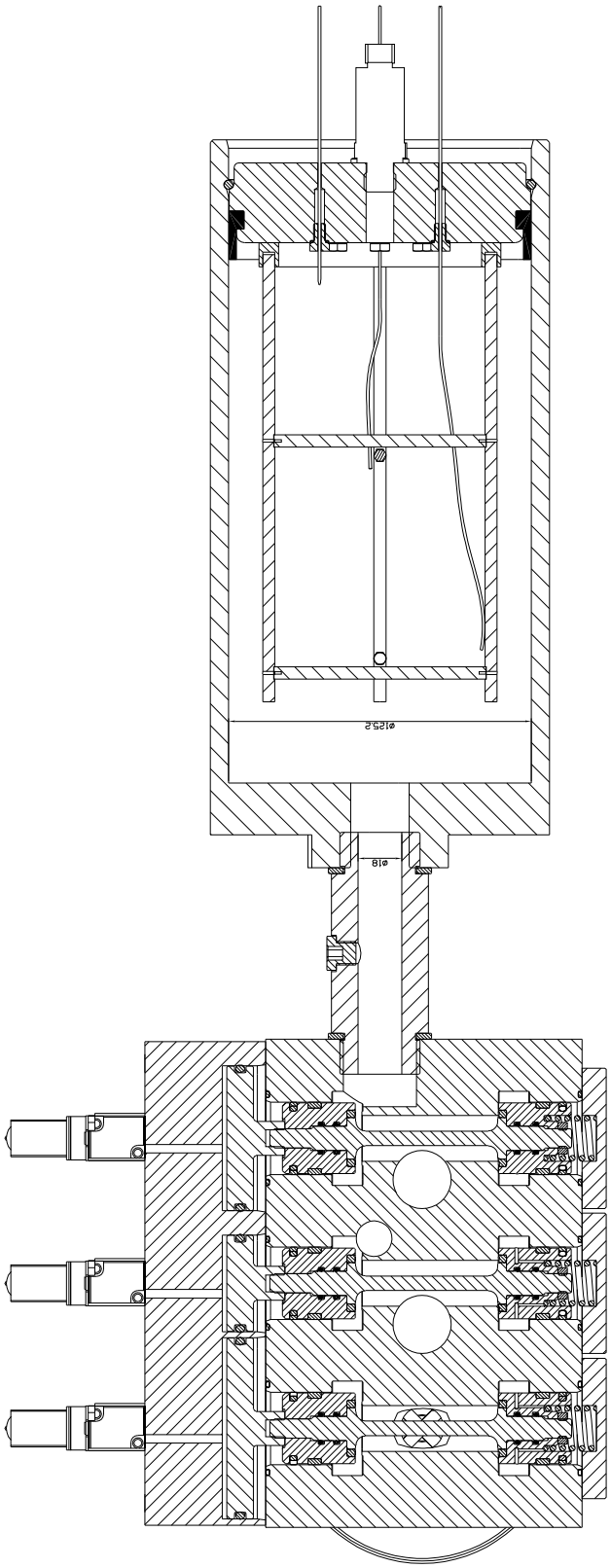

Figure 6.7: Section view of recycling vessel piped to valve manifold

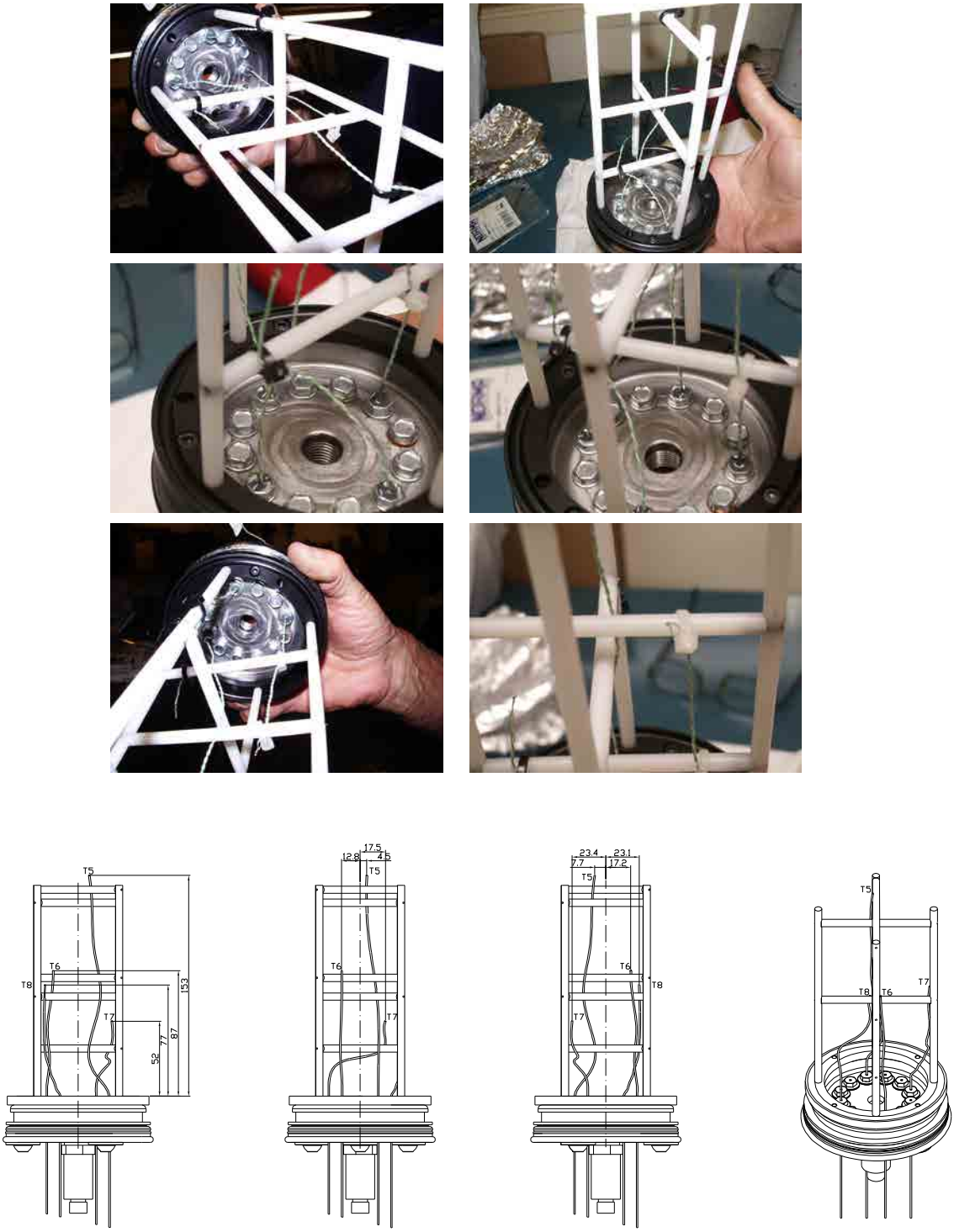

Figure 6.8: Thermocouple location inside the cavity mould (units in mm)

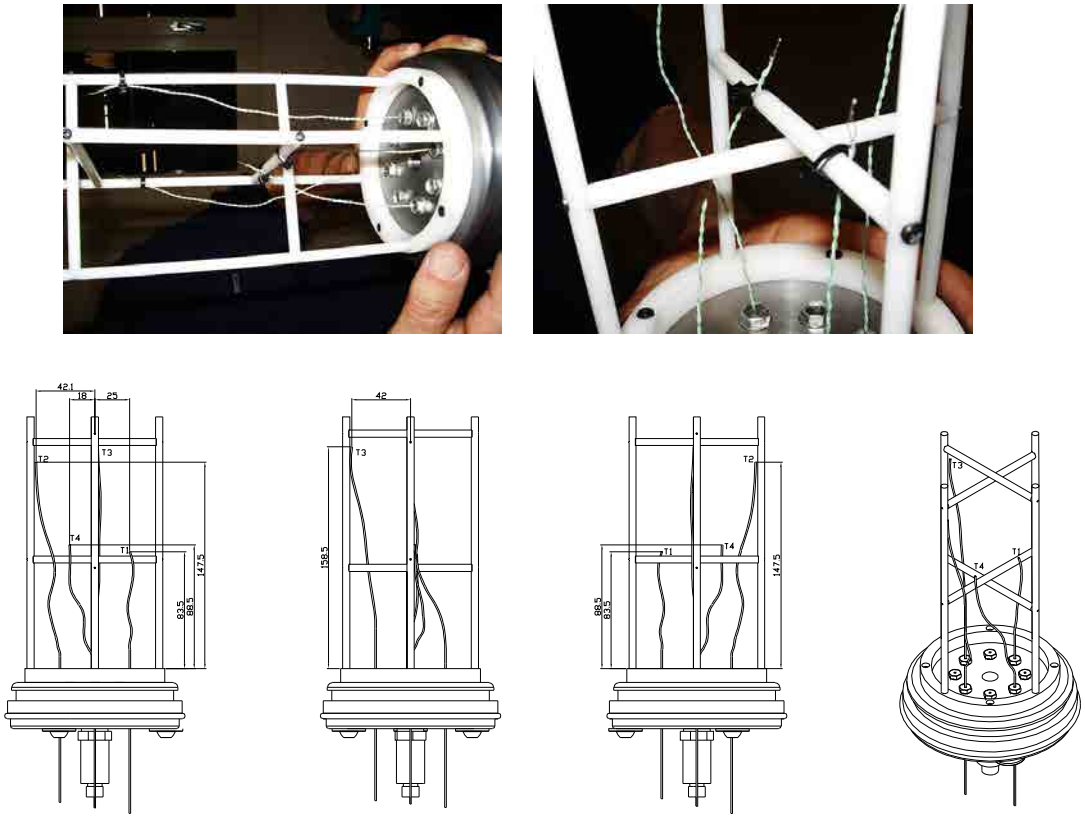

Figure 6.9: Thermocouple location inside the recycling tank (units in mm)

The installation of the thermocouples through the walls was set-up in that way that no trapped gas could exist under the present configuration, therefore the possibility of having jets or turbulence caused by air exiting from voids was disregarded. However special attention was paid to the structure used to hold the thermocouples inside the cavity. As depicted in fig.6.8 and fig.6.9, a plastic support was assembled to the cover of the vessel. The plastic material helped to avoid any influence to the thermocouples, and also the fixing method used to attach the thermocouples to the structure. The support was designed in order to withstand the dynamic pressure generated during the charging and discharging phases.

6.2.1 Manufacturing method of thermocouples

In order to reduce the thermal capacitance of the thermocouple as much as possible so the convective wave effect could be minimized, the junction size was specially controlled.

The method originally used to build the termocouples junction was silver-soldering, however the thermocouples did not provide the correct temperature readings. As it is well-known, when the thermocouple wires are soldered together, a third metal is introduced into the thermocouple circuit, but as long as the temperatures on both sides of the thermocouple are the same, the solder should not cause any error. To minimize the uncertainties a different technique was applied. The method was based on generating enough energy that the two wires fused into one. The construction process consisted of twisting the two ends of the wires until reaching a uniform shape, and then connecting the other side of the wires to earth (AC ground). The positive charge was connected to a piece of retort carbon which was submerged into methyl alcohol. When putting in contact the end of the twisted wires with the retort carbon a massive amount of energy passed through the wire generating the junction (see fig.6.10).

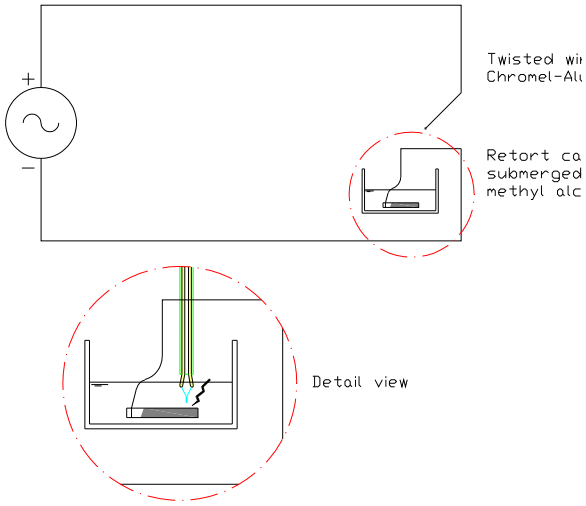

Figure 6.10: Schematic of thermocouple fabrication

6.2.2 Electrical noise effect

The calibration of the thermocouples when through several stages. The first measurements showed up the existence of electric noise, so to protect the measuring units from outside electrical and magnetic sources all electronic components were isolated and grounded. After checking the functionality of each thermocouple with a tempera-

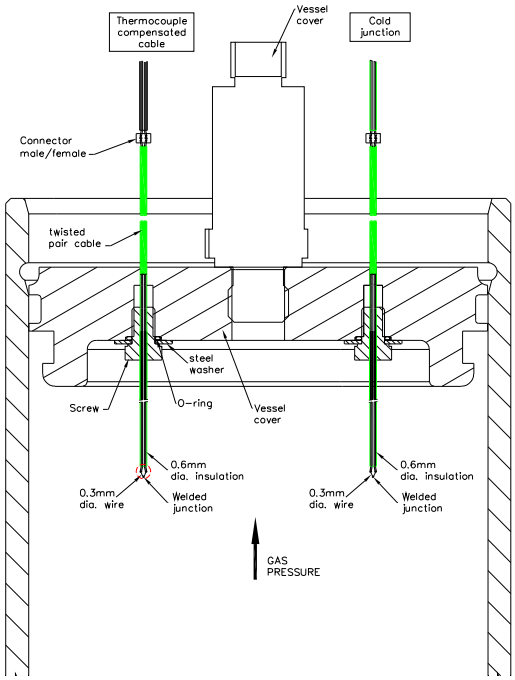

Figure 6.11: Thermocouple wall bushing in the cavity

ture tester (YC-747D Data logger Thermometer; resolution: 0.1°C; range: −100°C to 1300°C; accuracy: ± 0.1% rdg to +0.7°C), the two ends of each thermocouple were clamped to the terminals of a K-type connector. The length of the sensor lead wires was reduced in order to minimize the influence of any external signal which could affect the readings. Then, the connection to the thermocouple amplifier (fig.6.12) was accomplished with a shielded cable. From that point in the circuit, the signal passed through a signal conditioner and finally reached the data adquisition device. After different trials the measurements were considered to be accurate enough to not use cold junction compensation. At this point it is important to emphasize that the thermocouple amplifier was also designed and built in our laboratory, therefore the accuracy of the prototype had to be checked and validated. The whole unit was introduced inside a metal box which protected the electronic components from electrical interferences, acting as a Faraday cage.

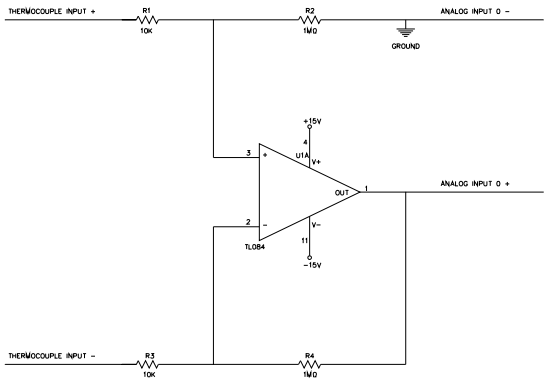

Figure 6.12: Voltage signal amplifier

Unfortunately despite taking all the necessary countermeasures to ensure the correct functionality of the measuring equipment, thermocouple decalibration was experienced in several occasions after several months of experimental activity. In fact this fault condition made to question if the experimental results were acceptable. As known, decalibration describes the process of unintentionally altering the physical makeup of the thermocouple wire. The reasons behind can be diffusion of atmospheric particles into the metal caused by temperature extremes. However, that will not be the case of our test, so the main causes of malfunction were attributed on one side to cold-working metal, which is an effect that can occur when the wire is drawn through a conduit or strained by rough handling or vibration, and by the other side to the air force generated during the charging process to the various containers. Therefore several calibration tests were conducted to validate the whole test set-up and the steps are described in cronogological order in the following sections.

6.2.3 Analysis of temperature signal

The first experimental tests in relation to temperature measurement were carried out on a test bench which was originally conceived to measure the flow rate characteristics of calibrated orifices. The test results helped to determine the correct functionality of the data acquision equipment. As mentioned previously, the thermocouples were developed and built-up in our laboratory, therefore, it was expected that errors and

dimensional deviations amongst different thermocouples may arise during the construction of the units. Those deviations, in case of the welded joints varied between 0.66mm and 0.97mm, which were considered to be non-critical for the purpose of the experiment, and they were intrinsically taken into account by the calibration process.

The first temperature measurements were taken without assembling the thermocouples under the final operating conditions. This approach was followed in order to determine the behaviour of the signal without applying a specific sampling rate. Those readings raised a serious concern regarding the electrical noise that was affecting the signal. However despite the influence of the existing electrical intereferences, there was also another factor to take into account, which was the building method used to produce the thermocouples. As above-mentioned silver-soldering seemed to be the main cause behind the irregular readings observed on the test results. The weld was not resistant enough to withstand the air force when charging the air containers. Therefore it was concluded that a different welding technique had be used to overcome this issue, so after several attempts the technique discussed in a previous section was considered to be the correct thermocouple production method.

Once the measurements obtained with the new generation of thermocouples were reasonable consistent, a series of experiments were performed on units adequately assembled on bulkhead fittings (refer to Fig.6.13). It is quite noticeable that the electrical noise was affecting the thermocouple signal so additional countermeasures had to be applied to prevent noise from entering the system. Therefore in order to get the cleanest signal possible, shielded wires, analog filtering and signal averaging techniques were used, and the result is shown in fig.6.14 and 6.15. In particular the averaging technique, which consisted of taking 20 readings at a rate of 1000samples/s, contributed significantly to minimize the electrical noise. By doing so, the influence of the AC signal periodicity could be filtered, and, additionally, the influence of higher harmonics was also mitigated.

In this case the pressure and temperature signal were wired through an analog filter, which selectively attenuated a band of frequencies within the Nyquist frequency range. At the same time the filter was connected to a NI PCI-6035E multifunction data acquisition board. This board has a TTL output that was used to control the pulsing

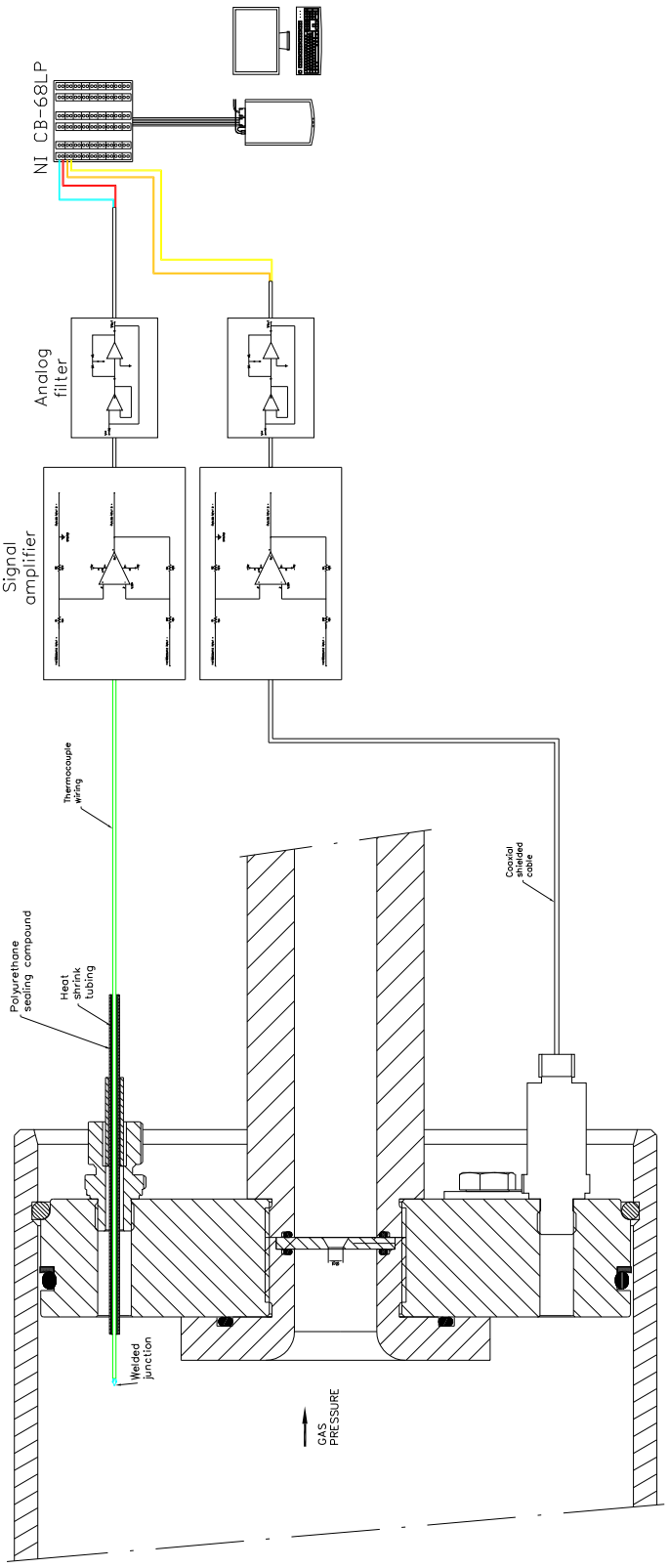

Figure 6.13: Discharge test set-up for signal analysis

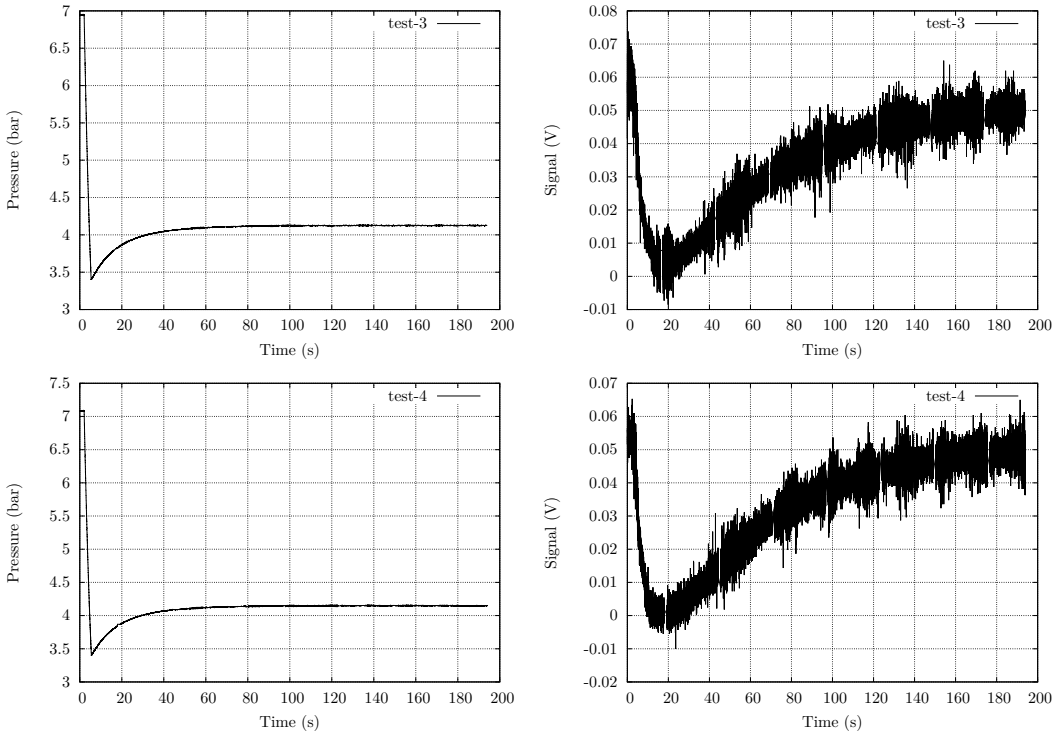

Figure 6.14: First generation thermocouples characteristics.
Discharge test characteristics based on d=5mm orifice plate

frequency. LabView software was used to write all of the needed programs. At this stage two main programs were written for data acquisition and control. One program was responsible for gathering both temperature and static pressure signals. And a second program performed the discharge sequence which allowed the opening and closing of the shut-off valve. In fact the first program acted as a subroutine, which was used by the second program. The code was written to be run in automatic mode and all data were stored for later processing. According to the Nyquist sampling theorem, the nominal sampling interval required to avoid aliasing should be at least twice the highest frequency contained in the signal ($f_s \geq 2f_c$). The Finite Fourier Transform of the signal was used to determine the normalized frequency with maximum energy along the domain. This analysis allowed to confirm that the sampling rate was always within the value stated by the Nyquist theorem.

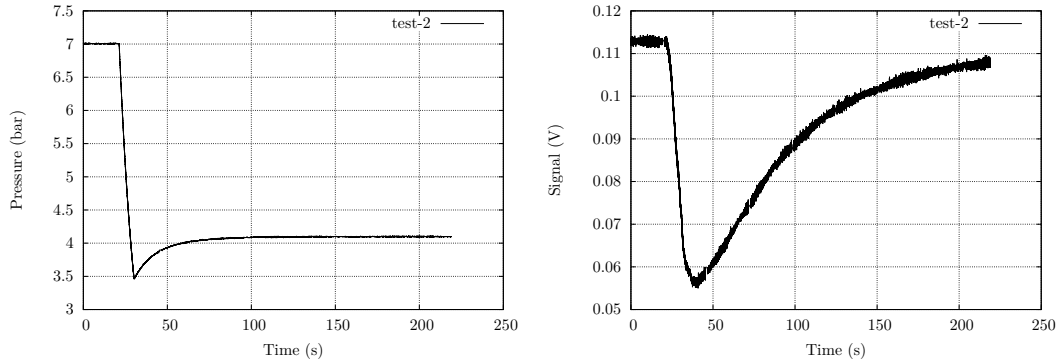

Figure 6.15: Results after applying countermeasures against electrical noise. Discharge test characteristics based on d=5mm orifice plate

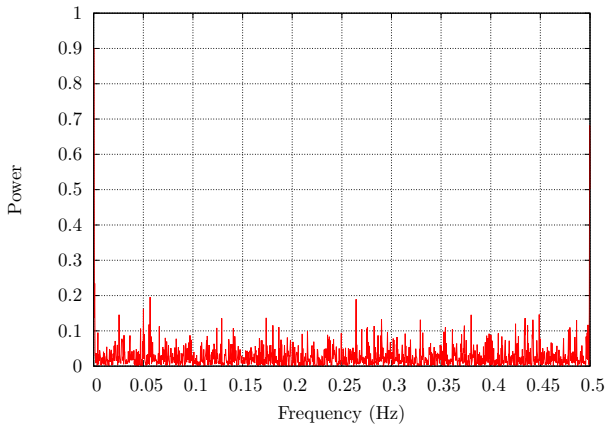

Figure 6.16: Single-sided amplitude spectrum of thermocouple signal

6.2.4 Cold junction evaluation

Another aspect that was assessed during the thermocouple production was the use of a reference junction, since it is recognised that the connection between a thermocouple and a voltemeter automatically generates additional metallic junctions. Therefore in order to determine the functionality of the thermocouples when using a cold junction, the test set-up shown in figure 6.17 was used. Two different thermocouple configurations were investigated. The purpose of the test was to check the variability in outcome measures of distilled water at room temperature. On the left-side appear the readings of a termocouple without cold-junction, and on the right-side are displayed the readings

Fluid Temperature	Samples of junctions			
	T1	T2	T3	T4
max	27.68	27.65	27.65	27.80
min (°C)	25.80	25.95	25.91	26.03
std	0.162	0.161	0.158	0.159
mean (°C)	26.60	26.76	26.78	26.89
median (°C)	26.61	26.76	26.80	26.92
precision (±°C)	0.94	0.85	0.87	0.89
accuracy (%)	2.3	2.9	3.0	3.4

Table 6.2: Temperature measurements with cold-junction compensation (distilled water at 26°C)

of a termocouple with cold-juntion compensation (see fig.6.18). At first glance the use of cold-juntion shows lower variability, however further analysis proves that the temperature variation when using cold-juntion compensation is 1.88°C while the variation when using a connection without cold-junction is 1.13°C (min 21.82°C, max 22.95°C, mean 22.37°C). Therefore based on those results, the cold-junction compensation did not appear to favour more accurate temperature readings, so an additional test was conducted to measure the repetitivity amongst different temperature measurements (refer to table 6.2).

Before proceeding with a final configuration a comparision between a thermocouple with cold junction compensation and another one connected to the signal amplifier by a K type compensated cable was performed. In essence, both thermocouples were identical however the aim of the test was to determine the influence the cold-junction over the temperature reading under the same testing conditions. The results are shown in figure 6.19. The conclusion of the test was that cold-junction did not contribute significantly on improving the thermocouple accuracy and from the precision point of view the characteristics of the units was very similar. Therefore despite being the correct approach to add a cold reference to each thermocouple, it was finally decided to consider that due to the electrical noise present in all the measurements a thermocouple system incorporating all the countermeasures previously detailed plus the use of K type compensating cable will provide the expected accuracy.

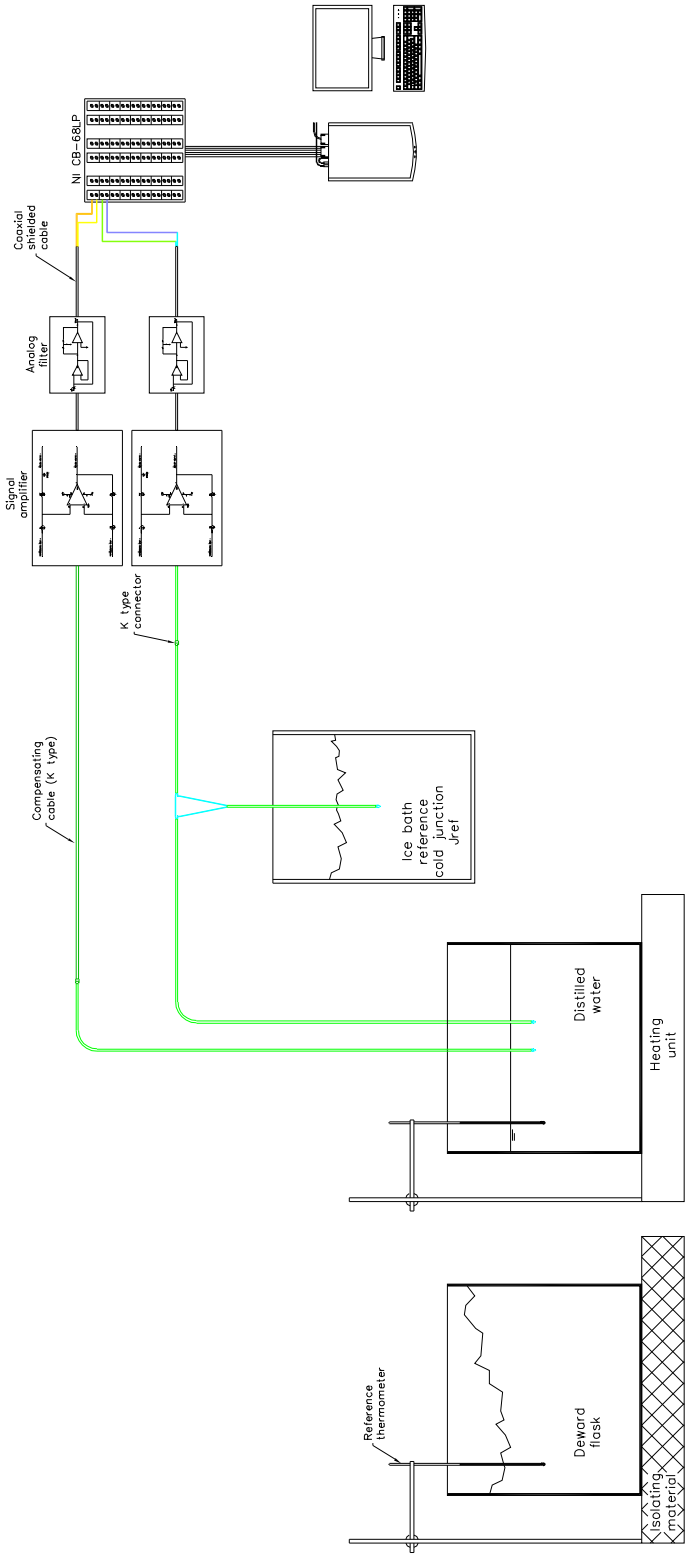

Figure 6.17: Schematic of the temperature acquisition set-up

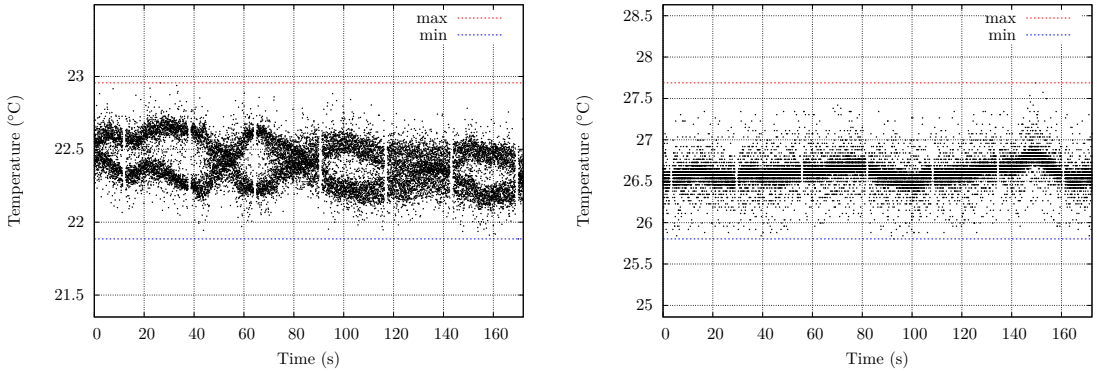

(a) (b)

Figure 6.18: Data acquisition lay-out test. (a) Measurements without cold reference or compensating cable. (b) Measurements with cold reference and without compensating cable

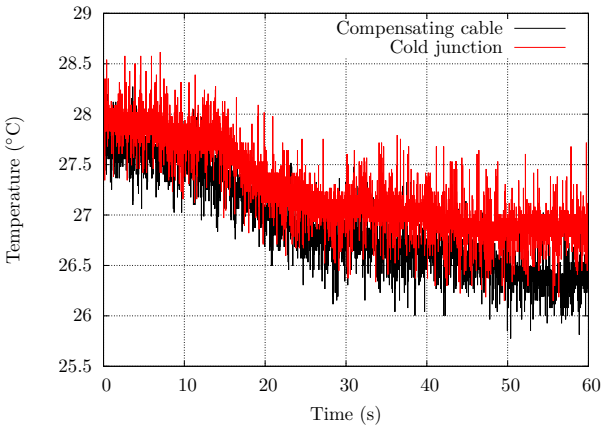

Figure 6.19: Correlation between thermocouples with and without cold junction

6.3 Flow-rate characteristics of pneumatic components

The test methods applied to determine the flow-rate characteristics of the valve manifold were the so-called discharge and isothermal methods respectively. The mentioned methods are based on the Japanese proposals presented at the beginning of the century. The revision of the ISO 6358:1989 Standard at the end of the nineties highlighted some disadvantatges of the ISO experimental procedure, and prompted researchers to investigate alternatives to remedy the existing deficiencies. The revision of the standard

concluded in a series of proposals, from which two of them, the ISO 6358-3 (Isothermal discharge test) and the ISO 6358-5 (Simple discharge test) (153),(154), were adopted in this work to calculate the sonic conductance C and critical pressure ratio b of the pneumatic components. In fact those two proposals merged into one several years later.

6.3.1 Simple discharge method

Initial experiments based on the simple discharge test, which in fact is a variant of the isothermal discharge method, were designed to validate the test set-up. Special attention was taken to the following items:

- The distance between the tank and the rectifier tube was designed to be as short as possible.
- The gas used for all the measurements was compressed air.
- The solenoid valve was chosen to have by one side, a shifting time able to ensure that test data collection started only after the solenoid valve shifted, and by the other side, a sonic conductance at least five times the estimated sonic conductance of the test component.
- The pressure sampling time was set according to the relation $\triangle t \leq 1.5 \cdot 10^{-3} \frac{V}{C}$, in order to ensure at least 100 data to calculate C.
- The junction of the flow port with the internal surface of the tank was designed to be convergent shaped so as to avoid pressure loss. Additionally the volume of the tank was determined to satisfy the relation $2 \cdot C \leq V$. At this point it is worth to mention that the original configuration of the test did not include the stuffed material used for reducing the air temperature change in the tank. The first tests only determined the C value not the critical pressure ratio of the component. On the other hand, and previously commented, the original set-up contributed to validate the correct performance of the termocouples so a less sophisticated configuration helped to modify the arrangement with the shortest amount of time.

Once the complete circuit was checked out, the air was regularly supplied from a compressed air bottle to the tank. The measurements started once steady-state conditions

of temperature and pressure in the tank were reached. The determination of the initial pressure, p_s, could be obtained using a formula $p_s \geq \frac{100}{b} + 100\,[kPa]$ based on the estimated critical pressure ratio b of the component under test. After reaching the stated pressure, the shut-off valve was closed, and the test procedure was initiated. The initial pressure and temperature conditions were logged into the data adquisition unit and after a given period of time the 2-way solenoid valve was switched on. Once the pressure in the tank dropped to 350kPa the solenoid valve was switched off, and the remaining air in the tank was left until both pressure and temperature reached the steady-state conditions. The test circuit used to validate the testing method differed from the concept proposed by the standard (see fig.6.20). The main difference lied in the fact that the test component was located at the reservoir output instead of being positioned after the on/off solenoid valve.

In order to minimize the turbulence a bellmouth design was incorporated to the tank outlet. The resulting arrangement allowed measuring both the temperature and pressure of the air upstream of the component under test and the downstream pressure before the solenoid valve. The embedded design despite reducing the number of connections between components is not suitable when testing a valve.

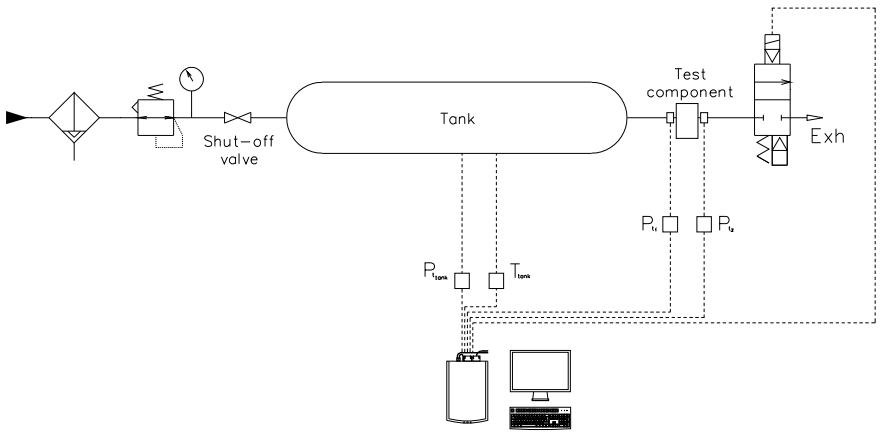

Figure 6.20: Simple discharge test circuit according to ISO-6358

Assuming adiabatic change in the air tank during discharge, the sonic conductance was calculated with the following expression:

		diameter (mm)			
		3	4	5	8
Measured orifice diameter (mm)	1^{st} reading	2,96	3,92	5,04	8,34
	2^{nd} reading	2,95	3,90	5,04	8,35
	3^{rd} reading	2,98	3,89	5,05	8,33
	4^{th} reading	2,98	3,85	5,05	8,34
	5^{th} reading	2,98	3,88	5,05	8,35
Average orifice diameter (mm)		2,97	3,89	5,05	8,34
Theoretical effective area (mm^2)		6,93	11,87	20,00	54,66
Theoretical sonic conductance (dm^3/sbar)		1,39	2,37	4,00	10,93
Calculated sonic conductance (dm^3/sbar)	1^{st} reading	1,34	2,19	4,05	10,57
	2^{nd} reading	1,34	-	4,08	10,56
	3^{rd} reading	1,30	-	4,08	10,63
	4^{th} reading	-	-	4,16	-
Percent error	1^{st} reading	-3,65	-7,97	1,32	-3,32
	2^{nd} reading	-3,17	-	2,01	-3,37
	3^{rd} reading	-6,51	-	1,97	-2,75
	4^{th} reading	-	-	3,91	-

Table 6.3: Calculated sonic conductance according to simple discharge test

$$C = \frac{2}{(k-1)p_0}\frac{V}{t}\sqrt{\frac{T_0}{T_s}}\left\{\left(\frac{p_s}{p}\right)^{\frac{k-1}{2}} - 1\right\} \tag{6.1}$$

where C is the sonic conductance $[dm^3/(sbar)]$, V is the tank volume $[m^3]$, t is the time required for discharging $[s]$, p_s is the absolute initial pressure in the air tank $[bar]$, p is the absolute residual pressure in the air tank $[bar]$, T_0 is the absolute temperature of the standard reference atmosphere $(293.15°K)$ and T_s is the absolute initial temperature in the air tank $[°K]$.

The pressure and temperature characteristics depicted in fig.6.22 and fig.6.23 are used to determine the sonic conductance in each case. The results presented in Table 6.3 show the correlation between the theoretical sonic conductance for each orifice plate, taking into account that the influence of the existing upstream and downstream restrictions is negligible.

Figure 6.21: Stainless steel wire mesh inside the isothermal tank

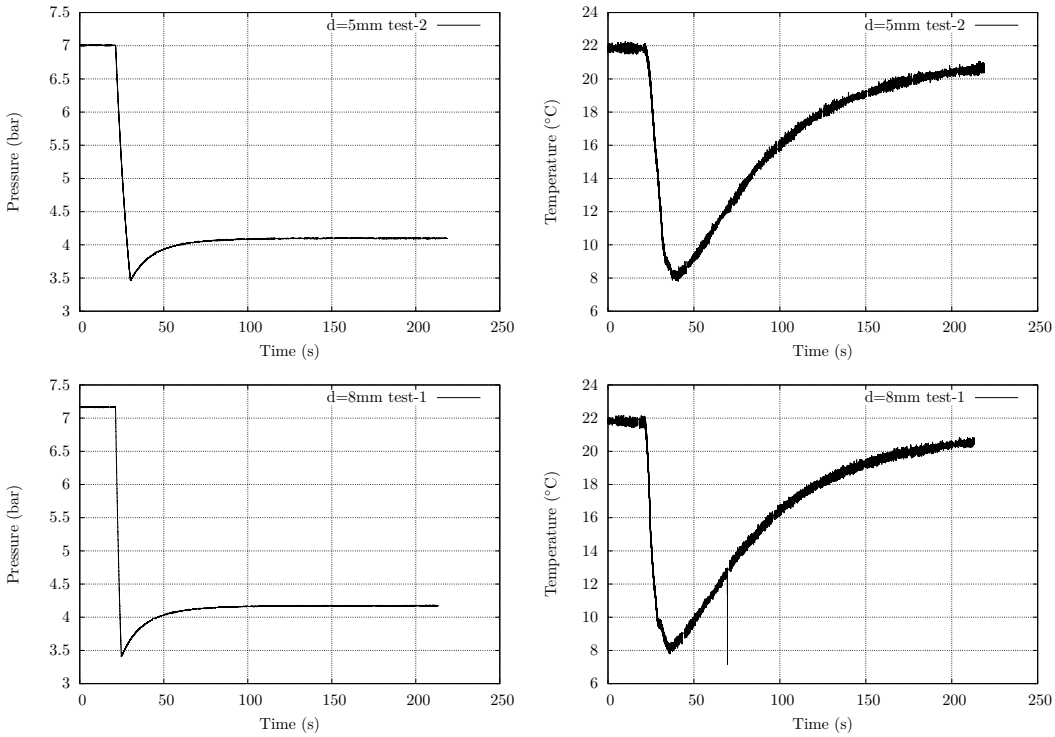

Figure 6.22: Experimental results based on simple discharge test

6.3.2 Isothermal discharge method

Unlike the previous pneumatic set-up, the isothermal test requires building a special tank able to keep the inner air temperature constant during the discharge process. The volume of the isothermal tank was determined to safisty the following relation:

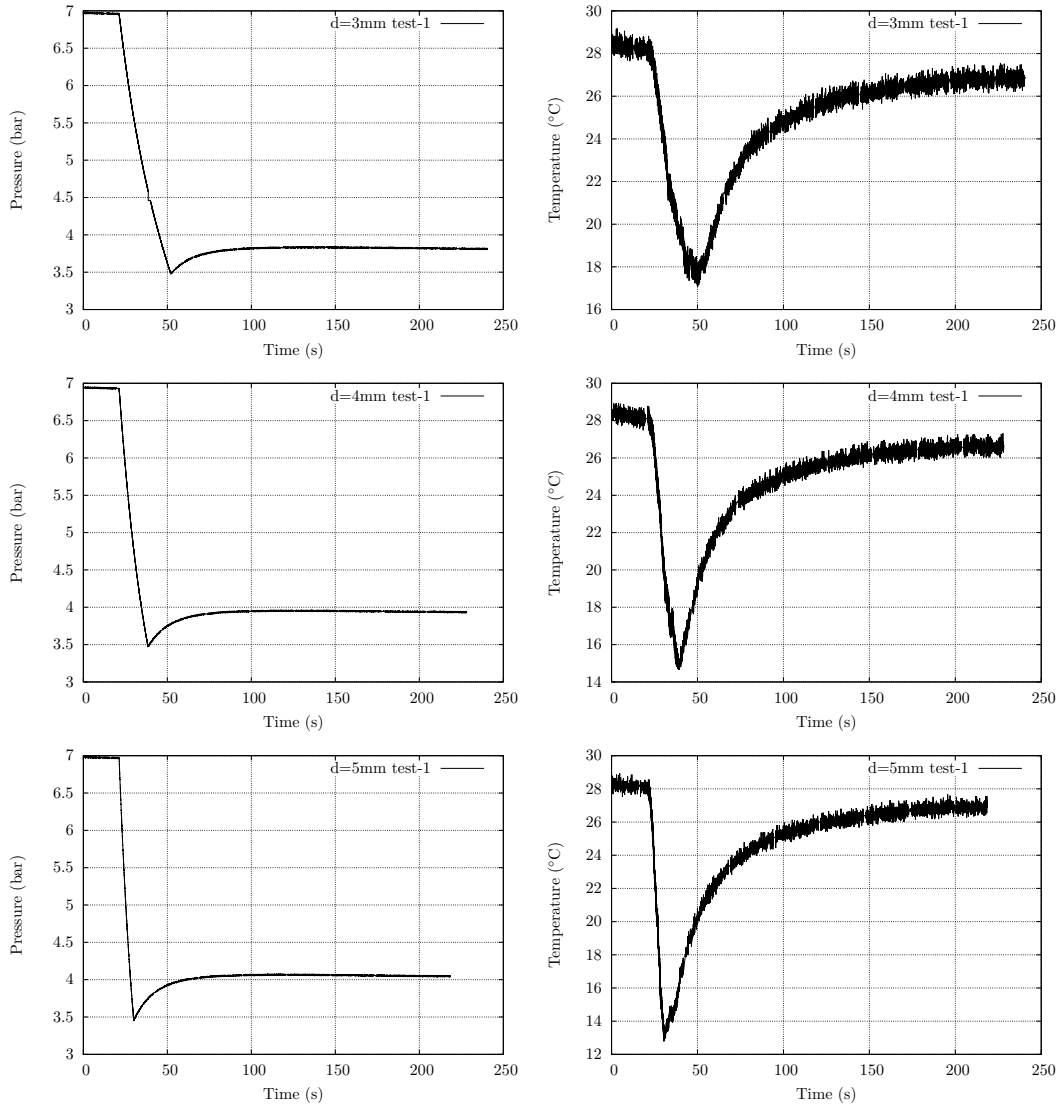

Figure 6.23: Experimental results based on simple discharge test

$$0.01 \cdot p_s \cdot C \leq V \tag{6.2}$$

where C is in this case the estimated sonic conductance $[dm^3/(sbar)]$, p_s is the initial pressure in the tank [kPa] and V is the isothermal tank volume $[dm^3]$.

Therefore the accumulator used in earlier experiments was modified according to the arrangement described in figure 6.24. As a result, the effective air volume became

$32.5dm^3$, which allowed determining the sonic conductance of the equipment to be tested no larger than $5dm^3/(sbar)$.

In order to ensure the correct wire density within the designated volume ($32.5dm^3$), half of the tank was filled with stainless steel 0.1mm diameter wires, while the rest was filled with a perforated PVC tube that communicated the inlet port with the internal volume. It shoud be noted that the isothermal tank volume is the net value obtained by substracting the volume of the stuffed material from the volume of the empty air tank.

Kawashima et al.(181) [see also (113),(114),(182),(177),(199)] determined that in order to keep the temperature change error within 0.5% the rate of pressure drop in the air tank during air discharge had to be not greater than $100kPa/s$. Furthermore, the quality of the isothermal condition in the chamber were directly influenced by the density of the metal wire as well as the heat transfer area. Additionally the material and diameter of the metal wire were chosen to ensure a temperature drop within $3K$ or less during the test.

One aspect in which the present set-up differs from the experience described by Kawashima, is the way the wires were arranged inside the tank. Instead of wrapping a mass of wires to become a metallic net, two woven-wire stainless steel sheets were adequately rolled up until reaching a density of $0.4kg/dm^3$. The structure could be easily assembled and prevented the wires from flowing out of the discharge port. Below are the specifications of the stainless steel (AISI 304) wire mesh:

- Mesh no: 120 (French inch)
- Wire diameter (mm): 0.10
- Aperture width (mm): 0.131
- Open area (m^2): 32%
- Weight (kg/m^2): 0.545
- Total mass (kg): 14.1

Figure 6.25 displayed the experimental results for different diameter orifices. As can be observed the temperature drop could be mantained below $3°K$ with the aforementioned stuffed mass density.

The sonic conductance, previously obtained from equation (6.1), could be now used to determine the critical pressure ratio b and the subsonic index m by applying a non-linear

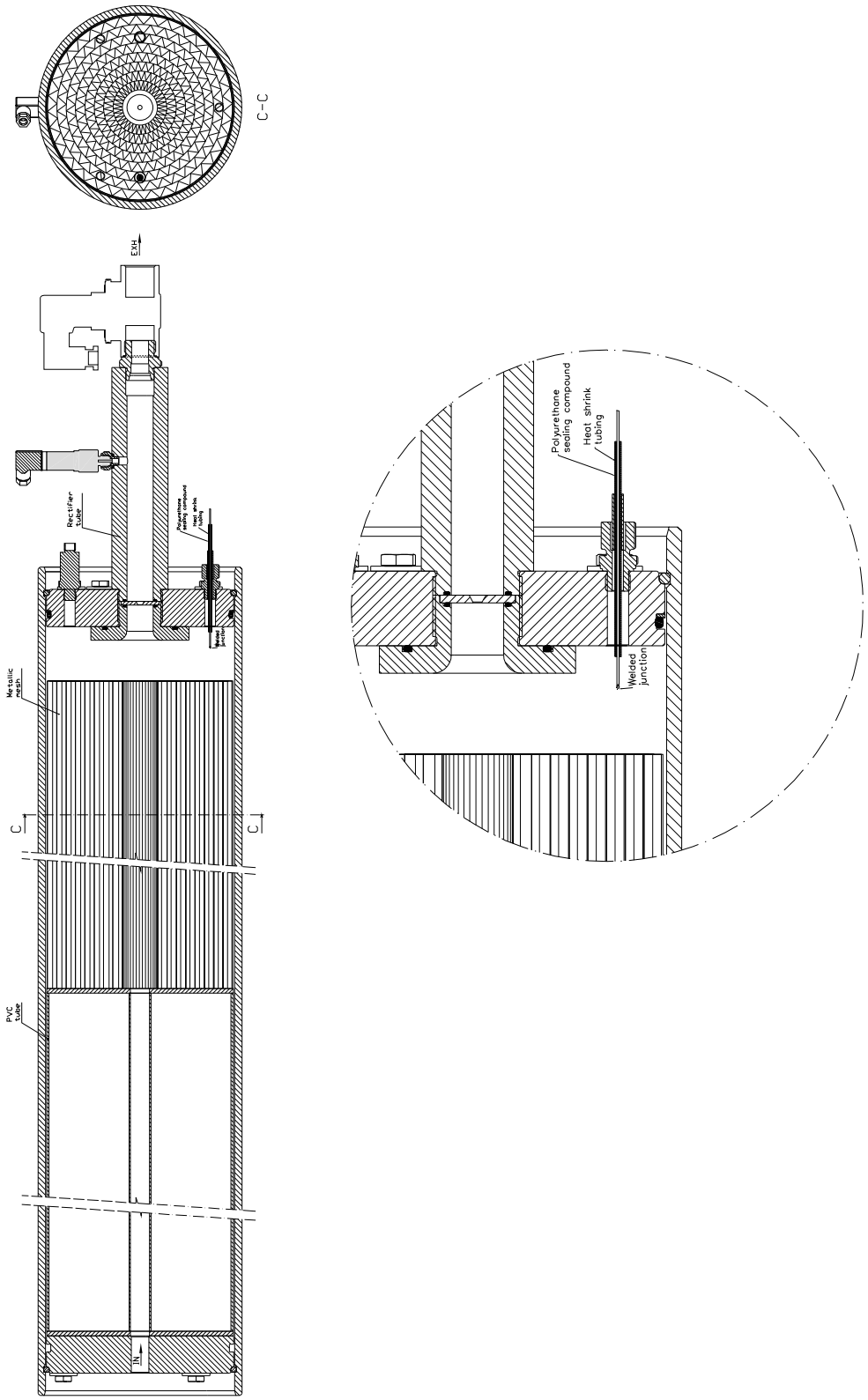

Figure 6.24: Isothermal tank section view and details of the thermocouple mounting position

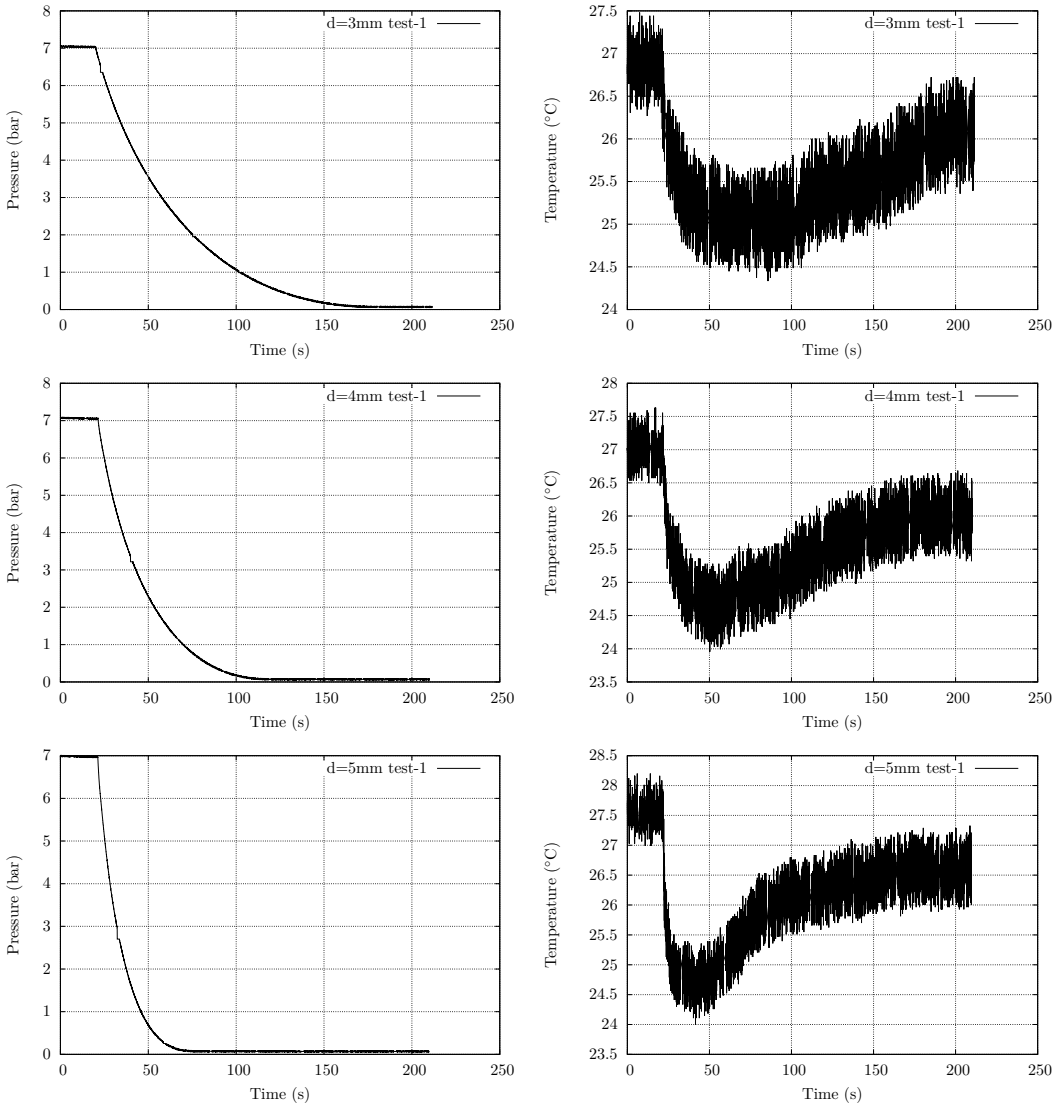

Figure 6.25: Isothermal discharge test with calibrated orifices

least-square method.

$$p_{cal3(i)} = p_{3(i-1)} - 10^{-5} \cdot \triangle t \frac{R}{V} C \varrho_0 p_{1(i-1)} \sqrt{T_s T_0} \left[1 - \left(\frac{\frac{p_{2(i-1)}}{p_{1(i-1)}} - b}{1 - b} \right)^2 \right]^m \tag{6.3}$$

where, $p_{1(i)}$ is the pressure measured between time t_c and t_d $[kPa]$, $p_{3(i)}$ is the pressure measured between time t_c and t_d $[kPa]$, p_{3c} is the pressure corresponding to time

		diameter (mm)				
		3	4	5	6	8
Critical pressure ratio	1^{st} reading	0.569	0.620	0.636	0.648	-2.135
	2^{nd} reading	0.598	0.675	0.630	0.696	-1.611
	3^{rd} reading	0.591	-	0.689	-	-
Pressure change (kPa/s)		25.4	442.9	56.4	61.3	101.4

Table 6.4: Critical pressure ratio of calibrated orifices assuming m=0.5

$t_c[kPa]$, t_c is the time of the sudden-turn point corresponding to pressure p_1 and p_2, t_d is the time elapsed while the pressure drops from the initial pressure p_s to p_{3d} $[s]$, $\triangle t$ is the sampling time for the pressure data $[s]$, p_{3d} is the pressure 100kPa below from the initial pressure or $p_{3d} = p_s - 100$ $[kPa]$, ϱ_0 is the mass density of air at the standard reference conditions $\left[1.185\frac{g}{dm^3}\right]$, $p_{1(i-1)}$ is the pressure p_1 measured at times $i-1$ $[kPa]$, $p_{2(i-1)}$ is the pressure p_2 measured at times $i-1$ $[kPa]$, $p_{3(i-1)}$ is the pressure p_3 measured at times $i-1$ $[kPa]$, and n is the number of pressures measured between time t_c and t_d.

The experimental results shown in table 6.4 might call into question the validity of the testing method, however it must be noticed that the accuracy of the measurements is directly affected by the size of the tank volume. In other words, despite of reaching an even distribution of metal wires within the assigned volume, the size of the purpose-designed isothermal tank only allows determining the critical pressure ratio of components with a sonic conductance below $5dm^3/(s \cdot bar)$. Therefore, in reviewing the results shown in table 6.4, it may be concluded that the effectiveness of the method decreases significantly when measuring the critical pressure ratio of an orifice with an equivalent diameter exceeding 6mm.

6.3.3 Determination of flow characteristics of the valve manifold

Based on the same testing principles described above, the sonic conductance and critical pressure ratio of the different flow paths defined by the internal geometry of the valve, were also determined (refer to fig. 6.26). As a matter of fact, the size of the isothermal tank was too small to ensure the correct calculation of the critical pressure ratio (refer to table 6.6). As previously stated sonic conductance values over $5dm^3/(s \cdot bar)$ lead to non-reliable results with the existing isothermal tank, while the results shown in table

6.5, calculated with a volume of $75.9dm^3$, are within the allowable accuracy of the method. It must be noted that in order to understand the influence of the poppet valve restrictions on the flow between the internal volumes of the valve manifold, the sonic conductance was not only determined between the operating ports of the manifold but also between the plugged ports.

The results confirmed that the tank volume directly influences the measurement accuracy during discharge, and also contributes to ensure an isothermal process.

6.3.4 Set-up of the blowing unit

As shown in figure 6.27 the complete set-up was horizontally positioned. The high pressure tank was supplied with a compressed air bottle charged up to 200 bar, while the low pressure vessel was provided with compressed air from the existing line. Both tanks were intended to minimize the pressure pulsations. The units were connected to the corresponding ports of the valve manifold, and similarly the output ports of the valve manifold were piped to the so-called cavity and recycling chambers. As mentioned in previous sections the static pressure inside the tanks was measured with pressure sensors, while the instantaneous gas temperature inside each volume was monitored with self-manufactured thermocouples. Data-logging as well as the operating sequence of the pilot valves was monitored and programmed with Labview respectively.

The operating conditions of the single-station blowing unit were defined on the basis of the blowing stages applied by the PET manufacturers. The valve opening/closing sequencing arose from systematic testing. The initial trials helped to identify the limitations of the first prototypes. The maximum operating pressure under which the valve manifold was able to work varies between 20 and 30 bar respectively. Based on those results as well as on the limited size of the high-pressure tank the blowing test was set-up in order to work up to a maximum operating pressure of 25 bar.

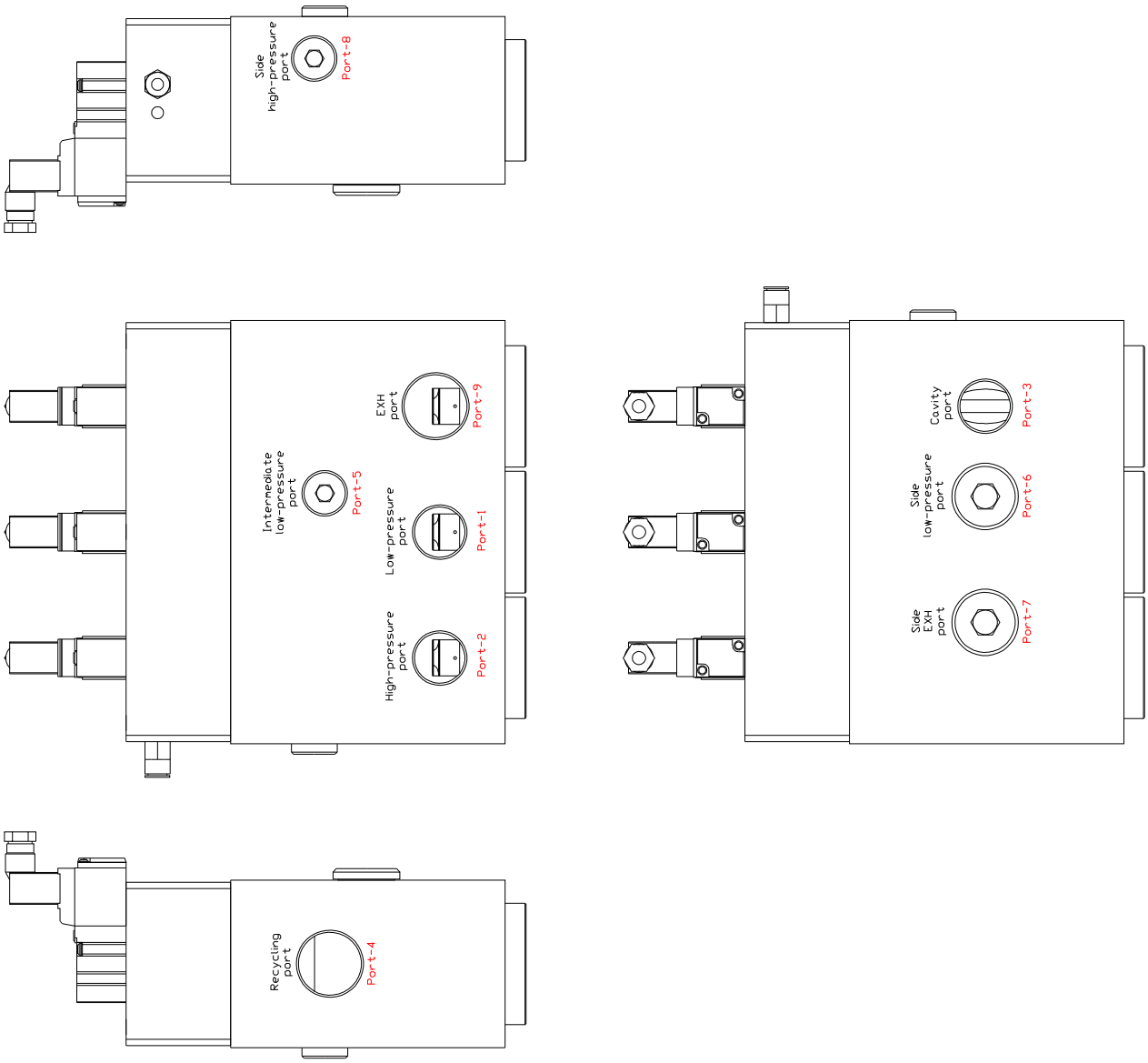

Figure 6.26: View of the valve manifold ports

Flow path		Sonic conductance $(dm^3/(s \cdot bar)$
Port 9 - Port 7	1^{st} reading	14.982
	2^{nd} reading	15.206
	3^{rd} reading	-
Port 8 - Port 3	1^{st} reading	8.450
	2^{nd} reading	8.449
	3^{rd} reading	-
Port 3 - Port 9	1^{st} reading	10.756
	2^{nd} reading	8.455
	3^{rd} reading	8.443
Port 3 - Port 4	1^{st} reading	8.371
	2^{nd} reading	8.294
	3^{rd} reading	-
Port 1 - Port 3	1^{st} reading	10.284
	2^{nd} reading	10.260
	3^{rd} reading	-
Port 4 - Port 3	1^{st} reading	8.349
	2^{nd} reading	8.352
	3^{rd} reading	-
Port 4 - Port 7	1^{st} reading	14.331
	2^{nd} reading	14.335
	3^{rd} reading	-
Port 1 - Port 6	1^{st} reading	14.708
	2^{nd} reading	14.767
	3^{rd} reading	-
Port 2 - Port 3	1^{st} reading	14.995
	2^{nd} reading	14.991
	3^{rd} reading	-
Port 7 - Port 9	1^{st} reading	14.089
	2^{nd} reading	13.978
	3^{rd} reading	-
Port 5 - Port 6	1^{st} reading	8.434
	2^{nd} reading	8.439
	3^{rd} reading	-
Port 7 - Port 4	1^{st} reading	13.614
	2^{nd} reading	13.583
	3^{rd} reading	-

Table 6.5: Sonic conductance of the valve manifold

Flow direction	Critical pressure ratio
Port 3 - Port 9	-1.329
Port 3 - Port 4	-1.736
Port 1 - Port 3	-0.435
Port 4 - Port 3	-0.176
Port 2 - Port 3	-1.717

Table 6.6: Critical pressure ratio of the valve manifold assuming m=0.5

The recycling stage always takes place after closing V_1. At this point the air flows through the pipe connected between the cavity chamber and the manifold, circulates through the valve manifold until reaching the recycling chamber. At certain stage, the air in the recycling chamber equalizes the pressure in the cavity chamber, being the point when the recycling process ends, and the remaining air in the cavity chamber is released to the atmosphere. As a matter of fact, the use of an additional recycling process may be also considered at this point, however a different concept design of the valve manifold should be used. It must be noted, that the amount of energy available in the cavity chamber drops as the pressure decreases so an additional recycling stage should be questioned.

Based on the existing concept, the operating valve sequence plays a very important role during the first stage of the blowing process. The response time of the valves must be taken into account when defining the working cycle. The first experimental results helped to understand that the pressure in the cavity chamber usually exceeded the primary pressure when being supplied by the recovery tank. During the low pressure blowing stage the pressure in the cavity chamber should not overtake the assigned low pressure level, however the response time of V_2 is not fast enough to prevent this type of functioning. Therefore it is necessary to energize V_2 before the pressure level in the cavity chamber reaches the requested value. This pressure peak generated during the low pressure blowing stage can be explained by the fact that there is not regulating device acting between the two vessels, so the internal geometry of the valve manifold as well as the existing pneumatic connections will constrain the efficiency of the system.

The situation described above only occurs if the pressure in the recovery tank at the

Figure 6.27: Views of the air blowing test

end of the blowing cycle has reached a designated pressure level. Usually this level for the experimental tests under discussion, is one and a half times or more the primary pressure (P_{low}).

Table 6.7 describes the complete range of configurations that may be tested according to the existing design.

6.4 Influence of the piping on the recycling process

With the purpose of searching the effect of the pressure waves travelling along the pipes a series of sensors were mounted on the pipe lines connected between the valve manifold and the vessels. Kistler (601A) piezo-electric pressure transducers were placed at three adjacent positions (refer to figure 6.40), which in fact were opposite to the mounting holes where the static pressure transducers were located. These sensors, however, could only be used when using the long type pipe version as the short type pipe solution was not long enough to physically position the three measuring units.

Despite having a limited high-pressure volume which was able to ensure a constant pressure during the test process, the results are sufficiently consistent. Figures 6.28 to 6.33 show the pressure characteristics for different connections between the valve manifold and the blowing vessel and recycling vessel respectively. Generally the recycling rate oscillates between 11 and 12 bar when the high pressure stabilizing reservoir is able to guarantee a pressure level which fluctuates between 22 and 23.4 bar respectively. The results show that a sudden pressure raise within the high-pressure reservoir is directly translated into an increase of recycling rate, no matter which piping lay-out is applied. Therefore in order to avoid misleading conclusions those graphs were disregarded for the purpose of this analysis.

A deeper examination reveals that when only considering the long pipe connections between the valve manifold and the recycling vessel, the recyling rate varies between 11 and 11.8 bar (high-pressure supply rate 22-23.4bar), while a short pipe connection reaches a recycling rate between 11.4 and 12 bar (high-pressure supply rate 22-23.4 bar). Moreover, despite having a continuous pressure drop in the stabilizing high-pressure tank after energizing V_1, the configuration which ensures a better performance from recycling point of the view is the one with constant diameter and shorter pipe length.

For all the cases the influence of the connection between the valve manifold and the blowing vessel seems to not be relevant during the recycling process, in fact the valve manifold acts as a reflecting wall which avoids the travelling waves to reach the recycling pipe.

Furthermore, a closer view to the various lay-outs when maintaining a constant pipe diameter between the valve manifold and the blowing vessel, shows that a short pipe with diameter reduction causes almost no effect to the recycling process (recycling rate fluctuates between 11.4 and 11.9 bar with a high-pressure supply line varying between 22 and 23.3bar). As is the case with short pipes with constant diameter and those with increasing diameter towards the recycling vessel, the pressure at the end of the recycling process varies between 11.2 and 12 bar with a pressure level in the stabilizing tank between 22 and 23.4 bar. In addition to this, when assemblying long pipes the recycling ratio stays around 11.3 bar for all the cases, which means that the internal geometry of the pipe did not affect the recycling efficiency.

Despite having some positive results the recycling performance amongst difference configurations does not seem to be very different, in fact, there is a little variation between them. Therefore in order to determine how a tapered shape could influence the recycling rate, dynamic pressure sensors were used to assess the pressure characteristics in long pipes. The reader should note that the term long pipe in this context is exclusively used to differentiate the two types of lenghts used for the connections.

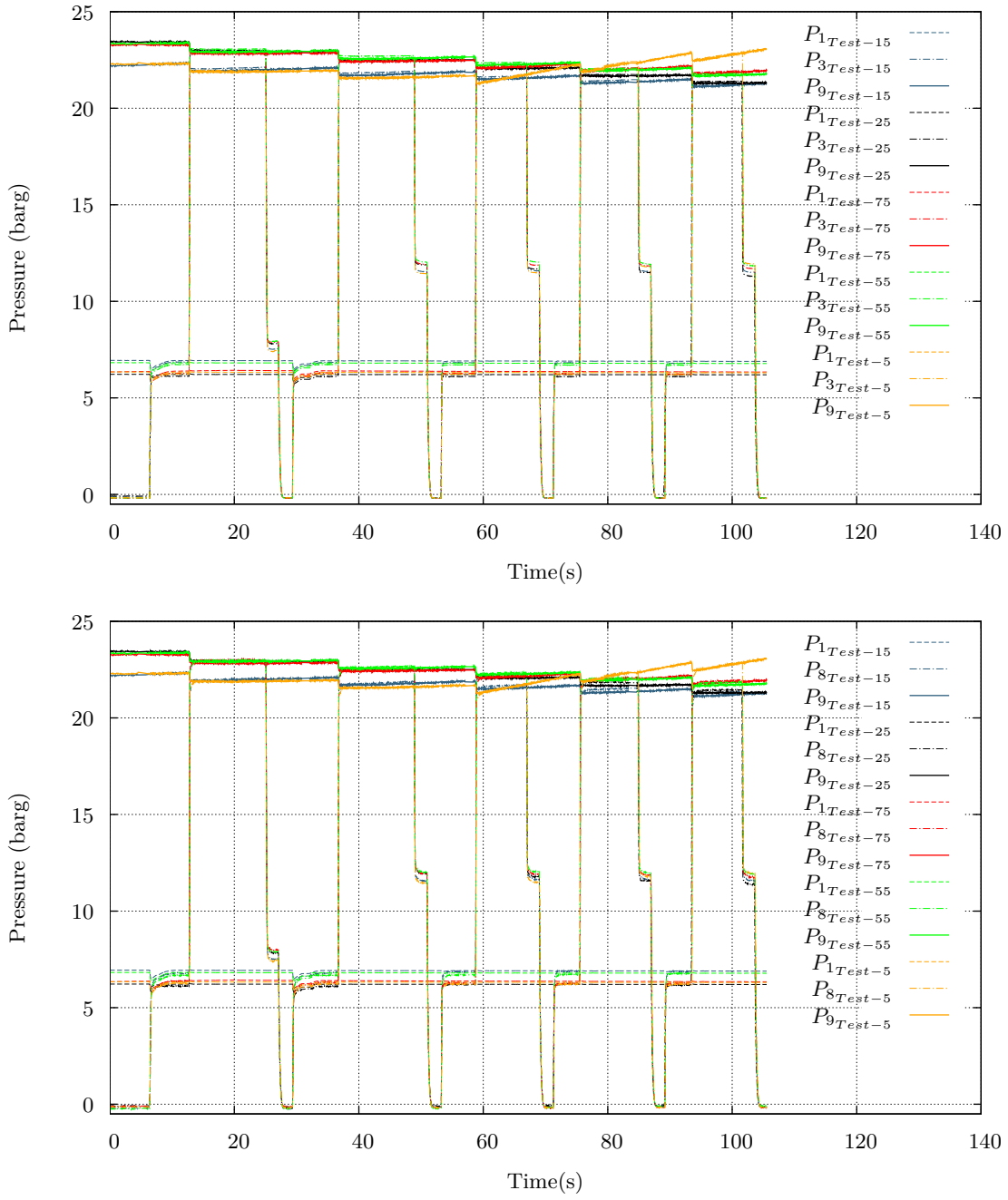

Figure 6.28: Pressure characteristics within the cavity vessel for the following set-ups: Test-5, Test-15, Test-25, Test-55, Test-75 (refer to Table 6.7 and Table 11.1)

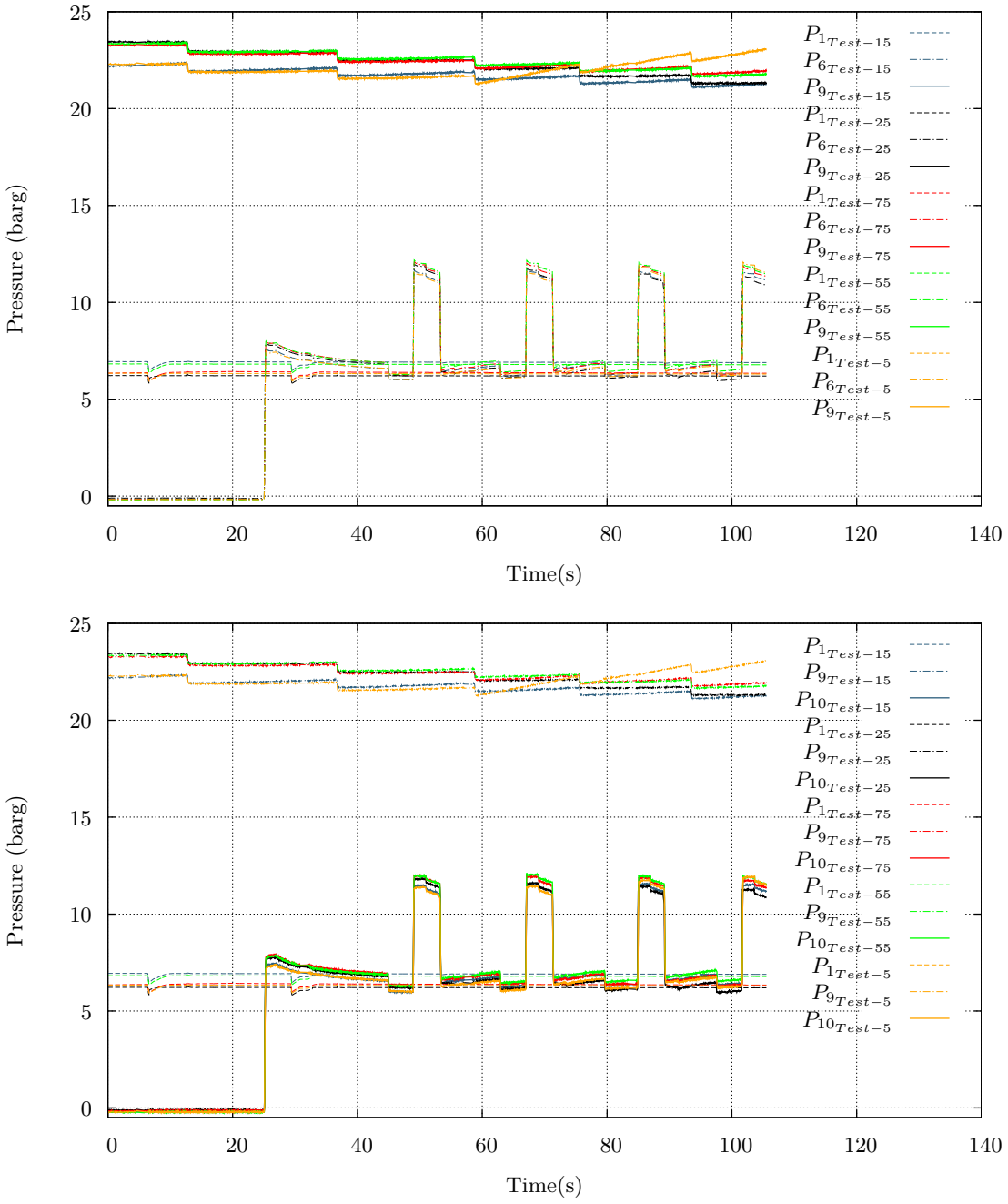

Figure 6.29: Pressure characteristics within the recycling vessel for the following set-ups: Test-5, Test-15, Test-25, Test-55, Test-75 (refer to Table 6.7 and Table 11.1)

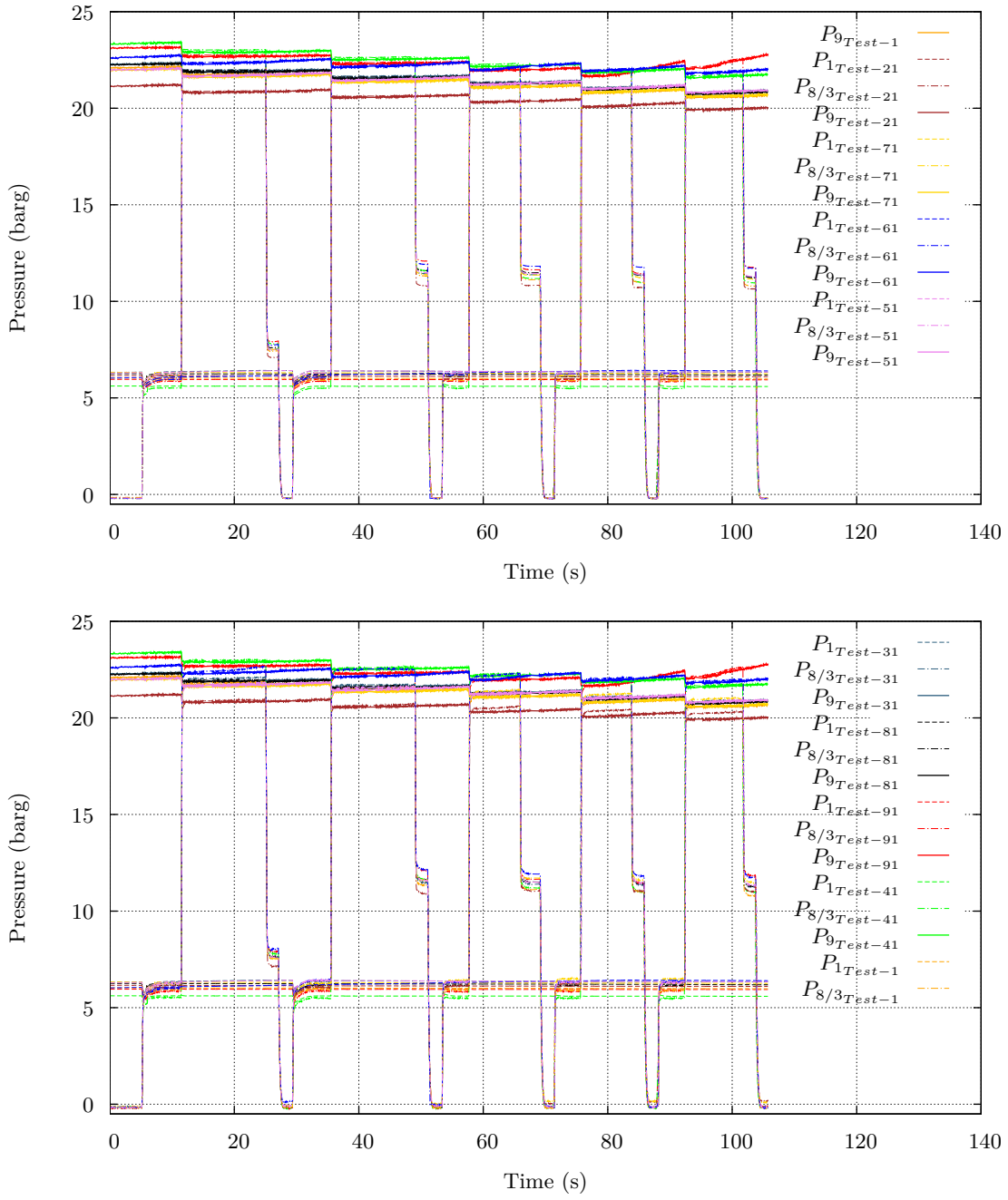

Figure 6.30: Pressure characteristics within the cavity vessel for the following set-ups: Test-1, Test-21, Test-31, Test-41, Test-51, Test-61, Test-71, Test-81, Test-91 (refer to Table 6.7 and Table 11.1) Note: Shared legend for both graphs

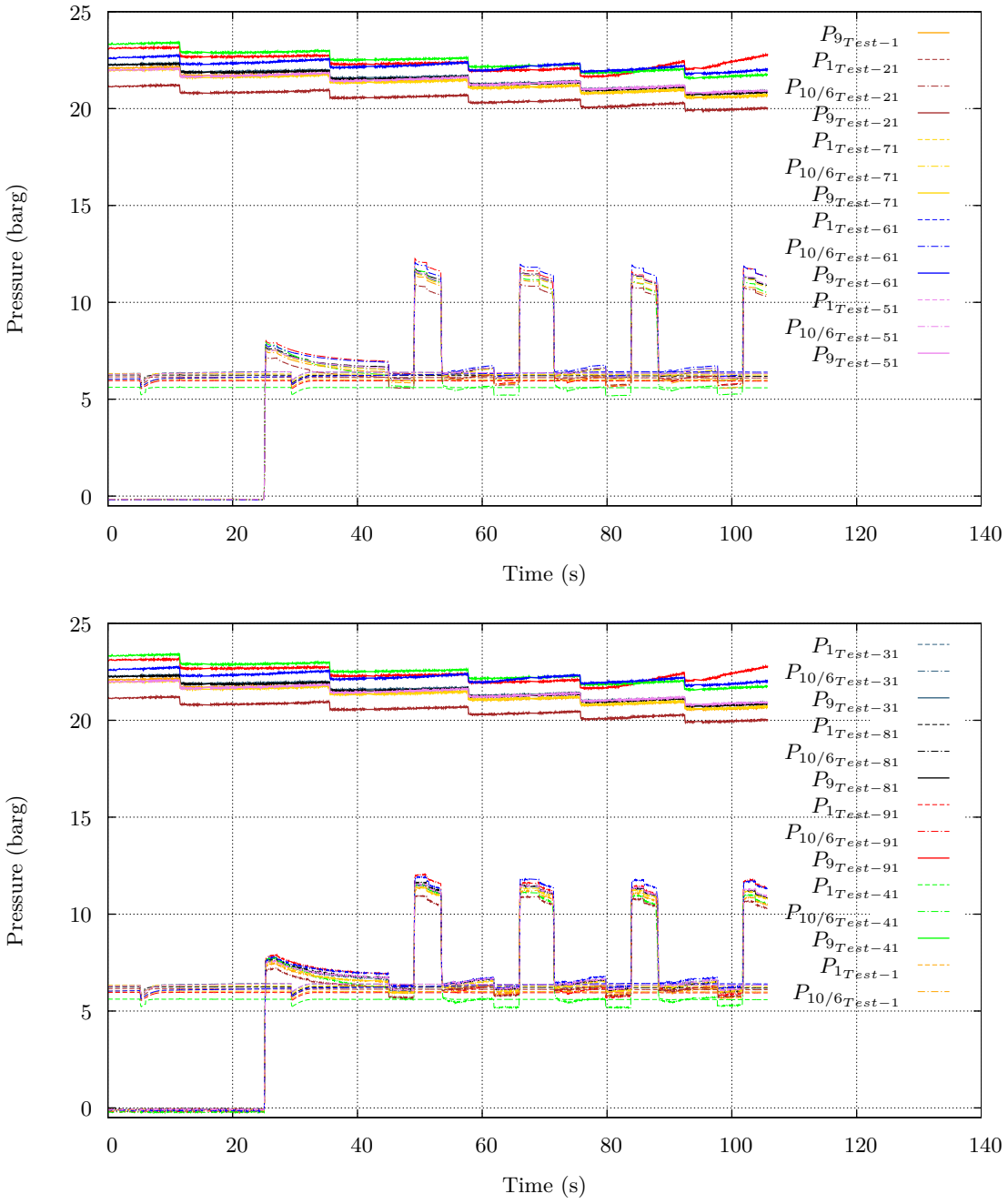

Figure 6.31: Pressure characteristics within the recycling vessel for the following set-ups: Test-1, Test-21, Test-31, Test-41, Test-51, Test-61, Test-71, Test-81, Test-91 (refer to Table 6.7 and Table 11.1) Note: Shared legend for both graphs

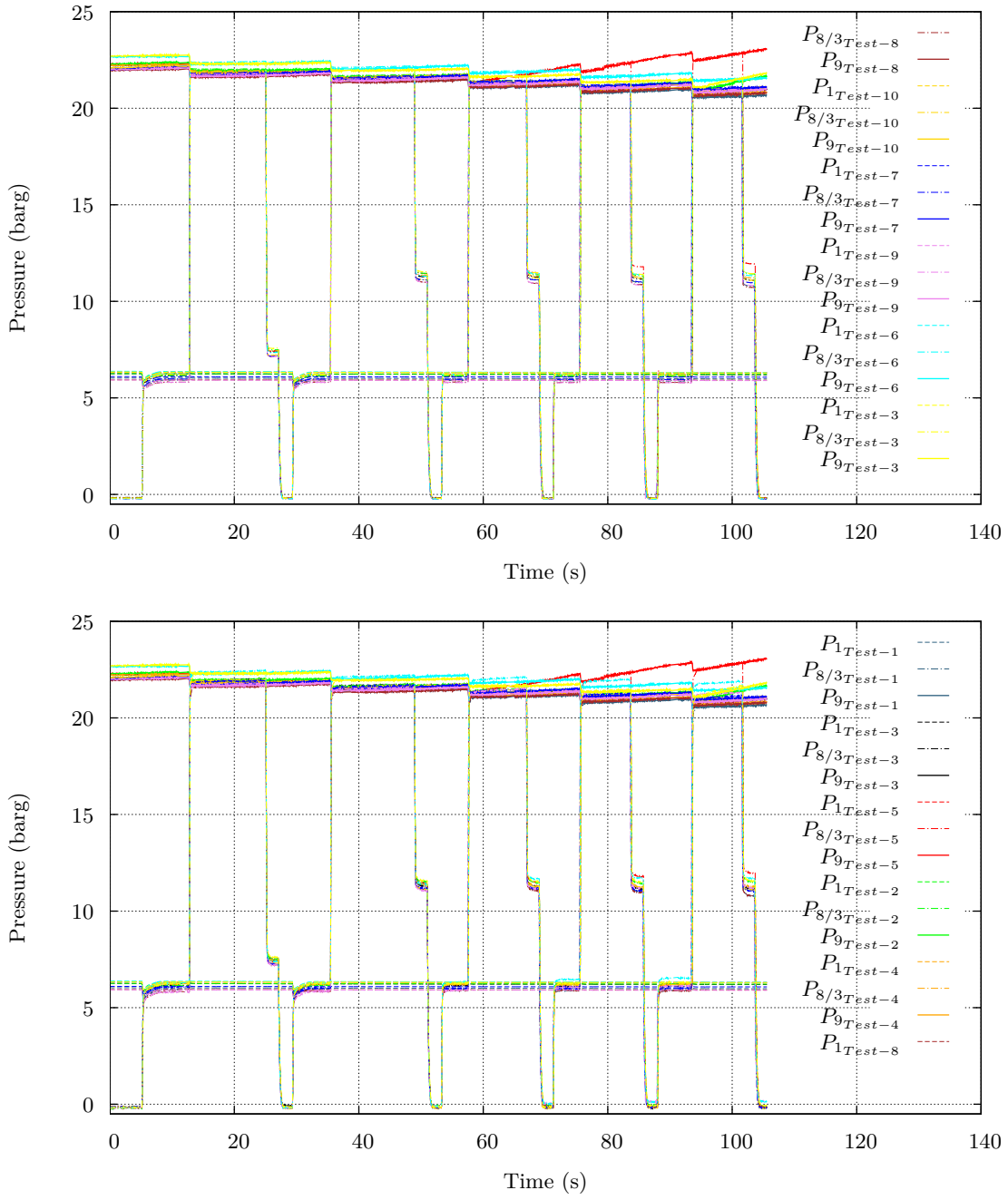

Figure 6.32: Pressure characteristics for the following set-ups: Test-1, Test-2, Test-3, Test-4, Test-5, Test-6, Test-7, Test-8, Test-9, Test-10 (refer to Table 6.7 and Table 11.1)
Note: Shared legend for both graphs

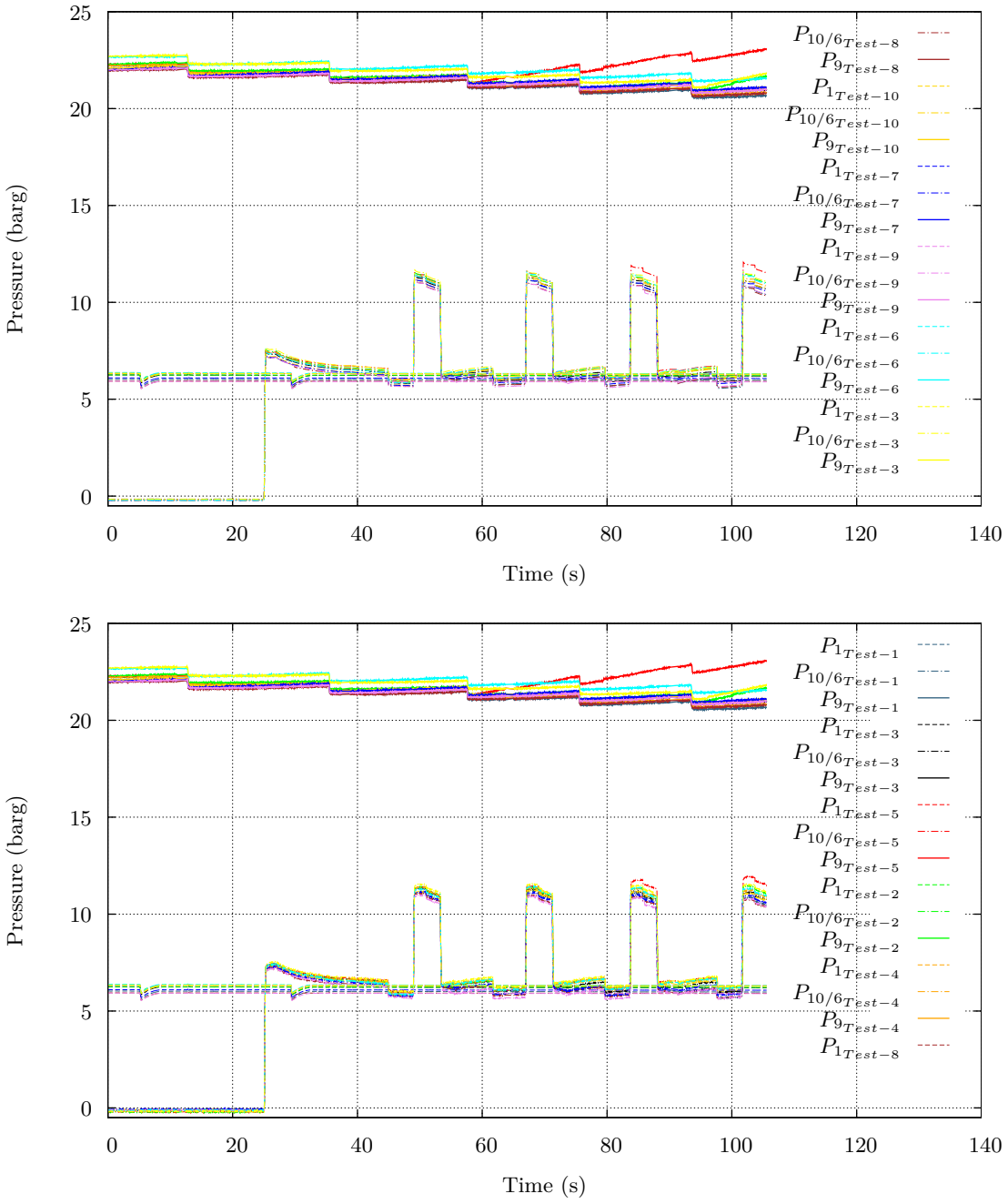

Figure 6.33: Pressure characteristics for the following set-ups: Test-1, Test-2, Test-3, Test-4, Test-5, Test-6, Test-7, Test-8, Test-9, Test-10 (refer to Table 6.7 and Table 11.1)
Note: Shared legend for both graphs

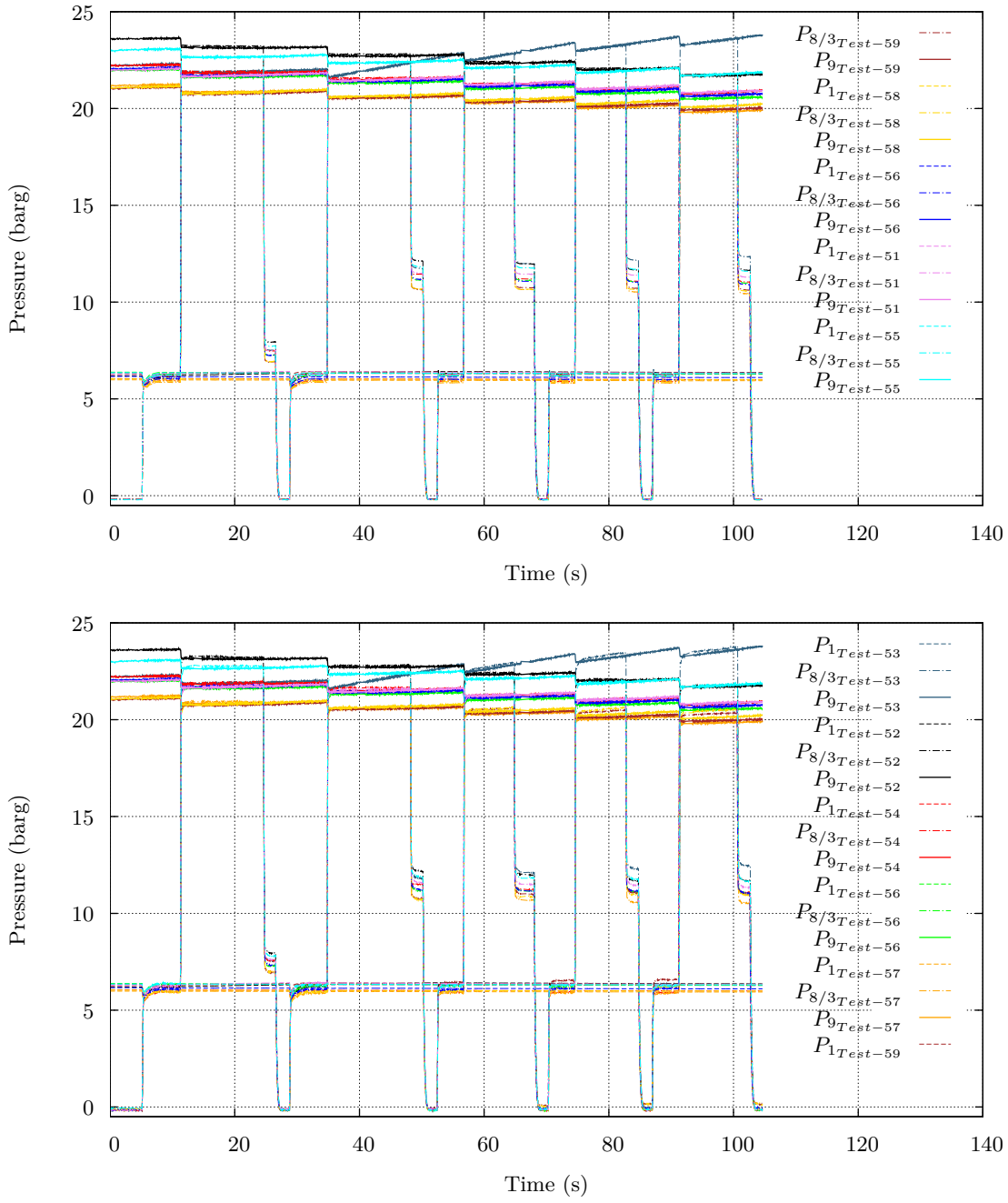

Figure 6.34: Pressure characteristics for the following set-ups: Test-51, Test-52, Test-53, Test-54, Test-55, Test-56, Test-57, Test-58, Test-59 (refer to Table 6.7 and Table 11.1) Note: Shared legend for both graphs

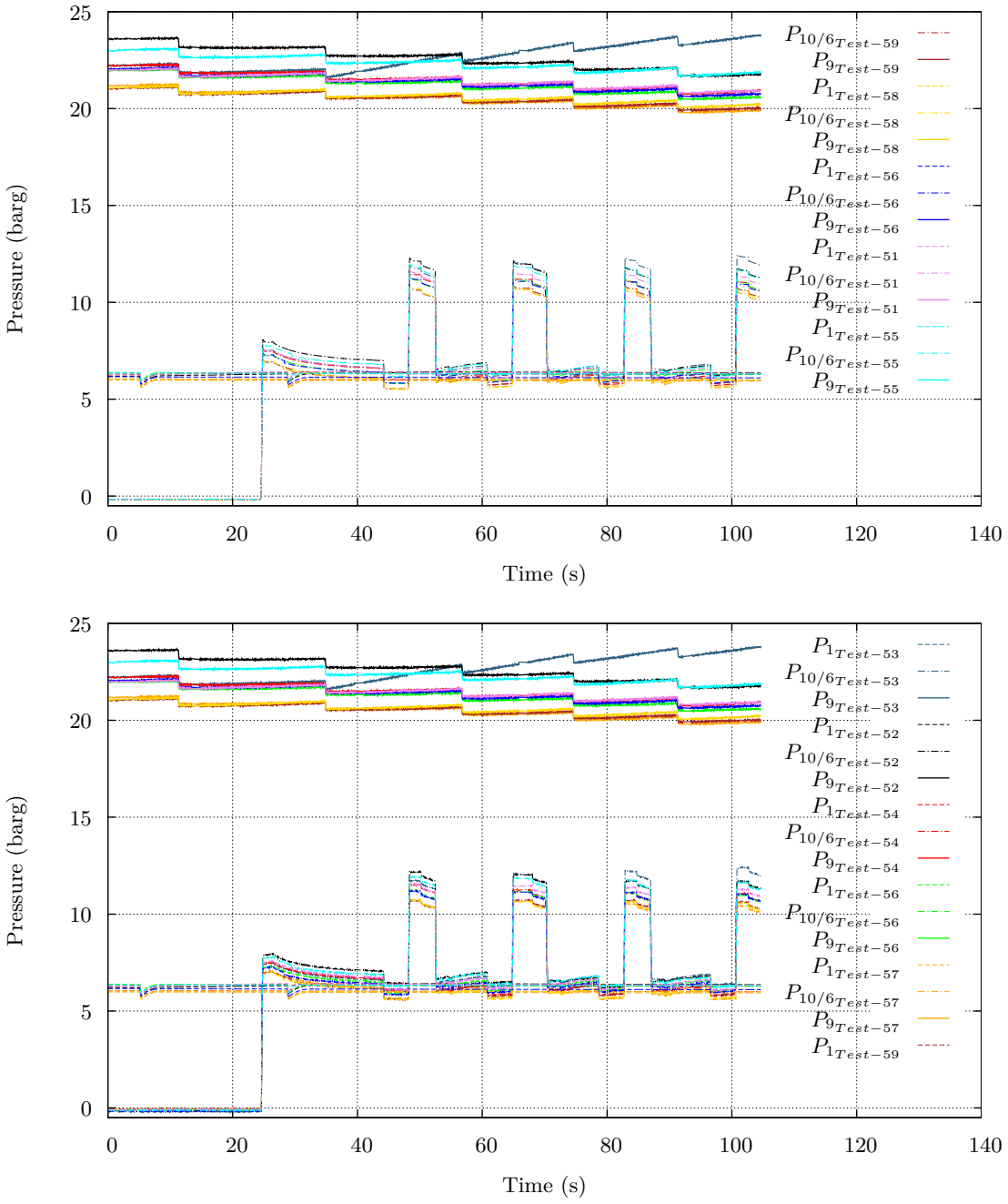

Figure 6.35: Pressure characteristics for the following set-ups: Test-51, Test-52, Test-53, Test-54, Test-55, Test-56, Test-57, Test-58, Test-59 (refer to Table 6.7 and Table 11.1) Note: Shared legend for both graphs

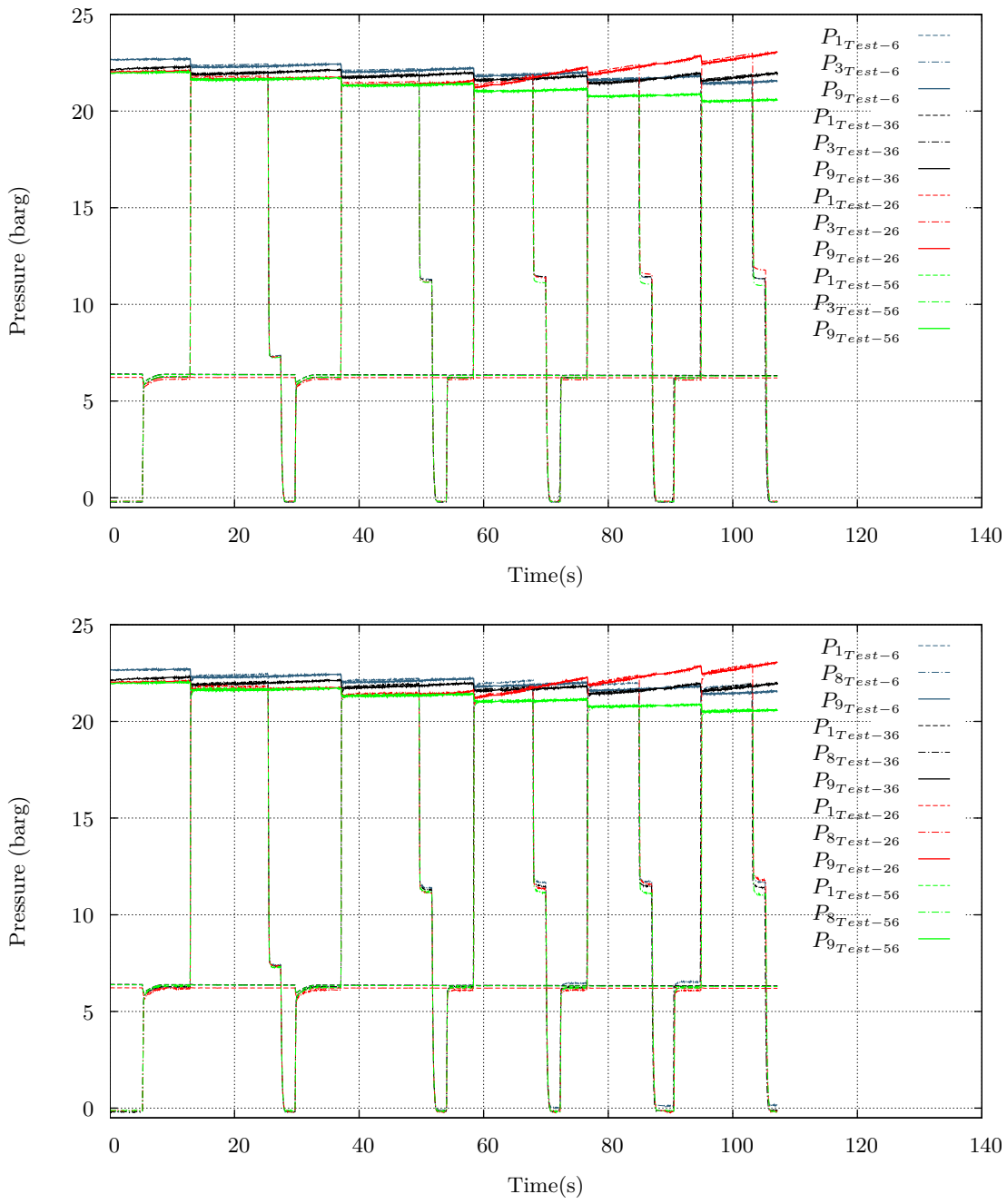

Figure 6.36: Pressure characteristics for the following set-ups: Test-6, Test-26, Test-36, Test-56 (refer to Table 6.7 and Table 11.1)

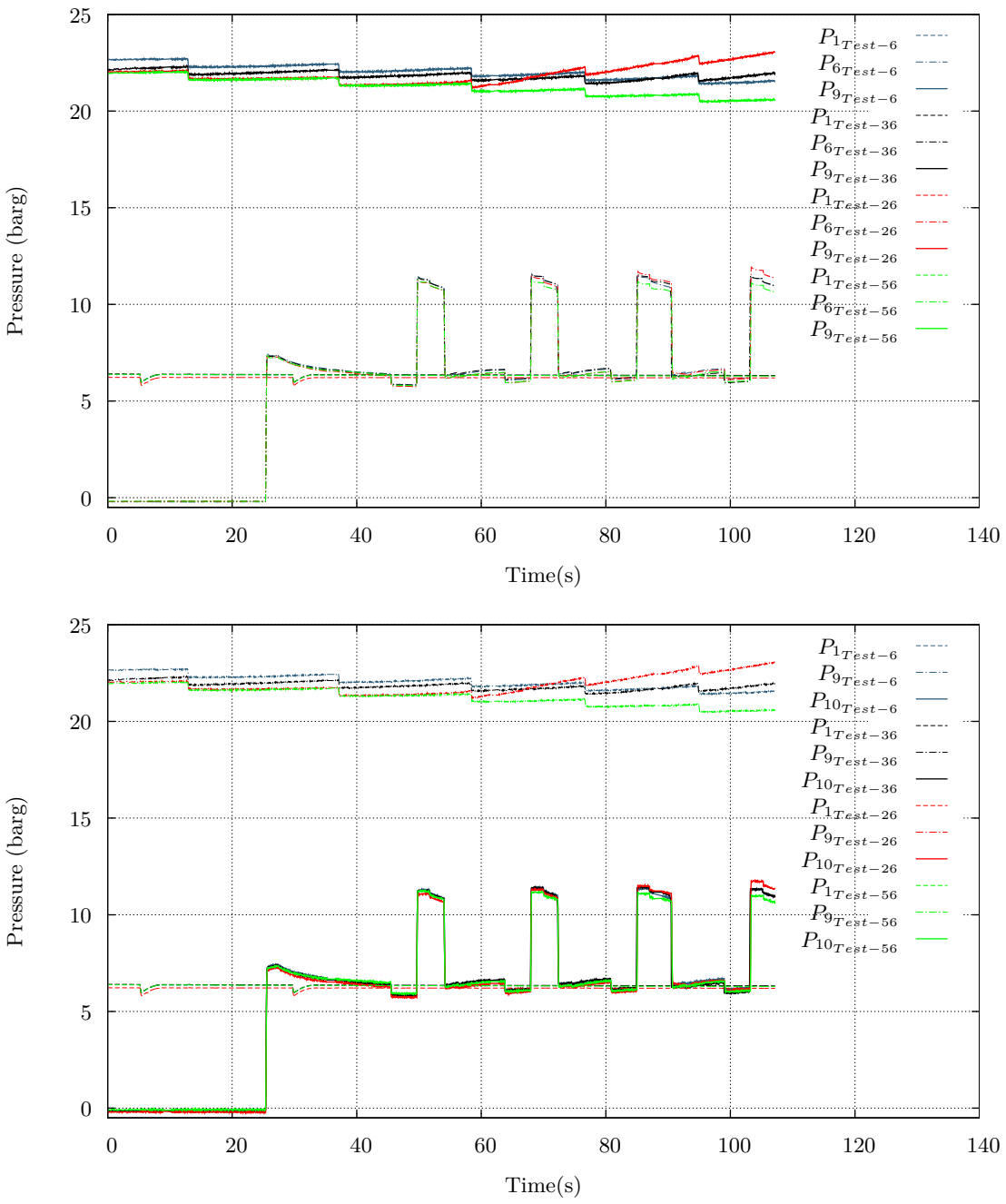

Figure 6.37: Pressure characteristics for the following set-ups: Test-6, Test-26, Test-36, Test-56 (refer to Table 6.7 and Table 11.1)

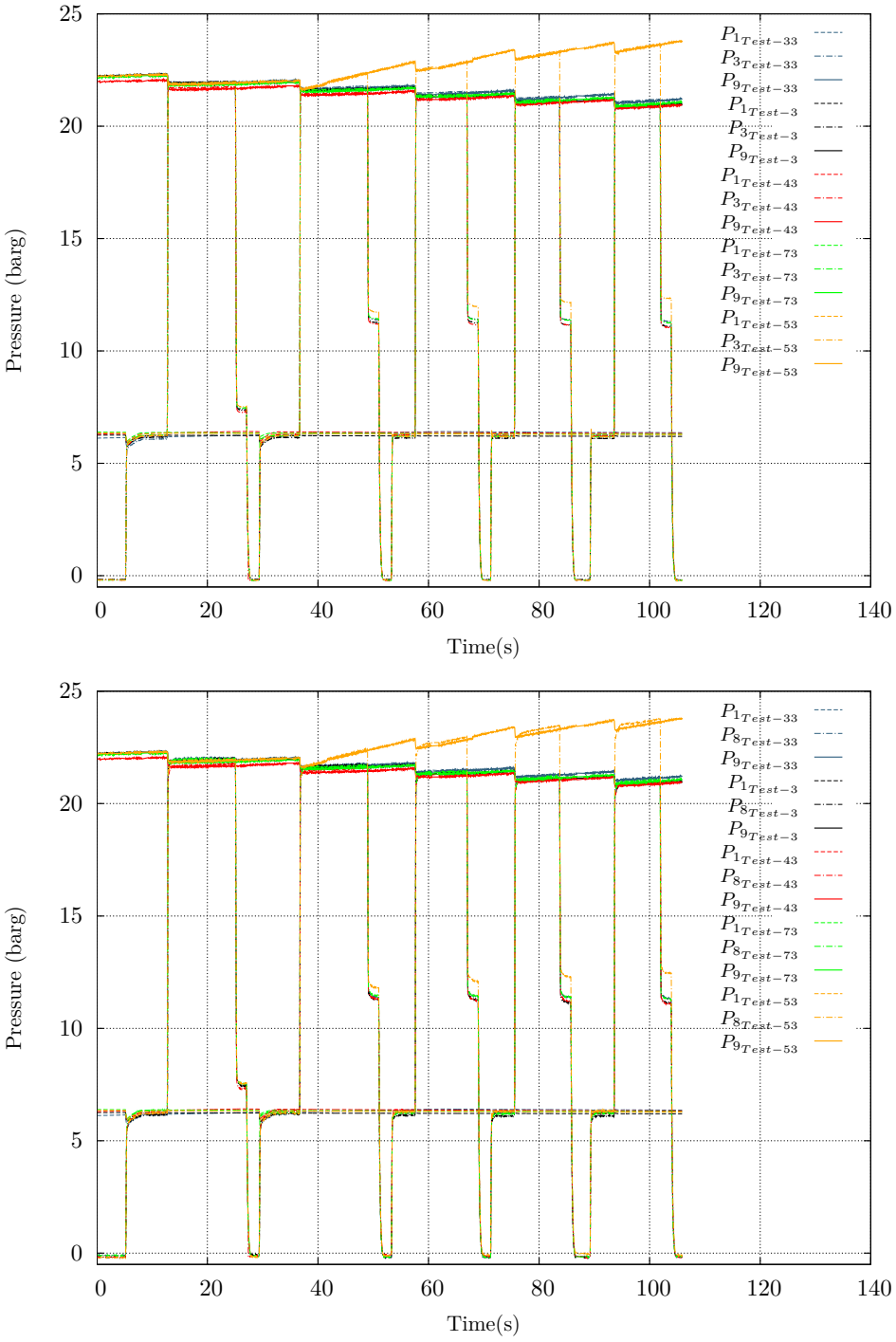

Figure 6.38: Pressure characteristics for the following set-ups: Test-3, Test-33, Test-43, Test-53, Test-73 (refer to Table 6.7) and Table 11.1)

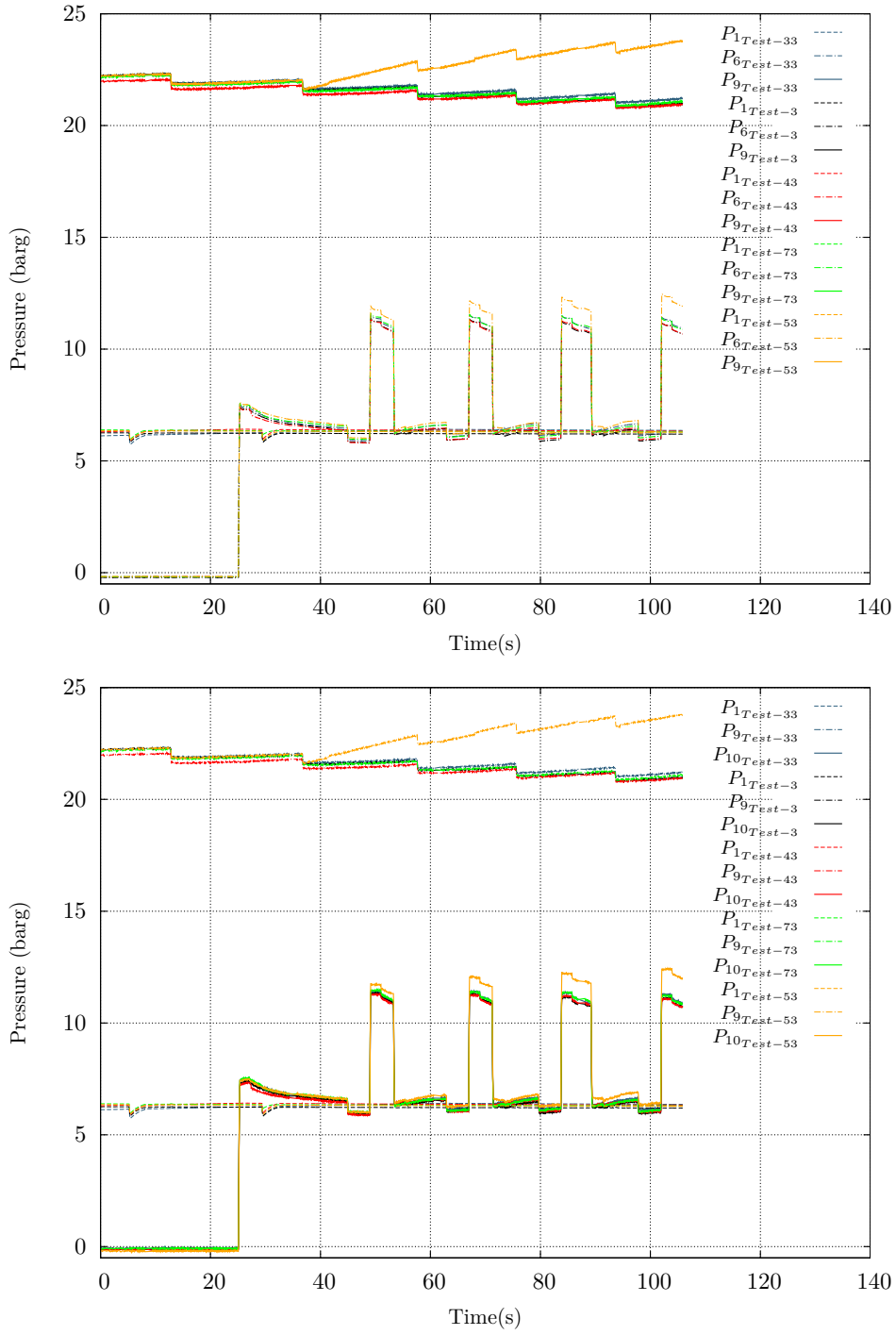

Figure 6.39: Pressure characteristics for the following set-ups: Test-3, Test-33, Test-43, Test-53, Test-73 (refer to Table 6.7) and Table 11.1)

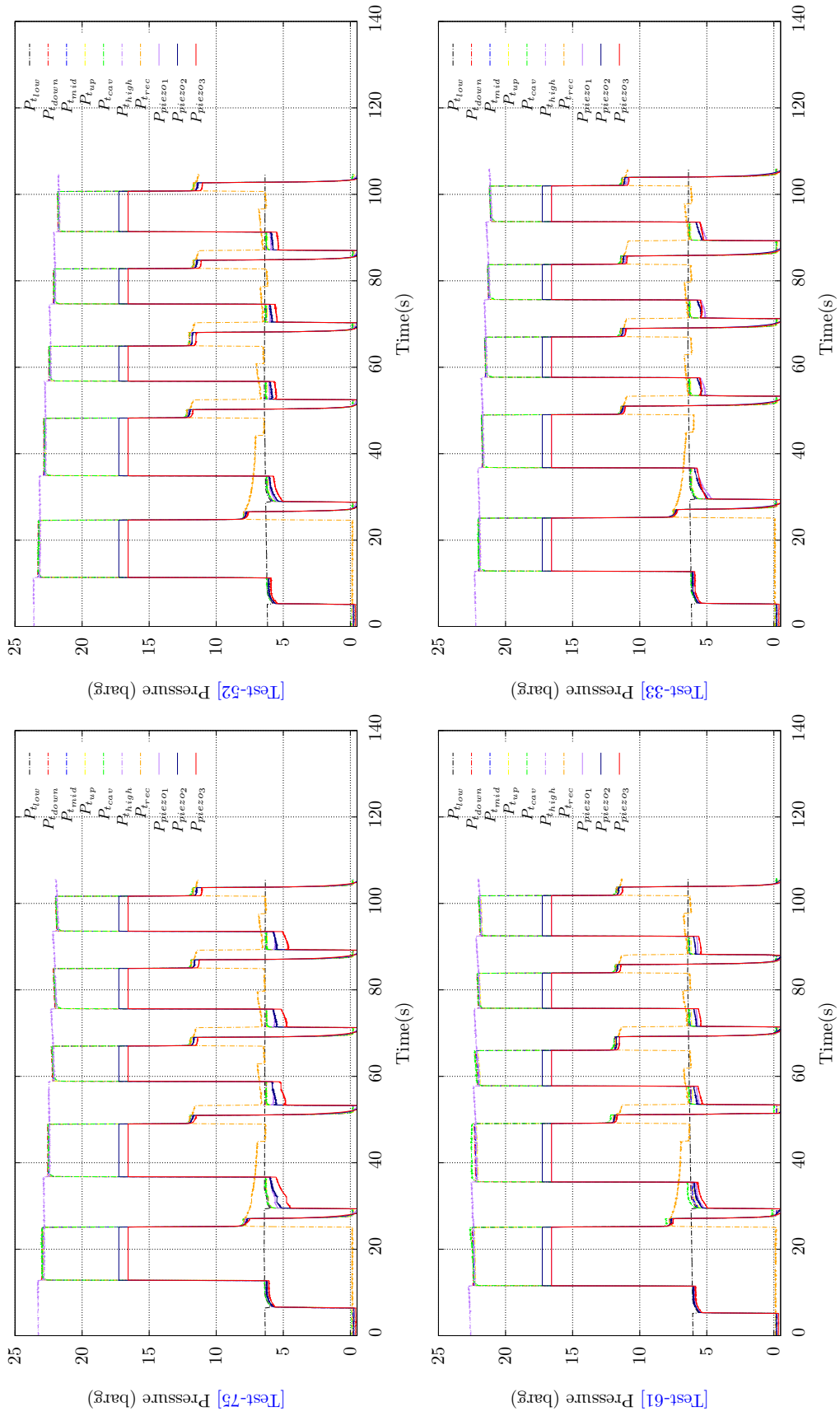

Figure 6.40: Pressure readings taken with piezoelectric pressure sensors (refer to Table 6.7)

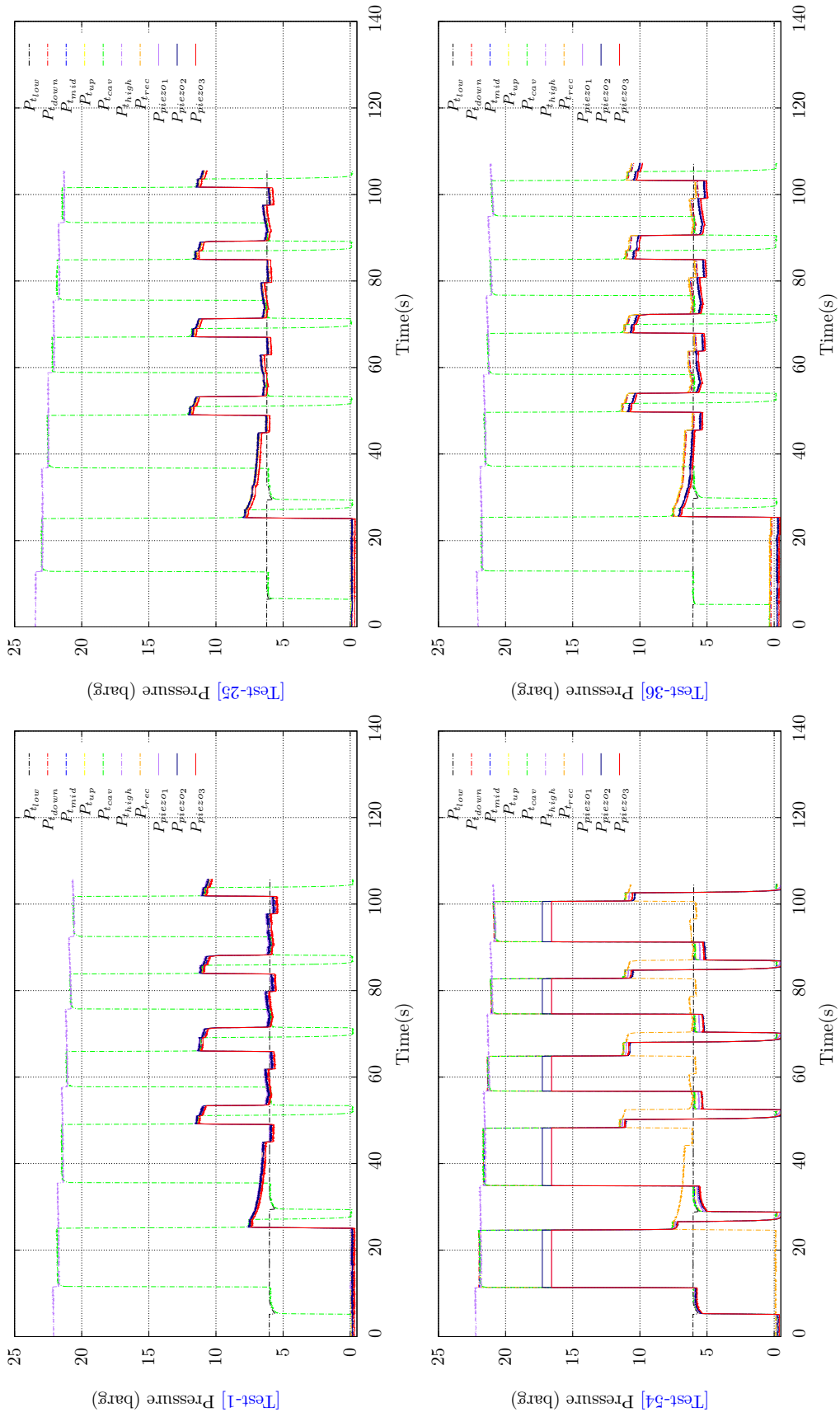

Figure 6.41: Pressure readings taken with piezoelectric pressure sensors (refer to Table 6.7)

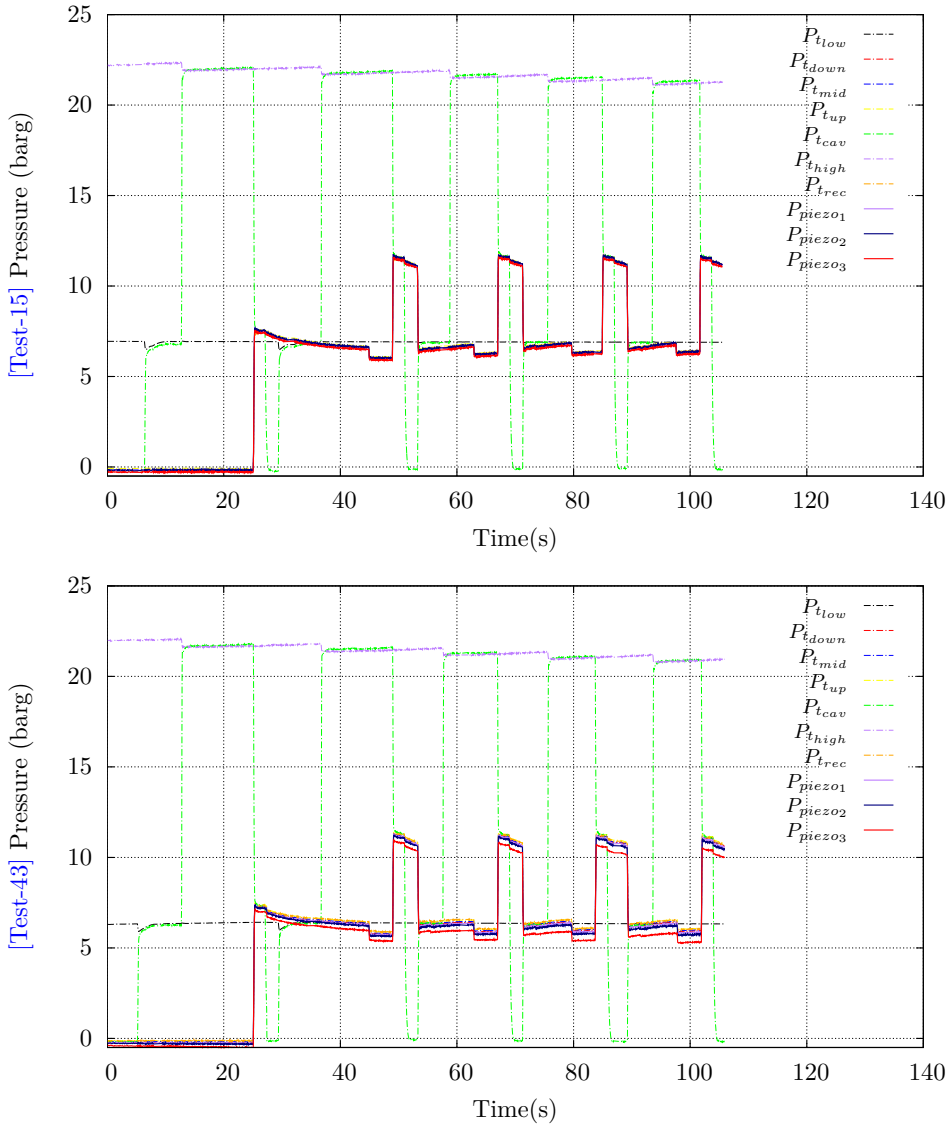

Figure 6.42: Pressure readings taken with piezoelectric pressure sensors (refer to Table 6.7)

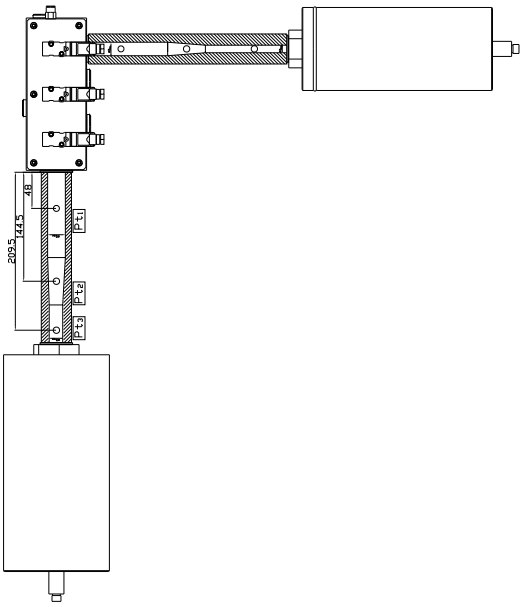

(a) Test-15

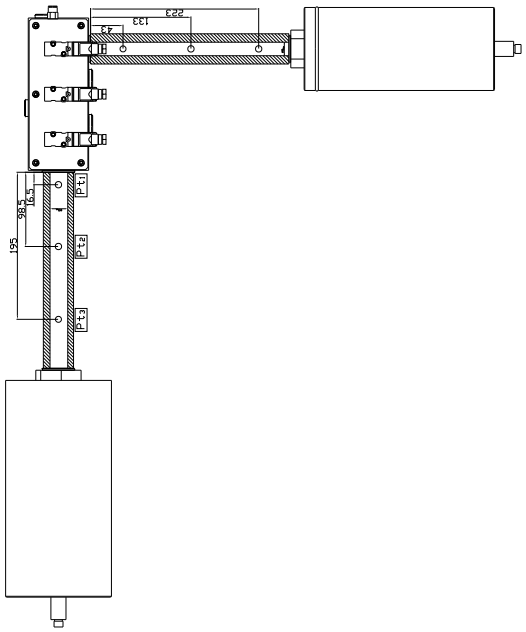

(b) Test-25

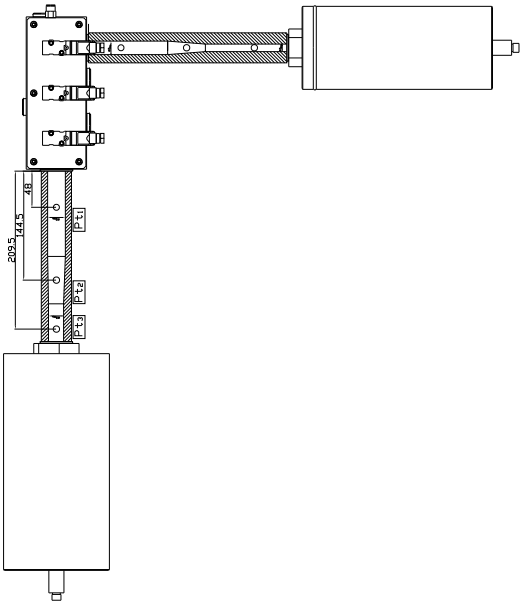

(c) Test-75

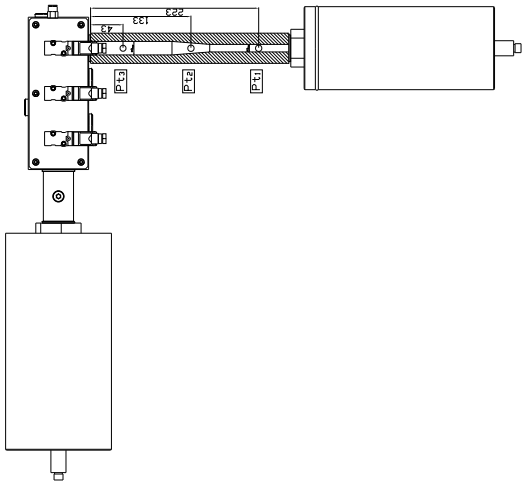

(d) Test-1

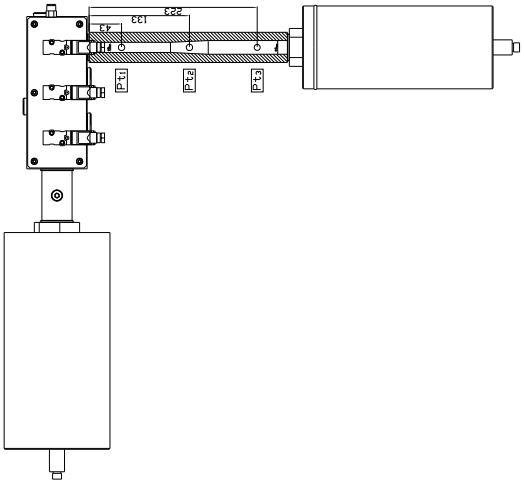

(f) Test-52

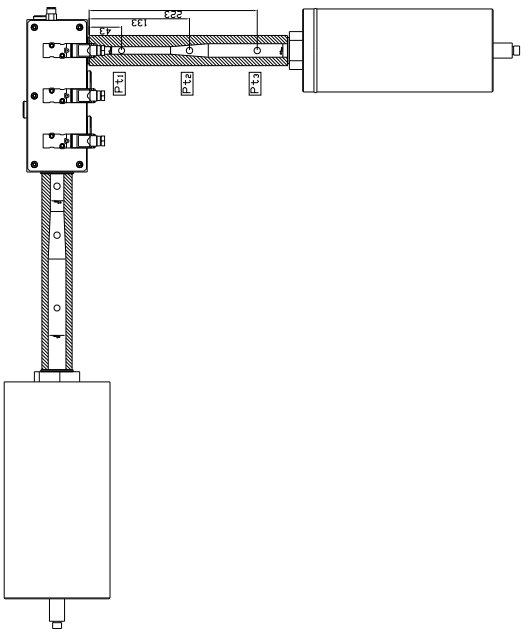

(h) Test-33

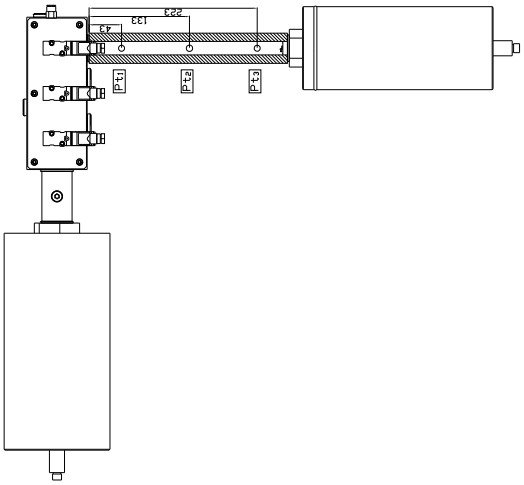

(e) Test-61

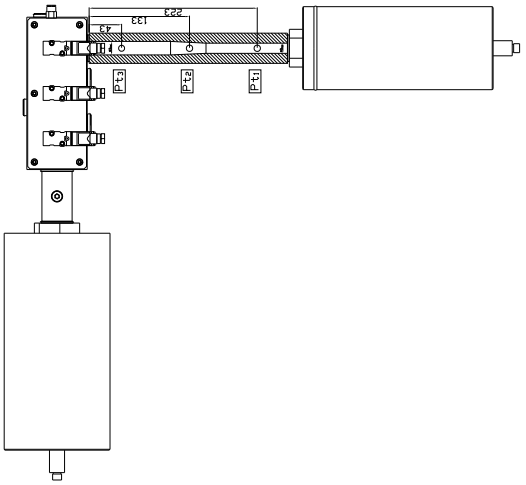

(g) Test-54

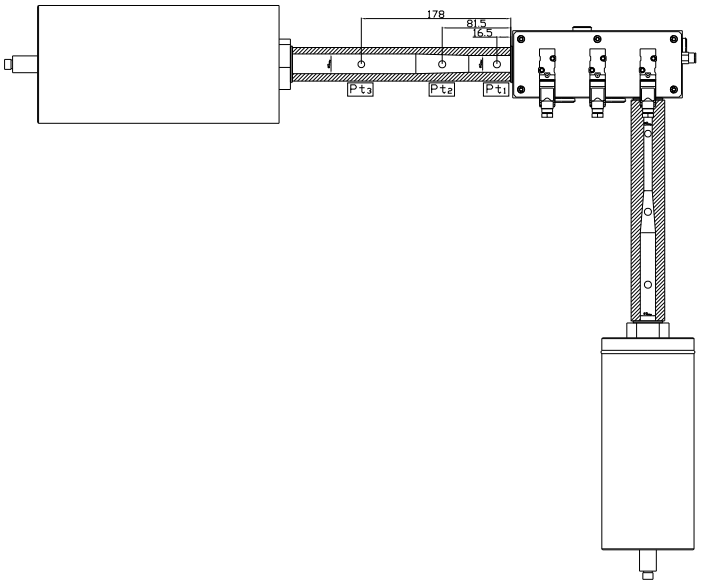

(i) Test-43

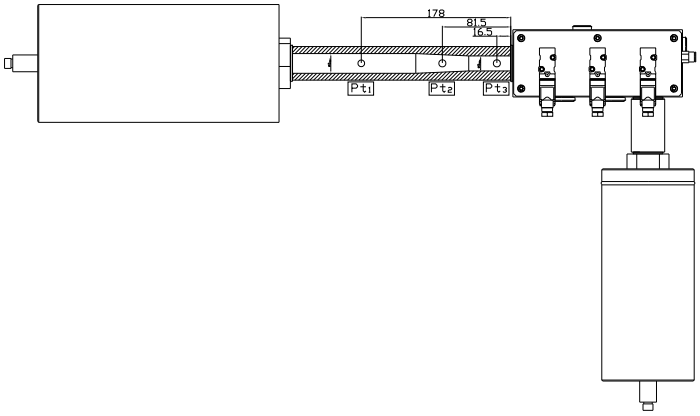

(j) Test-36

Figure 6.43: Position of piezoelectric pressure sensors according to test set-up

			$L_{cav_1} = 300$						$L_{cav_2} = 100$					
			$D_{1_{cav}}/D_{2_{cav}}$						$D_{1_{cav}}/D_{2_{cav}}$					
			ø18-ø18	ø15-ø18	ø10-ø18	ø18-ø15	ø18-ø10	18-18	ø13,75-ø18	ø10-ø18	ø18-ø13,75	ø18-ø10
$L_{rec_1} = 260$	D_{rec_1}/D_{rec_2}	ø23.5-ø23.5	Test-1	Test-2	Test-3	Test-4	Test-5	Test-6	Test-7	Test-8	Test-9	Test-10
		ø23.5-ø20	Test-11	Test-12	Test-13	Test-14	Test-15	Test-16	Test-17	Test-18	Test-19	Test-20
		ø23.5-ø18	Test-21	Test-22	Test-23	Test-24	Test-25	Test-26	Test-27	Test-28	Test-29	Test-30
		ø18-ø23.5	Test-31	Test-32	Test-33	Test-34	Test-35	Test-36	Test-37	Test-38	Test-39	Test-40
		ø20-ø23.5	Test-41	Test-42	Test-43	Test-44	Test-45	Test-46	Test-47	Test-48	Test-49	Test-50
$L_{rec_1} = 100$	D_{rec_1}/D_{rec_2}	ø23.5-ø23.5	Test-51	Test-52	Test-53	Test-54	Test-55	Test-56	Test-57	Test-58	Test-59	Test-60
		ø23.5-ø20	Test-61	Test-62	Test-63	Test-64	Test-65	Test-66	Test-67	Test-68	Test-69	Test-70
		ø23.5-ø18	Test-71	Test-72	Test-73	Test-74	Test-75	Test-76	Test-77	Test-78	Test-79	Test-80
		ø18-ø23.5	Test-81	Test-82	Test-83	Test-84	Test-85	Test-86	Test-87	Test-88	Test-89	Test-90
		ø20-ø23.5	Test-91	Test-92	Test-93	Test-94	Test-95	Test-96	Test-97	Test-98	Test-99	Test-100

Table 6.7: Matrix of test set-ups (dimensions in mm)

6.5 Near isothermal compressed air storage - Experimental analysis

As a matter of fact the compression and expansion process which takes place within the blowing and recycling vessels do not take place isothermally, a proposal to achieve such stage was forward. The concept is based on the same principle used when determining the critical pressure of a pneumatic component. As discussed in previous sections the heat capacity of some materials may be useful to ensure a pseudo-constant pressure stage during the charge and discharge of gas to/from the container. From the images shown in figure 6.45 it is possible to understand how the thermocouples mounted in the recycling vessel were encapsulated with a fine-meshed filter made of plastic which allowed the air going through and avoided the particles to be in contact with the thermocouple joints.

With small chunks and short trips of aluminium a compact non-fixed structure was generated inside the vessel. A stainless steel fine-mesh was located at the entrance of the vessel so the small pieces of aluminium could not leave the tank. The results of this experiment are depicted in figure 6.46. It must be pointed out that even though the temperature in the blowing cavity reached 70°C, the temperature variation within the recycling tank did not exceed 5°C, therefore the result was quite satisfactory.

Figure 6.45: (Left view) Plastic encapsulation to prevent from direct contact with the medium. (Right view) Filling material to ensure isothermal condition

The test shows that the transient air temperatures can be maintained below 30°C, which is in fact a value far below the temperatures achieved when a non-isothermal

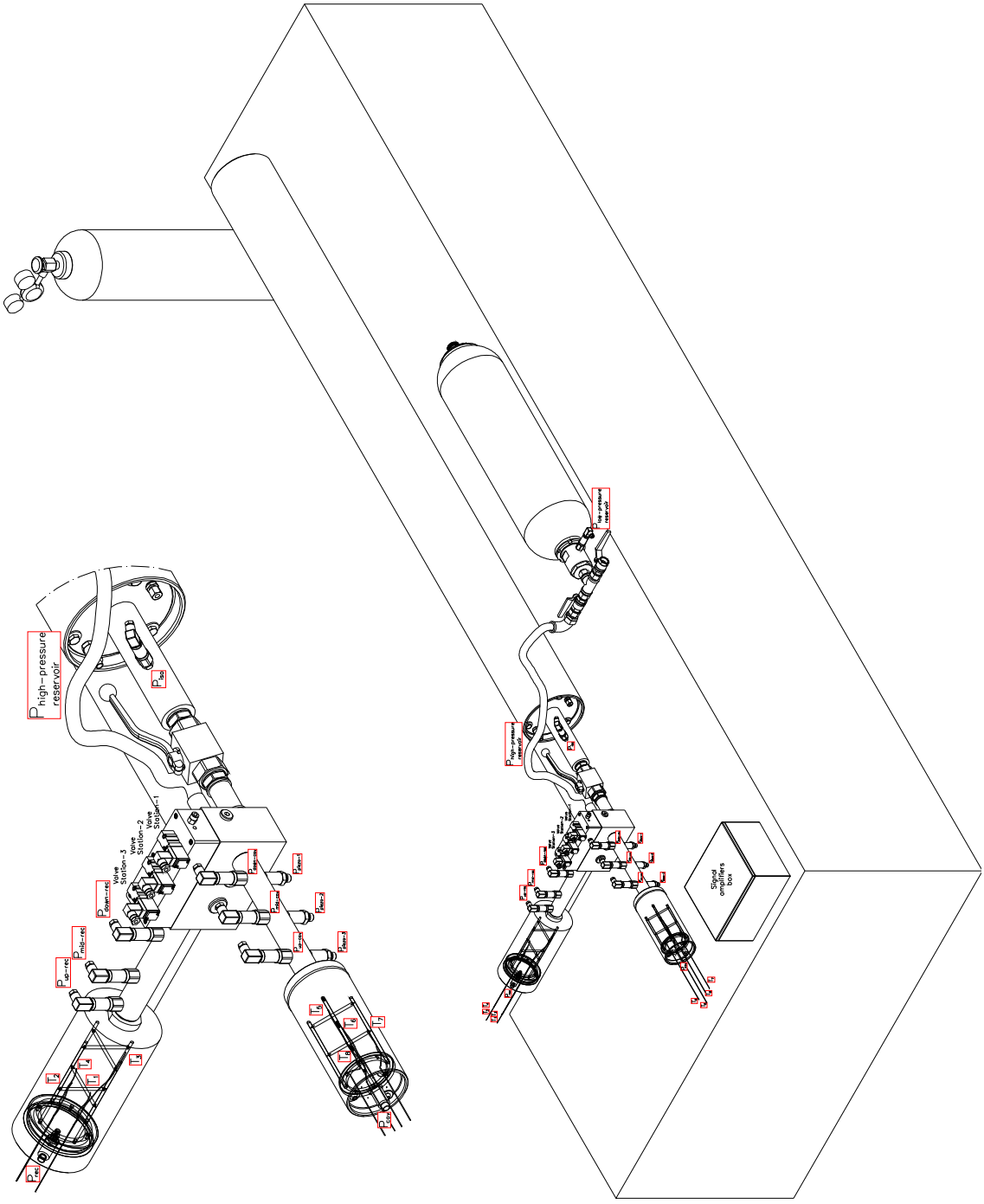

Figure 6.44: Distribution of the temperature and pressure sensors on the test lay-out

recovery tank is used. Based on the experimental results obtained in Chapter 5 for an air container subjected to a continuous charge and discharge process, it may be understood that the isothermal concept would ensure a lower heat transfer with the surroundings, which will lead to higher rates of available air energy to be recycled.

On the other hand, it must be noticed that the isothermal condition contributes to have a constant pressure in the chamber once the recycling process finalizes. A comparison with the experimental results depicted in Chapter 11, proves that the heat transfer is clearly responsible for the pressure decay within the recycling vessel at the end of the first cycle. Nevertheless, this parameter becomes more critical when the recycling ratio is getting higher. The reason being is that the first cycle does not provide enough air to the recycling vessel to reach the required pressure level to supply air to the cavity for the next blowing phase. Obviously, until this condition is not fulfilled the low pressure line will feed the cavity, and therefore, the pressure decay will occur. In case of having lower recycling ratios the recycling tank will provide air to the cavity after the first cycle and, as the results shown in Chapter 11 indicate the pressure is not dropping anymore, on the contrary it experiences a slight increase which is associated to a stabilization period caused by the pressure waves travelling in the recycling pipe after closing V_3.

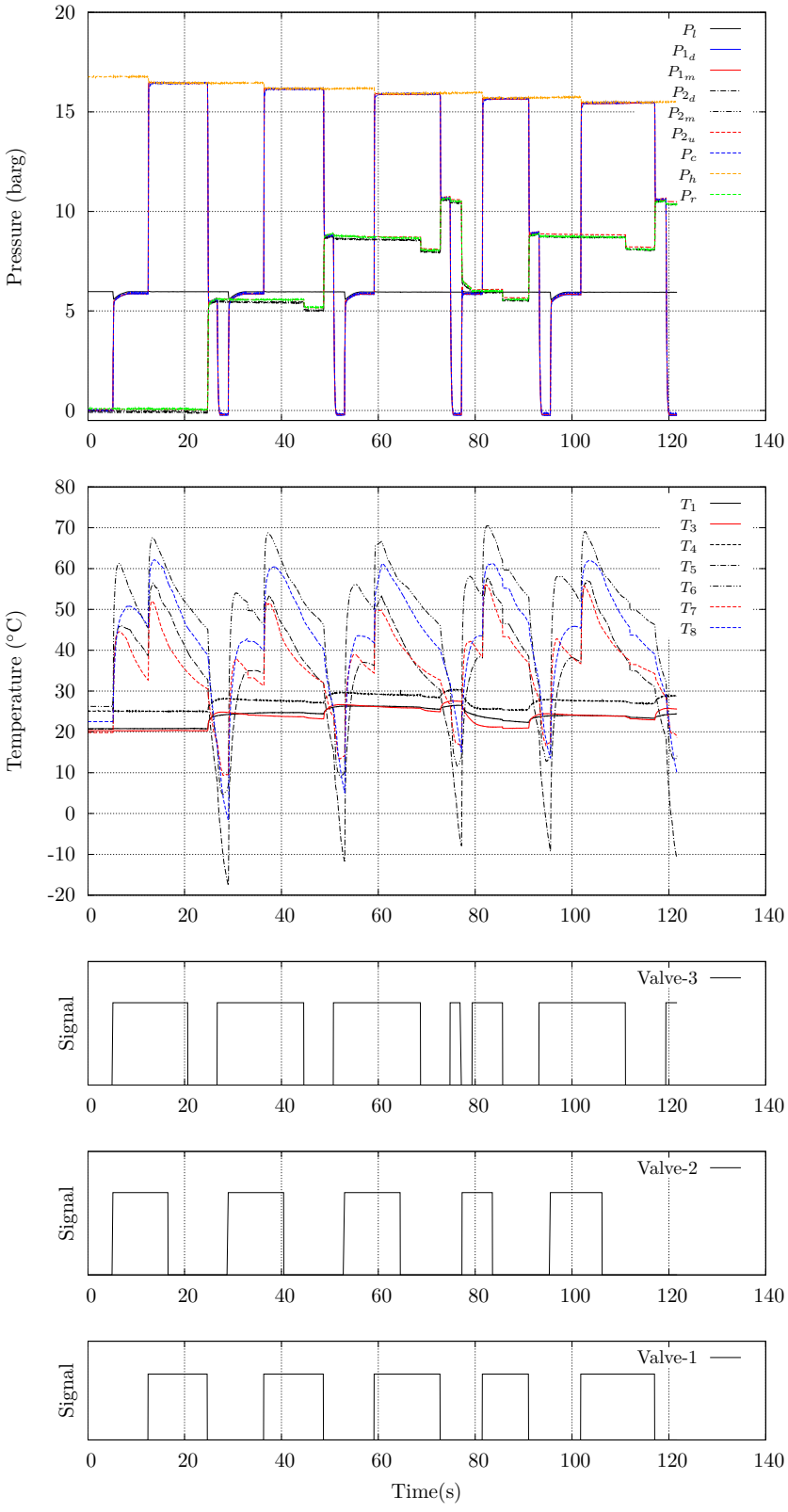

Figure 6.46: Test-25 (refer to table 6.7 on Chapter 6)

6.6 Conclusion

The design of a pneumatic valve manifold typically used in air blowing industrial applications has been presented in this chapter. The dynamics, previously analysed in Chapter 4 from mathematical point of view, is in this case experimentally characterized by applying novel testing techniques. The results clearly stated the need of reviewing the existing set-up, specially when trying to determine the sonic conductance and critical pressure ratio of pneumatic units with an equivalent orifice above 6mm. On the other hand, the validity of the two testing methods could also be demonstrated by means of the CFD model discussed in Chapter 4.

A test rig specially designed to reproduce the air blowing stages usually applied during the manufacturing process of PET bottles is described in detail. The pressure and temperature history along several operating cycles was registered and compared under different configurations. Even though the increase or decrease of the cross-sectional area of the interconnecting pipes was thought to be a parameter affecting the air recovery process, it could be proved that the expansion or reduction towards the chambers did not have a significant impact. Nevertheless the pipe length as well as the death volume of the pneumatic system had a relevant influence on achieving higher recovery rates.

Finally an isothermal recovery vessel was tested under a particular piping lay-out. The minimization of the temperature fluctuation over a series of operating cycles contributed to minimize the pressure decay during the storage time. Reviewing the results obtained in Chapter 5 it could be concluded that the isothermal container ensured a lower heat transfer with the surroundings, and therefore almost eliminate the exergy lost due to heat transfer.

Chapter 7

Synthesis of the mathematical model and conclusion

"Une seule partie de la physique occupe la vie de plusieurs hommes,
et les laisse souvent mourir dans l'incertitude."
Voltaire, *"Élements de la philosophie de Newton" (1843)*

The experimental results discussed in Chapter 5 highlighthed the need of using a compact pneumatic design, which ensures less amount of non-active air in the system and at the same time minimize the required energy to transfer the air between vessels. This chapter, however, will review the values predicted with different mathematical models. All the codes generated for this study were programmed with Fortran language, and reproduced the operating conditions experimentally applied in Chapter 6.

The code is split up into three main subroutines. The first package is able to solve the system of fluid flow governing equations through the pipes by means of the Method of Characteristics. The method, however, is applied under the assumption that the existence of strongs shocks may be neglected. In this case the valve manifold is considered to be a simple flow restriction, therefore the dead volume of the pneumatic unit is not taking into account. On the other hand, the second package applies the same solving method but with the fundamental difference that the fluid properties through the valve manifold are numerically determined. Finally, the last package solves the governing equations at the pipes by using an approximate Riemann solver, which is

also combined with the solving method applied in the second package for the equations governing the valve manifold.

As demonstrated by other authors (309) the geometric characteristics of the pipes inter-connecting different pneumatic components have got a noticeable influence on the pneumatic system response time. The pipes not only have a resistance effect on the dynamic characteristics of a pneumatic cylinder but also the volume effect may be predominant. In our particular case, the volume of the valve manifold and pipes will act as a retardant at each operating cycle.

As a result of the simulations conducted over a wide range of configurations, it was possible to assess the impact of the mathematical model on the recycling process. Those models not only included different solvers for the fluid flow through the interconnecting pipes between the valve manifold and the corresponding vessels, but also for the heat transfer at the air containers.

7.1 Simulation results of the air blowing process

As previously discussed the flow through the valve manifold was originally assessed by an equivalent effective area which had been experimentally measured. When doing so, it could be demonstrated that the correlation between empirical and predicted values was far from being similar, in fact the pressure history from recycling point of view was surprisingly efficient. The reason being was that the dead volume of the valve manifold as well as the dynamics of the operating sequence, under which the valve manifold is usually operated, were not taken into account and obviously played a significant role on the result. Therefore these first attempts were taken as a way to continous searching for a mathematical model which was able to predict the correct pressure characteristics. Based on that premise, the valve manifold was discretized into several internal volumes (refer to Chapter 4), which allowed quantifying the effect over a certain number of cycles.

Figures 7.3 to 7.6 illustrate the pressure characteristics based on different test set-ups. The results demonstrate a fairly clear correlation between the experimental and predicted results when using the Method of Characteristics as well as the HLL solver in combination with the numerical method developed to determine the influence of the

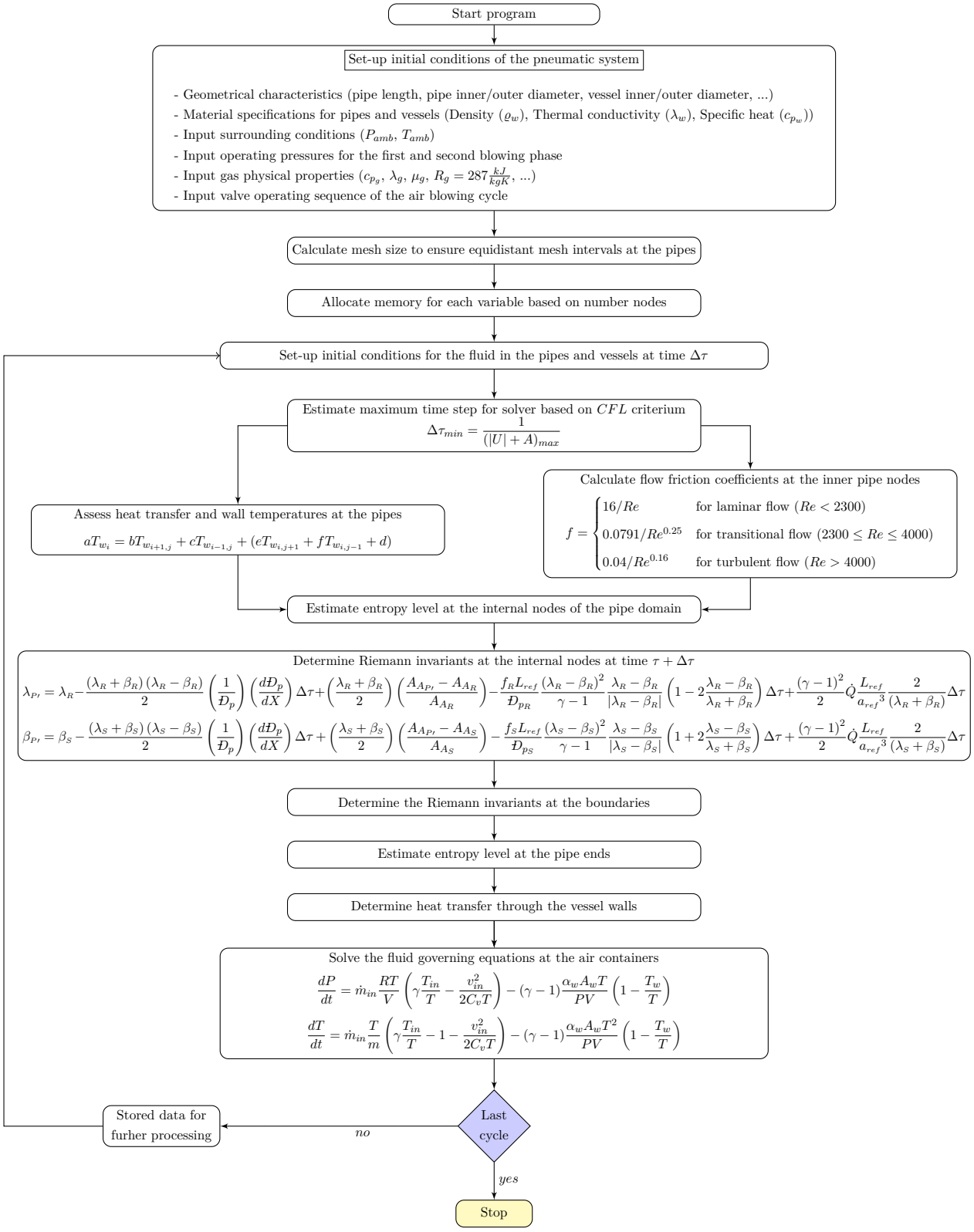

Figure 7.1: Flow chart of the FORTRAN code developed based on the Method of Characteristics

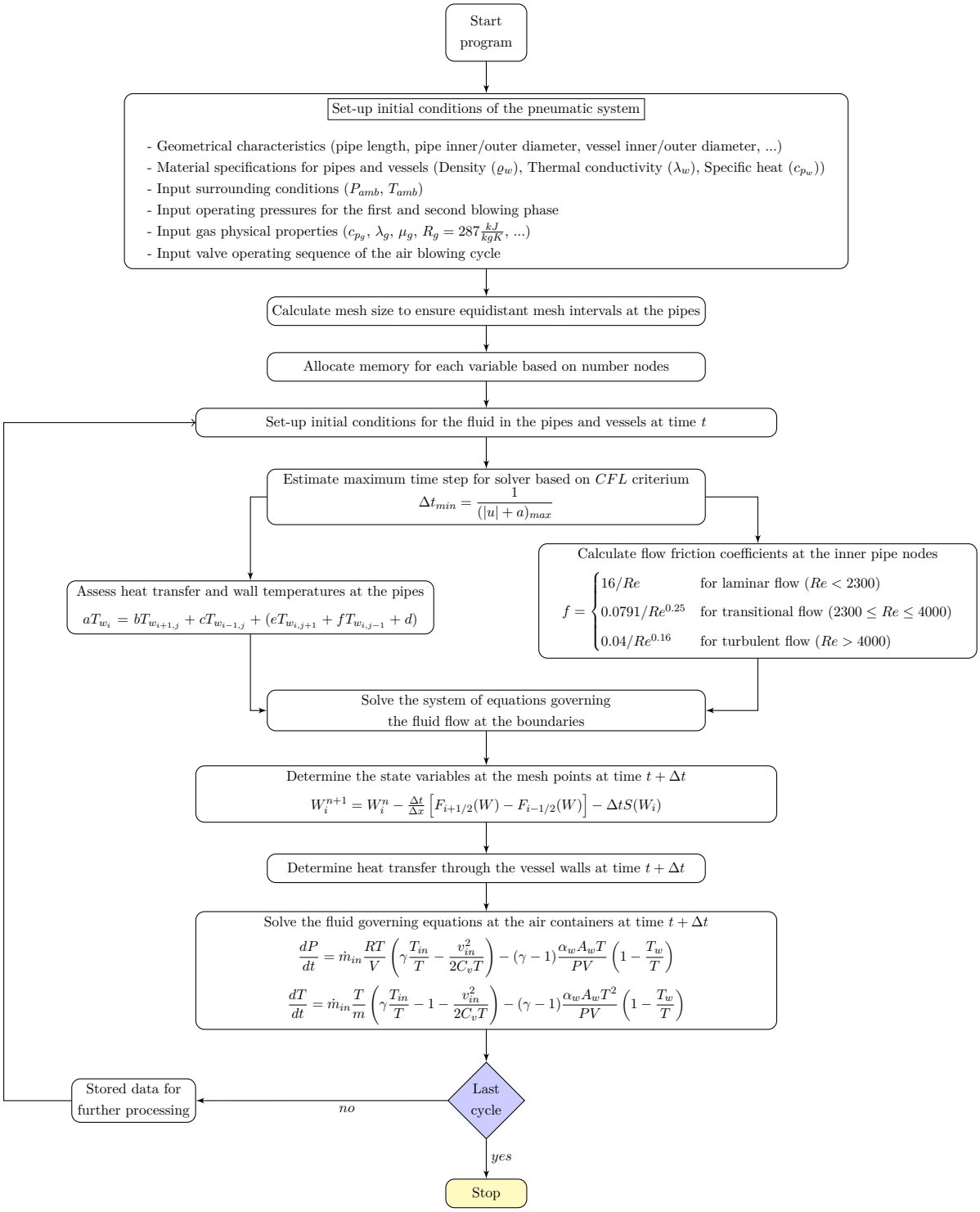

Figure 7.2: Flow chart of the FORTRAN code developed based on the HLL Riemann solver with source terms

valve manifold. On the contrary, when employing non-dimensional parameters (C, b) to estimate the flow between the valve manifold ports, the result differs significantly from the empirical values. It must be noted that this approach was exclusively applied in combination with the Method of Characteristics which is highlighted in blue in the graph legend. From this point, therefore, the discussion will be focused on the results obtained when taking into account the internal volume of the valve manifold.

The progressive increase in pressure experienced within the recycling vessel, after feeding the cavity tank with recycled air, could not be reproduced with any of the solving methods. As discussed in Chapter 5 the inner wall temperature plays a significant role on the heat transfer through the vessel, which tends to decrease as the inner wall gets warmer. Even if the Method of Characteristics provides a more realistic prediction, it is still below the maximum experimental recycling ratio that may be reached with the different pipe configurations. On the other hand this mathematical method faces some difficulties when referring to the stability of the flow at the boundaries. In this case the assumptions applied are not sufficiently consistent since the inner volume where the flow charge and discharge is quite small. On the contrary, the HLL Riemann solver shows a more accurate picture of the phenomenon occurring at the pipe ends joined to the valve manifold, which may be explained by the fact that the kinetic energy at the boundaries was not disregarded. As a matter of fact the pressure fluctuations observed during the simulation of the high pressure blowing phase by the Method of Characteristics were associated to the previous explanation.

On the other hand when changing the state of valve V_3 at the end of the recycling phase, the remaining air in the cavity is exhausted to atmosphere. The empirical results show a transition time which has not been reproduced by the simulation. As a matter of fact this delay was not intentionally generated during the experimental set-up. The reason behind this behavior is based on the fact that the time required to equalize the pressure in the cavity and the recycling vessel was lower than the set-up time given to switch on valve V_3. The mathematical model, however, automatically alters the state of valve V_3 at the time that the pressure in the two tanks becomes the same. This discrepancy is only affecting the cycle time but not the recycling ratio.

All the illustrations indicate a promising correlation between the empirical and pre-

dicted values, however the recycling rate is always below the experimental readings (refer to table 7.1).

Figures 7.7 and 7.8 depict the predicted mean average temperature within the cavity and recycling vessel when using the HLL Riemann solver for the fluid flow at the pipes. The comparison with the empirical results clearly underlines a correct trend, however the heat transfer model was not capable of describing with better precision the temperature values during the charging and discharging process. As a matter of fact the predicted temperature in the cavity vessel cools down below the experimental values during the air discharge.

7.2 Conclusion

The primary intent of this work has been to demonstrate the limitations on improving the efficiency of a standard high-pressure pneumatic application. Specifically, attention has been focused on analyzing an air-blowing PET bottle single-station unit. In pursuing this goal, it has been necessary to apply various mathematical methods in order to learn about the particular aspects of the unsteady flow through the pipes, develop a special valve manifold and later manufacturing, and finally, reproduce the industrial operating conditions, taking into account the existing limitations of our test facility, and monitor the pressure and temperature characteristics under different configurations.

Owing to the wide variety of set-ups that may be considered it must be pointed out that the conclusions drawn here pertain to the tests performed in this work.

The conclusions are:

1. The experimental set-up phase was proved to be capable of reproducing the industrial conditions normally used by the PET plastic bottle manufacturers. The major drawback, associated to the maximum pressure level that could be ensured during the high-pressure air blowing stage, was not an obstacle to validate the functionality of the pneumatic system. Certainly the experimental tests on numerous pneumatic lay-outs helped to prove that the use of tapered pipes with a gradual increase or decrease in diameter, had very little impact on the recovery process. A review of the empirical results highlighted that the more efficient

Recycling pressure rate at different operating cycles (bar)	Test set-up					
	Test-1			Test-56		
	1^{st} cycle	2^{nd} cycle	3^{rd} cycle	1^{st} cycle	2^{nd} cycle	3^{rd} cycle
Experimental	12.37	12.23	12.05	12.27	12.20	12.10
HLL solver	10.78	10.31	10.55	10.32	10.19	10.48
Method of Characteristics	11.67	11.22	11.04	11.31	11.28	11.29
$\% \left[\frac{(HLL-Exp)}{Exp}\right]$	14.75	18.62	14.22	18.9	19.72	15.46
$\% \left[\frac{(MOC-Exp)}{Exp}\right]$	6.00	9.00	9.15	8.49	8.16	7.17

Recycling pressure rate at different operating cycles (bar)	Test set-up					
	Test-26			Test-76		
	1^{st} cycle	2^{nd} cycle	3^{rd} cycle	1^{st} cycle	2^{nd} cycle	3^{rd} cycle
Experimental	12.10	12.29	12.52	12.39	12.35	12.24
HLL solver	10.45	12.12	10.48	11.26	12.16	11.14
Method of Characteristics	10.72	10.63	10.72	11.24	11.69	12.29
$\% \left[\frac{(HLL-Exp)}{Exp}\right]$	15.82	1.40	19.47	10.04	1.56	9.87
$\% \left[\frac{(MOC-Exp)}{Exp}\right]$	12.87	15.62	16.79	10.23	5.65	-0.41

Table 7.1: Comparison of maximum recycling pressure rate according to Test-1, Test-56, Test-26 and Test-76

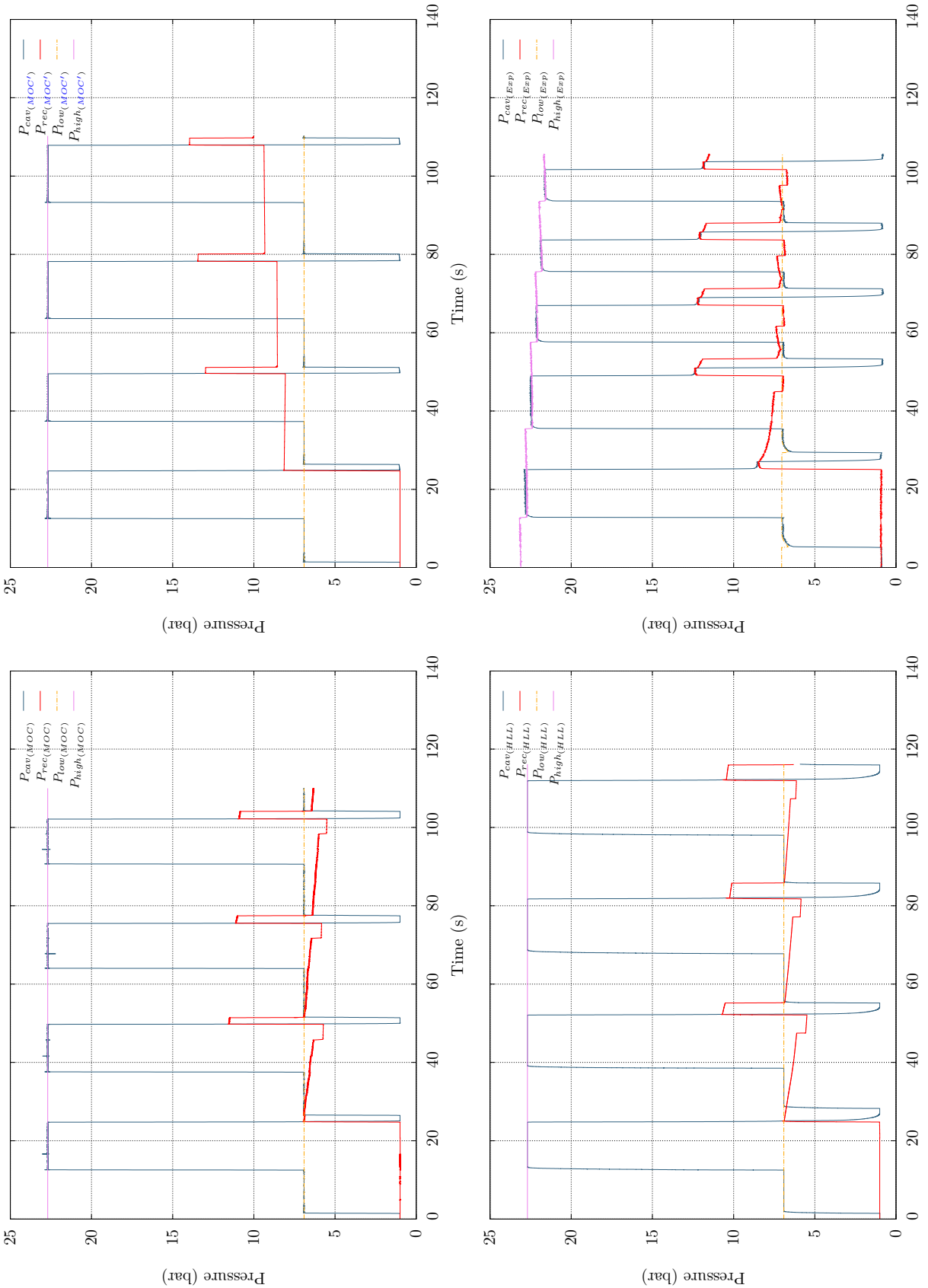

Figure 7.3: Pressure characteristics according to Test-1 (refer to Table 6.7). **HLL**: Subscript that refers to HLL Riemann solver in combination with the valve manifold model, **MOC**: Subscript that refers to Method of Characteristics in combination with the valve manifold model, **exp**: Subscript that refers to the experimental results and **MOC′**: Subscript that refers to the Method of Characteristics in combination with the valve manifold represented by a simple restriction

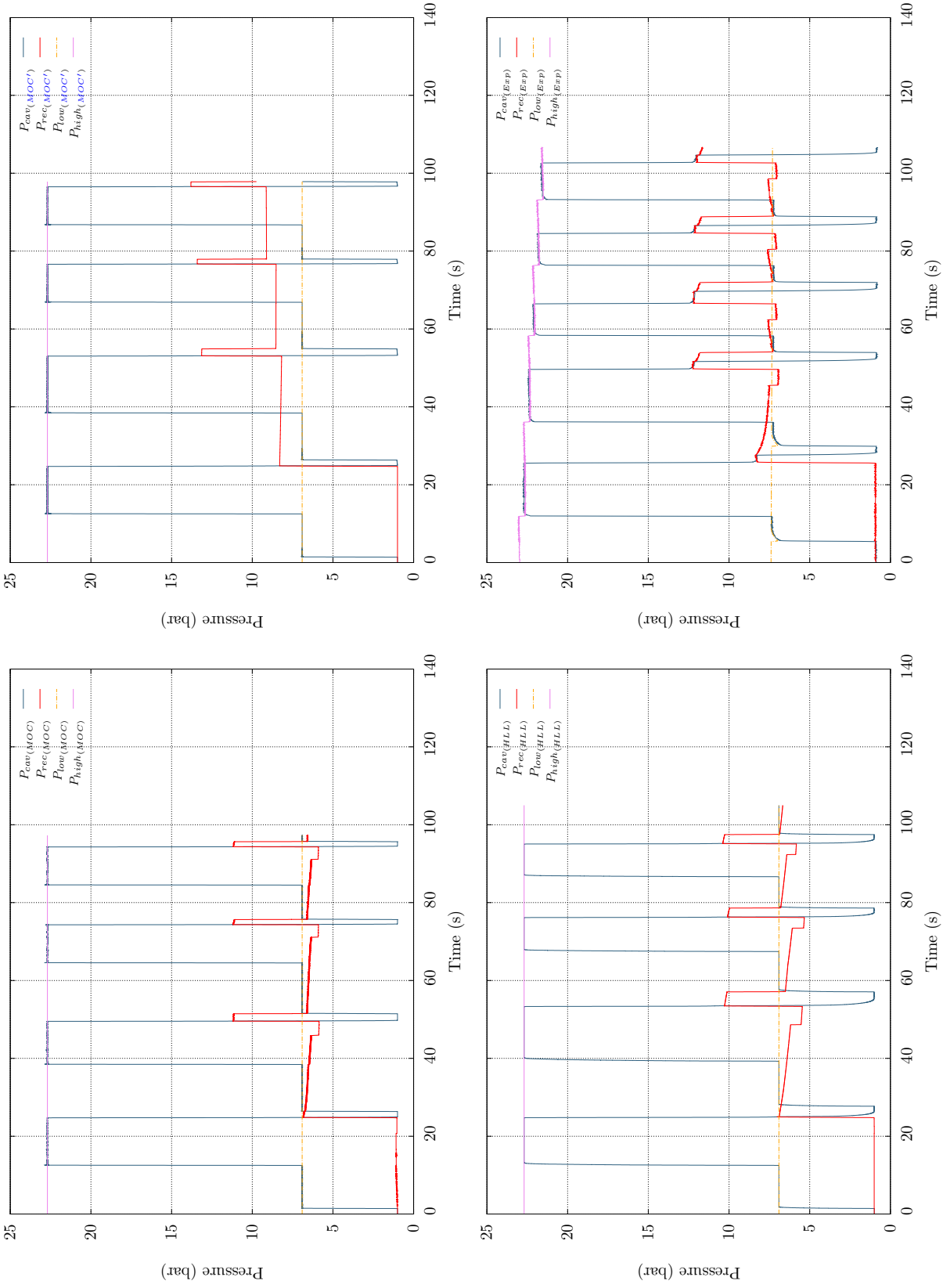

Figure 7.4: Pressure characteristics according to Test-56 (refer to Table 6.7). **HLL**: Subscript that refers to HLL Riemann solver in combination with the valve manifold model, **MOC**: Subscript that refers to Method of Characteristics in combination with the valve manifold model, **exp**: Subscript that refers to the experimental results and **MOC'**: Subscript that refers to the Method of Characteristics in combination with the valve manifold represented by a simple restriction

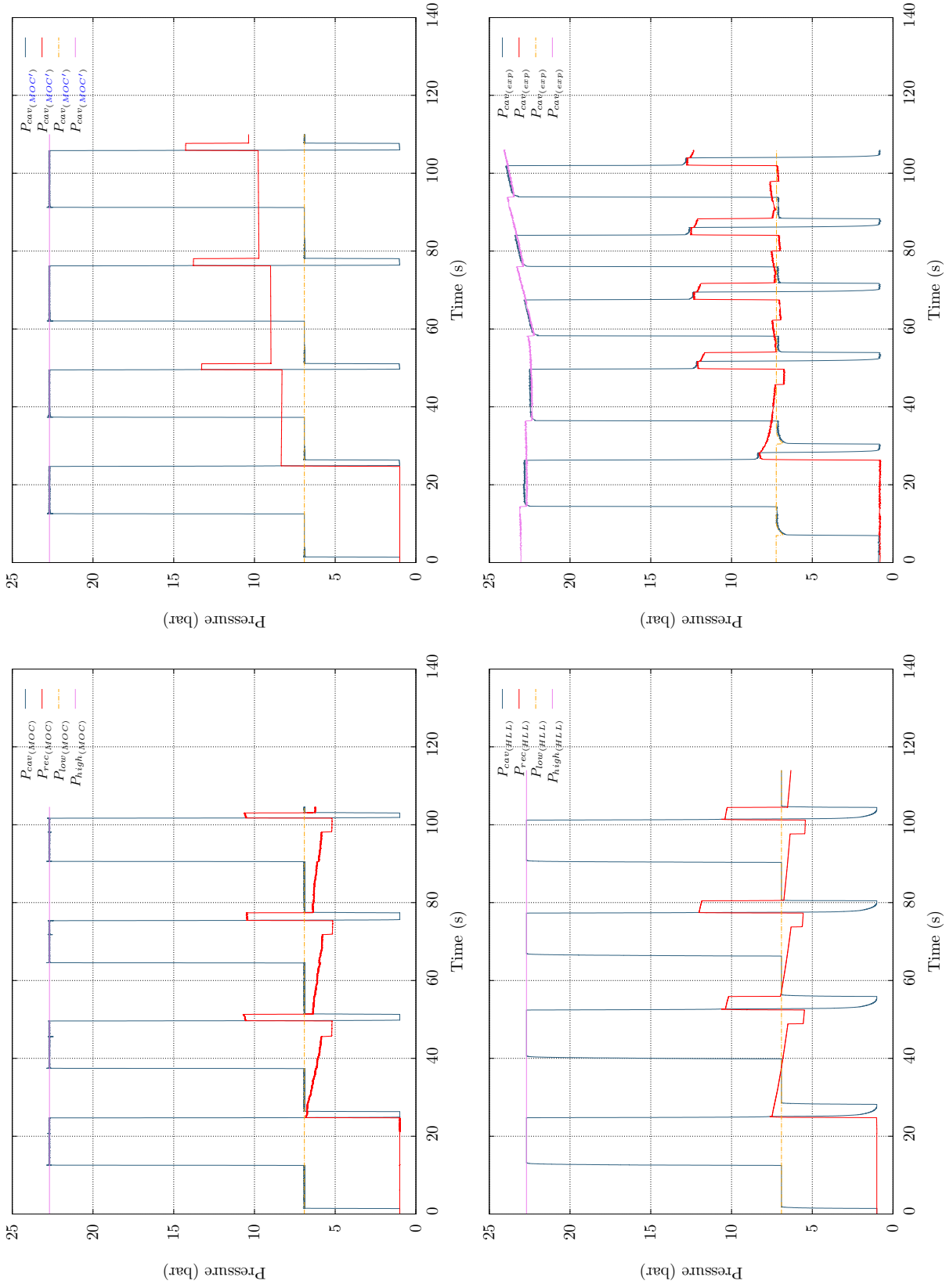

Figure 7.5: Pressure characteristics according to Test-26 (refer to Table 6.7). **HLL**: Subscript that refers to HLL Riemann solver in combination with the valve manifold model, **MOC**: Subscript that refers to Method of Characteristics in combination with the valve manifold model, **exp**: Subscript that refers to the experimental results and **MOC'**: Subscript that refers to the Method of Characteristics in combination with the valve manifold represented by a simple restriction

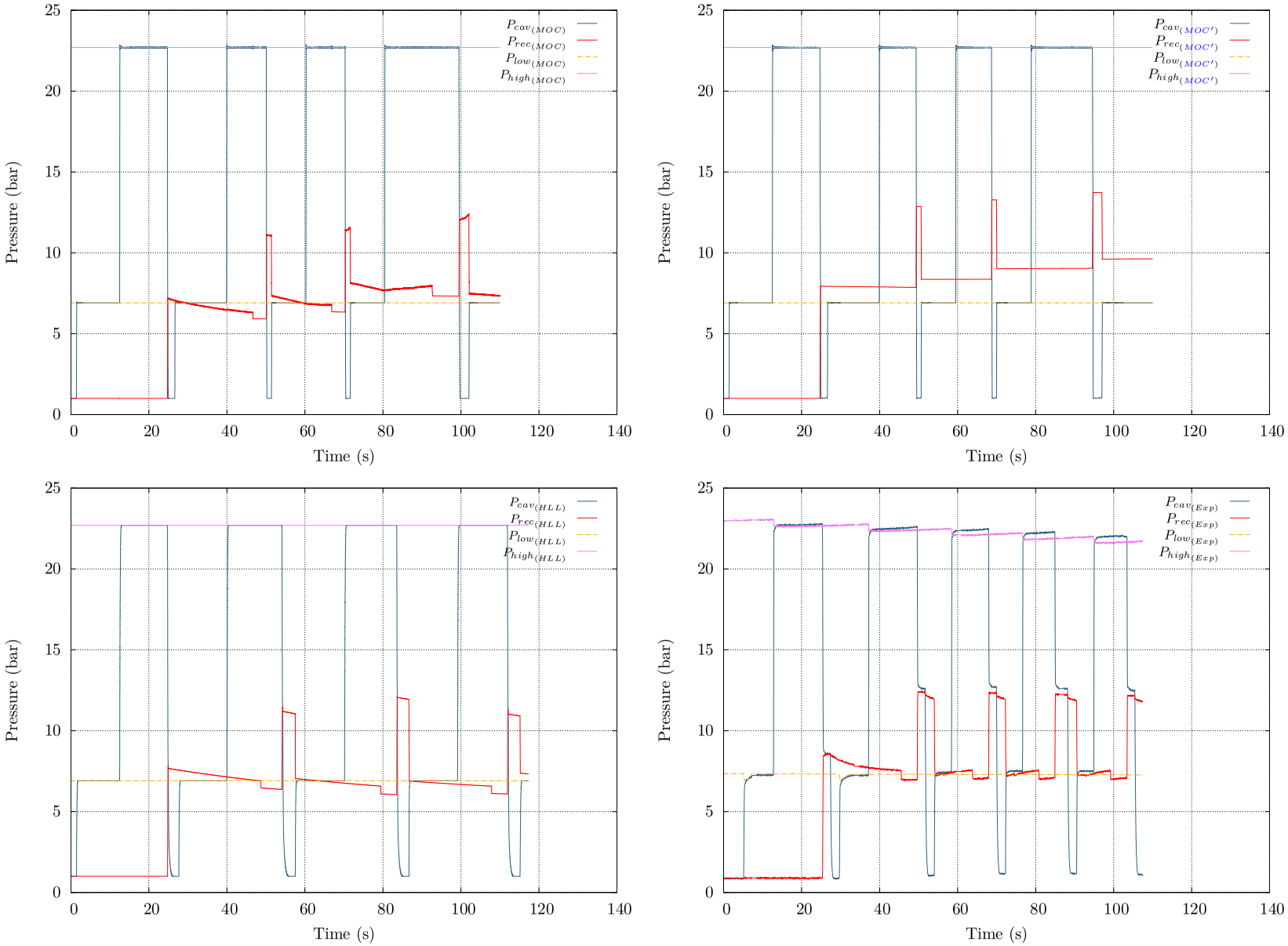

Figure 7.6: Pressure characteristics according to Test-76 (refer to Table 6.7). **HLL**: Subscript that refers to HLL Riemann solver in combination with the valve manifold model, **MOC**: Subscript that refers to Method of Characteristics in combination with the valve manifold model, **exp**: Subscript that refers to the experimental results and **MOC′**: Subscript that refers to the Method of Characteristics in combination with the valve manifold represented by a simple restriction

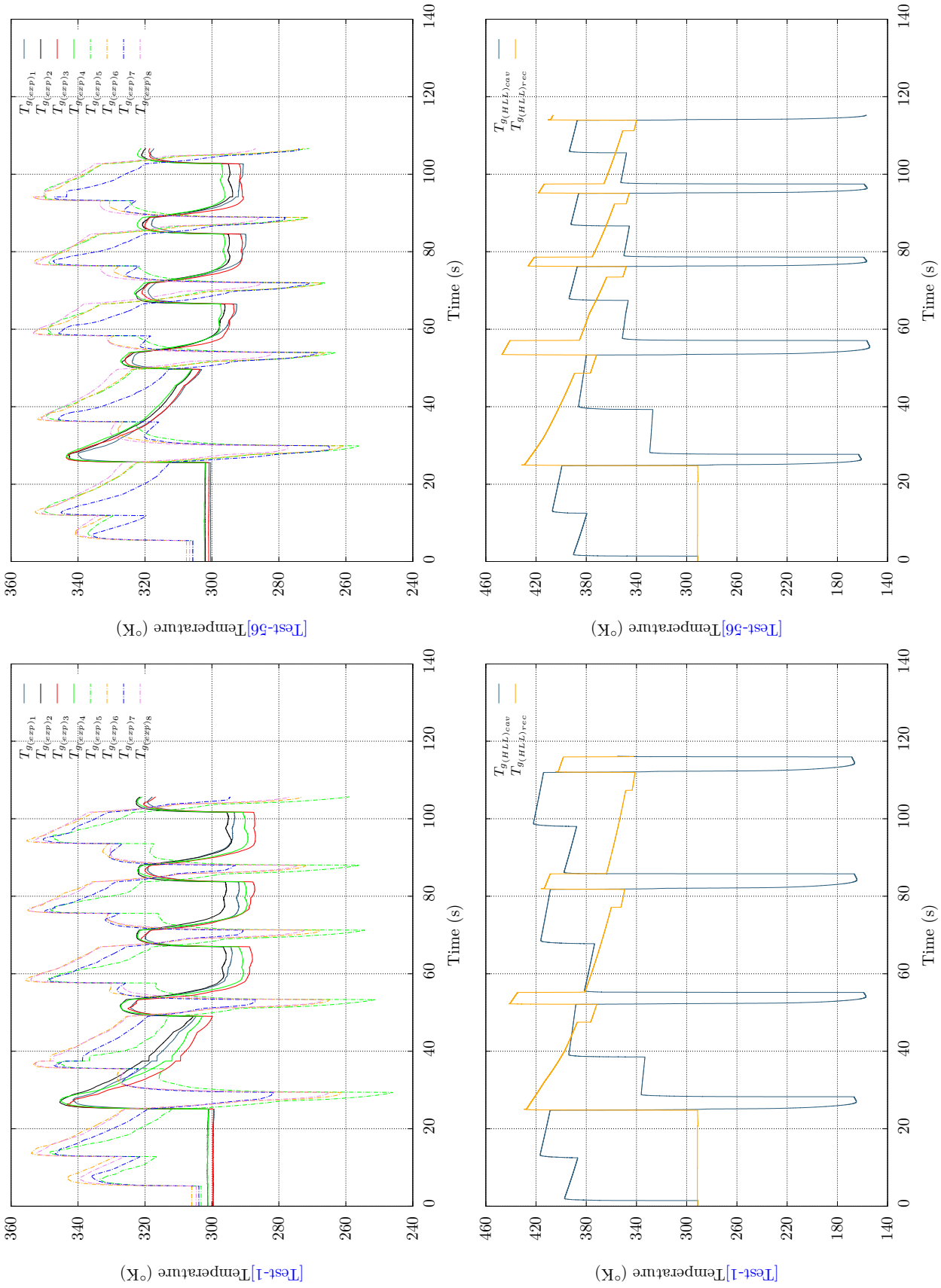

Figure 7.7: Temperature characteristics within the cavity and recycling vessel for Test-1 and Test-56 (refer to Table 6.7). **HLL**: Subscript that refers to HLL Riemann solver in combination with the valve manifold model, **exp**: Subscript that refers to the experimental results

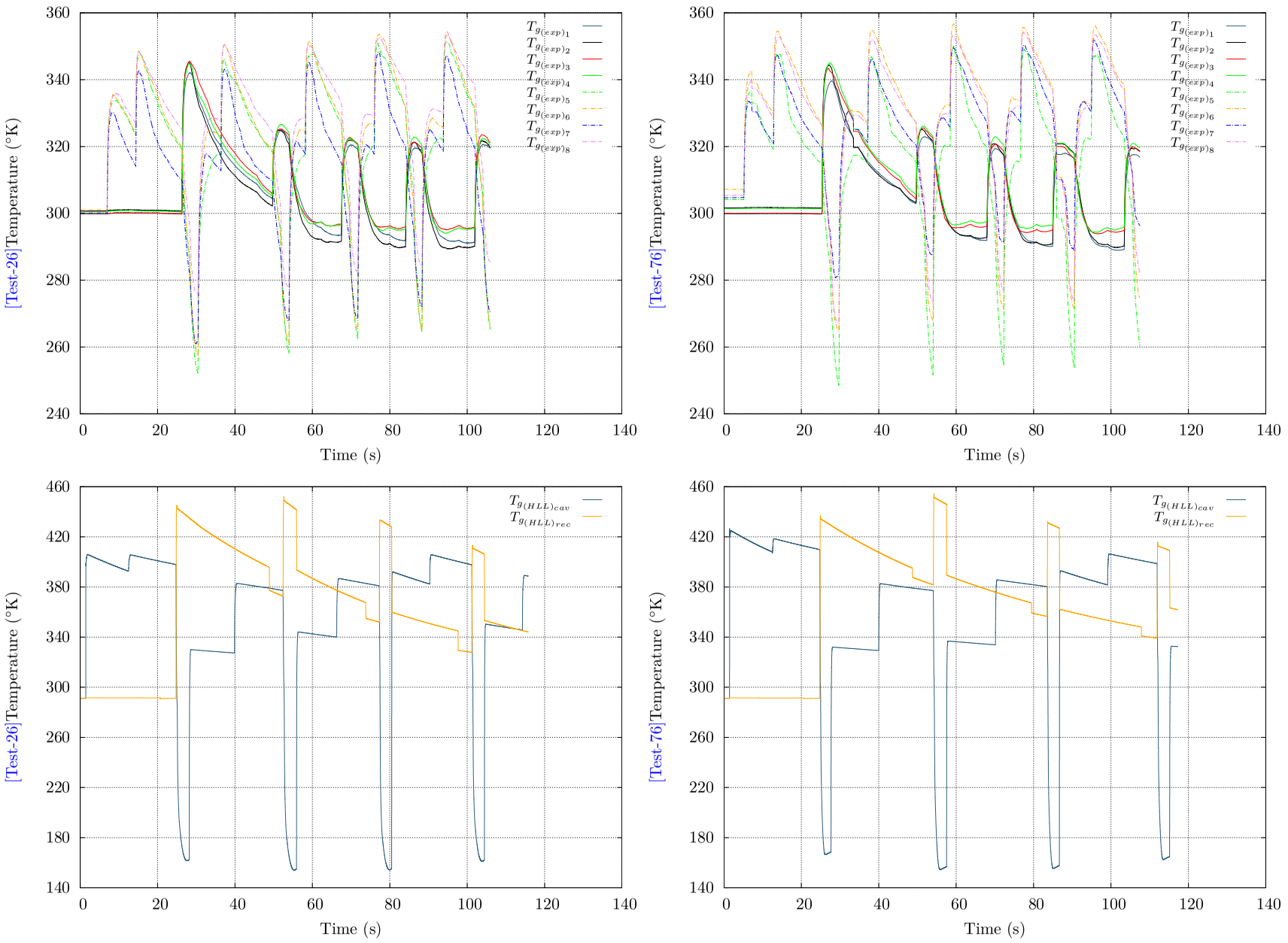

Figure 7.8: Temperature characteristics within the cavity and recycling vessel for Test-26 and Test-76 (refer to Table 6.7). **HLL**: Subscript that refers to HLL Riemann solver in combination with the valve manifold model, **exp**: Subscript that refers to the experimental results

configuration was the one that combined shorter tubes for the air blowing line as well as for the air recovery line. That solution also ensured less heat transfer and pressure losses through the interconnecting pipes.

2. The pressure history during the air-blowing experiments exhibited a clear dependence on the heat transfer through the vessel walls and, more significantly, through the walls of the connecting pipes. Based on the fact that the energy loss through the vessel walls has a significant influence on the available energy, the idea of using an isothermal recovery tank was put forward. The experiments conducted on the isothermal recovery vessel exhibited an excellent result, which contributed to minimize the heat transfer and, therefore, the pressure decay during the storage time.

3. As demonstrated, the amount of recycled air supplied to the cavity vessel during the low-pressure air blowing phase, allowed avoiding the use of a low-pressure compressor. It must be noticed that the air recovery ratio could feed the air blowing line during the low pressure stage after the first operating cycle. This solution, therefore, ensures a high efficiency rate, however it must be kept in mind that in case of increasing the cavity volume (bottle) the recycling line must also experience a percentage increase in order to balance the pressure/volume rate between both.

4. The design of a valve manifold including air recovery port could be successfully accomplished and revealed the strong impact on the pressure characteristics over a certain number of operating cycles. From this last point, it could be concluded that the manifold could not be considered as a simple restriction for the air flow and the internal design plays a very important role on the amount air that can be recovered.

5. The numerical models demonstrated to be in agreement with the experimental data, specially when coupling the unsteady fluid flow governing equations at the pipes with the set of equations ruling the pressure and temperature characteristics within the valve manifold. Nevertheless the simulation of the air blow test set-up became a complex task. The different variants used to reproduce the experimental conditions ended up concluding that the more reliable mathematical

model was the HLL Riemann solver accompanied by the resolution of the equations governing the flow through the valve manifold. The misalignment observed when using the Method of Characteristics were associated to the effectiveness of the assumptions applied to the boundary conditions. As a matter of fact the pressure characteristics became very irregular when increasing the pipe diameter.

6. The simple discharge method was proved to be a powerful tool to determine the sonic conductance and critical pressure ratio of a pneumatic component, however in our particular case due to the size of the tank it also exposed certain constraints specially when exceeding sizes over 6mm in equivalent diameter. Alternatively, finite element analysis was considered to be a fair approximation to estimate the discharge coefficient through the valve openings. The correlation of the simulated values with the experimental results obtained with calibrated orifices confirmed the efficacy of the calculation method.

7.3 Suggestions for future work

This dissertation has been devoted to the study of a particular industrial process and other fields could be also investigated, however based on the above-mentioned outputs the author suggests to continue searching on the following areas:

1. Implementing a mathematical model which couples 3D fluid flow through the valve manifold and 1D fluid flow at the pipes. The main inconvenients found when applying the Method of Characteristics could be overtaken by those numerical techniques.

2. An extension of the previous point including real gas effects on the equation of state should be discussed.

3. Additionally the need of reconsidering the valve manifold design in order to go for a more compact solution with the same technical specifications poses several challenges. A concept that would avoid using pipes to connect the valve manifold with the neighbouring pneumatic components would reduce the existing dead volume and will guarantee less energy losses, however the feasibility of such proposals always face problems related to the characteristics of each particular machine

design. This approach, should also be accompanied by a series of experimental tests that will help to monitor the pressure and temperature characteristics in the inner volumes of the valve manifold.

4. In parallel, and based on the fact that the air recovery phase does not add a significant delay to the total cycle time, a second recycling stage might be taken into consideration. This additional process would be directly influenced by the vessel size, since once the pressure equalizes at the cavity and recycling vessel respectively, the remaining air in the cavity vessel should be delivered to a second recycling tank, and depending on the cavity volume the second recycling stage will become meaningless.

5. Further tests should be performed with various isothermal tanks in order to confirm the validity of the method when trying to determine the sonic conductance and critical pressure ratio of pneumatic components with similar size to the valve manifold used in this work or greater.

Chapter 8

Appendix A

8.1 Governing equations at the pipe ends when applying the Method of Characteristics

Based on the fact that the flow through the pipe end or restriction can be considered as quasi-steady, the following expressions are derived taking into account the different conditions that may be arised at the pipe end.

1. Flow from the pipe to the chamber through a partially open end:

   (a) Subsonic flow:

   Based on the fact that the flow at the pipe end is considered to be isentropic, the following equation is obtained when assuming that no pressure recovery will take place between the pipe end and the chamber.

   Building the governing equations between the end pipe and the chamber, it results,

$$u_p = \frac{2}{\gamma - 1} a_0 (p_i - p_r) \tag{8.1}$$

$$u_t^2 - u_p^2 = \frac{2}{\gamma - 1} a_0^2 \left[(p_i + p_r - 1)^2 - p_t^2 \right] \tag{8.2}$$

$$\frac{u_p}{u_t} = \phi \left(\frac{p_t}{p_i + p_r - 1} \right)^5 \tag{8.3}$$

   where equation (8.1) refers to the particle velocity in the pipe, equation (8.2) is the Bernoulli's equation from pipe to port, and similarly equation (8.3) corresponds to the continuity equation from pipe to port. In this case, the

subscripts i and r refer to incident and reflected pressure wave at the pipe end respectively.

Therefore using the notation $A = \frac{u_p}{a_0 p_c}$, $b = \frac{p_i + p_r - 1}{p_c}$, and $t = \frac{2p_i - 1}{p_c}$, and substituting in the previous system of equations, it reduces to,

$$5(t^2 - 2bt + b^2)b^{10} - 5(t^2 - 2bt + b^2)\phi^2 - \phi^2 b^2 + \phi^2 = 0 \tag{8.4}$$

(b) Sonic flow:
Similarly to the previous case but assuming that the throat velocity equals the local acoustic velocity as well as the no pressure recovery condition between between the throat and the chamber, the following expression is derived,

$$\phi = \frac{216}{25}\left(\frac{t}{b} - 1\right)\left(\frac{1}{1 + 5\left(\frac{t}{b} - 1\right)^2}\right)^3 \tag{8.5}$$

(c) Sonic threshold:
By using the particle velocity, continuity and energy equations the following expression can be obtained,

$$5\left(t - \left(\frac{36 - 25t^2}{5}\right)^{\frac{1}{2}}\right)\left(t + \left(\frac{36 - 25t^2}{5}\right)^{\frac{1}{2}}\right) = 36^3\phi \tag{8.6}$$

2. Flow from the chamber to the pipe through a partially open end:

(a) Subsonic flow:
The equations that describe the gas flow into the pipe are shown below:

$$u_p = \frac{2}{\gamma - 1} a_0 (p_r - p_i) \tag{8.7}$$

$$u_t^2 = \frac{2}{\gamma - 1} a_0^2 \left[p_c^2 - p_t^2\right] \tag{8.8}$$

$$u_t^2 - u_p^2 = \frac{2}{\gamma - 1} a_0^2 p_t^2 \left(\frac{1}{\phi}\frac{u_p}{u_t}\left(\frac{p_i + p_r - 1}{p_t}\right)^{\frac{2\gamma}{\gamma - 1}} - 1\right) \tag{8.9}$$

$$u_t(u_t - u_p) = \frac{5}{7}\frac{a_0^2}{\phi} p_t^2 \left[\left(\frac{p_i + p_r - 1}{p_t}\right)^{\frac{2\gamma}{\gamma - 1}} - 1\right] \tag{8.10}$$

Rearranging the above equations, it yields to the following system of non-linear equations that must be solved simultaneously,

$$\frac{\phi\xi}{5}\left(\xi^2 - 25b^2 + 50bt - 25t^2\right)\left(1 - \frac{\xi^2}{5}\right)^{\frac{5}{2}} - 5(b-t)b^7 + \phi\xi\left(1 - \frac{\xi^2}{5}\right)^{\frac{7}{2}} = 0 \quad (8.11)$$

$$\frac{7\phi}{5}\left(\xi^2 - 5\xi b + 5\xi t\right)\left(1 - \frac{\xi^2}{5}\right)^{\frac{5}{2}} - b^7 + \left(1 - \frac{\xi^2}{5}\right)^{\frac{7}{2}} = 0 \quad (8.12)$$

(b) Sonic flow:
Once again operating the system equations used for the subsonic case plus the sonic condition at the throat, we obtain:

$$\frac{5b^7(b-t)}{\phi\left(\frac{5}{6}\right)^3} + 5(b-t)^2 - 1 = 0 \quad (8.13)$$

(c) Sonic threshold:
From the momentum and energy equations it can be determined that,

$$t = \left(\left((1-\psi)\frac{7\phi}{5} + 1\right)^{\frac{1}{7}} - \frac{\psi}{5}\right)\left(\frac{5}{6}\right)^{\frac{1}{2}} \quad (8.14)$$

where

$$\psi = \left(\frac{(7\phi+5) \pm (5(1-\phi)(19\phi+5))^{\frac{1}{2}}}{12\phi}\right) \quad (8.15)$$

Note that $t = \dfrac{2p_i - 1}{p_c} = \dfrac{\lambda_p}{p_c}$ and $b = \dfrac{\lambda_p + \beta_p}{2p_c}$, can also be expressed as a function of the pseudo-Riemann invariants.

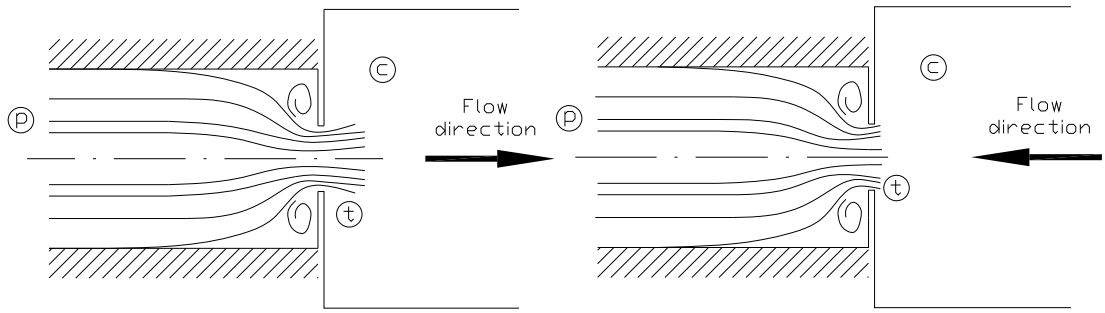

(a) Outflow through a partially open end **(b)** Inflow through a partially open end

Figure 8.1: Flow characteristics at the pipe end

Chapter 9

Appendix B

9.1 Calibration method for measuring equipment

9.1.1 Termocouples calibration

All thermocouples were calibrated in the actual environment in which they would be used. Figure 9.1 shows the test lay-out. The calibration method was based on reading the thermocouple signal at two reference temperatures, which were the boiling and freezing points respectively. A thermally stabilised bath was filled with distilled water and once the targeted temperature was reached, the thermocouples were submerged into the bath and the measurements were logged by the data acquisition unit. The thermocouples were then immersed to a depth sufficient to overcome heat losses or gains, but always preserving them for being to close to the heating source, which was applied on the lower side of the glass enclosure. Additionally the welded wires were carefully spaced to avoid any interaction with other thermocouples as well as with the sides of the walls of the enclosure.

Table 9.6 shows the results of the calibration carried out on the thermocouples that were used to monitor the gas temperature inside the vessels at each working cycle. The temperature values varied between 0°C to 100°C and were measured with a reference thermometer which was previously calibrated with a Platinum Resistance Thermometer. Three calibrated thermothers were used to determine the accuracy of the thermocouples and the results of the calibration are shown below:

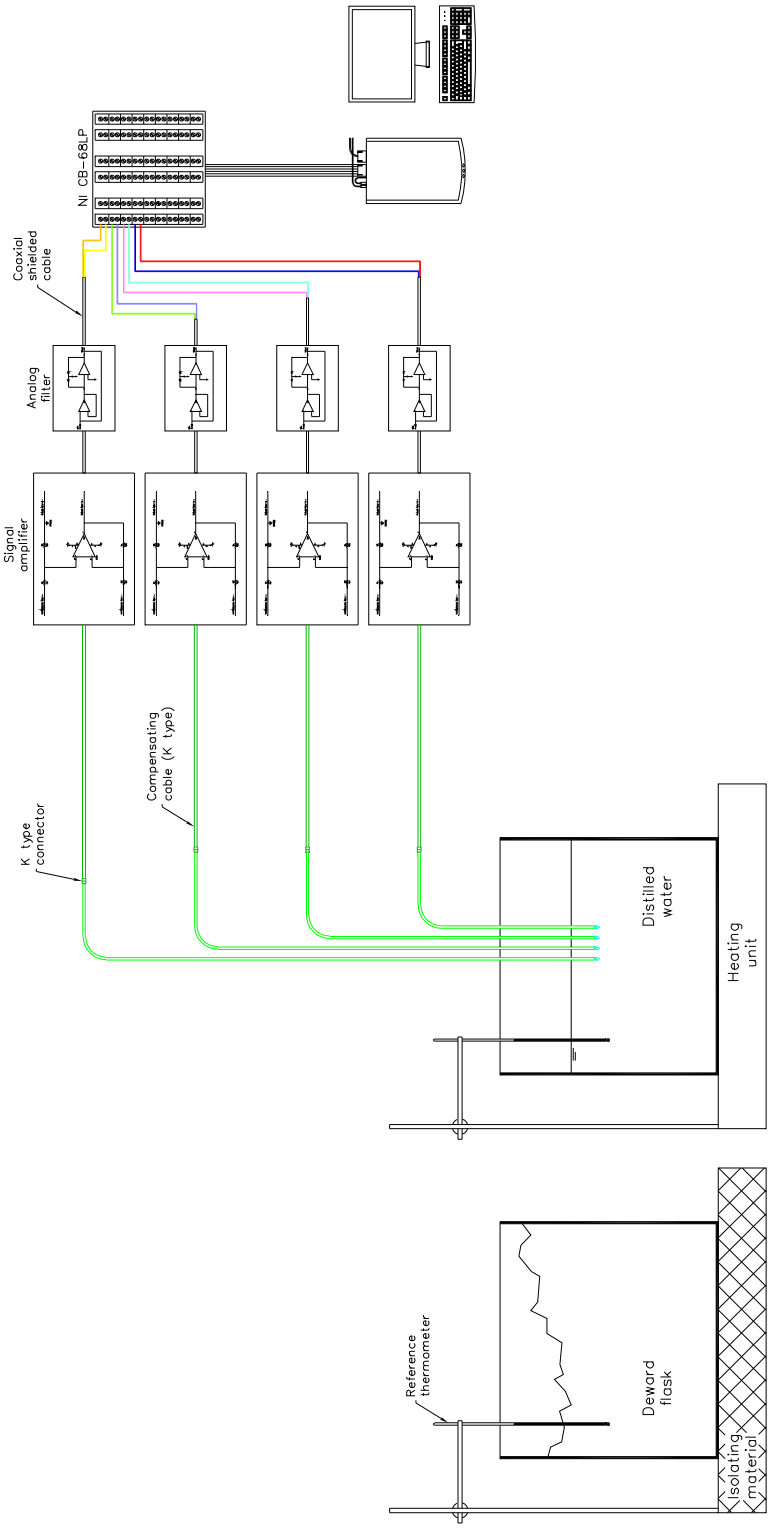

Figure 9.1: Termocouple calibration schematic set-up

T_{ref}	Reference Thermomether A (liquid-in-glass thermometer)				
(°C)	1^{st} reading	2^{nd} reading	Average value	Correction value	Uncertainty
0.10	0.0	0.0	0.0	0.1	±1.2
49.84	51.0	51.0	51.0	-1.2	±1.2
100.53	102.0	102.0	102.0	-1.5	±1.2

Table 9.1: Calibration of reference Thermomether A
(Scale division: 2°C / Resolution: 1°C)

T_{ref}	Reference Thermomether B (liquid-in-glass thermometer)				
(°C)	1^{st} reading	2^{nd} reading	Average value	Correction value	Uncertainty
-10.12	-10.0	-10.0	-10.0	-0.1	±0.59
49.84	50.5	50.5	50.5	-0.7	±0.60
100.52	101.5	101.5	101.5	-1.0	±0.60

Table 9.2: Calibration of reference Thermomether B
(Scale division: 1°C / Resolution: 0.5°C)

T_{ref}	Reference Thermomether C (liquid-in-glass thermometer)		
(°C)	Average value	Correction value	Uncertainty
20.0	20.5	-0.5	± 0.8
50.0	51.0	-1.0	± 0.8
100.0	102.0	2.0	± 0.8

Table 9.3: Calibration of reference Thermomether C
(Scale division: 1°C / Resolution: 0.5°C)

T_{ref}	Reference Thermomether D (thermocouple probe)				
(°C)	1^{st} reading	2^{nd} reading	Average value	Correction value	Uncertainty
0.16	1.8	1.8	1.8	-1.64	±0.50
20.19	21.0	21.0	21.0	-0.81	±0.50
49.82	50.2	50.2	50.2	-0.38	±0.50
99.75	98.0	98.0	98.0	-1.75	±0.50

Table 9.4: Calibration of reference Thermomether D (Scale division: 0.1°C)

9. APPENDIX B

T_{ref}	Reference Thermomether E (liquid-in-glass thermometer)				
(°C)	1^{st} reading	2^{nd} reading	Average value	Correction value	Uncertainty
49.86	50.0	50.0	50.0	-0.1	±0.2
69.30	69.3	69.3	69.3	0.0	±0.2
80.37	80.1	80.1	80.1	0.3	±0.2
90.34	90.1	90.1	90.1	0.2	±0.2
100.54	99.9	99.9	99.9	0.6	±0.2

Table 9.5: Calibration of reference Thermomether E (Scale division: 0.1°C)

The determination of the calibration curve allowed assessing the thermocouples precision in an oil bath (refer to figure 9.2). The unit consisted of a metal furnace were the thermocouples were immersed. The temperature in the bath was internally regulated and sequentially varied in order to read the thermocouple signal within the range in which the thermocouples will work during the charging and discharging process.

T_{ref}	Samples							
(°C)	T1	T2	T3	T4	T5	T6	T7	T8
0	0.035949	-0.042579	-0.058064	-0.291454	-0.024391	-0.274036	0.005711	-0.291491
0	0.03563	-0.042378	-0.058166	-0.29164	-0.024107	-0.274124	0.005901	-0.291746
0	0.035602	-0.042496	-0.058203	-0.291599	-0.024341	-0.27409	0.005842	-0.291817
100	0.453572	0.372026	0.357215	0.125739	0.390918	0.147281	0.419769	0.126673
100	0.450806	0.369576	0.35448	0.122971	0.387939	0.143672	0.415792	0.12264
100	0.449702	0.368793	0.353314	0.122016	0.387971	0.143716	0.415292	0.122582

Table 9.6: Calibration emf's of thermocouples at the freezing and boiling point of distilled water (values in mV)

(a) Calibration of the thermocouples by immersion in de-ionised water

(b) Thermocouples immersed in an oil-bath

Figure 9.2: Calibration of self-manufactured thermocouples

T_{ref}	Temperature readings																			
(°C)	25	44	45	46	47	48	49	50	51	52	53	54	57	60	61	69				
T1	25.01	44.15	45.29	46.50	47.53	48.50	49.38	50.37	51.45	52.39	53.44	54.48	57.59	60.64	61.70	69.58				
T2	24.66	44.89	45.90	46.93	47.85	48.72	49.61	50.60	51.77	52.73	53.79	54.91	58.01	60.81	61.63	70.32				
T3	24.71	44.10	45.15	46.22	47.21	48.08	48.95	49.94	51.04	51.94	53.05	54.14	57.29	60.38	61.08	69.41				
T4	24.43	43.97	45.05	46.14	47.17	48.17	49.05	50.11	51.16	52.21	53.29	54.35	57.43	60.38	61.06	69.32				
T5	24.44	43.53	44.66	45.78	46.83	47.83	48.97	50.00	51.11	52.17	53.30	54.37	57.41	60.46	61.46	69.53				
T6	23.79	43.85	44.82	45.85	46.88	47.76	48.86	49.83	50.96	52.00	53.13	54.13	57.22	60.29	61.28	69.33				
T7	24.86	43.60	44.61	45.73	46.84	47.79	48.96	49.99	51.19	52.17	53.31	54.39	57.60	60.72	61.69	69.63				
T8	24.33	43.91	44.85	45.93	46.96	47.81	48.91	49.87	51.07	52.09	53.24	54.30	57.31	60.52	61.49	69.32				

T_{ref}	Temperature readings																			
(°C)	70	71	74	76	78	79	81	83	85	87	88	89	90	91	93	100				
T1	70.12	71.51	73.75	75.91	77.93	79.21	81.19	83.03	85.22	87.34	88.41	89.63	90.38	91.44	93.50	100.37				
T2	70.73	72.14	74.74	76.83	78.87	80.08	82.18	84.05	86.14	88.25	89.36	90.52	91.32	92.42	94.54	101.45				
T3	69.66	71.16	73.49	75.63	77.64	78.82	80.85	82.98	85.15	87.11	88.17	88.99	90.09	91.30	93.56	100.80				
T4	70.25	71.73	74.20	76.34	78.25	79.36	81.39	83.35	85.58	87.53	88.65	89.43	90.52	91.83	93.93	101.27				
T5	70.38	71.93	74.22	76.23	78.06	79.29	81.41	83.57	85.50	87.53	88.62	89.66	90.78	91.97	94.19	100.67				
T6	70.09	71.61	74.16	76.15	78.17	79.24	81.40	83.45	85.18	87.36	88.45	89.42	90.50	91.78	93.93	100.32				
T7	70.54	71.87	74.16	76.25	78.20	79.44	81.47	83.45	85.56	87.53	88.78	89.71	90.93	91.92	94.27	100.85				
T8	70.20	71.69	73.92	75.86	77.93	79.00	81.15	83.25	84.94	87.17	88.30	89.29	90.43	91.56	93.71	100.28				

Table 9.7: Oil-bath measurements for calibrated thermocouples

9.1.2 Pressure sensors calibration

The sensors that helped to monitor the static and dynamic pressure at different locations of the test set-up were calibrated with a reference pressure gauge (Range: 0-10 bar, accuracy ±0.5% F.S.; Range: 0-100 bar, accuracy ±2.5% F.S.). The readings of the sensors were registered by a Labview code while an oleohydraulic circuit pumped oil to the reference gauge as well as to the pressure sensors. The results are shown in the following chart.

P_{ref}	Pressure sensors readings								
(bar)	P_{cav}	$P_{down_{cav}}$	$P_{mid_{cav}}$	$P_{up_{cav}}$	$P_{down_{rec}}$	$P_{mid_{rec}}$	$P_{up_{rec}}$	P_{high}	P_{rec}
0	0.004013	0.004016	0.004018	0.004011	0.003981	0.004014	0.004025	0.003979	0004019
10	0.005668	0.00567	0.00567	0.005656	0.005651	0.005655	0.005683	0.005625	0.005632
20	0.007186	0.007232	0.007236	0.007183	0.007196	0.007262	0.007231	0.007208	0.007208
30	0.008784	0.0088	0.00876	0.008724	0.0088	0.008815	0.008814	0.008768	0.008762
40	0.010385	0.010367	0.010376	0.010274	0.010373	0.010432	0.010387	0.010372	0.010398
50	0.012038	0.012008	0.012004	0.011966	0.012035	0.012045	0.012042	0.012008	0.012034

Table 9.8: Calibration emf's of pressure sensors (values in mA)
(Output signal: 4-20mA; Thread: G1/8"; Calibrated range: 0-50bar)

P_{ref}	Pressure sensor readings	
(bar)	P_{low}	P_{iso}
0	0.028932	-0.012947
1	1.095321	1.065046
2	2.094805	2.052205
3	3.081971	3.048545
4	4.084866	4.03344
5	5.093109	4.997559
6	6.090742	6.034932
7	7.101642	7.059902
8	8.092758	8.056147
9	9.088256	9.045396
10	9.999695	–

Table 9.9: Calibration emf's of pressure sensors (values in VDC)
(Output signal: 0-10VDC; Thread: G1/2"; Calibrated range: 0-10bar)

The calibration results for the piezoelectirc pressure sensors are detailed below:

P_{ref}	Pressure sensor readings		
(bar)	P_{piezo_1}	P_{piezo_2}	P_{piezo_3}
0	-0.0035485	-0.0161049	-0.0140753
10	0.3078588	-0.2864312	0.3042907
20	0.6070868	0.5857490	0.6055752
30	0.9026917	0.8760004	0.9138874
40	1.1965970	1.1671672	1.2152269
50	1.5014699	1.4625244	1.5207766

Table 9.10: Calibration emf's of pieozoelectric pressure sensors (values in VDC) (Sensitivity: 10V/5000pC; Adaptor thread: M10; Calibrated range: 0-50bar)

Note that the subindex is associated to the location of each sensor within the test lay-out described in Chapter 6.

Chapter 10

Appendix C

10.1 Thermodynamic properties of the fluid

Regarding the thermophysical properties of the air the table below shows the necessary parameters to be used.

Physical properties - Air	
At/mol wt (kg/mol): 28.966	Critical temperature (K): 132.6
Gas constant (kJ/kgK): 0.287040	Critical pressure (MPa): 3.77

$c_{p_{air}} = \sum \left[B\,(N)\,T^N\right]$	$\lambda_{air} = \sum \left[C\,(N)\,T^N\right]$
	Temperature range: $250 < T < 1050K$
$A(0) = 0.103409E + 1$	$C(0) = -2.276501E - 3$
$A(1) = -0.2848870E - 3$	$C(1) = 1.2598485E - 4$
$A(2) = 0.7816818E - 6$	$C(2) = -1.4815235E - 7$
$A(3) = -0.4970786E - 9$	$C(3) = 1.73550646E - 10$
$A(4) = 0.1077024E - 12$	$C(4) = -1.066657E - 13$

$\mu_{air} = \sum \left[B\,(N)\,T^N\right]$	
Temperature range: $250 \leqslant T < 600K$	Temperature range: $250 \leqslant T \leqslant 1050K$
$B(0) = -9.8601E - 1$	$B(0) = 4.8856745$
$B(1) = 9.080125E - 2$	$B(1) = 5.43232E - 2$
$B(2) = -1.17635575E - 4$	$B(2) = -2.4261775E - 5$
$B(3) = 1.2349703E - 7$	$B(3) = 7.9306E - 9$
$B(4) = -5.7971299E - 11$	$B(4) = -1.10398E - 12$
$B(5) = 0.0$	$B(5) = 0.0$
$B(6) = 0.0$	$B(6) = 0.0$

Chapter 11

Appendix D

11.1 Overview of experimental results

This section includes the experimental resultsall the tests conducted in order to determine the variation of the physical properties of the fluid at different locations of the pneumatic set-up. The subindex given to the each sensor at detailed below:

Pressure sensor	Description
$P_1 = P_{t_{low}}$	Low pressure supply line
$P_2 = P_{t_{down}}$	Transducer localed near the valve manifold at the pipe connected between valve manifold and cavity tank
$P_3 = P_{t_{middle}}$	Transducer positioned midway between the valve manifold and the cavity tank
$P_4 = P_{t_{up}}$	Transducer localed near the cavity tank
$P_5 = P_{t_{down}}$	Transducer localed near the valve manifold at the pipe connected between valve manifold and recycling tank
$P_6 = P_{t_{middle}}$	Transducer positioned midway between valve manifold and recycling tank
$P_7 = P_{t_{up}}$	Transducer localed near the recycling tank
$P_8 = P_{t_{cav}}$	Transducer positioned on the rear cover of the cavity tank
$P_9 = P_{t_{high}}$	High pressure supply line
$P_{10} = P_{t_{rec}}$	Transducer positioned on the rear cover of the recycling tank

Table 11.1: Nomenclature of each pressure transducer within the test set-up

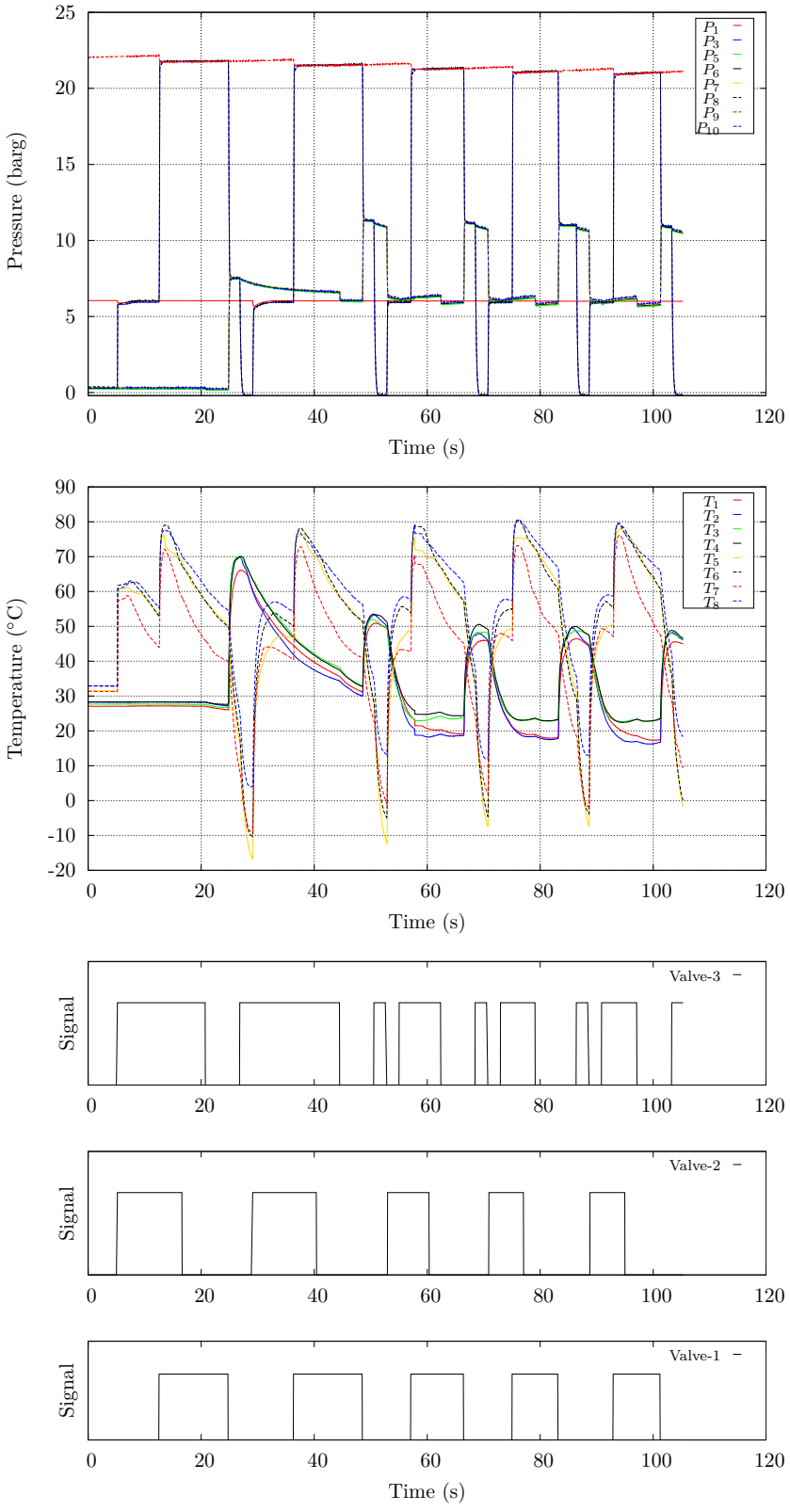

Figure 11.1: Test-36 (refer to table 6.7)

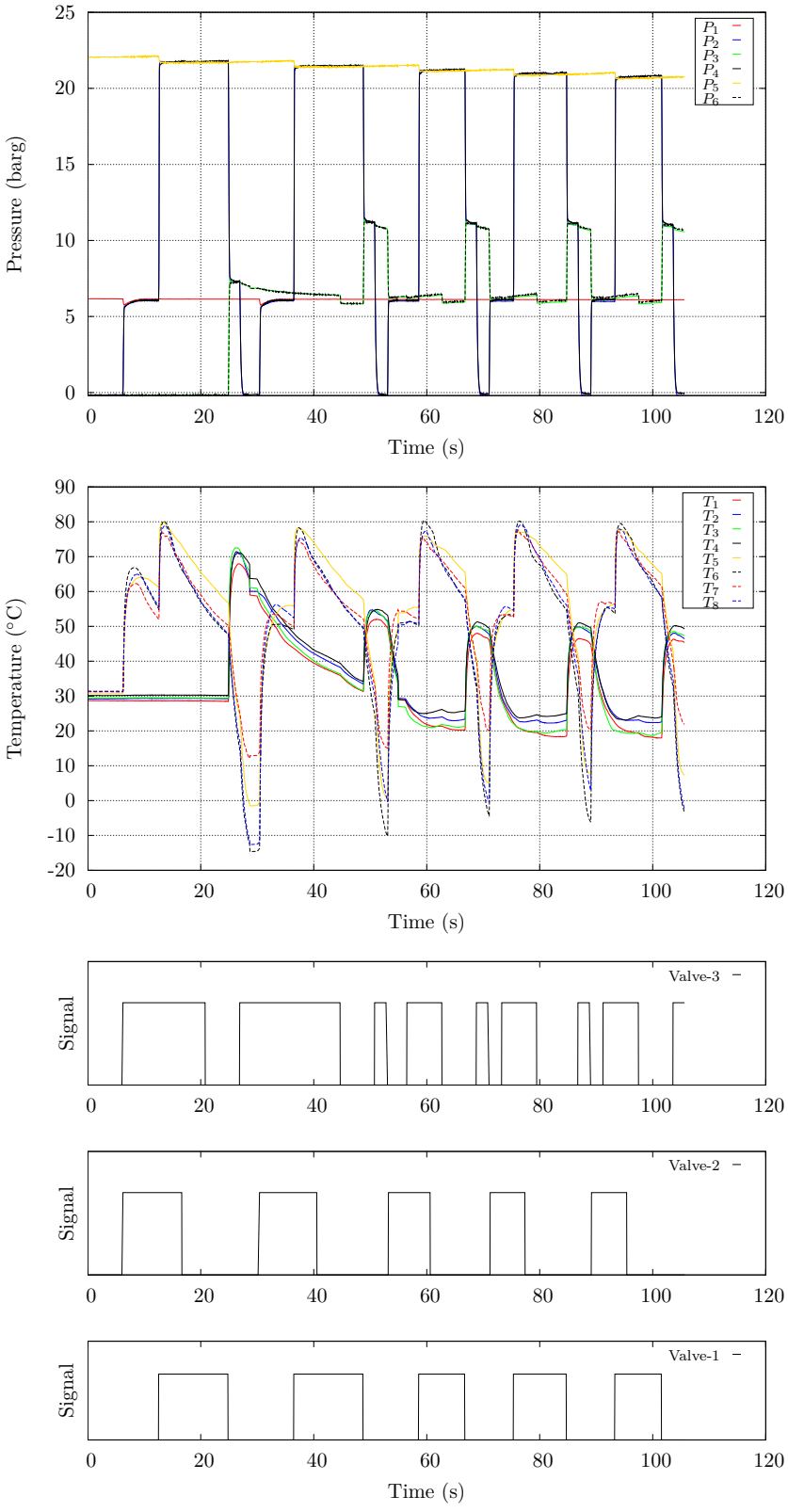

Figure 11.2: Test-57 (refer to table 6.7)

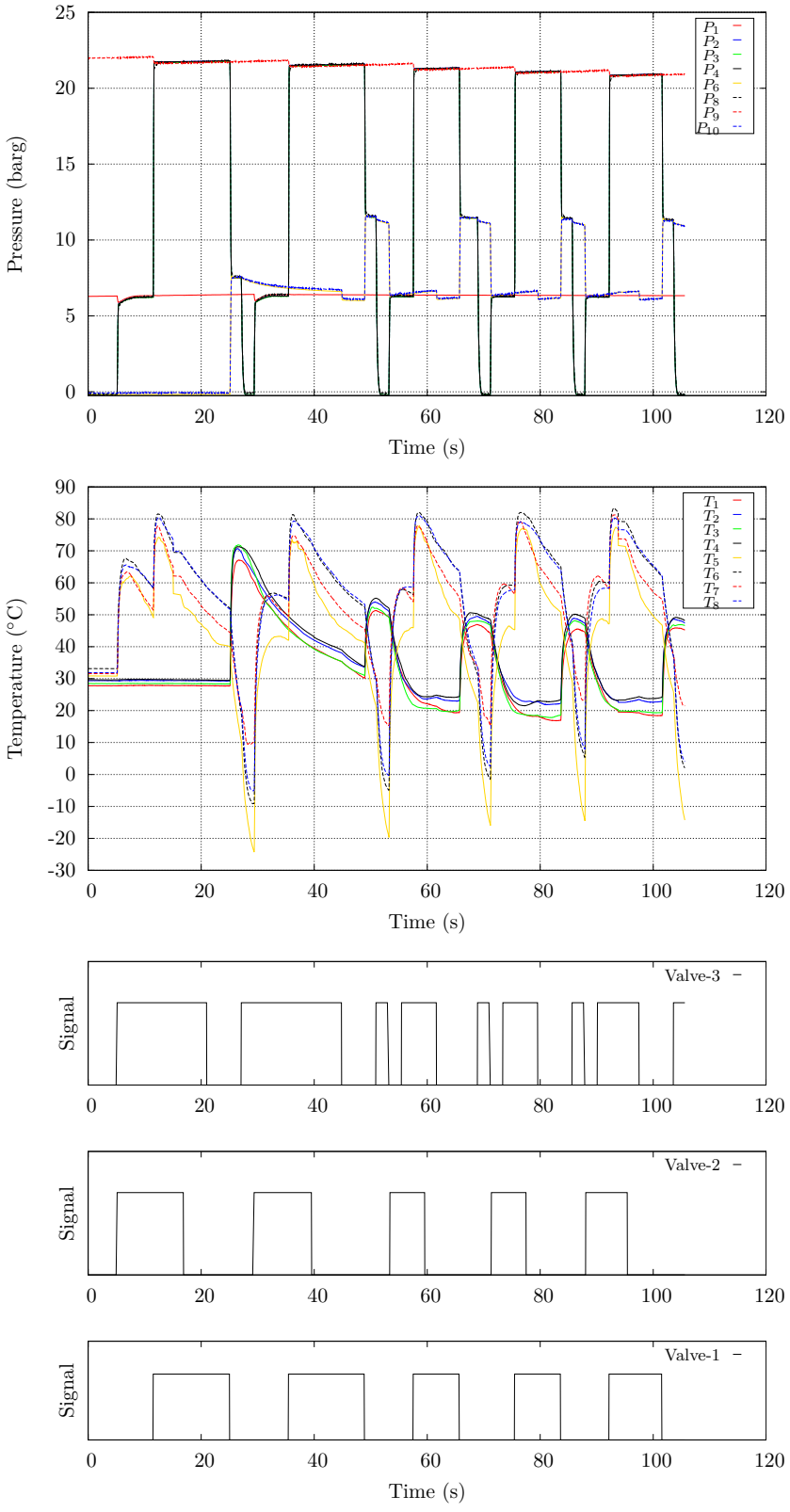

Figure 11.3: Test-56 (refer to table 6.7)

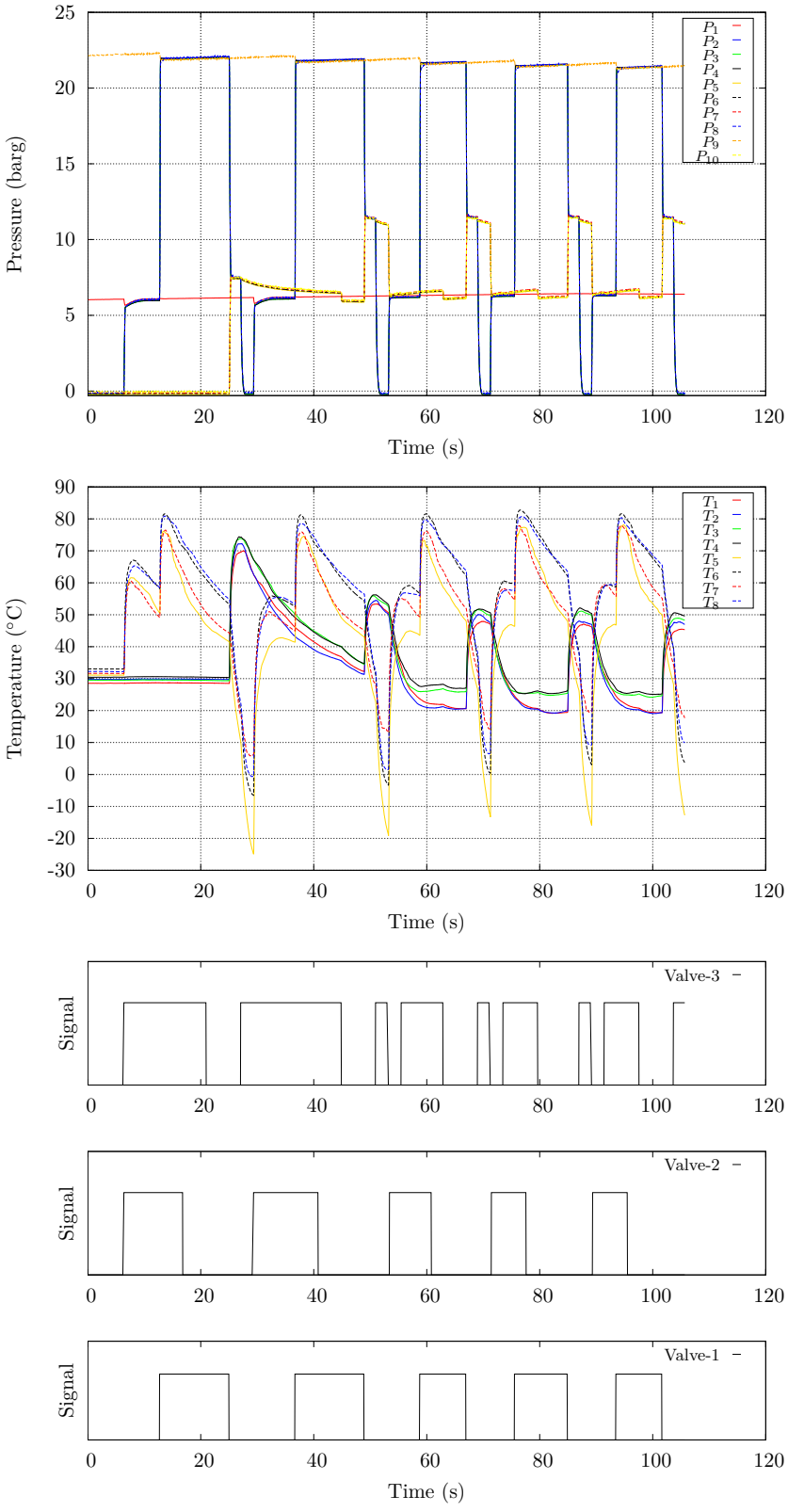

Figure 11.4: Test-25 (refer to table 6.7)

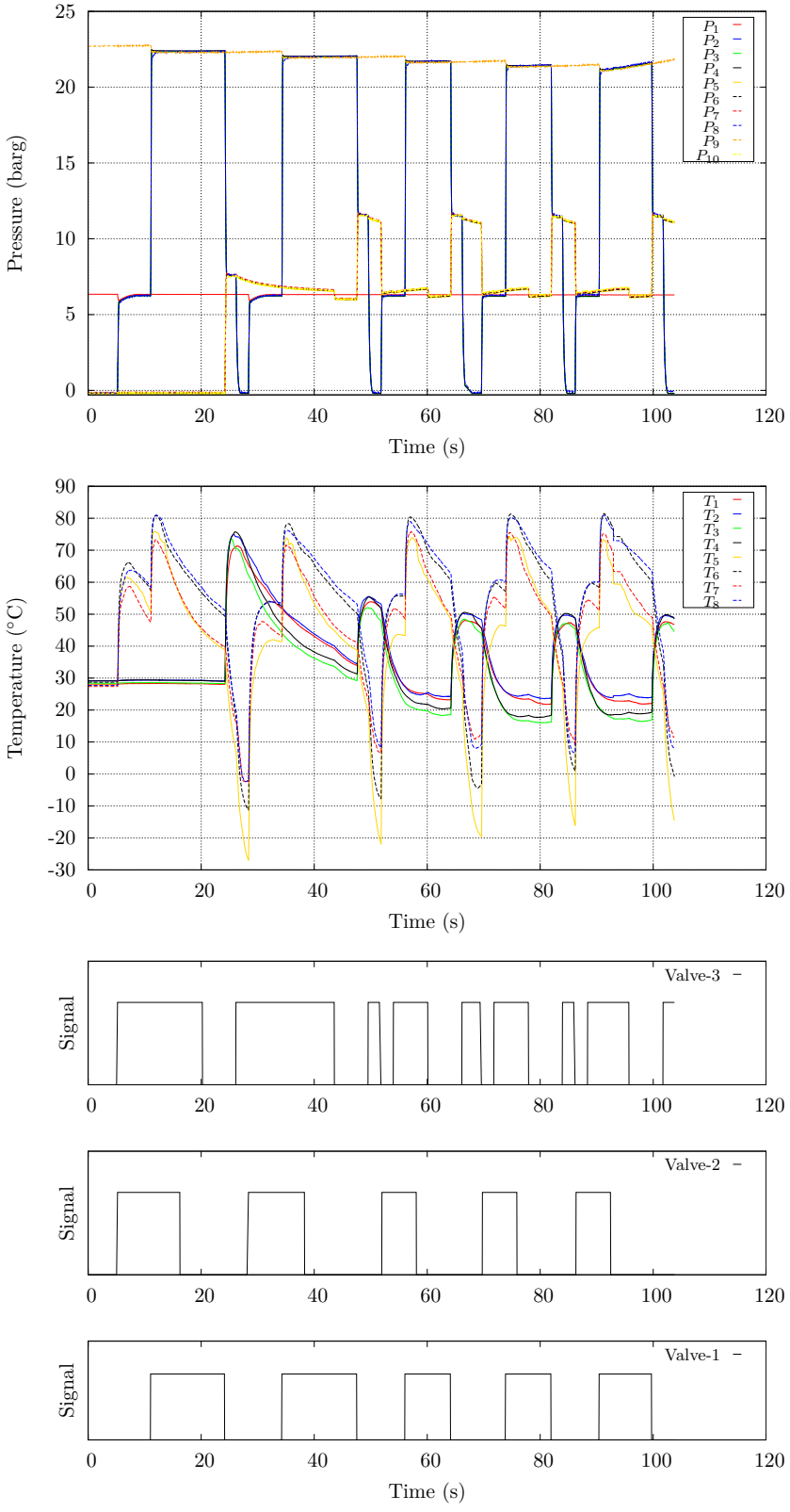

Figure 11.5: Test-3 (refer to table 6.7)

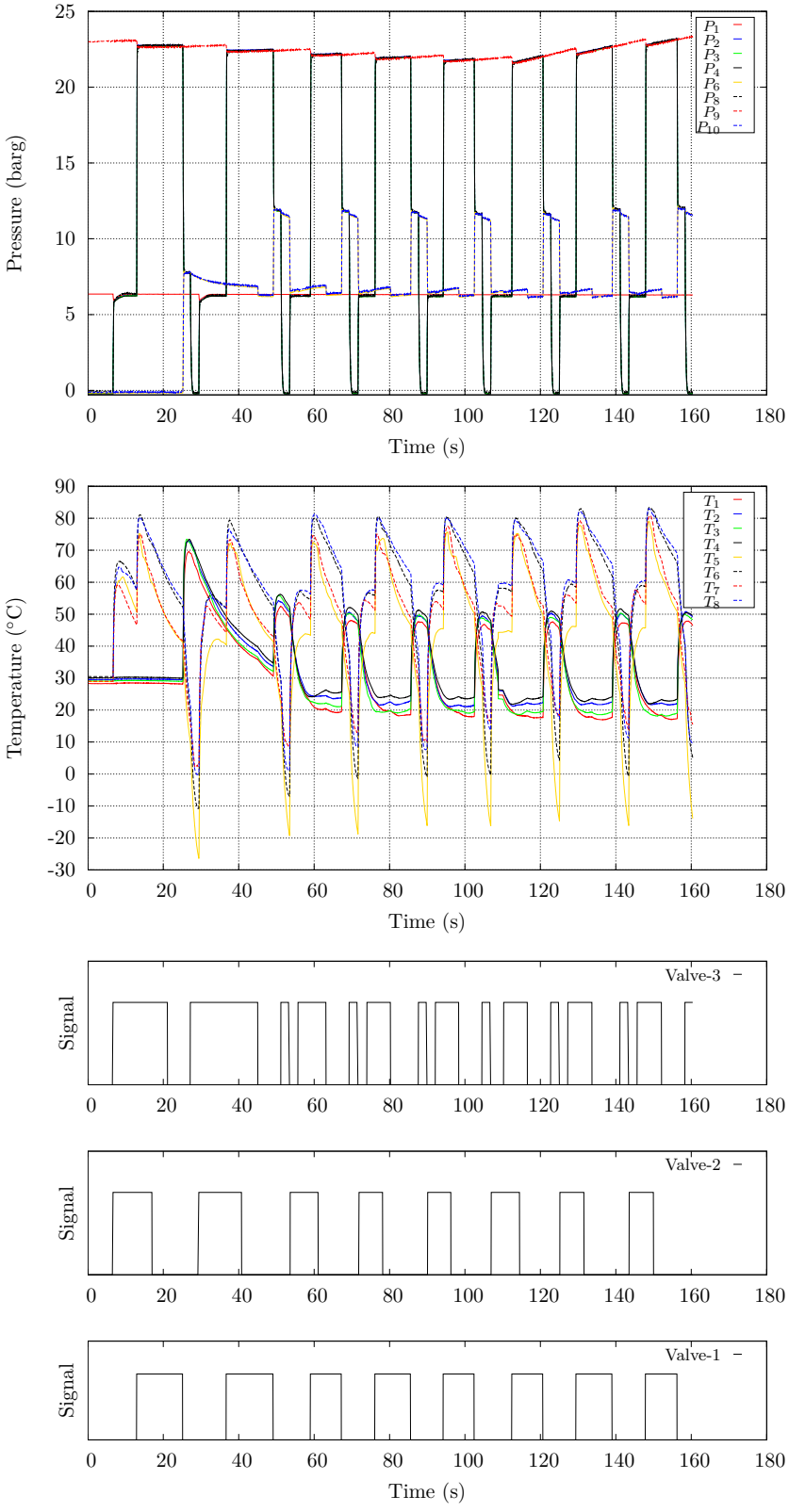

Figure 11.6: Test-55 (refer to table 6.7)

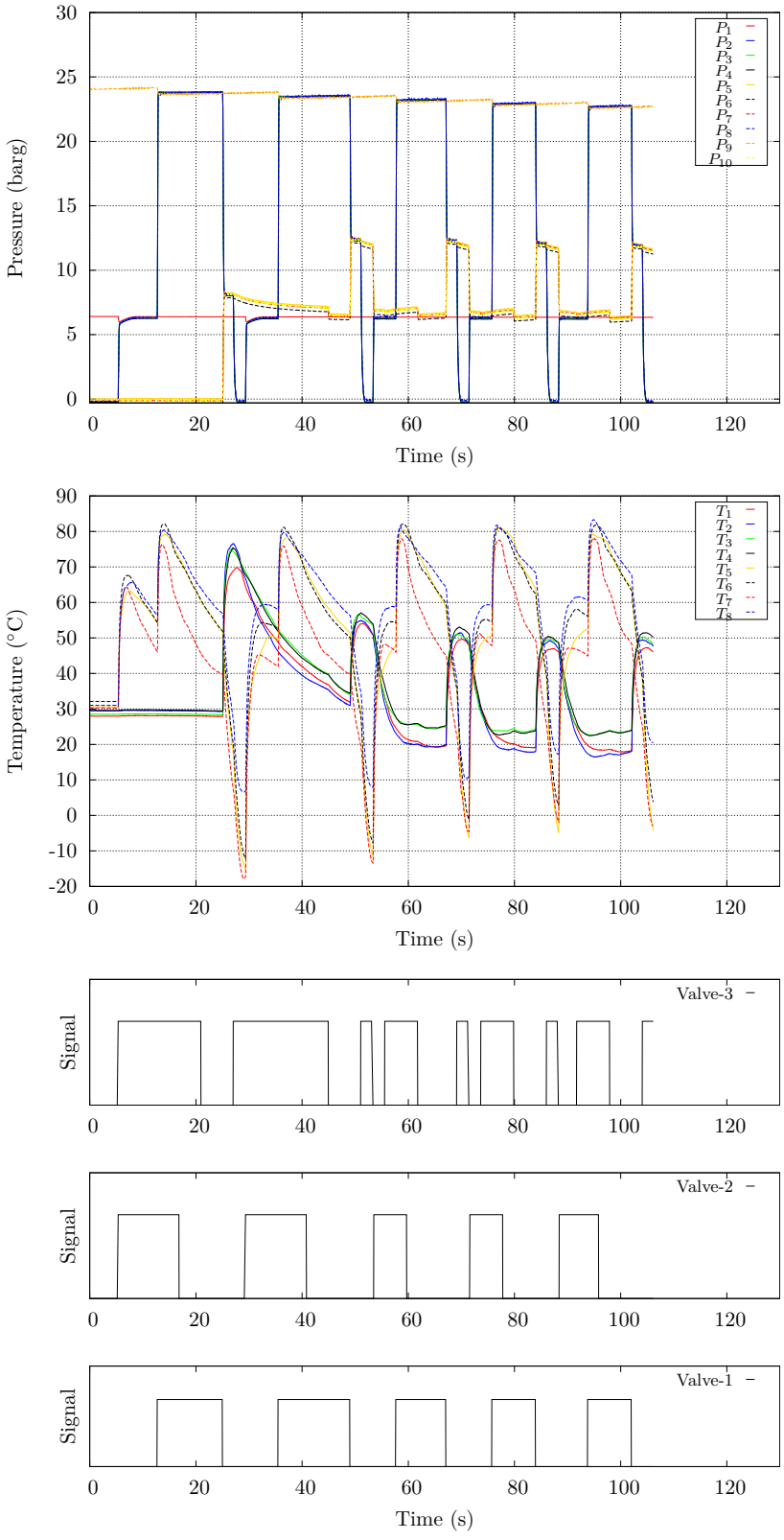

Figure 11.7: Test-24 [Piezoelectric pressure sensors mounted on recyling line] (refer to table 6.7)

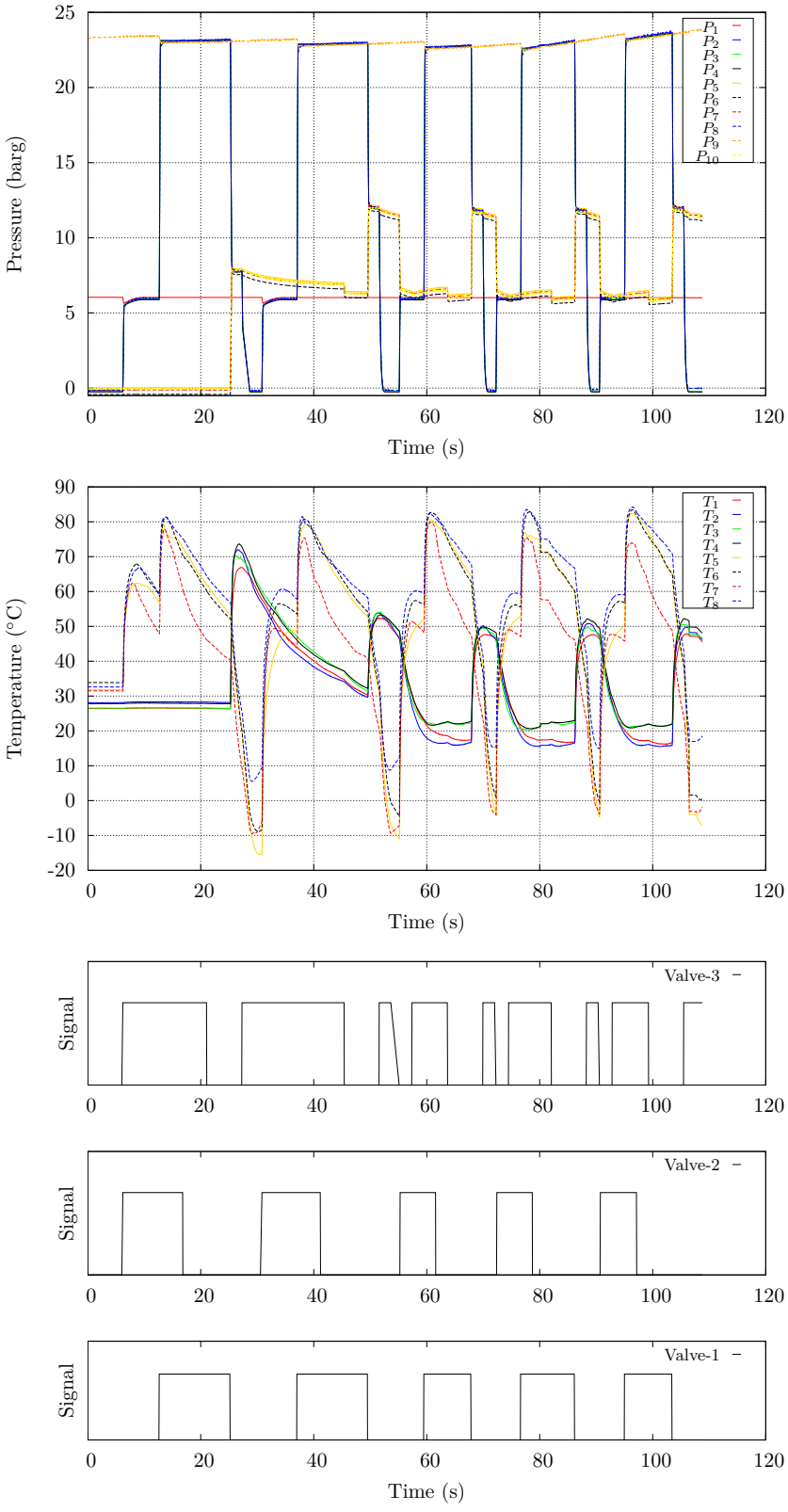

Figure 11.8: Test-24 [Piezoelectric pressure sensors mounted on blowing line] (refer to table 6.7)

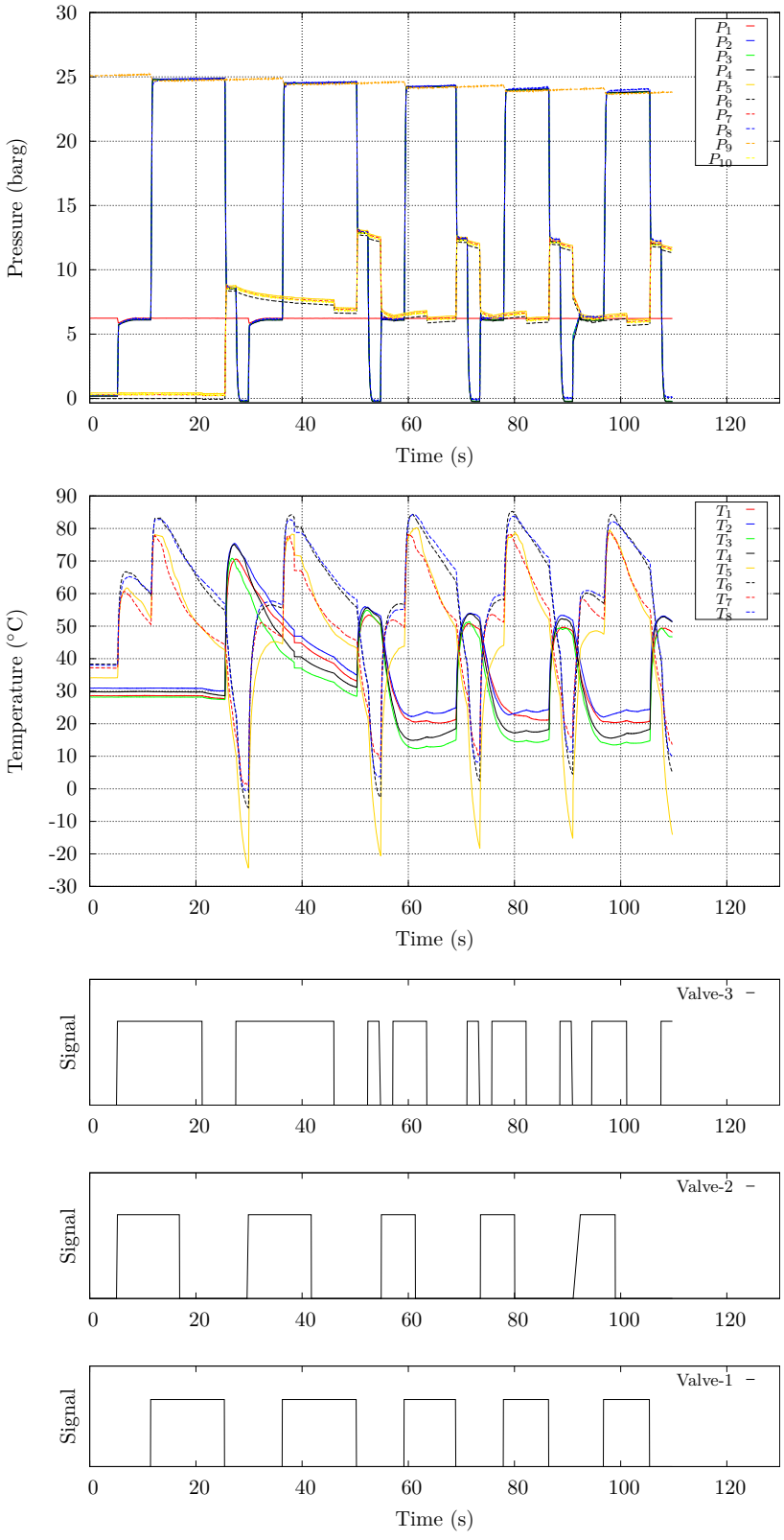

Figure 11.9: Test-15 [Piezoelectric pressure sensors mounted on blowing line] (refer to table 6.7)

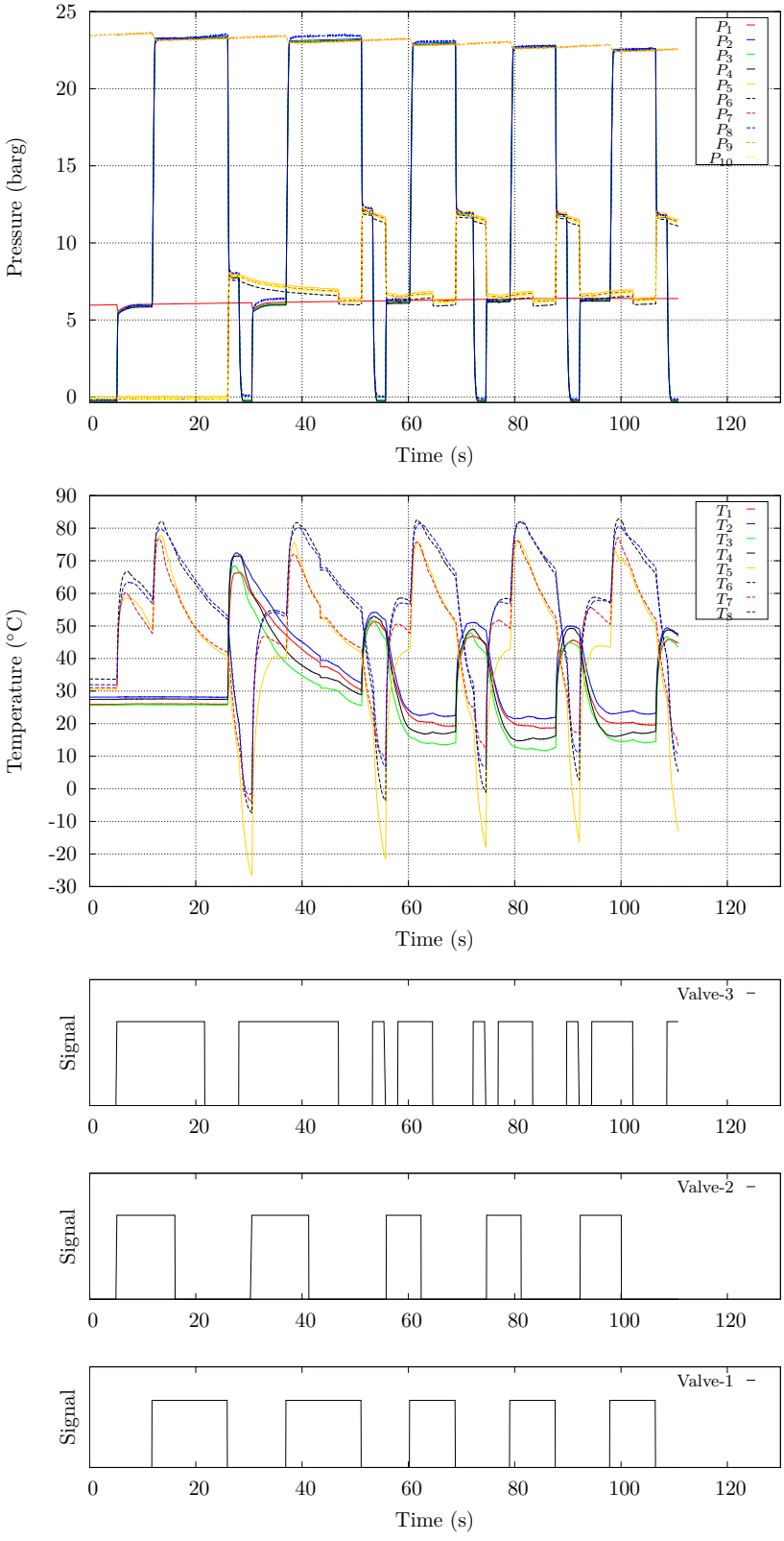

Figure 11.10: Test-15 [Piezoelectric pressure sensors mounted on recycling line] (refer to table 6.7)

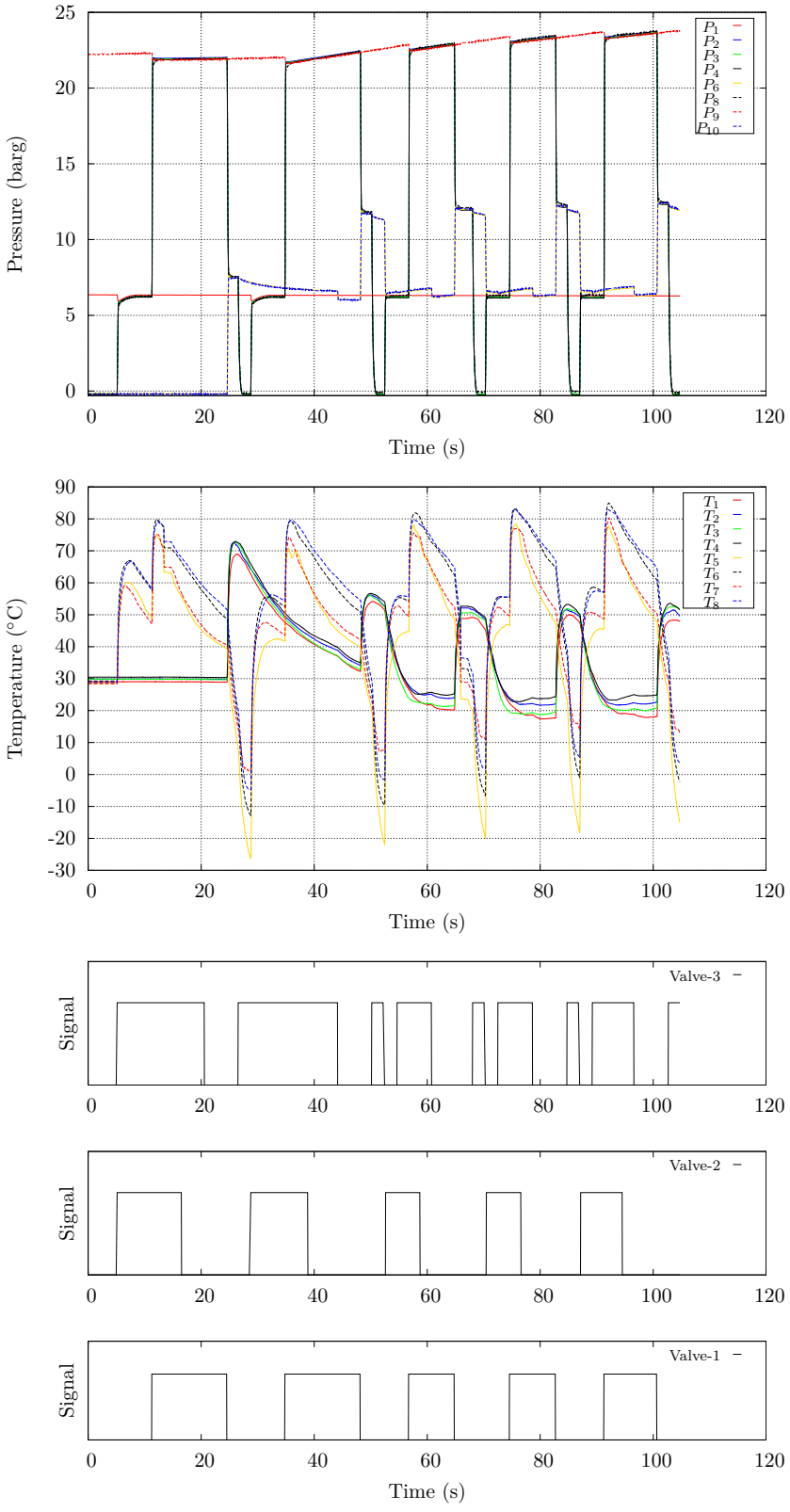

Figure 11.11: Test-53 (refer to table 6.7)

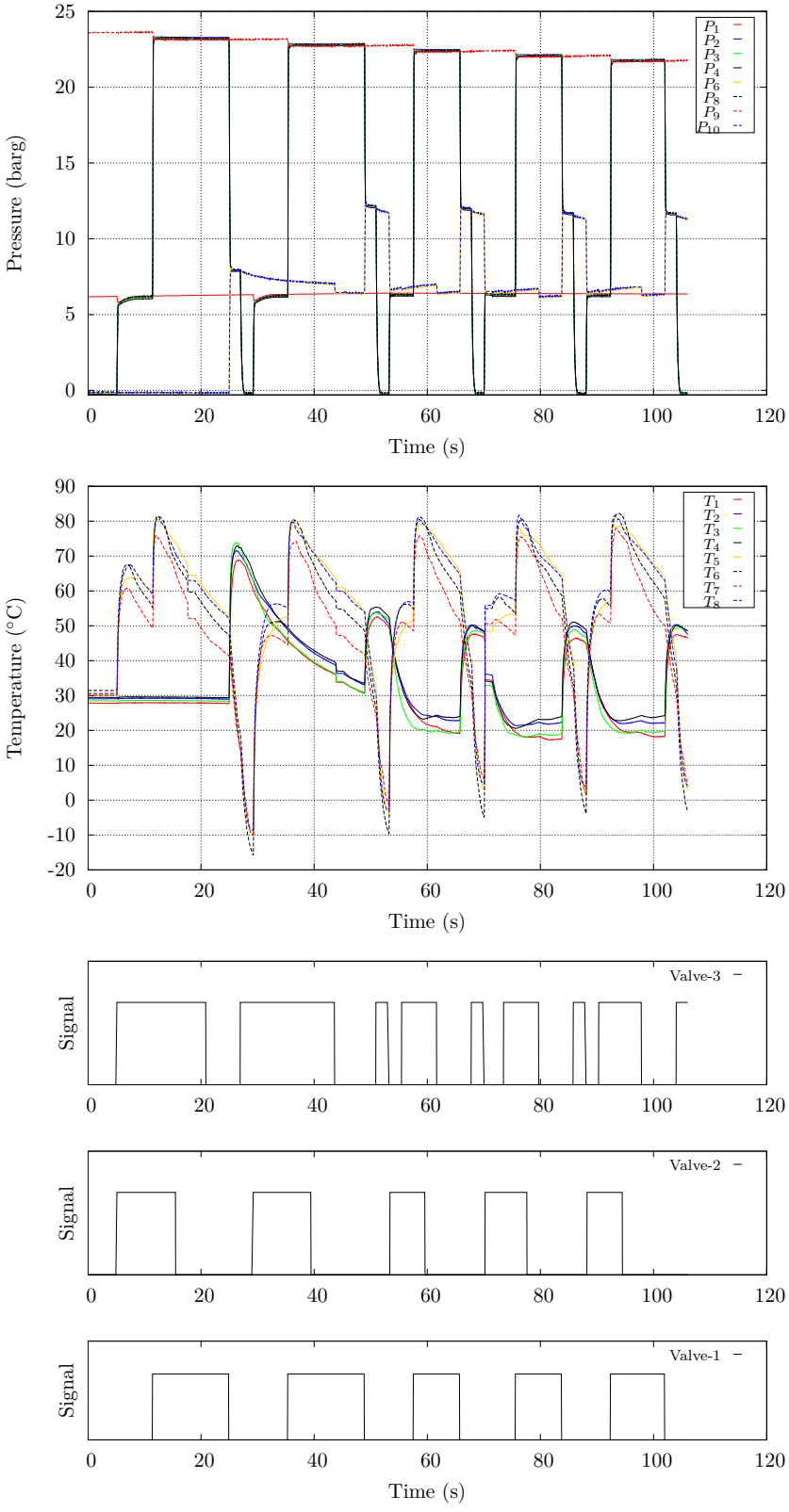

Figure 11.12: Test-52 (refer to table 6.7)

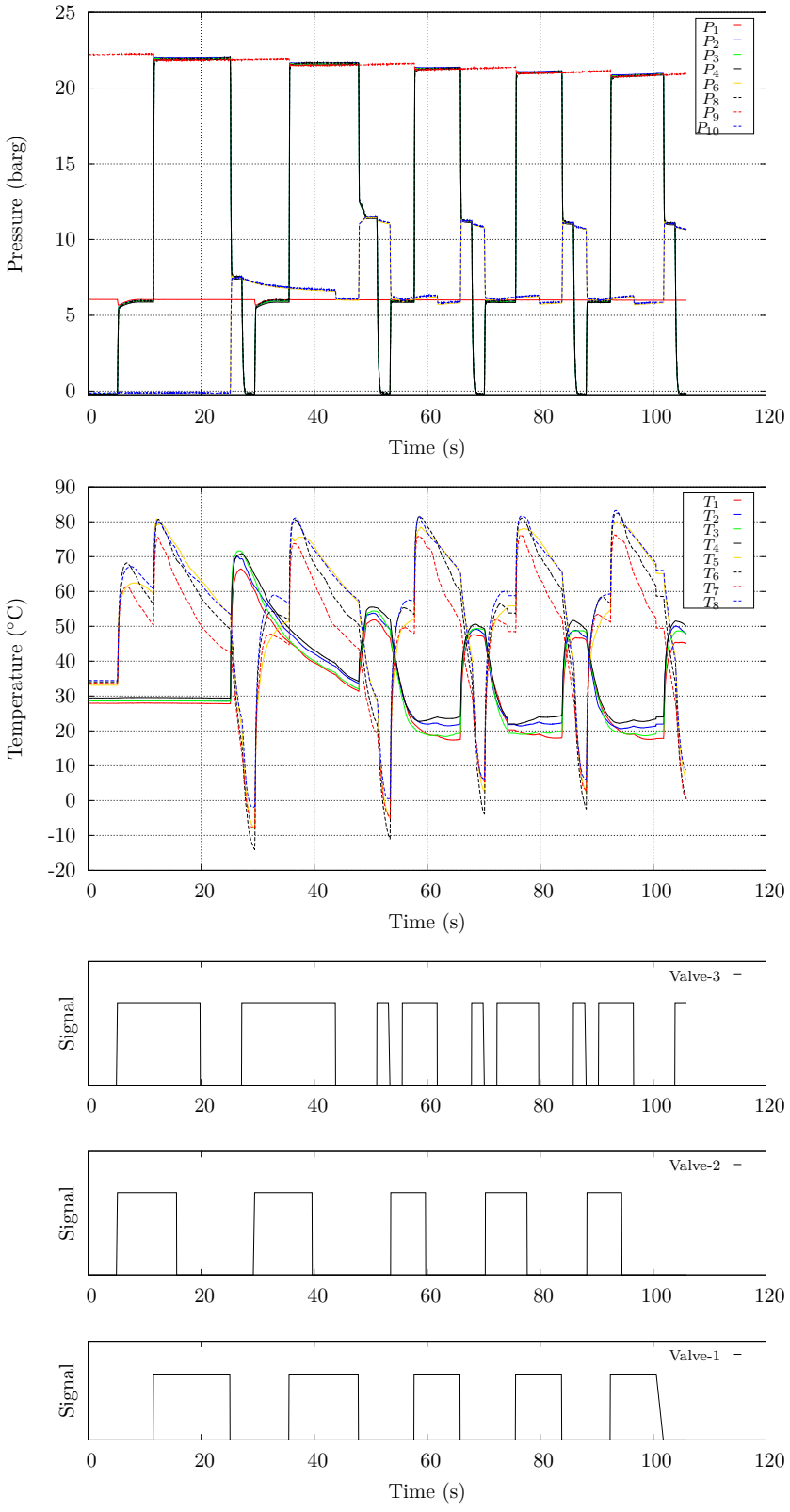

Figure 11.13: Test-54 (refer to table 6.7)

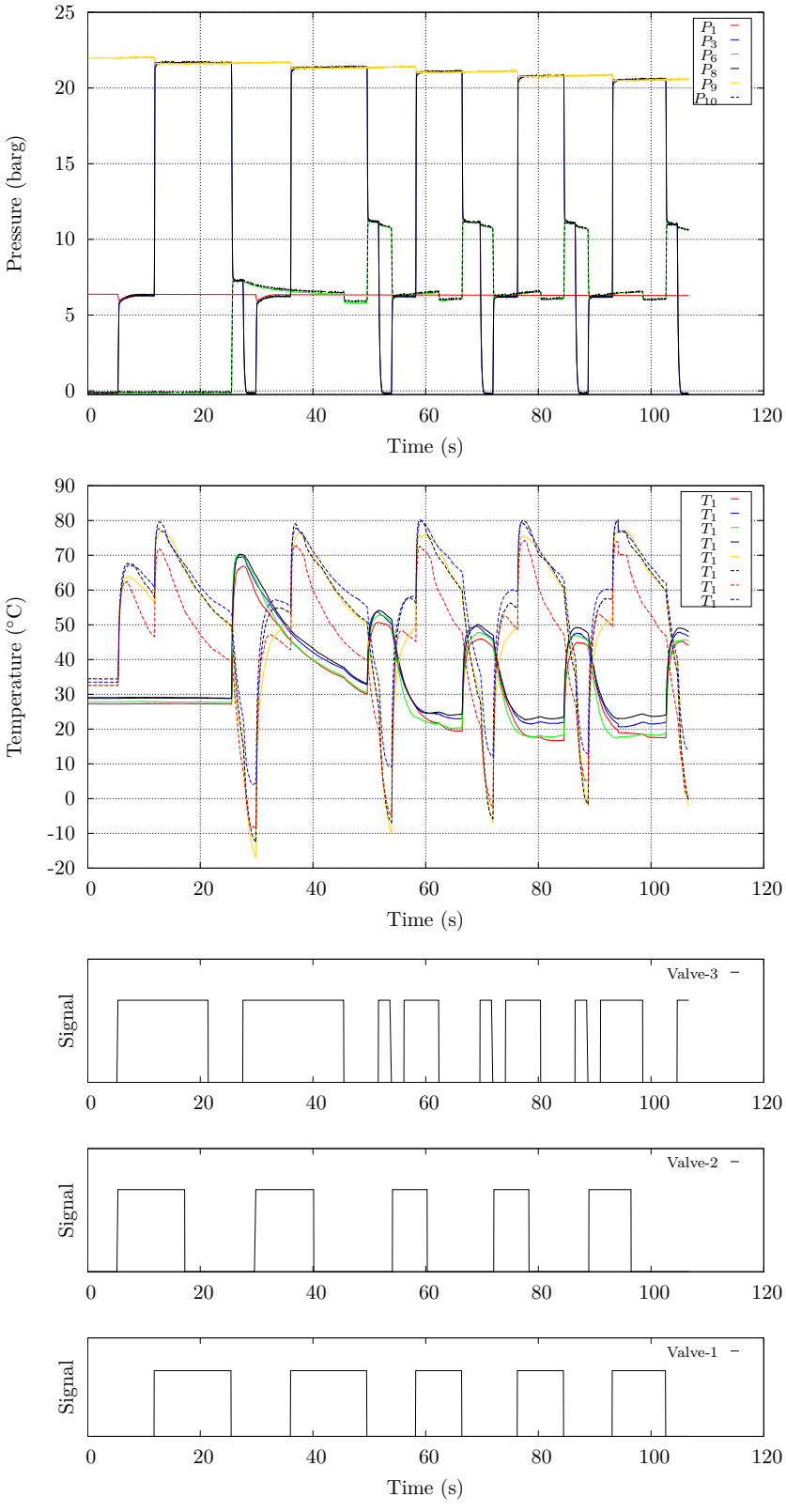

Figure 11.14: Test-56 (refer to table 6.7)

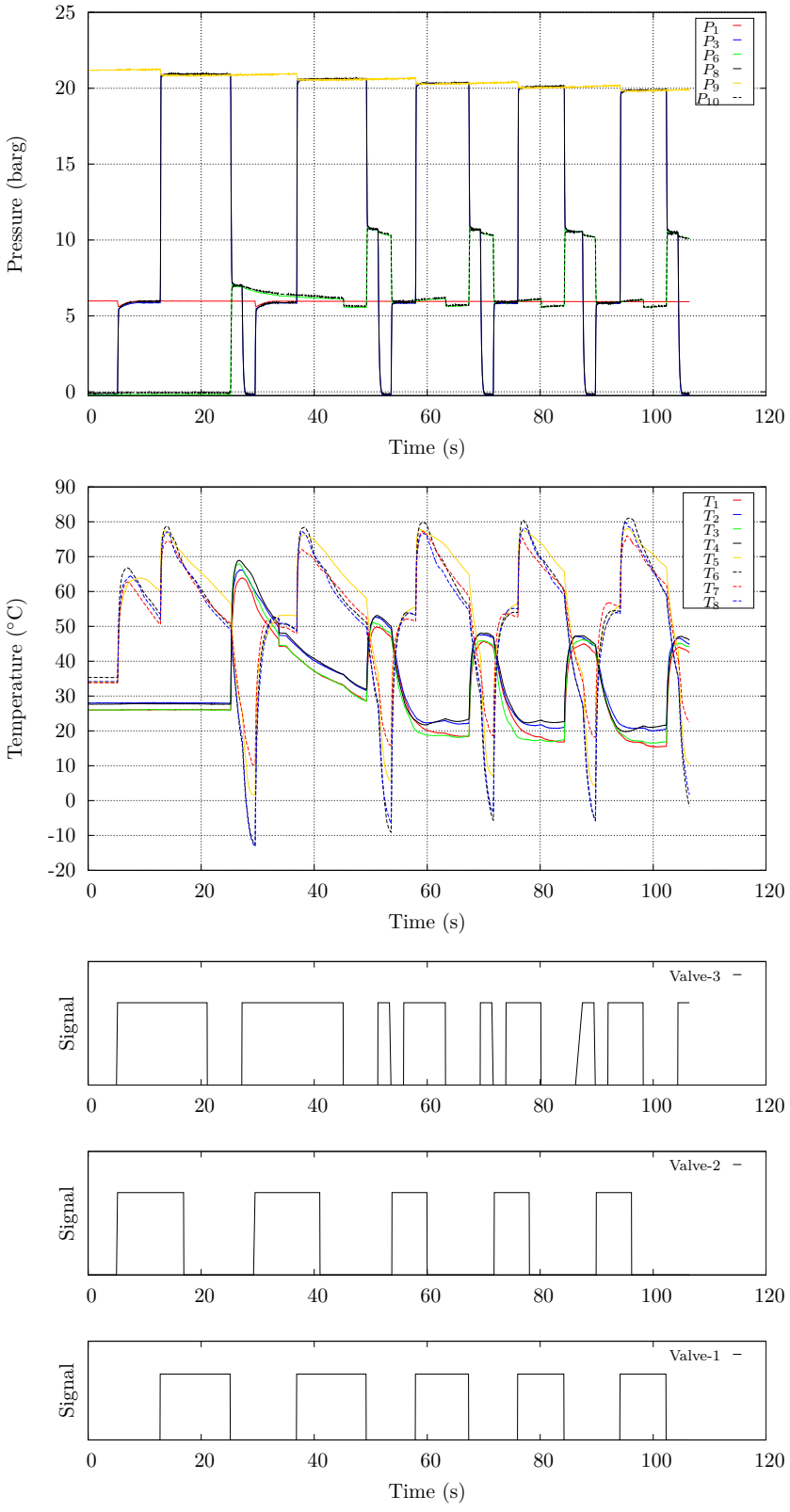

Figure 11.15: Test-57 (refer to table 6.7)

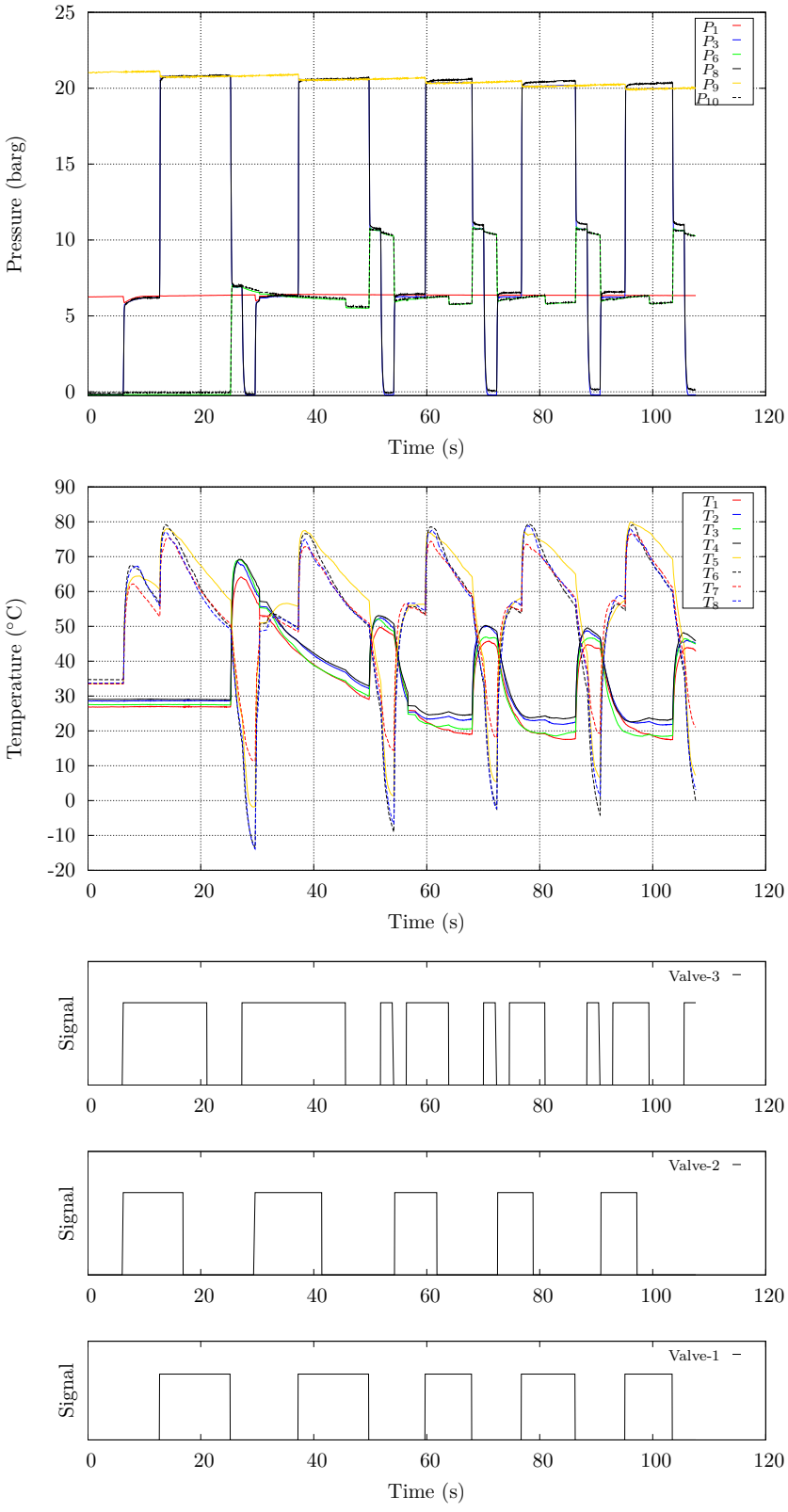

Figure 11.16: Test-59 (refer to table 6.7)

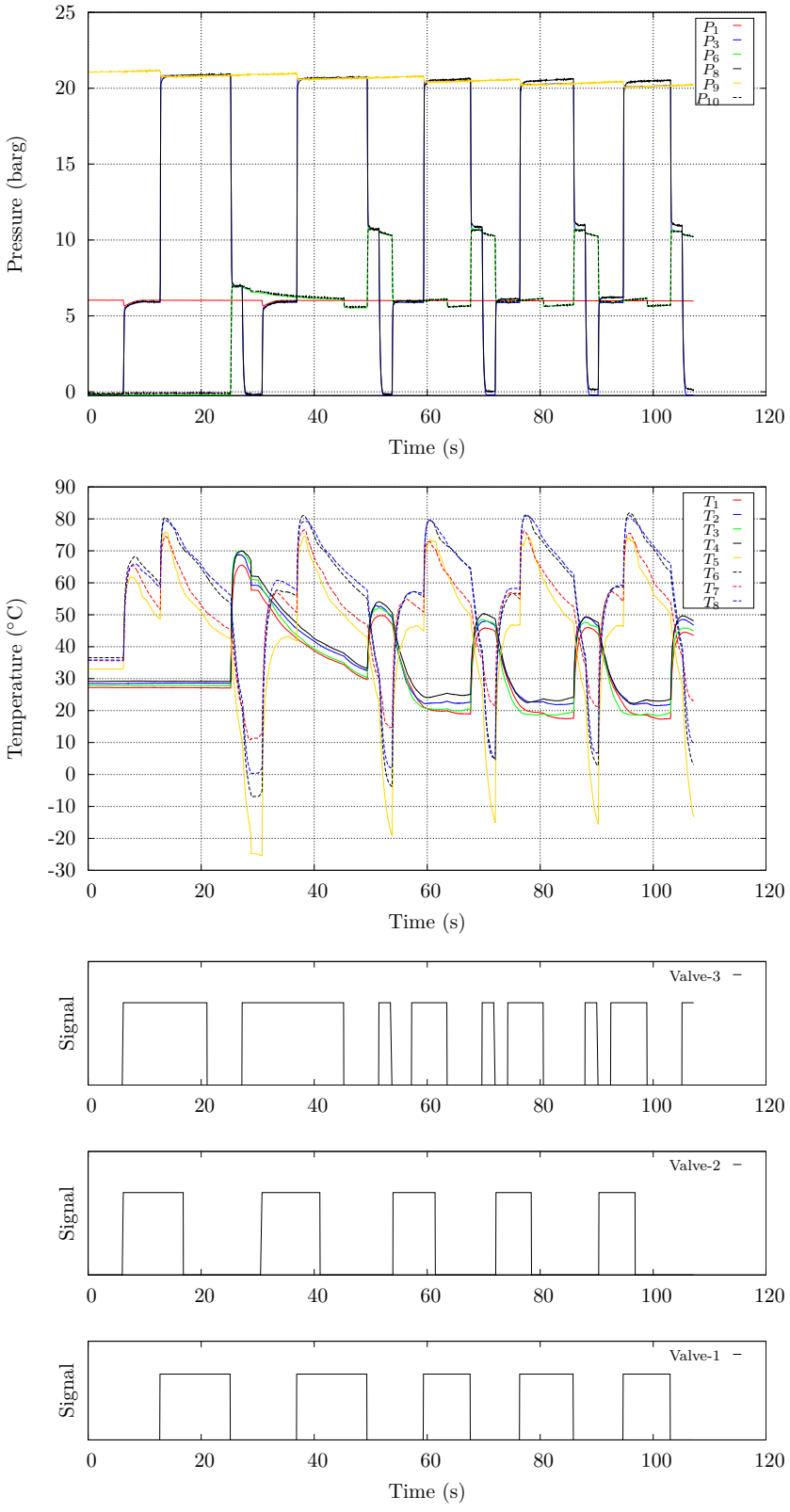

Figure 11.17: Test-58 (refer to table 6.7)

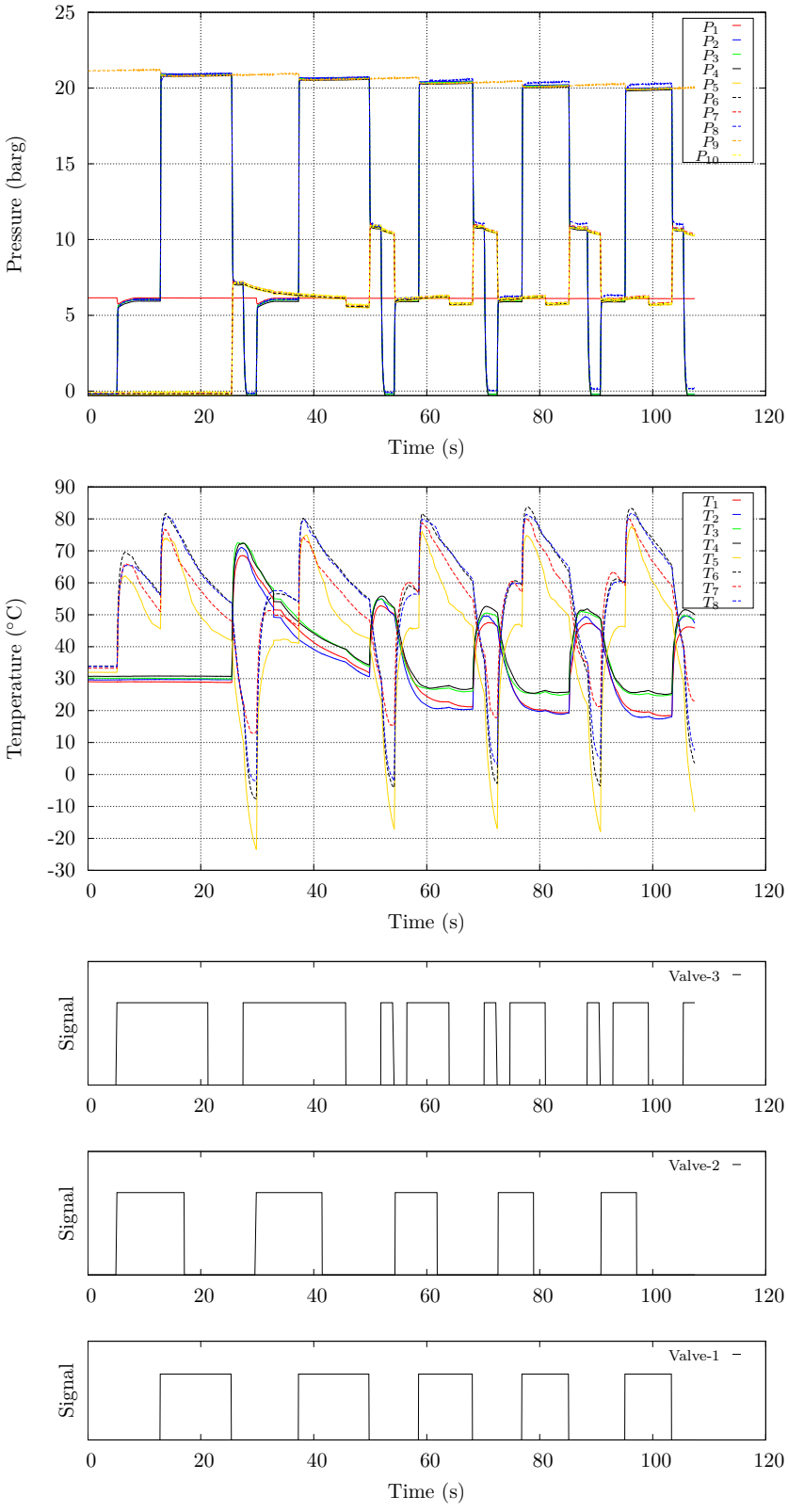

Figure 11.18: Test-21 [Piezoelectric pressure sensors mounted on recycling line] (refer to table 6.7)

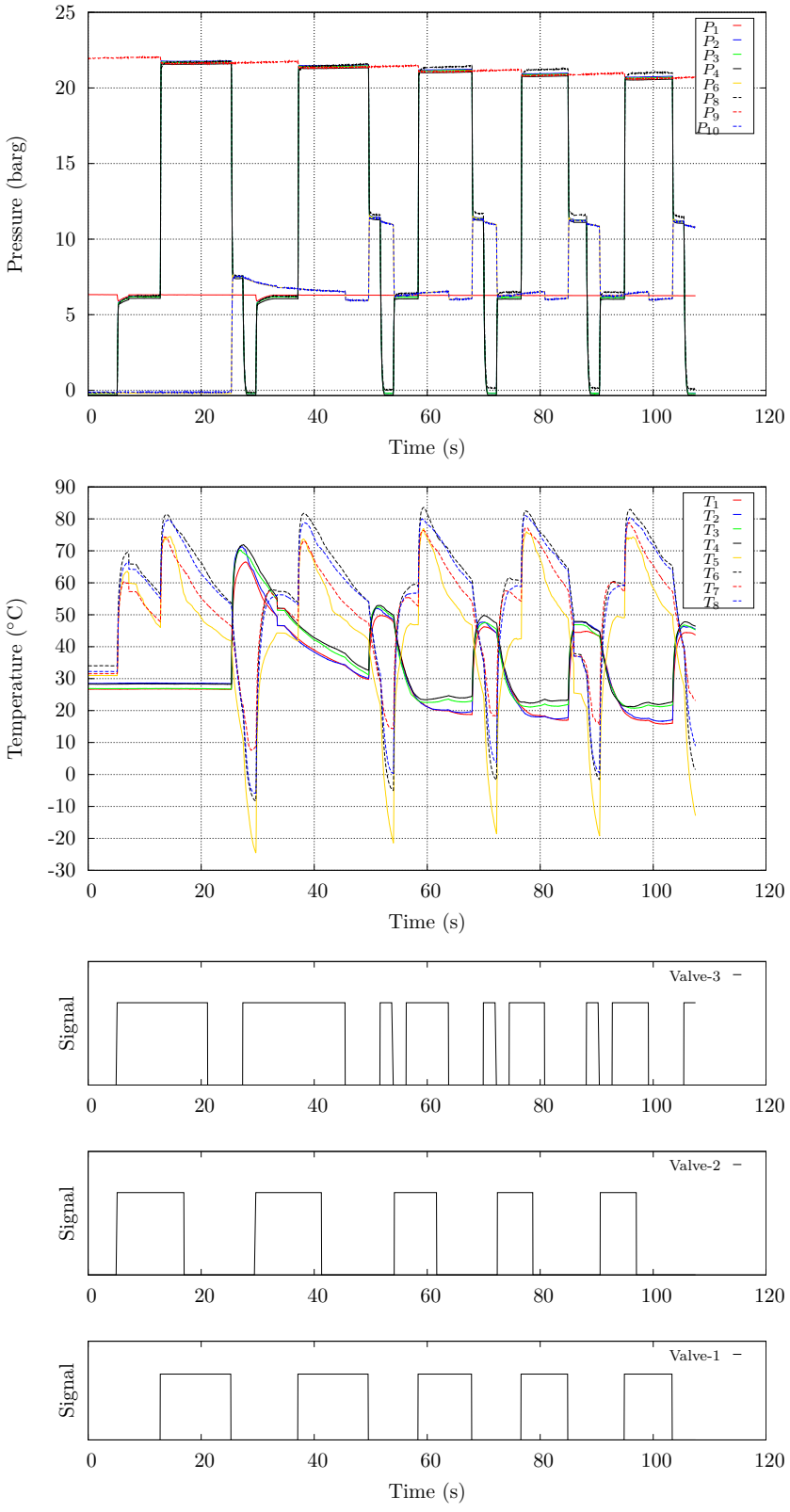

Figure 11.19: Test-71 [Piezoelectric pressure sensors mounted on blowing line] (refer to table 6.7)

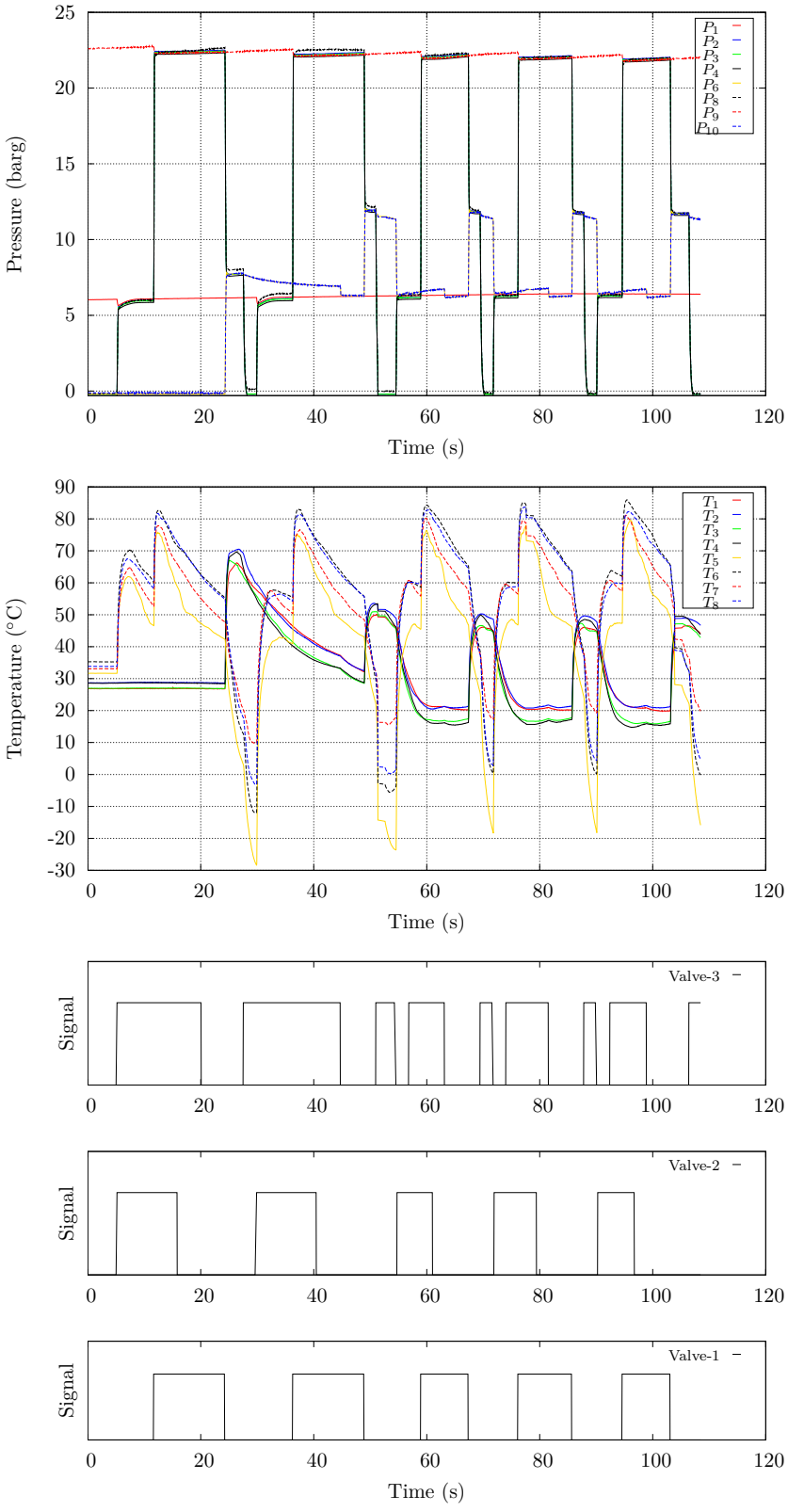

Figure 11.20: Test-61 (refer to table 6.7)

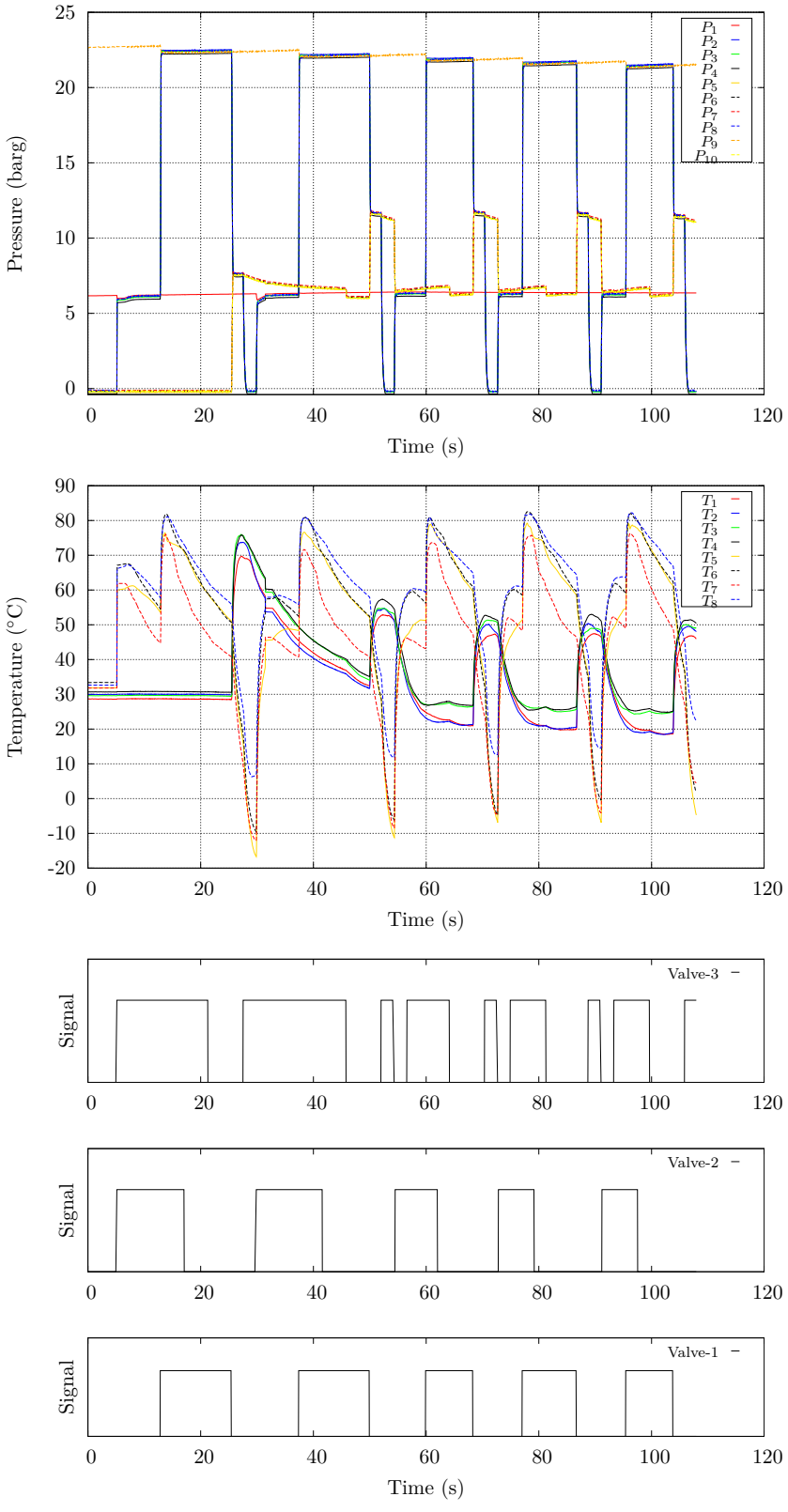

Figure 11.21: Test-24 (refer to table 6.7)

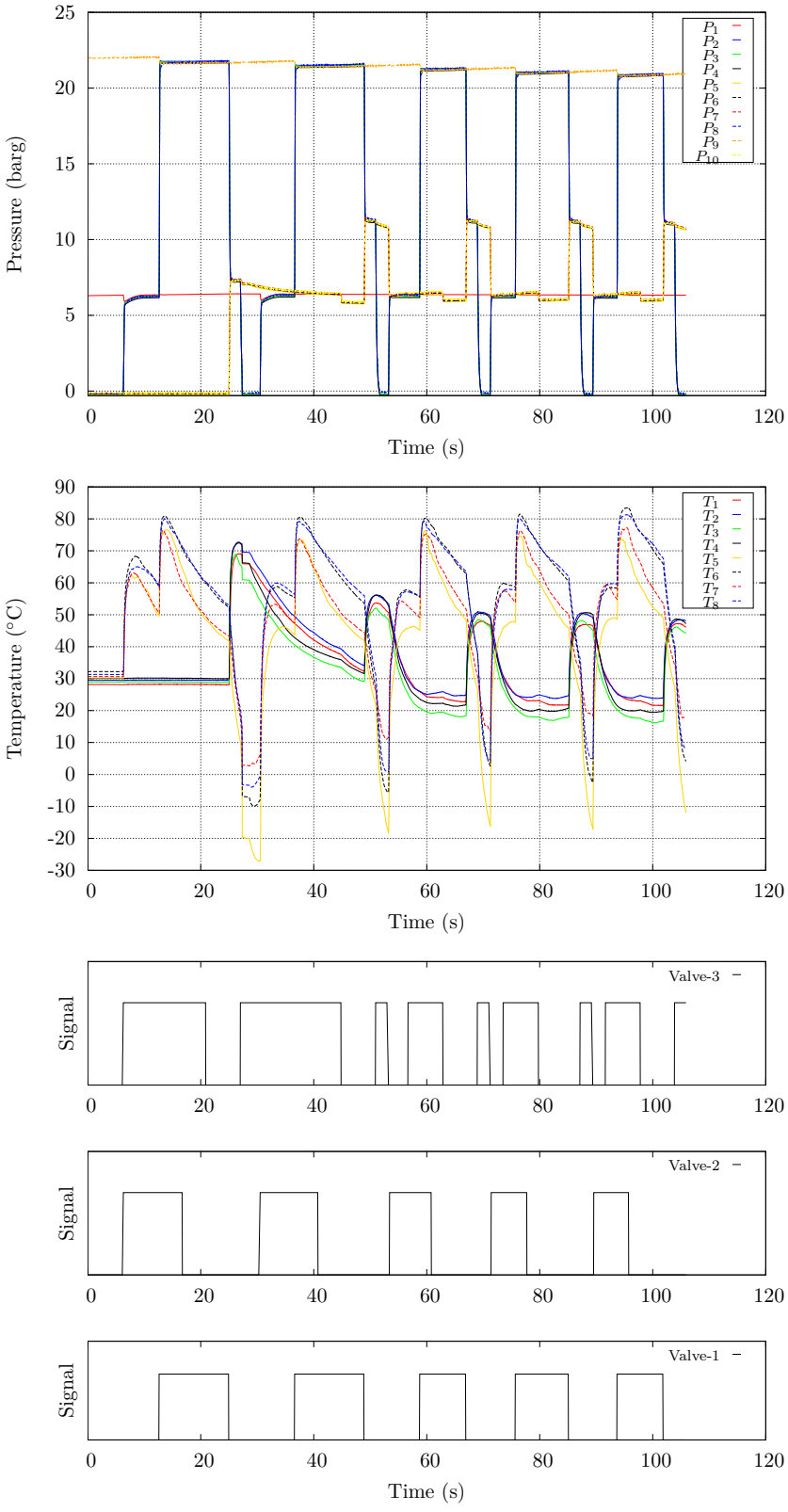

Figure 11.22: Test-43 (refer to table 6.7)

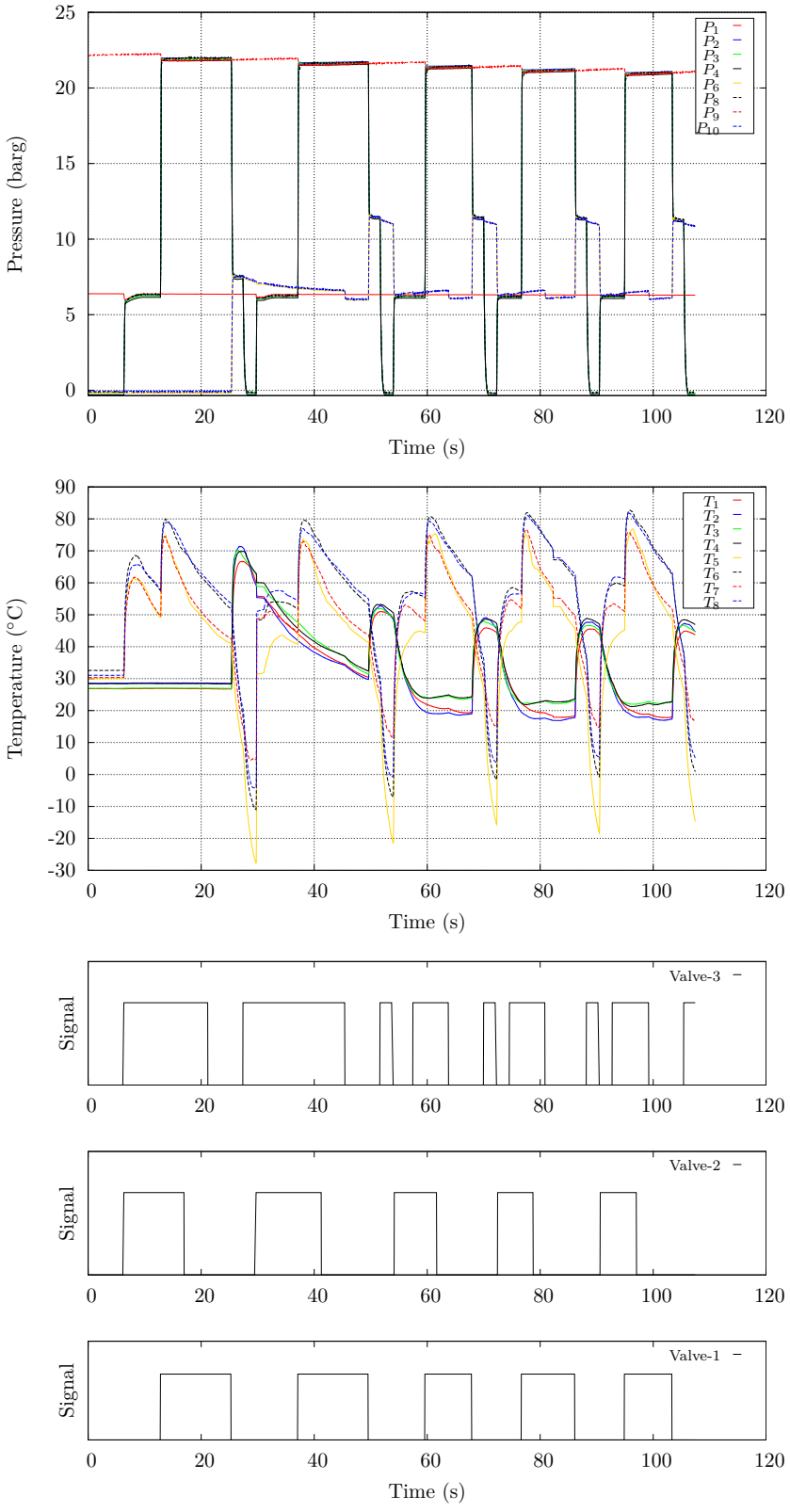

Figure 11.23: Test-73 (refer to table 6.7)

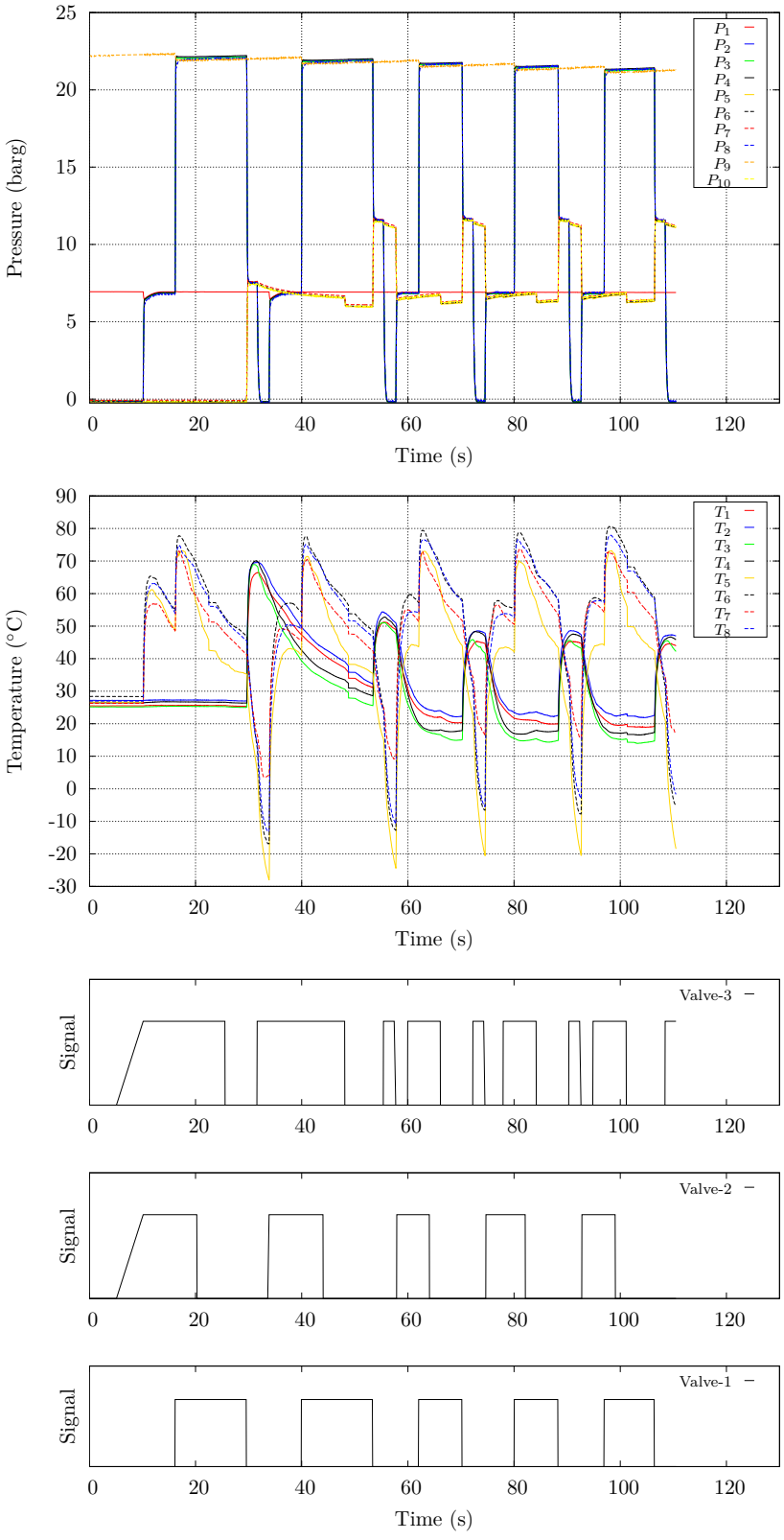

Figure 11.24: Test-15 (refer to table 6.7)

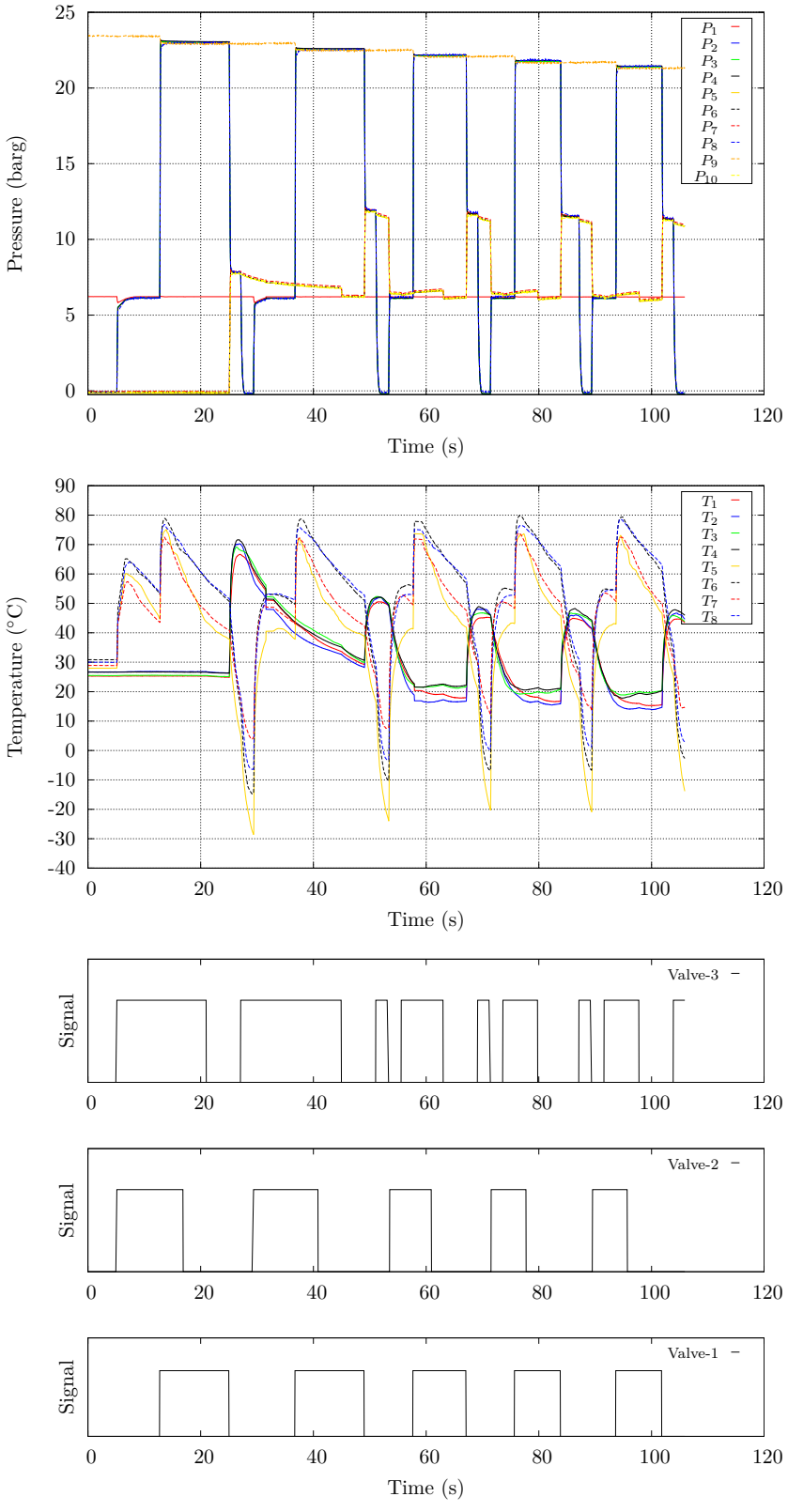

Figure 11.25: Test-25 (refer to table 6.7)

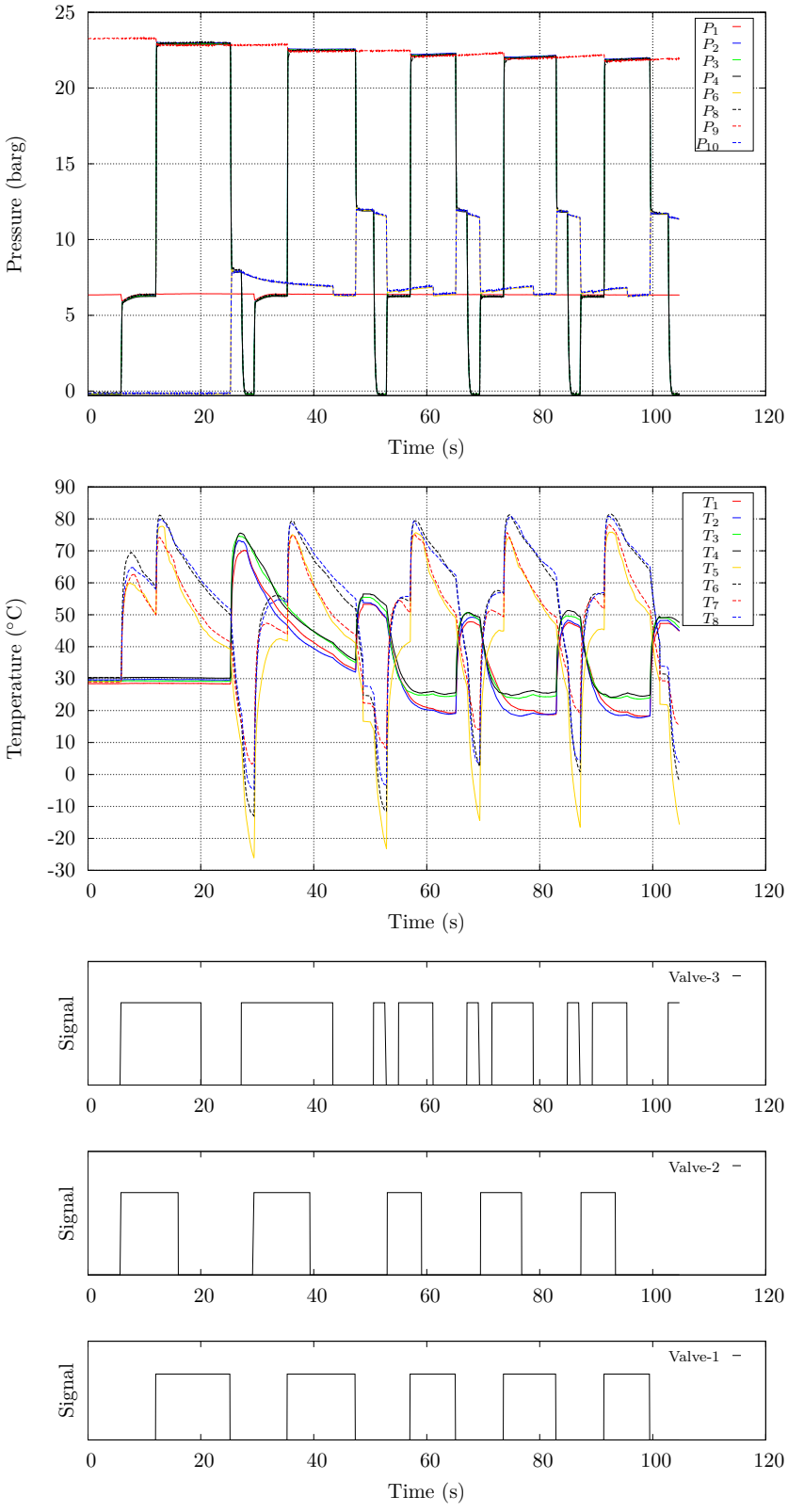

Figure 11.26: Test-75 (refer to table 6.7)

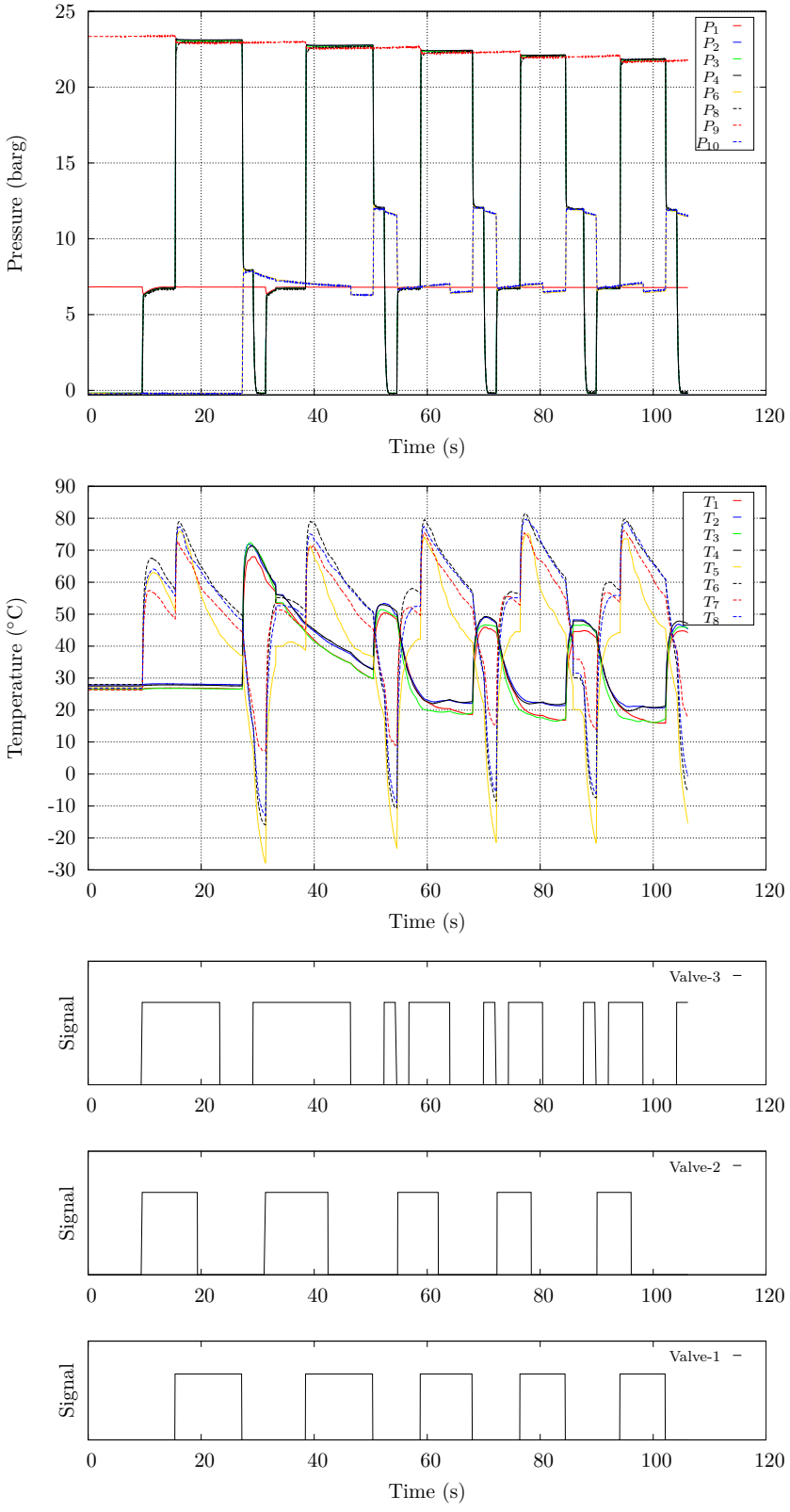

Figure 11.27: Test-55 (refer to table 6.7)

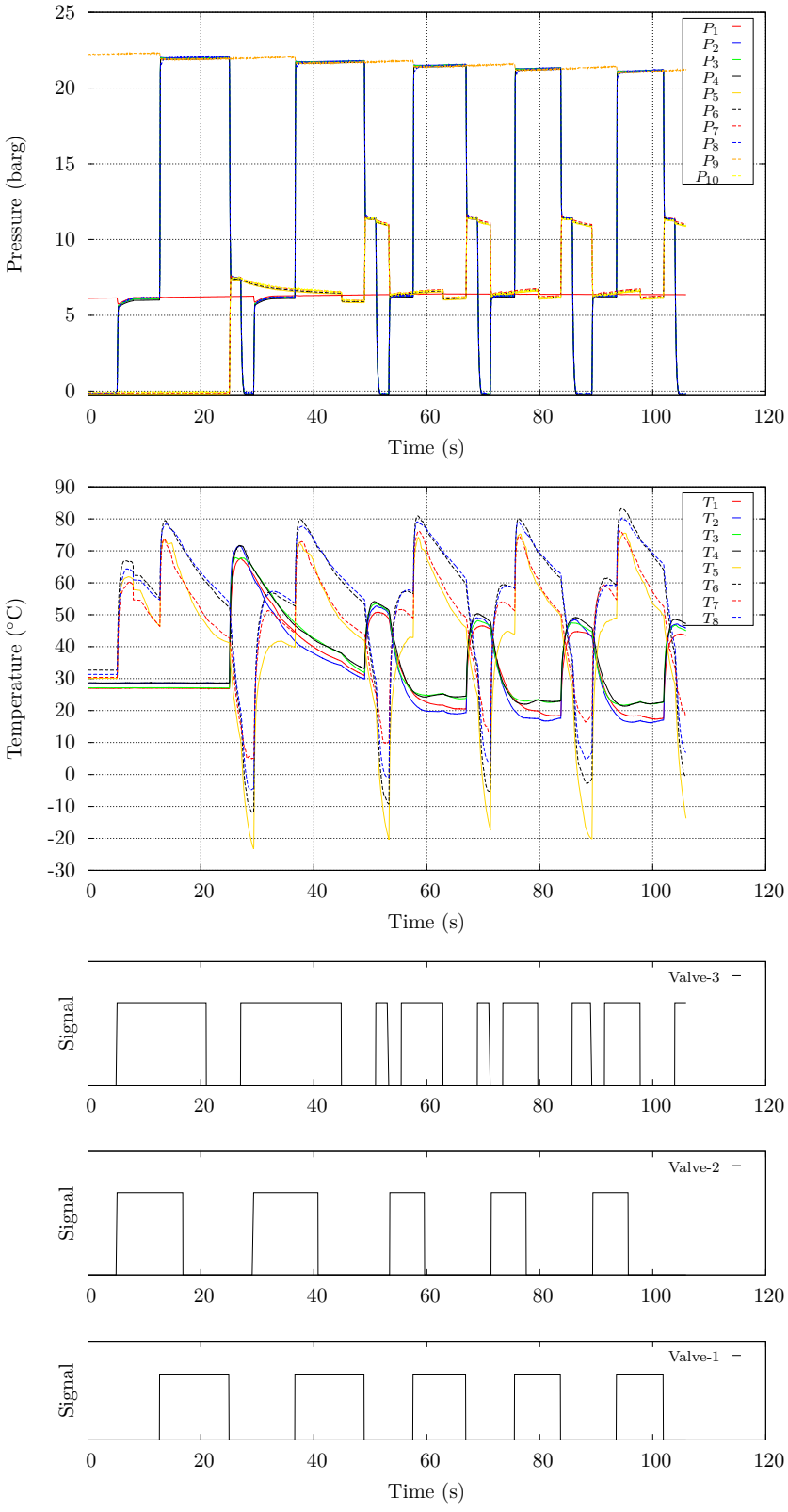

Figure 11.28: Test-33 [Piezoelectric pressure sensors mounted on blowing line] (refer to table 6.7)

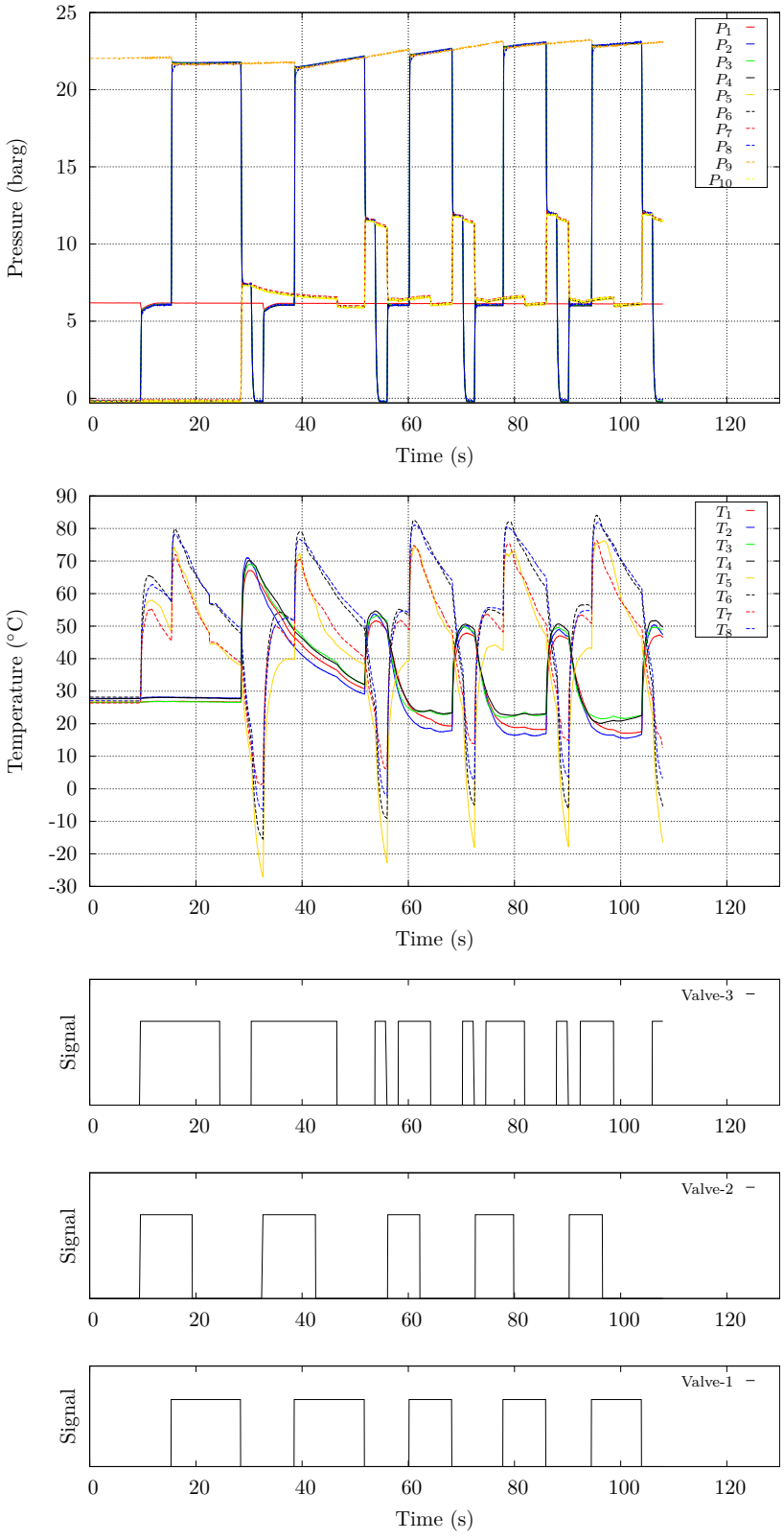

Figure 11.29: Test-33 [Piezoelectric pressure sensors mounted on recycling line] (refer to table 6.7)

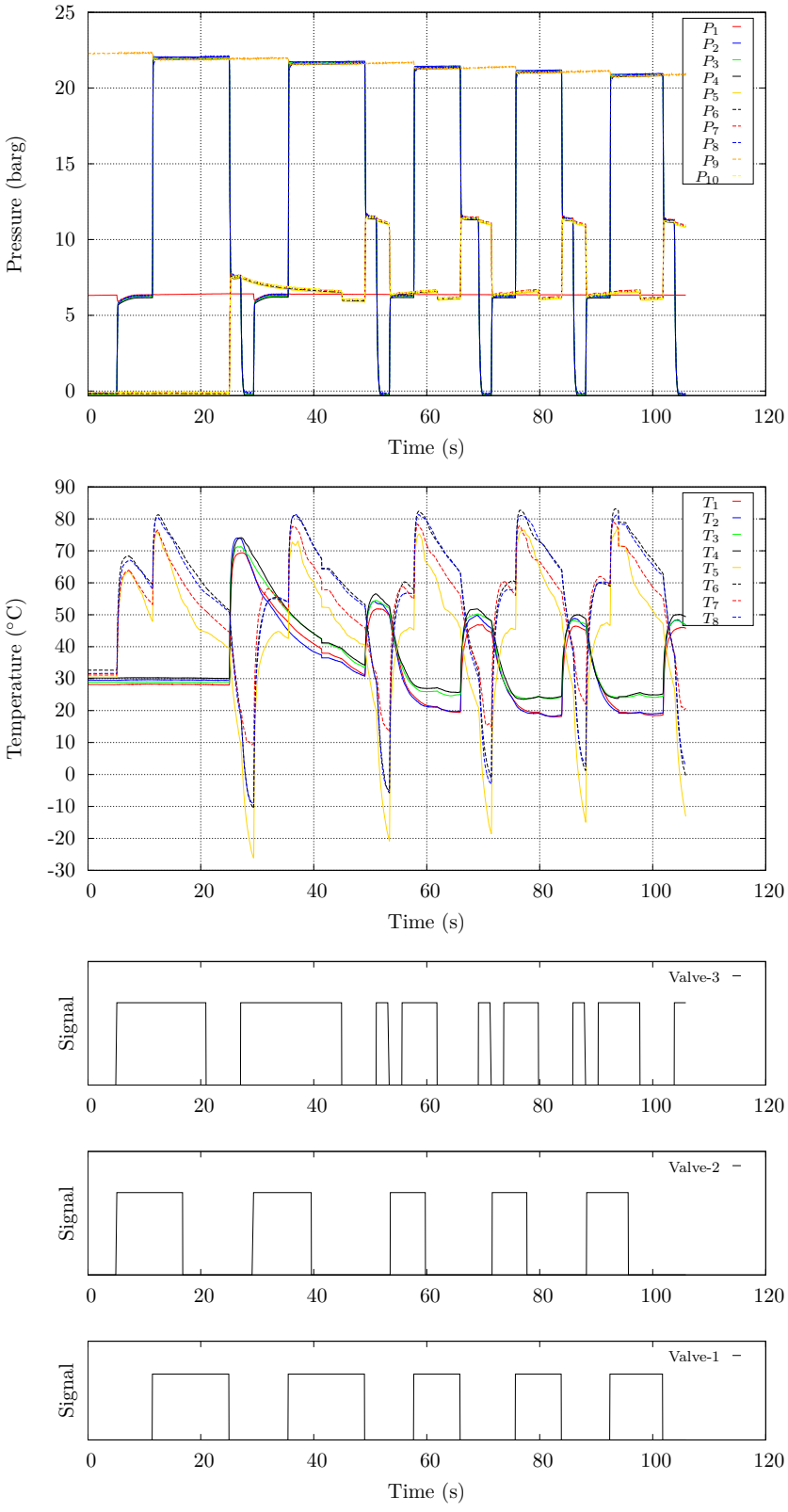

Figure 11.30: Test-31 (refer to table 6.7)

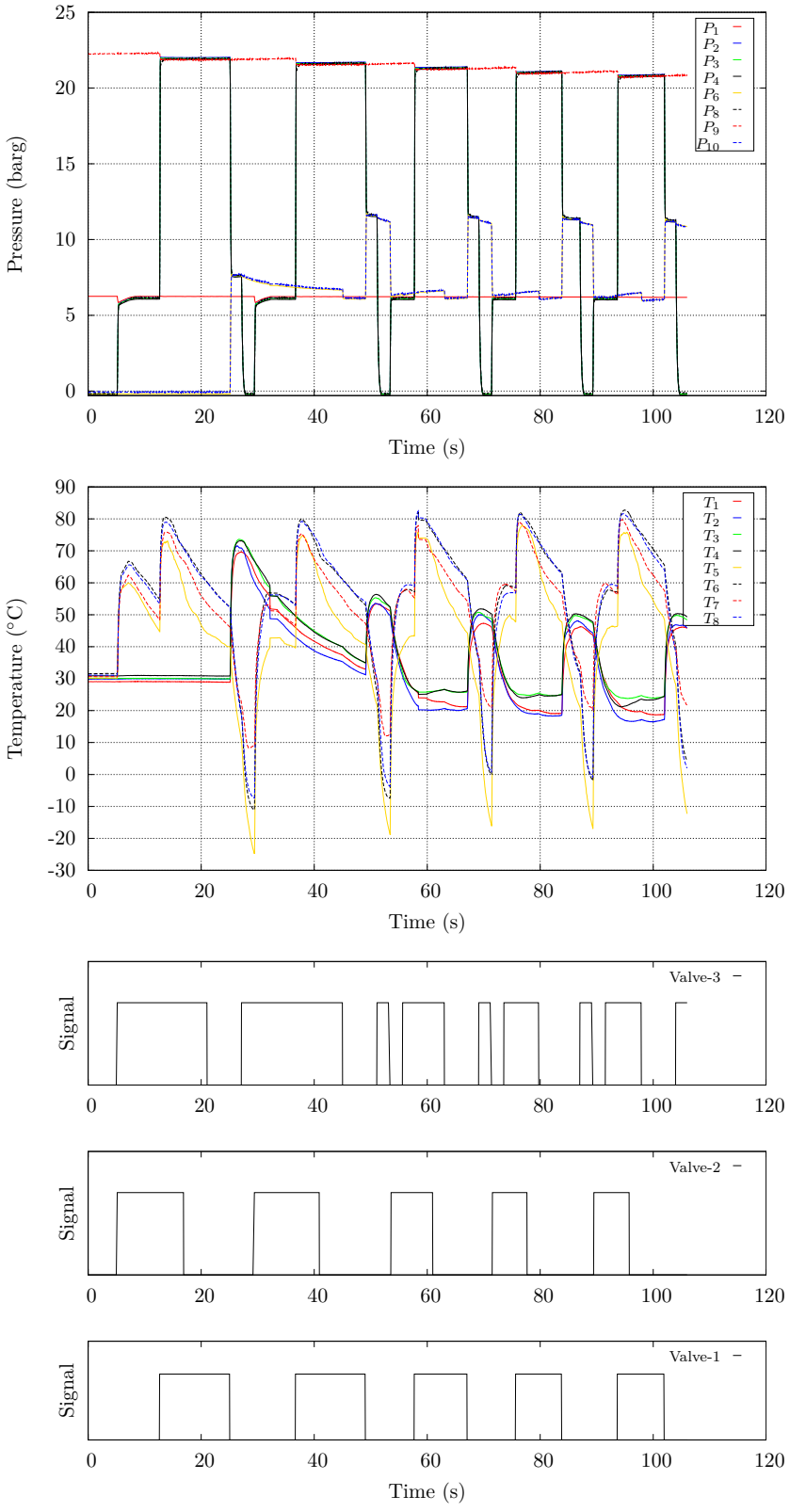

Figure 11.31: Test-81 (refer to table 6.7)

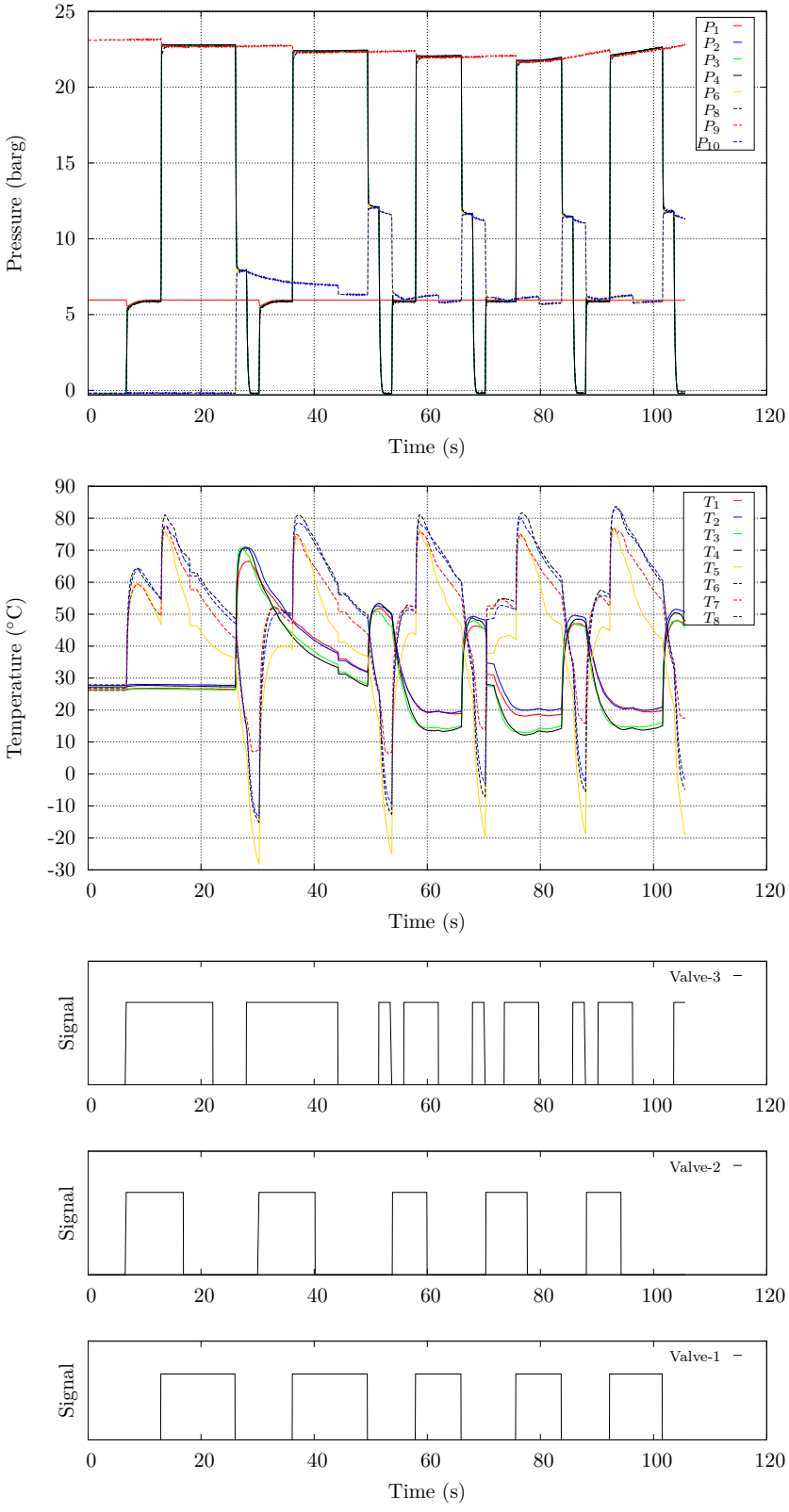

Figure 11.32: Test-91 (refer to table 6.7)

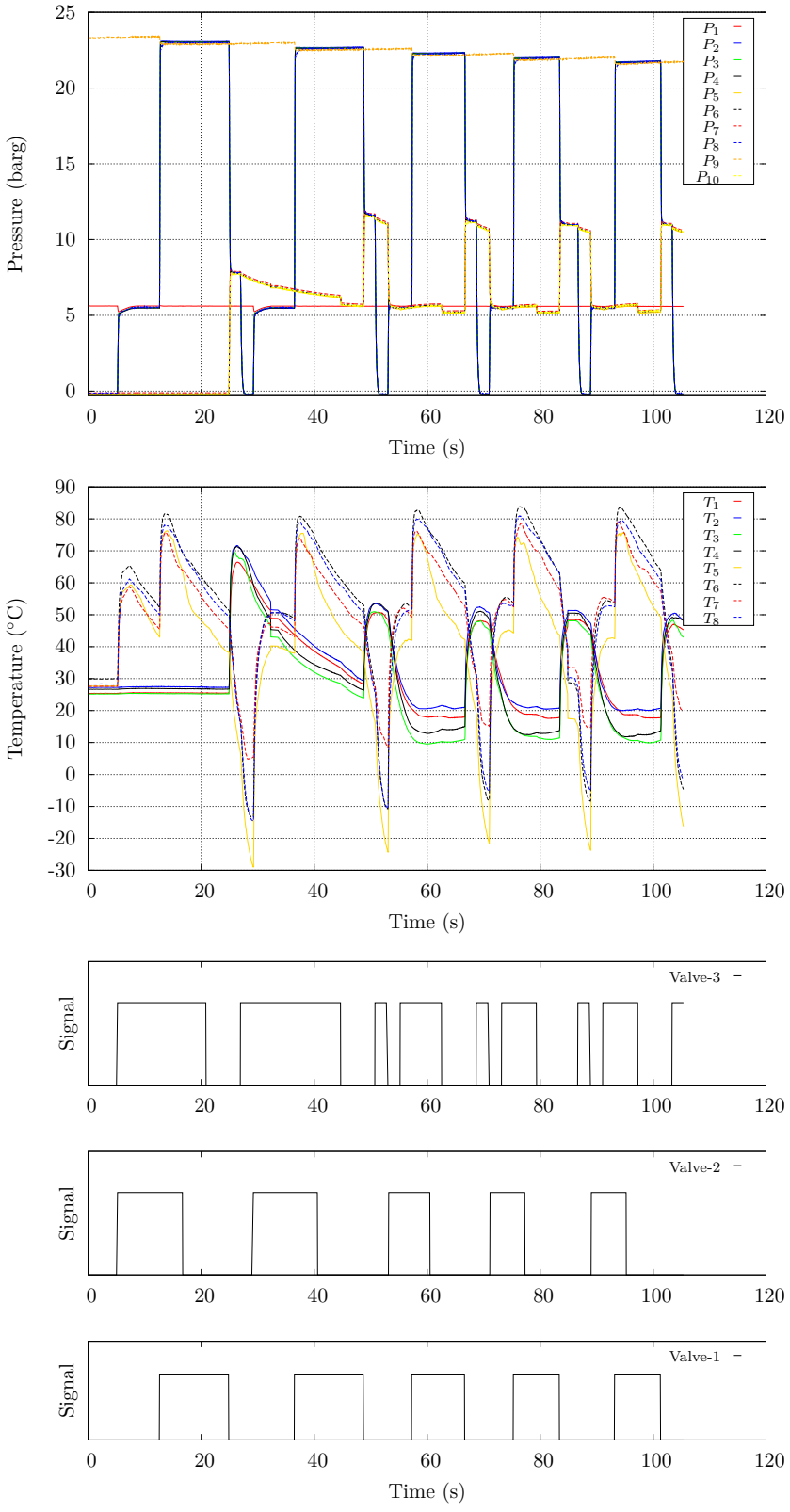

Figure 11.33: Test-41 (refer to table 6.7)

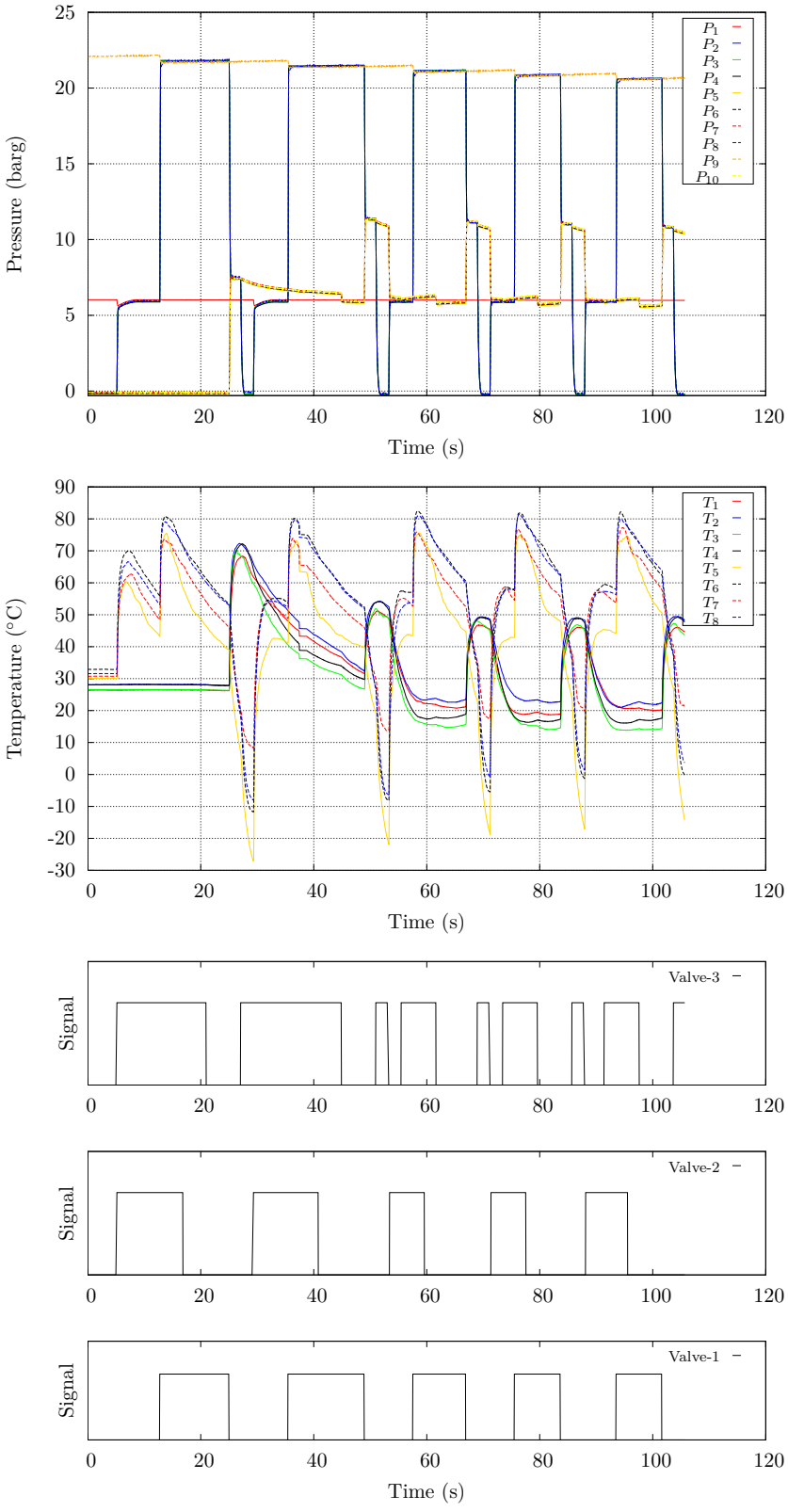

Figure 11.34: Test-1 (refer to table 6.7)

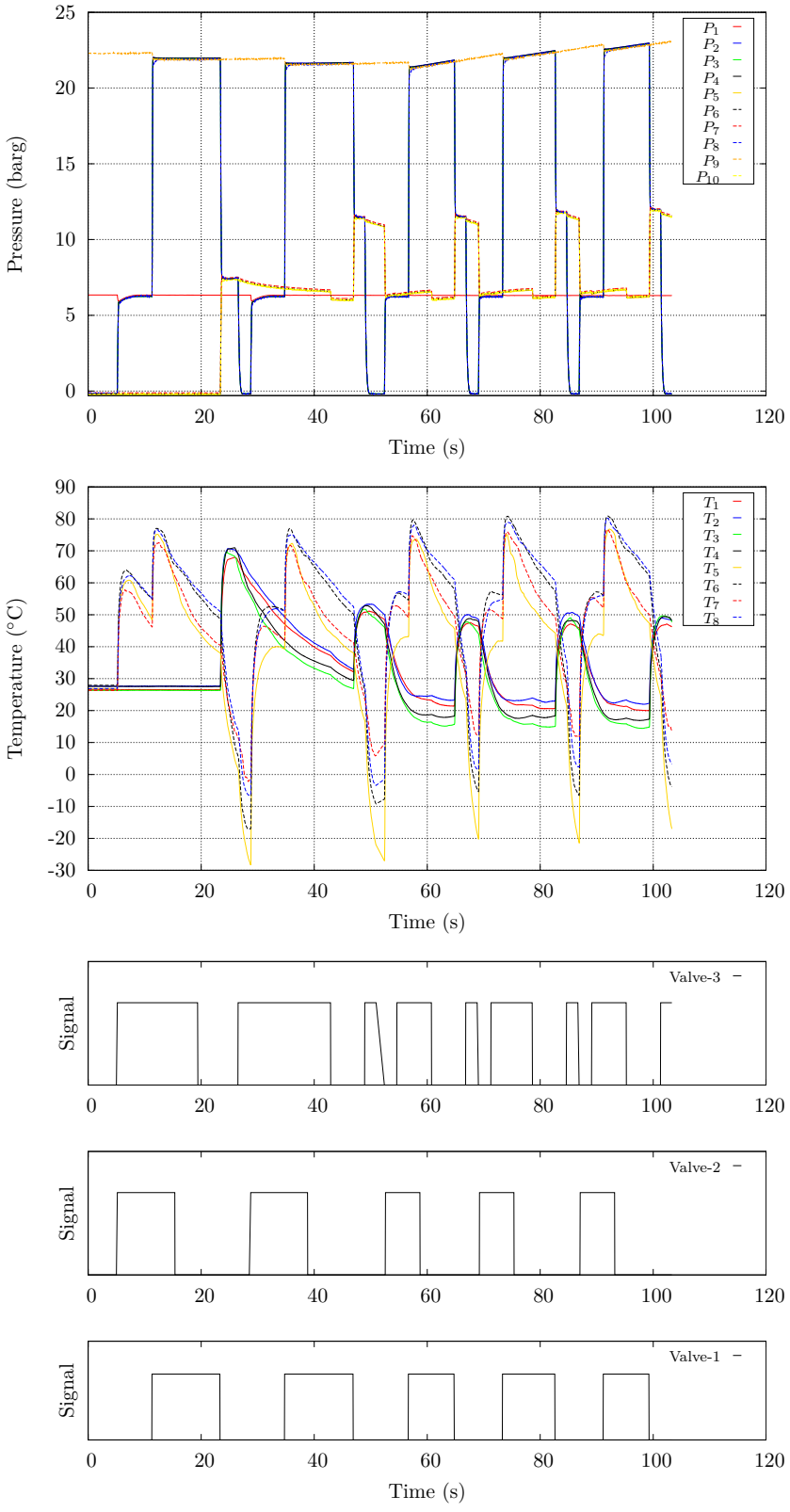

Figure 11.35: Test-5 (refer to table 6.7)

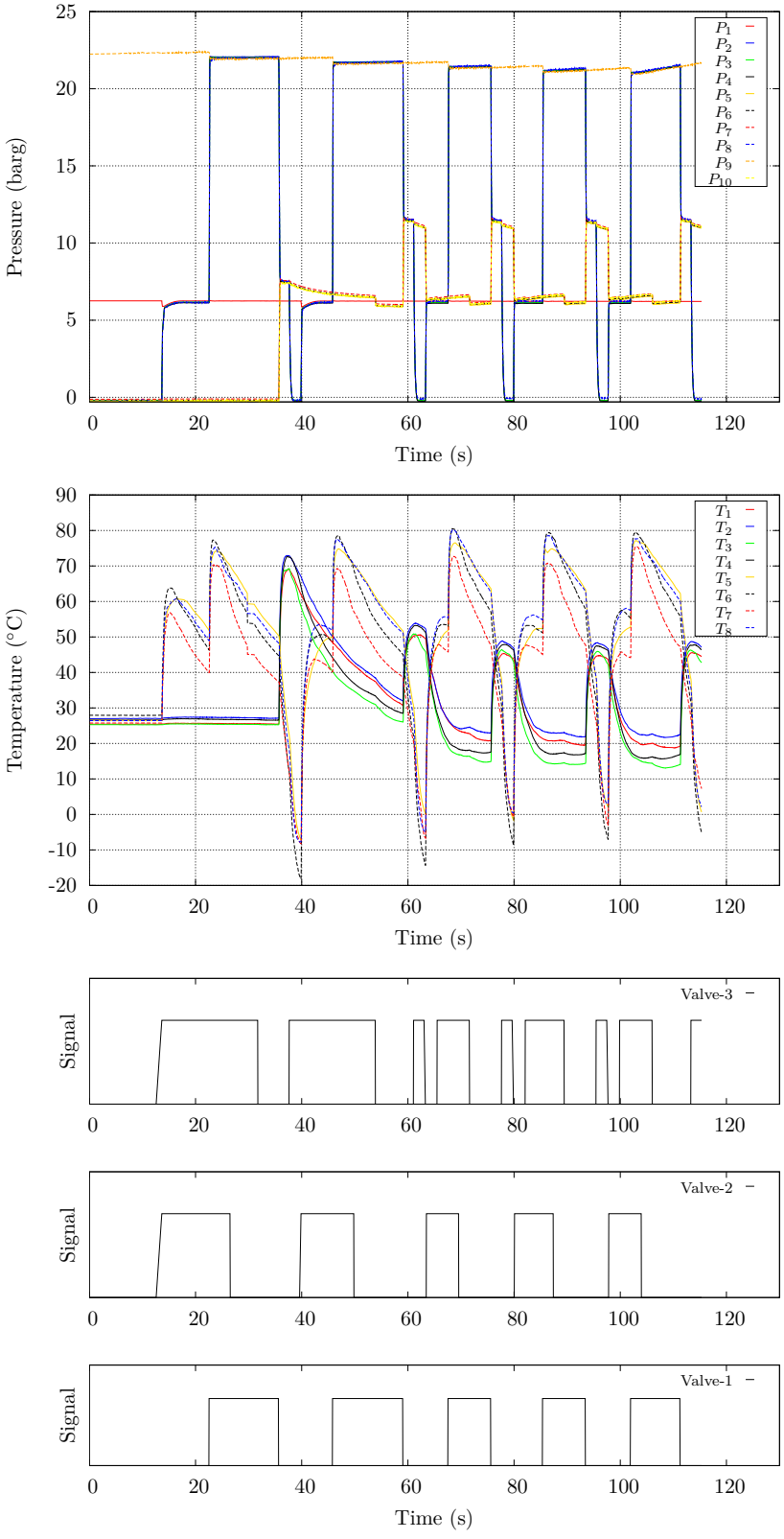

Figure 11.36: Test-2 (refer to table 6.7)

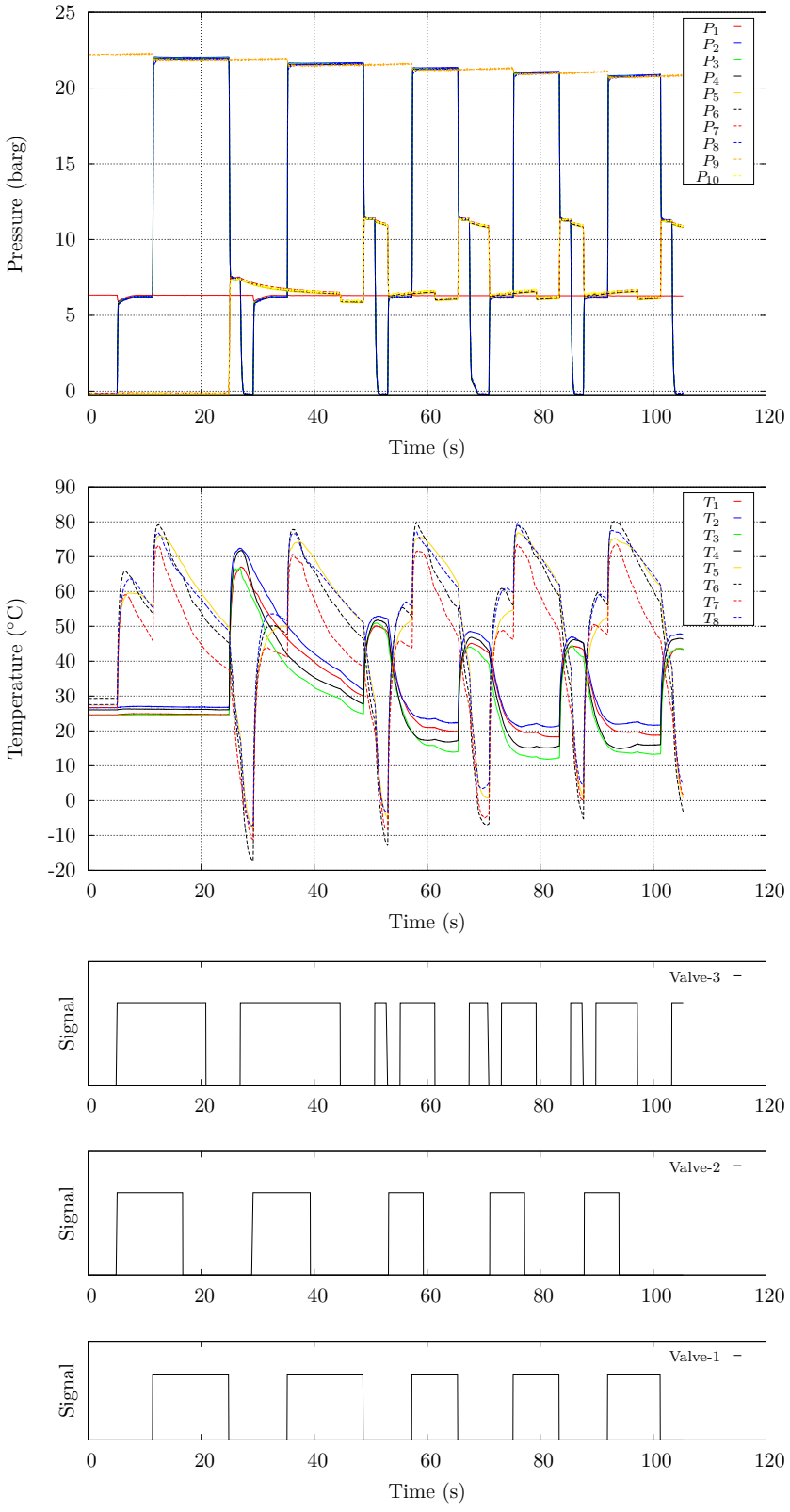

Figure 11.37: Test-4 (refer to table 6.7)

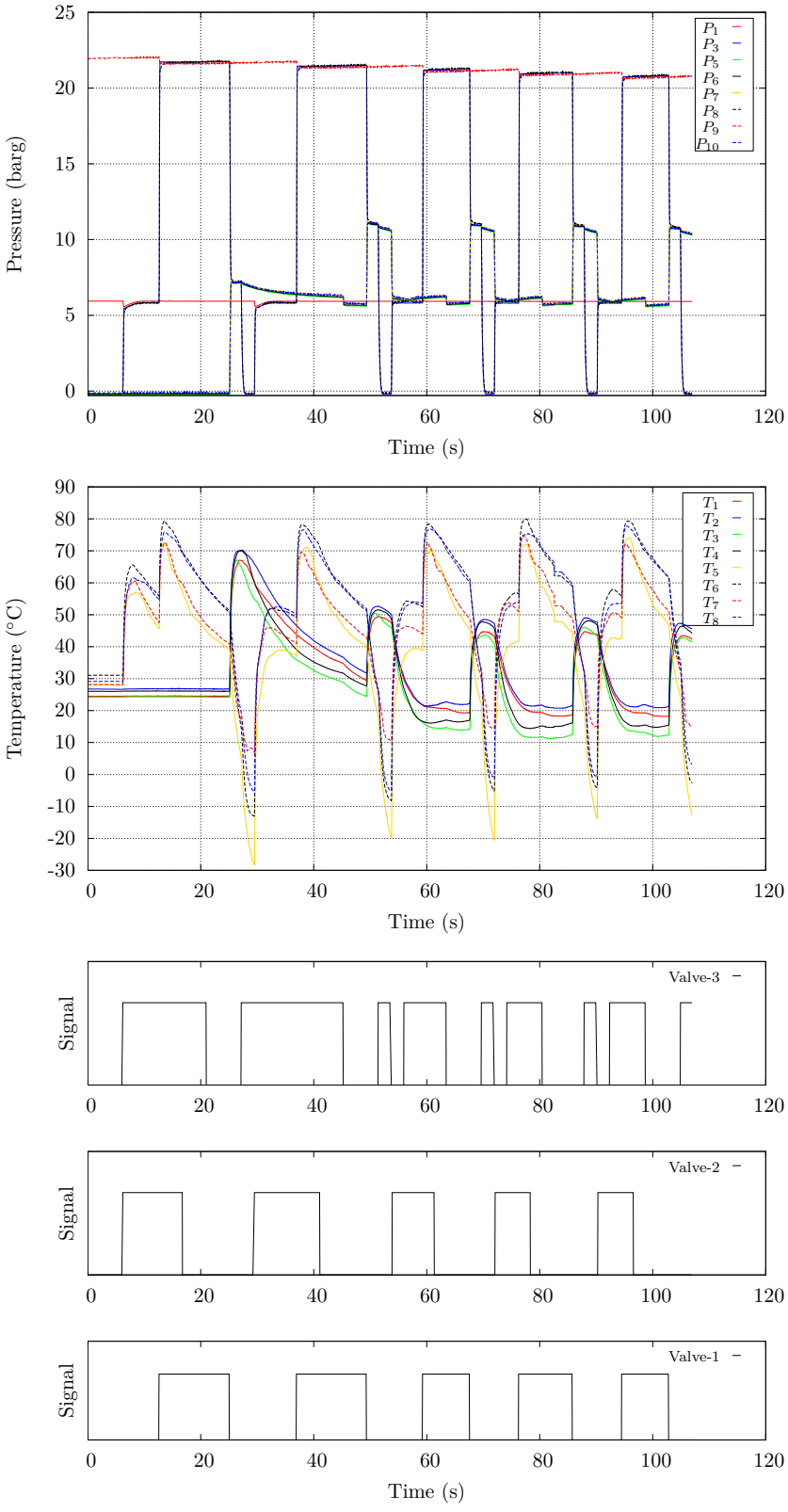

Figure 11.38: Test-8 (refer to table 6.7)

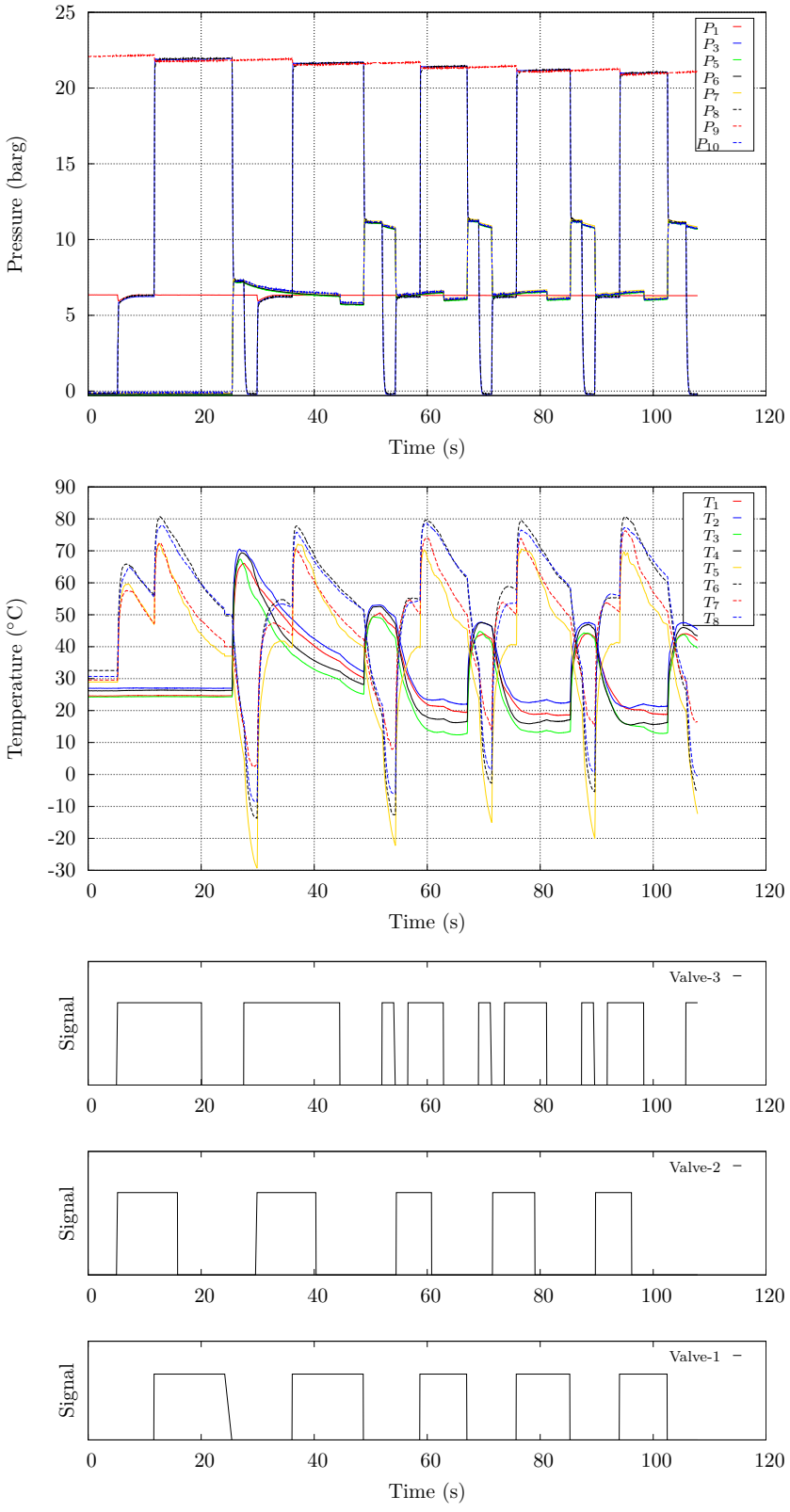

Figure 11.39: Test-10 (refer to table 6.7)

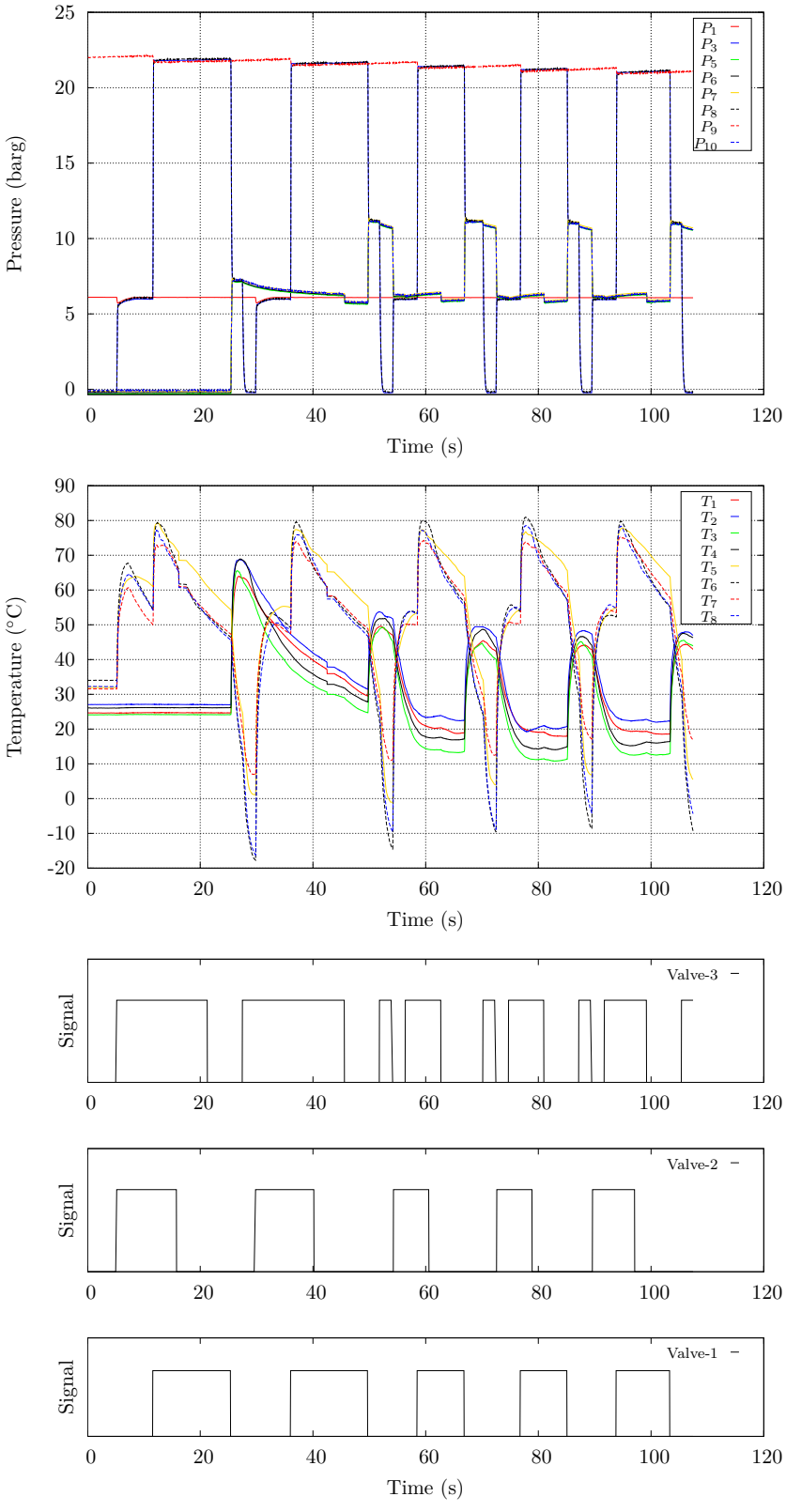

Figure 11.40: Test-7 (refer to table 6.7)

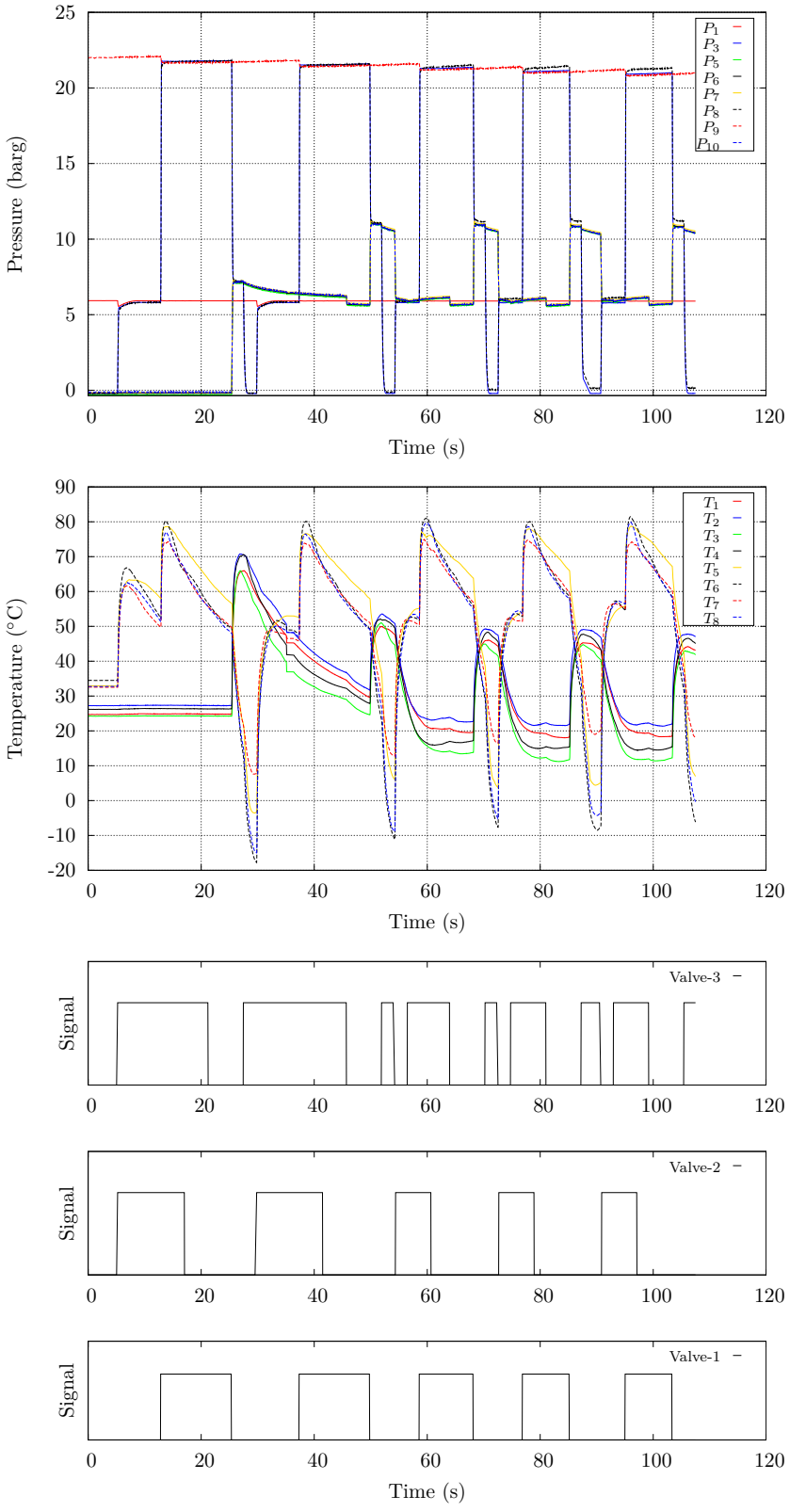

Figure 11.41: Test-9 (refer to table 6.7)

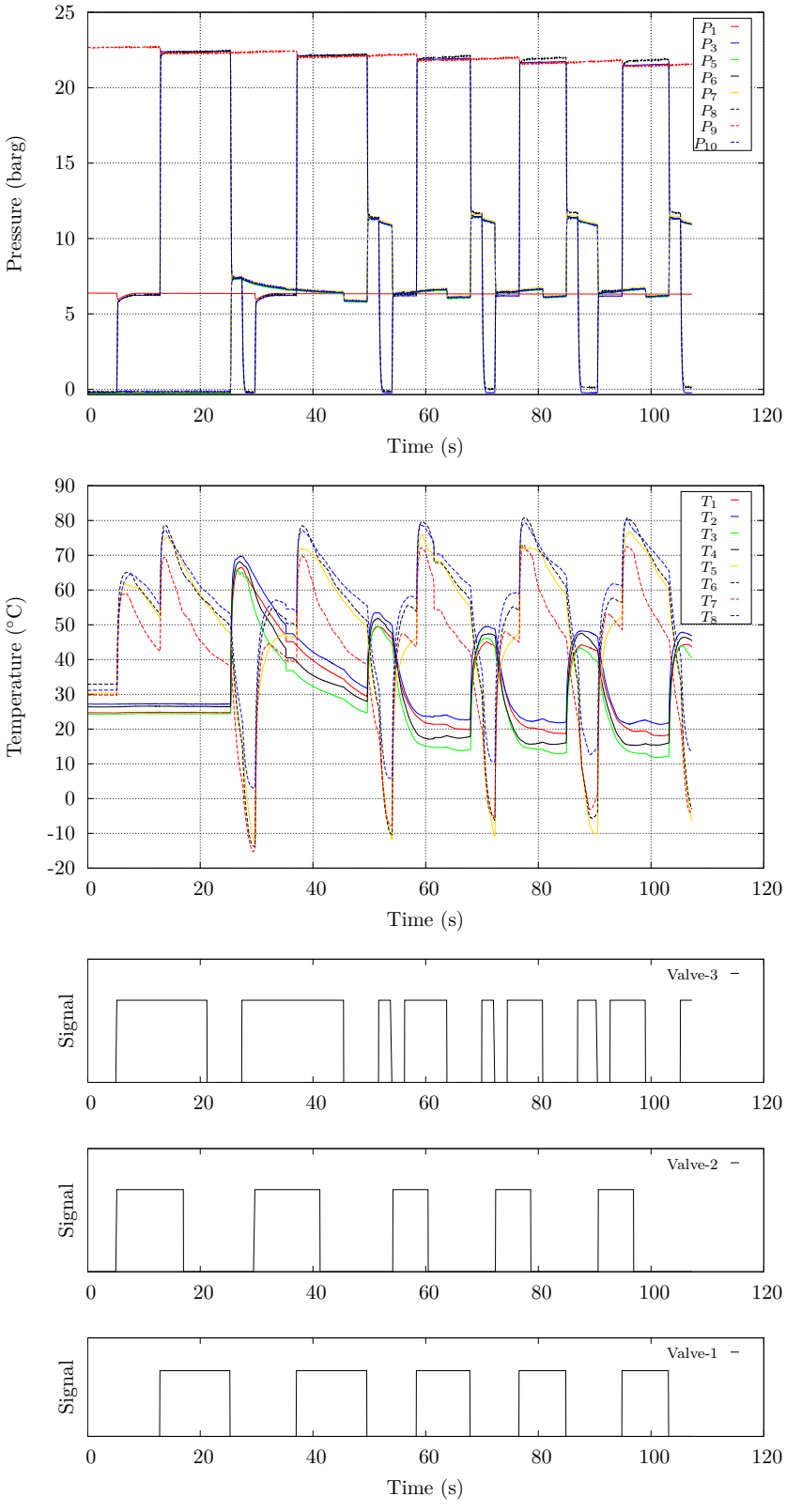

Figure 11.42: Test-6 (refer to table 6.7)

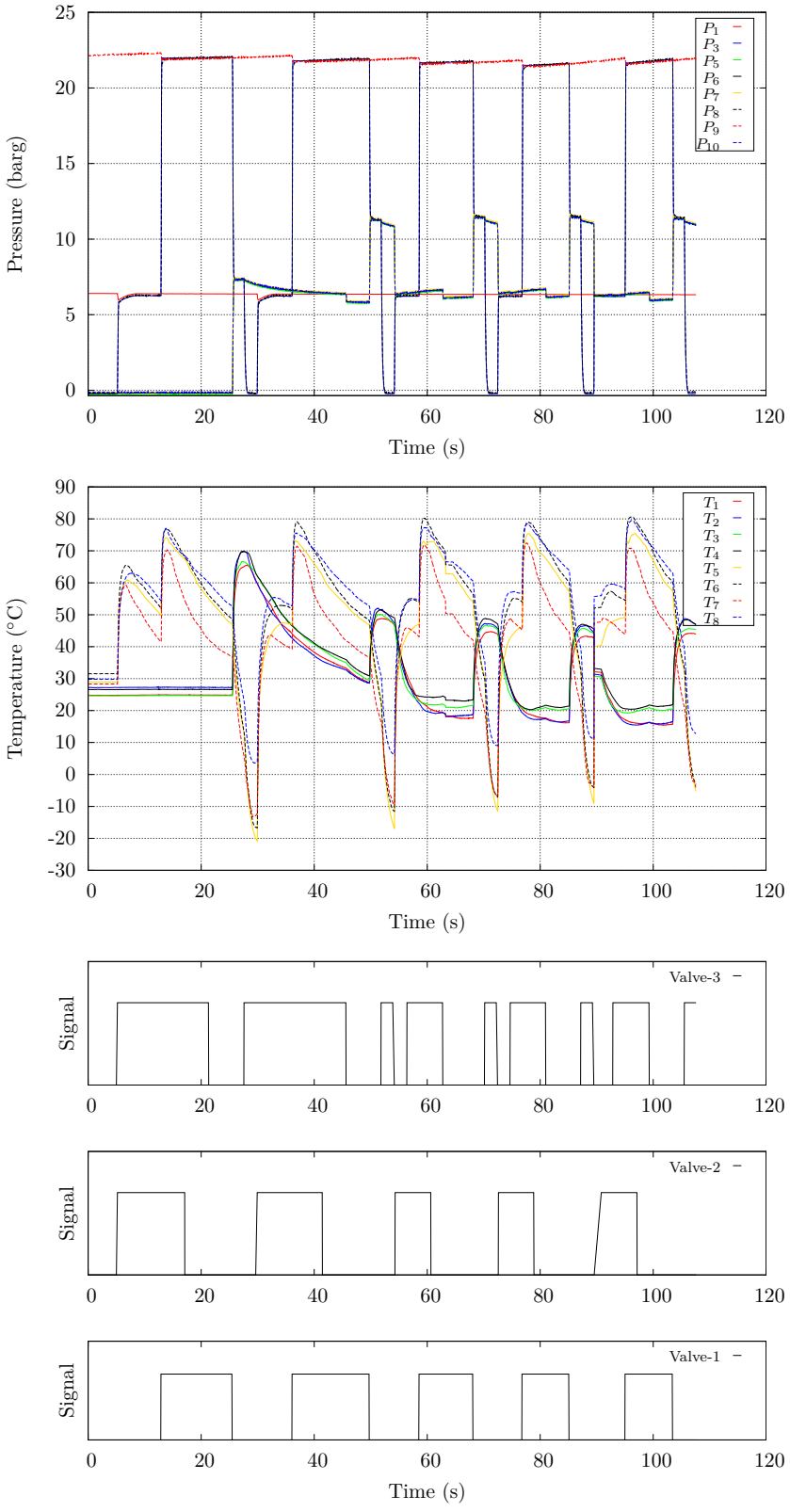

Figure 11.43: Test-36 (refer to table 6.7)

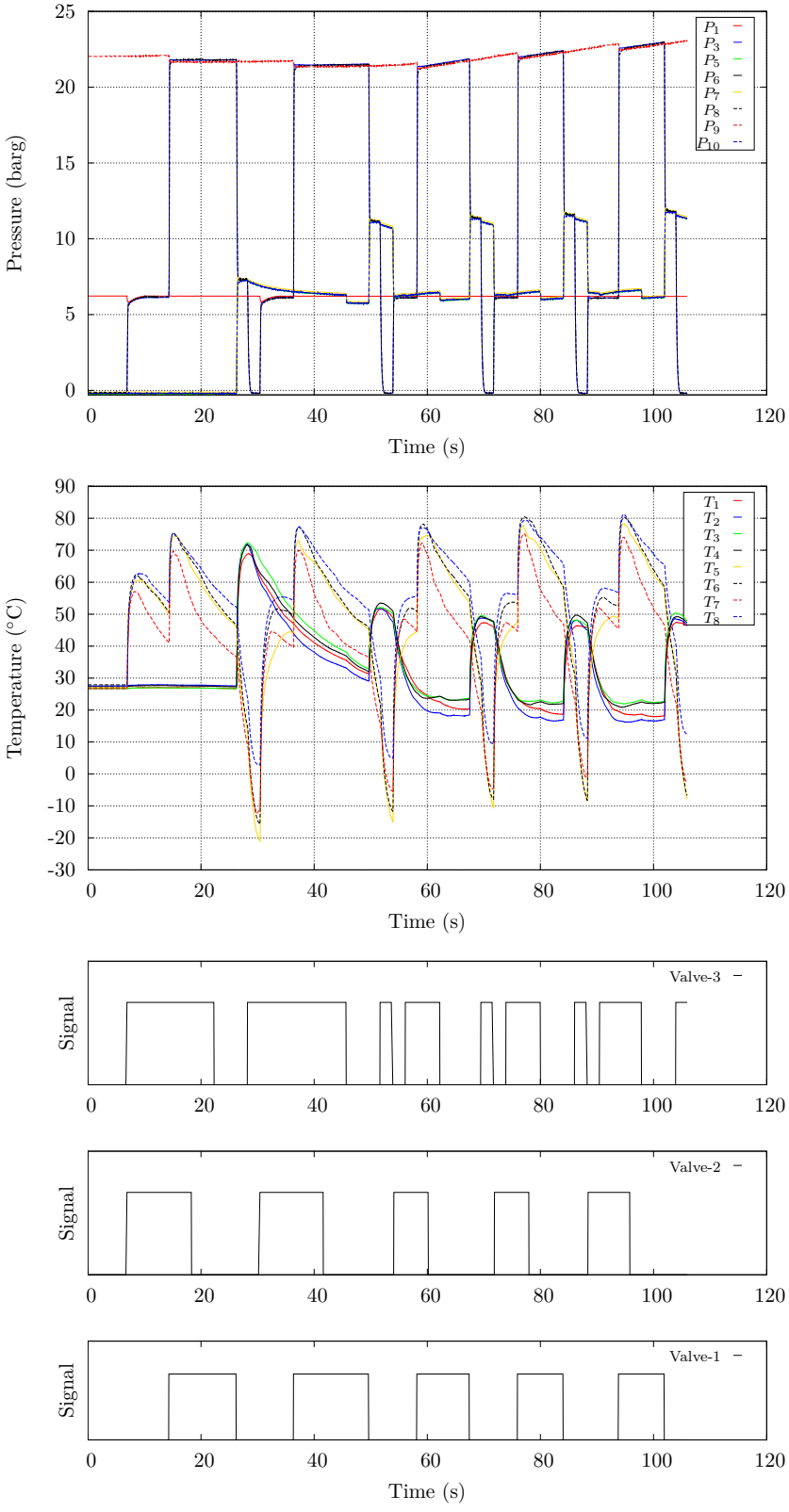

Figure 11.44: Test-26 (refer to table 6.7)

References

[1] Ansys CFX-Solver Theory Guide. *ANSYS Inc.*, 2013. 86

[2] Acosta, M. and Tamagno, J. Modelado cuasi unidimensional del movimiento de un pistón en el interior de un tubo. *Mecánica Computacional*, 2004.

[3] Agudelo, J., Sánchez, C., and Agudelo, A. Aplicación de un modelo de acción de ondas al estudio de la renovación de la carga en motores de cuatro tiempos. *Ingeniería y Desarrollo*, 2005.

[4] Aigner, R. Internal flow and valve dynamic in a reciprocating compressor. *Doctoral Dissertation*, 2007.

[5] Al-Dakkan, K., Barth, E., and Goldfarb, M. A multiple-objective sliding mode approach for the energy saving control of pneumatic servo-systems. *ASME International Mechanical Engineering Congress & Exposition*, 2003. 12

[6] Al-Ibrahim, A. Transient air temperature and pressure measurements during the charging and discharging processes of an actuating pneumatic cylinder. *Master Thesis*, 1991. 94

[7] Al-Ibrahim, A. and Otis, D. Transient air temperature and pressure measurements during the charging and discharging processes of an actuating pneumatic cylinder. *Proceedings of the 45^{th} National Conference on Fluid Power*, 1992. 94

[8] Albrecht, P. and Conow, H. Apparatus for blow molding hollow articles, in particular bottles. *Gildemeister Corpoplast - European Patent US4214860 (A)*, 1977.

[9] Andersen, B. The analysis and design of pneumatic systems. *John Wiley and Sons, Inc.*, 1967. 96

[10] Anderson, R. and Perry, Y. Mathematical modelling of a two spool flow control servovalve using a pressure control pilot. *Transactions of the ASME*, 2002.

[11] Andrighetto, P., Valdiero, A., and Carlotto, L. Study of the friction behavior in industrial pneumatic actuators. *ABCM Symposium Series in Mechatronics*, 2006. 81

[12] Arinaga, T., Kawakami, Y., Terashima, Y., and Kawai, S. Approach for energy-saving of pneumatic systems. *Proceedings of the 1st FPNI-PhD Symposium Hamburg*, 2000. 8

[13] Arnau, J., Company, R., Roselló, M., and Climent, H. A collocation method to compute one-dimensional flow models in intake and exhaust systems of internal combustion engines. *Mathematical and Computer modelling*, 2004.

[14] Arnau, J., Romero, J., Roselló, M., and Arnau, E. Treatments of geometry source terms in ce-se method to improve the mass conservation property in tapered ducts of internal combustion engines. *4º Congreso Internacional, 2º Congreso Nacional de Métodos Numéricos en Ingeniería y Ciencias Aplicadas*, 2007.

[15] Bailey, R. Design factors involved in a high pressure air coal blasting method. *National Conference on Fluid Power Association*, 1992. 13

[16] Balasoiu, V. and Popoviciu, M. Theoretical simulation of static and dynamic behavior of electro-hydraulic servo valves. *The 6th International Conference on Hydraulic Machinery and Hydrodynamics*, 2011.

[17] Bartsch, P. and Borzi, A. On the modelling and simulation of boundary flow through partially open pipe ends. *Zeitschrift für angewandte Mathematik und Physik*, 2004.

[18] Bassett, M., Winterbone, D., and Pearson, R. Calculation of steady flow pressure loss coefficients for pipe junctions. *Proceedings of the Institution of Mechanical Engineers*, 2001.

[19] Bassett, M., Fleming, N., Pearson, R., and Winterbone, D. A multiple-pipe junction model for one-dimensional gas dynamic simulations. *Society of Automotive Engineers*, 2003.

[20] Bean, H. Formulation of equations for orifice coefficients. *Journal of Basic Engineering*, 1971.

[21] Bélanger, J. Description and use of a computer program for unsteady one-dimensional calculations of shock tunnel processes. *Master Thesis*, 1990.

[22] Belforte, G. and Gastaldi, L. Dimensionamento delle linee di distribuzione dell'aria compressa e dei riduttori de pressione. *Oleodinamica Pneumatica Lubrificazione*, 1997.

[23] Belforte, G. and Raparelli, T. Scenari d'autore. *Oleodinamica Pneumatica Lubrificazione*, 1998.

[24] Bencze, F. Examination of unsteady gas flow in the suction pipe of reciprocating compressors. *Periodica Polytechnica*, 1969.

[25] Benedict, R. and Schulte, R. A note on the critical pressure ratio across a fluid meter. *Journal of Fluids Engineering*, 1973.

[26] Benedict, R. and Steltz, W. Handbook of generalized gas dynamics. *Journal of Engineering for Gas Turbines and Power*, 1962.

[27] Benson, R. Discharge of gas from cylinder to atmosphere. *The Engineer*, 1955. 51

[28] Benson, R. Experiments on two-stroke engine exhaust ports under steady and unsteady flow conditions. *Proceedings of the Institution of Mechanical Engineers*, 1959.

[29] Benson, R. The thermodynamics and gas dynamics of internal combusiton engines Vol. 1. *Oxford University Press*, 1982. 30, 51

[30] Benson, R. and Toms, R. Pulse converters in non-steady flow. 5^{th} *Australasian Hydraulics and Fluid Mechanics Conference*, 1974.

[31] Benson, R., Garg, R., and Woollatt, D. A numerical solution of unsteady flow problems. *International Journal of Mechanical Sciences*, 1963. 30, 32

[32] Benson, R., Azim, A., and Ucer, A. Some further analysis of reciprocating compressor systems. *International Compressor Engineering Conference*, 1974.

[33] Berger, E. Friction modelling for dynamic system simulation. *American Society of Mechanical Engineers*, 2002. 81

[34] Blagojevic, D. and Stojiljkovic, M. Increasing energy efficiency of the execution part of pneumatic system by restoring energy. *Mechanical Engineering, Vol. 6*, 2008. 12

[35] Blagojevic, V., Seslija, D., and Stojiljkovic, M. Cost effectiveness of restoring energy in execution part of pneumatic system. *Journal of Scientific & Industrial Research*, 2011. 12

[36] Blair, G. Design and simulation of two-stroke engines. *The Ronald Press Company*, 1996. 49

[37] Blair, G. and Arbuckle, J. Unsteady flow in the induction system of a reciprocating internal combustion engine. *Mid-Year Meeting Detroit*, 1970.

[38] Blair, G. and Ashe, M. The unsteady gas exchange characteristics of a two-cycle engine. *Society of Automotive Engineers*, 1976.

[39] Blair, G. and Cahoon, W. A more complete analysis of unsteady gas flow through a high-specific-output two-cycle engine. *Society of Automotive Engineers*, 1972. 54

[40] Blochmann, E. Apparatus for blow moulding plastic preforms having a reduced dead volume. *Krones AG - European Patent US2010285169(A1)*, 2009. 23

[41] Bober, W. and Chow, W. Nonideal isentropic gas flow through converging-diverging nozzles. *Journal of Fluids Engineering*, 1990.

[42] Bober, W. and Chow, W. Nonideal gas effects for the venturi meter. *Journal of Fluids Engineering*, 1991.

[43] Borisenko, V., Kutishchev, M., and Mukoid, V. Numerical simulation of gas-dynamics processes in a pipe open at one end. *Journal of Applied Mechanics and Technical Physics*, 1999.

[44] Botha, F. An explicit method for the analysis of transient compressible flow in pipe networks. *Master Thesis - Potchefstroom University*, 2003.

[45] Botta, N. and Jeltsch, R. A numerical method for unsteady flows. *Seminar für Angewandte Mathematik - Research Report no. 94-11*, 1994.

[46] Botta, N. and Jeltsch, R. A numerical method for unsteady flows. *Applications of Mathermatics*, 1995.

[47] Bourges, G., Eliach, J., and Medina, M. Modelización numérica de un compresor monocilindrico de desplazamiento positivo. *Mecánica Computacional*, 2006.

[48] Brunner, A., Blochmann, E., and Geltinger, N. Method and device for blow molding containers. *Krones AG - European Patent EP1974892(A2)*, 2009. 22

[49] Buffard, T. and Hérad, J. A conservative fractional step method to solve non-isentropic euler equations. *Computer Methods in Applied Mechanics and Engineering*, 1997.

[50] Buffard, T., Gallouët, T., and Hérard, J. A sequel to a rough godunov scheme - application to real gases. *Computers and Fluids*, 2000.

[51] Bunel, C. and Martin, M. Method and installation for making containers by blowing thermoplastic blanks. *Sidel - European Patent PCT/FR98/01553*, 1999. 16

[52] Cai, M. Energy comparison of electric and pneumatic actuators. *5^{th} JFPA International Symposium on Fluid Power*, 2002. 11, 137

[53] Cai, M., Kawashima, K., and Kagawa, T. Simulation for energy savings in pneumatic system. *System modelling and Simulation, Springer*, 2006. 11, 137

[54] Cai, M., Kawashima, K., and Kagawa, T. Power assessment of flowing compressed air. *Journal of Fluids Engineering*, 2006. 10, 137

[55] Carello, M., Ivanov, A., and Mazza, L. Perdite si pressione in linee di distribuzione dell'aria compressa. *Oleodinamica Pneumatica Lubrificazione*, 1998.

[56] Carlsson, P. Flow through a throttle body - a comparative study of heat transfer, wall surface roughness and discharge coefficient. *Doctoral Dissertation*, 2007.

[57] Castillo, F., Luc Dugard, E., and Talon, V. Restriction model independent method for non isentropic outflow valve boundary problem resolution. *Society of Automotive Engineers*, 2012.

[58] Castillo, F., Luc Dugard, E., Talon, V., and Pascal Chesse, D. Intra-pipe restriction non-homentropic boundary resolution method. *Society of Automotive Engineers*, 2013.

[59] Chakravarthy, S. Development of upwind schemes for the euler equations. *NASA Contractor Report 4043*, 1987.

[60] Chalet, D. Étude et modélisation des ondes de pression dans les géométries complexes. Application à la simulation du fonctionnement d'un moteur à combustion interne. *Thèse de Doctorat*, 2003.

[61] Chalet, D. and Cheese, P. Analysis of unsteady flow through a throttle valve using cfd. *Engineering Applications of Computational Fluid Mechanics*, 2010.

[62] Chalet, D., Cheese, P., and Hetet, J. Boundary conditions modelling of one-dimensional gas flows in an internal combustion engine. *International Journal of Engine Research*, 2008.

[63] Chalet, D., Cheese, P., Hetet, J., and Tauzia, X. Inflow boundary condition for one-dimensional gas dynamics simulation code of internal combustion engine manifolds. *Proceedings of the Institution of Mechanical Engineers*, 2009.

[64] Chang, J., Gürap, O., Filipi, Z., and Assanis, D. New heat transfer correlation for an hcci engine derived from measurements of instantaneous surface heat flux. *Society of Automotive Engineers*, 2004.

[65] Chen, Z., Gao, B., and Zi-Niu, W. Compressible flow equations based on moving coordinates determined by the wave speed. *International Journal for Numerical Methods in Fluids*, 2007.

[66] Chiou, J., Chiang, M., and Chen, C. Numerical simulation method applied to the multi-expansion exhaust system of a two-stroke engine. *Proceedings of the Institution of Mechanical Engineers*, 1994.

[67] Chou, P. and Karpp, R. Solution of blast waves by the method of characteristics. *Drexel Institute of Technology, Report no. 125-7*, 1965.

[68] Chou, P. and Karpp, R. Solution of blast waves by the method of characteristics. *Drexel Institute of Technology, Report no. 125-7*, 1965.

[69] Cline, C. and Harvey, O. Nonlinear control and active damping of a forced-feedback metering poppet valve. *Doctoral Dissertation*, 2007.

[70] Coates, S. and Blair, G. Further studies of noise characteristics of internal combustion engine exhaust systems. *National Combined Farm,Construction & Industrial Machinery and Powerplant Meetings*, 1974.

[71] Coelho, R., Lage, P., and Silva, A. A comparison of hyperbolic solvers for ideal and real gas flows. *Brazilian Journal of Chemical Engineering*, 2006.

[72] Colella, P. A direct eulerian muscl scheme for gas dynamics. *Society for Industrial and Applied Mathematics*, 1985.

[73] Coney, M., Stephenson, P., Malmgren, A., Linnemann, C., and Morgran, R. Development of a reciprocating compressor using water injection to achieve quasi-isothermal compression). *International Compressor Engineering Conference*, 2002.

[74] Connor, L. and Taylor, F. The centered one-dimensional unsteady expansion of a vibrationally relaxing nitrogen-oxygen mixture. *NASA Technical note D-3805*, 1967.

[75] Copigneaux, P., Tobaly, P., and Godin, M. Isentropic expansion of dry saturated vapor application to the design of safety valves. *Journal Pressure Vessel Technology*, 1984.

[76] Corberán, J. and Gascón, L. New method to calculate unsteady 1-d compressible flow in pipes with variable cross section. application to the calculation of the flow in intake and exhaust pipes of i.c. engines. *ICE-Vol. 23, Engine modelling*, 1995.

[77] Corberán, J. and Gonzálvez, J. A global model for piston compressors with gas dynamics calculation in the pipes. *International Compressor Engineering Conference*, 1998.

[78] Corberán, J., Royo, R., and Gascón, L. Esquemas numéricos avanzados para el cálculo del flujo por el interior de los motores de combustión interna alternativa. *Mecánica Computacional Vol. XXIII*, 2004.

[79] Costall, A. A one-dimensional study of unsteady wave propagation in turbocharger turbines. *Doctoral Disseratation*, 2007.

[80] Costilow, E. and Neumann, H. Design of axisymmetric exhaust nozzles by method of characteristics incorporating a variable isentropic exponent. *Technical Report R-33*, 2000.

[81] Craigen, J. Mathematical model of a pulsating combustor. *Doctoral Dissertation*, 1975.

[82] Cruz, F., de Negri, V., and Guenther, R. Mathematical modelling of an electropneumatic pressure regulator servo-valve. *ABCM Symposium in Mechatronics*, 2004.

[83] de Giorgi, R., Bideaux, E., and Sesmat, S. Dynamic thermal model of a discharging process of a pneumatic chamber. *Proceedings of 4^{th} FPNI-PhD Symposium*, 2006. 116

[84] de Giorgi, R., Kobbi, N., Sesmat, S., and Bideaux, E. Thermal model of a tank for simulation and mass flow rate characterization purposes. *Proceedings of 7th JFPS International Symposium on Fluid Power*, 2008. 116

[85] de Haller, P. Méthode graphique pour la résolution de quelques problèmes de dynamique des gaz. *Revue Technique Sulzer*, 1945.

[86] de las Heras, S. and Codina, E. La compression del gas in sospensioni idropneumatiche. *Oleodinamica Pneumatica Lubrificazione*, 1997.

[87] Detrois, C. Method for blow moulding. *Krones AG - European Patent EP1974892(A2)*, 2007. 20, 22

[88] Dobremelle, M. Etude dynamique et thermique de l'écoulement d'un fluide monophasique compressible: application aux tubulures d'un moteur thermique. *Rev. Gén. Therm.*, 1973. 118

[89] Donat, R. and Martínez, A. A flux-limited second order scheme for hyperbolic conservation laws with source terms. *Monografías de la Real Academia de Ciencias de Zaragoza*, 2009.

[90] Dubois, F. Partial riemann problem, boundary conditions, and gas dynamics. *Published in Absorbing Boundaries and Layers, Domain Decomposition Methods: Applications to Large Scale Computations*, 2000.

[91] Dubois, F. and Le Floch, P. Boundary conditions for nonlinear hyperbolic systems of conservation laws. *Second International Conference on Hyperbolic Problems - Aachen*, 1988.

[92] Dustin, M. Analog computer study of design parameter effects on the stability of a direct-acting gas pressure regulator. *NASA Technical Note D-6267*, 1971.

[93] Dutton, J. and Coverdill, R. Experiments to study the gaseous discharge and filling of vessels. *International Journal of Engineering*, 1997. 95

[94] Ehrlich, S. Conserving energy used for pneumatic systems. *Foundry M & T*, 1976. 3

[95] Elasfouri, A., Robert, M., and Rochelle, P. Perméabilité des moteurs diesel à quatre temps et étude de línfluence de la rotation de la charge d'air. *Entropie*, 1972.

[96] Elliot, J. Apparatus and method for blow moulding articles. *EBAC Ltd - Patent no. GB 2431372 A*, 2007. 19

[97] Ellis, W. Conserving energy in pneumatic systems. *National Conference on Fluid Power Association*, 1977. 3

[98] Els, P. and Grobbelaar, B. Heat transfer effects on hydropneumatic suspension systems. *Journal of Terramechanics*, 1999.

[99] Faezian, A., Modarres, M., and Onorati, A. N-junction modelling in perforate silencers for internal combustion engines. *Scientia Iranica*, 2005.

[100] Fatsis, A., Lafond, A., and Ribaud, Y. Analyse préliminaire d'un comprex à trois portes à l'aide d'un modèle numérique. *Aerospace Science and Technology*, 1998.

[101] Ferm, L. Non-reflecting boundary conditions for the steady euler equations. *Journal of Computational Physics 122,307-316*, 1995.

[102] Ferraresi, C., Franco, W., Quaglia, G., and Scopesi, M. Il risparmio energetico nei sistemi pneumatici. *Oleodinamica e Pneumatica*, 2008.

[103] Ferreira, T. and Lainor, J. Analysis of the influence of valve geometric parameters on the effective flow and force areas. *International Compressor Engineering Conference*, 1986.

[104] Fezoui, F. and Stoufflet, B. A class of implicit upwind schemes for euler simulations with unstructured meshes. *Institut National de Recherche en Informatique et en Automatique*, 1986.

[105] Finger, D. and Asbrand, H. Air recirculation in a blow-molding process. *Krones AG - European Patent no. PCT/DE2004/041973*, 2004. 18

[106] Fleischer, H. Energy savings in industry through air conservation. *National Conference on Fluid Power Association*, 1975. 3

[107] Fleischer, H. Why it pays to use air wisely. *National Conference on Fluid Power Association*, 1981. 3

[108] Fleischer, H. Designing energy-efficient pneumatic circuits. *Hydraulics & Pneumatics*, 1991. 10

[109] Fleming, J., Shi, P., and Brown, J. The importance of wall friction in the compressible of gas through a compressor valve. *International Compressor Engineering Conference*, 1984.

[110] Förster, K. Test cases for unsteady one-dimensional flow with variable cross-section. *Acta Mechanica*, 1998.

[111] Frisch, H. Device for automatically returning an actuating cylinder. *Hoerbirger Ventilwerke AG - European Patent no. DE3233739*, 1983. 6

[112] Fukushima, H., Handa, T., and Kodama, K. Process for the production of blow molded articles accompanied with the recovery of a blowing gas. *Air Products and Chemicals Inc - Patent No.4394333*, 1981. 14

[113] Funaki, T., Yamazaki, S., Kawashima, K., and Kagawa, T. Development of continuous unsteady flow generator for gases. *Proceedings of the 6th JFPS International Symposium on Fluid Power*, 2005. 171

[114] Funaki, T., Kato, T., Kawashima, K., and Kagawa, T. Development of unsteady gas flow generator with highly precise inlet flow rate control system. *Proceedings of the 7th International Symposium on Fluid Power*, 2008. 171

[115] Gascón, L. Estudio de esquemas en diferencias finitas para el cálculo del flujo compresible, unidimensional, no estacionario y no isoentrópico. *Tesis Doctoral*, 1995.

[116] Gascón, L. and Corberán, J. Construction of second-order tvd schemes for nonhomogeneous hyperbolic conservation laws. *Journal of Computational Physics*, 2001.

[117] Gauchel, W. Energy saving pneumatic systems. *O+P Ölhydraulik und Pneumatik*, 2006.

[118] Giacinto, M. and Valorani, M. Shock detection and discontinuity tracking for unsteady flows. *Computers & Fluids*, 1989.

[119] Godunov, S. A difference scheme for numerical solution of discontinuous solution of hydrodynamic equations. *Matematicheskii Sbornik*, 1959. 31

[120] Gordić, D., Babić, M., and Jovicić, N. Modelling of spool position feedback servovalves. *International Journal of Fluid Power*, 2004. 81

[121] Gosse, L. A well-balanced scheme using non-conservative products designed for hyperbolic systems of conservation laws with source terms. *Mathematical Models and Methods in Applied Sciences*, 2001.

[122] Guinot, V. Wave propagation in fluids. *John Wiley and Sons, Inc.*, 2008.

[123] Guo-Hua, T. and Xiang-Jiang, Y. A characteristic-based shock-capturing for hyperbolic problems. *Journal of Computational Physics*, 2007.

[124] Gupta, V. and Munjal, M. Time-domain-finite-wave analysis of the engine exhaust system by means of the stationary-frame method of characteristics - part i. theory. *Sadhana*, 1993.

[125] Gustavsson, E. modelling of wave propagation in combustion engines. *Scientia Iranica*, 2014.

[126] Güven¸, L. and Srinivasan, K. Modelling and parameter identification of a pneumatic constant force device. *Turkish Journal of Engineering & Environmental Sciences*, 2000.

[127] Hai, S. Solution of gas pulsation equations in compressor suction and discharge lines by mixed-mode approach. *International Compressor Engineering Conference*, 1976.

[128] Hammitt, F. Natural convection heat transfer in closed vessels with internal heat sources - analytical and experimental study. *Doctoral Dissertation*, 1958.

[129] Harju, B. Single acting pneumatic piston-cylinder unit. *European Patent Office - PCT/SE94/01187*, 1994. 6

[130] Harju, B. Single acting pneumatic piston-cylinder unit. *European Patent Office - PCT/SE96/01467*, 1996. 6

[131] Harju, B. Single acting pneumatic piston-cylinder unit. *European Patent Office - PCT/SE97/00349*, 1997. 6

[132] Harrison, M. and Pérez, R. A hybrid boundary for the prediction of intake wave dynamics in ic engines. *Journal of Sound and Vibration*, 2004.

[133] Har' El, N. Numerical solution of one-dimensional duct flow by method of characteristics. *Research Report*, 1994.

[134] Hatton, A. Unsteady thermodynamic processes. *The Engineer London*, 1957. 132

[135] Hepke, J. and Weber, J. Energy saving measures on pneumatic drive systems. *The 13th Scandinavian International Conference on Fluid Power*, 2013.

[136] Hermier, F. Système et procédé de soufflage de corps creux en matière plastique minimisant la consommation d'air haute pression. *Newtec International Group - Patent no. WO2004098862 A2*, 2004. 17, 20

[137] Hirdina, J. Process and device for the manufacture of a particularly heat-resistant hollow body. *Krones AG - European Patent no. PCT/EP2005/002399*, 2004. 17, 22

[138] Hirokazu, Y. *Asahi Chemical Ind Co Ltd Patent No. JPH05309726 (A)*, 1993. 15

[139] Holt, M. Review of godunov methods. *NASA Contractor Report 198322*, 1996.

[140] Hong, C. and Huang, G. Numerical computation of unsteady gas flow in the ducts of reciprocating engines. *Numerical heat transfer*, 1997.

[141] Hopkinson, B. The charging of two-cycle internal combustion engines. *Journal of the American Society for Naval Engineers*, 1914.

[142] Horlock, J. and Winterbone, D. The thermodynamics and gas dynamics of internal combustion engines Vol. 2. *Oxford University Press*, 1986.

[143] Horlock, J. and Woods, W. The thermodynamics of charging and discharging processes. *Proceedings of the Institution of Mechanical Engineers*, 1965. 126

[144] Hös, C. Dynamic behaviour of hydraulic drives. *Master Thesis*, 2005.

[145] Huang, J. Experimental shock tube study of ignition promotion for methane under engine relevant conditions. *Doctoral Dissertation*, 2001.

[146] Huang, S. and Chou, P. Solution of blast waves by a constant time scheme in the method of characteristics. *Drexel Institute of Technology, Report no. 125-9*, 1966.

[147] Huang, S. and Chou, P. Calculations of expanding shock waves. *Final Report*, 1968.

[148] Huang, S. and Chou, P. Calculations of expanding shock waves and late-stage equivalence. *Drexel Institute of Technology - Contract no. DA-18-001-AMC-876 (X)*, 1968.

[149] Hudson, J. A review on the numerical solution of the 1D Euler equations. *Manchester Institute for Mathematical Sciences*, 2006.

[150] Huping, Z., Senoo, M., and Oneyama, N. Development of calculation programs for energy saving in pneumatic systems. 7^{th} *International Symposium on Fluid Control, Measurement and Visualization*, 2003. 10

[151] Ignatiev, K., Pirumov, I., Chrustalyov, B., Perevozchikov, M., and Zdalinsky, V. Study of the valve element motion and the gas flow in the straight-flow valves. *International Compressor Engineering Conference*, 1992.

[152] Ikeda, M. Air operation method and apparatus of various drive devices of stretch blow molded part. *AK Tech Lab Inc - Japanese Patent No. JPH0985812*, 1995. 15, 22

[153] ISO/TC-131/SC-5. Pneumatic fluid power - components using compressible fluids - determination of flow-rate characteristics - part 3: Alternative test methods - isothermal discharge test. *ISO International Standard ISO/WD 6358-3*, 2005. 87, 166

[154] ISO/TC-131/SC-5. Pneumatic fluid power - components using compressible fluids - determination of flow-rate characteristics - part 5: Alternative test methods - simple discharge test. *ISO Internation Standard ISO/WD 6358-5*, 2005. 87, 166

[155] Jaisankar, S. and Raghurama, S. A central rankine hugoniot solver for hyperbolic conservation laws. *Journal of Computational Physics*, 2008.

[156] Jameson, A. Positive schemes and shock modelling for compressible flows. *International Journal For Numerical Methods in Fluids*, 1995.

[157] Janota, M., Hallam, A., Brock, K., and Dexter, S. The prediction of diesel engine performance and combustion chamber component temperatures using digital computers. *Proceedings of the Institution of Mechanical Engineers*, 1967.

[158] Jebar, H., Lichtarowicz, A., and Roylance, T. Thermodynamic analysis of charging processes. 4^{th} *International Fluid Power Symposium*, 1975. 94

[159] Jebar, H., Roylance, T., and Lichtarowicz, A. Nomogram methods for the design of pneumatic cylinder systems. *5th International Fluid Power Symposium*, 1978.

[160] Jenny, E. Utilisation de l'énergie des gaz d'échappement pour la suralimentation des moteurs diesel à quatre temps. *Revue Brown Boveri*, 1950.

[161] Jian, R. Development of fluid power control valves. *National Fluid Power Association*, 1992.

[162] Jin, S. Runge-kutta methods for hyperbolic conservation laws with stiff relaxation terms. *Journal of Computational Physics*, 1995.

[163] Jinn-Chuang, Y. and Kuang-Ping, C. Use of characteristics method with cubic interpolation for unsteady-flow computation. *International Journal for Numerical Methods in Fluids*, 1993.

[164] Johnson, A., Espina, P., Mattingly, G., and Wright, J. Numerical characterization of the discharge coefficient in critical nozzles. *NCSL Workshop & Symposium*, 1998.

[165] Johnson, R. Calculations of real-gas effects in flow through critical-flow nozzles. *Journal of Basic Engineering*, 1964.

[166] Johnson, R. Real-gas effects in critical flow through nozzles and tabulated thermodynamics properties. *Journal of Fluids Engineering*, 1964.

[167] Johnston, S. A characterization of unsteady gas discharge from a vessel. *Master Dissertation*, 1974.

[168] Jones, A. Noise characteristics and exhaust process gas dynamics of a small 2-stroke engine. *Doctoral Dissertation*, 1978.

[169] Jones, A. and Brown, G. Gas dynamics of the exhaust process and the radiated noise from two-stroke engines. *6th Australasian Hydraulics and Fluid Mechanics Conference*, 1977.

[170] Jones, A. and Brown, G. Determination of two-stroke engine exhaust noise by the method of characteristics. *NASA TM-84061*, 1981.

[171] Jover, D. and Storione, S. Container blowing device. *Technoplant Engineering S.A. - European Patent no. WO03/009993*, 2003. 17, 20

[172] Jover, D. and Storione, S. Method of gas blow forming packaging and device for implementing same. *Technoplant Engineering S.A. - European Patent EP1922206*, 2005. 19

[173] Joyner, U. Charts of pressure,density,and temperatures changes at an abrupt increase in cross-sectional area of flow of compressible air. *National Advisory Committee for Aeronautics*, 1945.

[174] Jurić, Z., Kulenović, Z., and Kulenović, D. Influence of the hydraulic relief valve poppet geometry on valve performance. *14^{th} International Research / Expert Conference*, 2010.

[175] Kagawa, T., Cai, M., Fujita, T., and Takeuchi, M. Energy consideration of pneumatic cylinder actuating system. *Sixth Triennal International Symposium on Fluid Control*, 2000. 10

[176] Kagawa, T., Cai, M., Kawashima, K., and Funaki, T. Energy conversion mechanics and power evaluation of compressible fluid in pneumatic actuator systems. *IECEC*, 2002. 11

[177] Kagawa, T., Wang, T., Terashima, Y., Morozumi, T., Mogami, T., and Oneyama, N. Determination of flow rate characteristics of small pneumatic valves using an isothermal chamber by pressure response. *International Conference on Fluid Control, Measurements, and Visualization*, 2003. 171

[178] Kandylas, I. and Stamelos, A. Engine exhaust system design based on heat transfer computation. *Energy Conversion & Management*, 1999.

[179] Kato, M., Kurohashi, M., Fulikawa, T., and Aoshima, M. Dynamic behaviour of valves with pneumatic chambers for reciprocating compressors. *International Compressor Engineering Conference*, 1988.

[180] Kato, M., Kurohashi, M., Fulikawa, T., and Aoshima, M. Dynamic behaviour of valves with pneumatic chambers for reciprocating compressors. *International Compressor Engineering Conference*, 1988.

[181] Kawashima, K. and Kagawa, T. Unsteady flow generator for gases using an isothermal chamber. *Measurement*, 2003. 171

[182] Kawashima, K., Ishii, Y., Funaki, T., and Kagawa, T. Determination of flow rate characteristics of pneumatic solenoid valves using an isothermal chamber. *Journal of Fluids Engineering*, 2004. 171

[183] Ke, J., Thanapalan, K., Wang, J., and Wu, H. Development of energy efficient optimal control for servo-pneumatic cylinders. *Control 2004, University of Bath*, 2004. 12

[184] Keenan, J. and Neumann, E. Friction in pipes at supersonic and subsonic velocities. *Technical note no. 963 - NACA*, 1945.

[185] Keeney, J. Investigation of compressed air energy storage efficiency. *Master Thesis*, 2013.

[186] Keller, M., Abderhalden, D., and Boos, P. Stackable valve system. *Norgren GmbH - European Patent US2011212213(A1)*, 2006. 23

[187] Kiijärvi, J. Diesel fuel injection system simulation. *Doctoral Thesis - Helsinki University of Technology*, 1997.

[188] Kim, Y., Lee, J., Kim, S., and Favrat, D. Potential and evolution of compressed air energy storage - Energy and exergy analyses. *Entropy*, 2012. 136

[189] Kobayashi, T. and Nishiyama, A. Operating method of blow molding apparatus. *NISSEI ASB Machine Co Ltd - Japanese Patent no. JPH0985812*, 2010. 22

[190] Kolobov, B., Kolobov, P., and Shepelenko, V. Numerical model of the aspiration system of an internal combustion engine. *Journal of Applied Mechanics and Technical Physics*, 1998.

[191] Komendera, J. Air savings through proper valve selection. *National Conference on Fluid Power Association*, 1971. 2

[192] Konrad, J. Compressed air energy storage - an exergy-based analysis of turbomachinery systems. *Doctoral Dissertation*, 2011.

[193] Koo, J. and Bae, C. Effect of breathing characteristics on the performance in spark-ignition engines. *FISITA World Automotive Congress*, 2000.

[194] Kornhauser, A. and Smith, J. A comparison of cylinder heat transfer expressions based on prediction of gas spring hysteresis loss. *American Society of Mechanical Engineers*, 1987.

[195] Kouremenos, D. and Antonopoulos, K. Sound velocity and isentropic exponents of real air on its compressibility chart. *International Journal of Heat and Fluid Flow*, 1991.

[196] Kouremenos, D., Antonopoulos, K., and Kakatsios, X. A correlation of the isentropic exponents of real gases. *International Journal of Heat and Fluid Flow*, 1988.

[197] Kriel, A. Pressure formulation and adaptive control of numerical algorithms for transient flow in pipe networks. *Doctoral Dissertation*, 2012.

[198] Krishnaswamy, K. On using unstable electrohydraulic valves for control. *Journal of Dynamic Systems, Measurement, and Control*, 2002.

[199] Kuroshita, K. and Suzuki, A. Study on measurement method of flow rate characteristics of pneumatic solenoid valve. *Transactions of the Japan Fluid Power System Society*, 2011. 171

[200] Kuroshita, K., Takeuchi, T., and Ichikawa, T. Study on the temperature characteristics of a pneumatic cylinder system (part 1, experimental investigation). *Hydraulics & Pneumatics*, 1985. 40

[201] Lakshminarayanan, P., Janakiraman, P., Gajendra Babu, M., and Murthy, B. Prediction of gas exchange processes in a single cylinder internal combustion engine. *Society of Automotive Engineers*, 1979.

[202] Levenez, Y. and Legris, R. Compressed fluid saving device. *United States Patent no. US4608910*, 1985. 7

[203] Leveque, R. Finite volume methods for hyperbolic problems. *Cambridge University Press*, 2002.

[204] Leveque, R. and Yee, H. A study of numerical methods for hyperbolic conservation laws with stiff source terms. *NASA - Technical Memorandum - 100075*, 1988.

[205] Licskó, G., Champneys, A., and Hõs, C. Nonlinear analysis of a single stage pressure relief valve. *IAENG International Journal of Applied Mathematics*, 2009.

[206] Linfield, K. A study of the discharge coefficient of jets from angled slots and conical orifices. *Doctoral Dissertation*, 2000.

[207] Lingaiah, K. Machine design data handbook. *McGraw-Hill Companies*, 1992.

[208] Linjama, M., E., M., Virvalo, T., and Koskinen, K. Low-pressure water hydraulics versus pneumatics - performance, efficiency and investments, a case study. *The Eighth Scandinavian International Conference on Fluid Power*, 2003.

[209] Litzenberg, M., Linke, M., and Berger, F. Method and device for blow forming containers. *SIG Technology Ltd - European Patent no. WO 2006/029584 A1*, 2004. 19

[210] Lockwood, R. and Patterson, W. The process of energy transfer from an intermittent jet to secondary fluid in an ejector-type thrust augmenter. *Advanced Research Division of Hiller Aircraft Company Report No. ARD-305*, 1962.

[211] López, E. Methodologies for the numerical simulation of fluid flow in internal combustion engines. *Doctoral Dissertation*, 2009. 66

[212] López, E. and Nigro, N. Validation of a 0D/1D computational code for the design of several kind of internal combustion engines. *Investigación aplicada latinoamericana*, 2010. 66

[213] Lorain, P. Étude thermodynamique du moteur diesel. *Revue Generale de Termique*, 1962.

[214] Luo, Y. System modelling and control design of a two-stage metering poppet-valve system. *Doctoral Dissertation*, 2006.

[215] MacLaren, J., Tramschek, A., and Pastrana, O. A study of boundary conditions encountered in reciprocating compressor systems. *International Compressor Engineering Conference*, 1976.

[216] MacLaren, J., Tramschek, A., Pastrana, O., and Sanjines, A. Advances in numerical methods to solve the equations governing,unsteady gas flow in reciprocating compressor systems. *International Compressor Engineering Conference*, 1976.

[217] Madsen, N. and Ramamoorthy, P. Isothermal, compressible-gas flow in horizontal pipes with an imperfect gas. *Transactions of the ASME*, 1979.

[218] Maeda, T. Studies on the dynamic characteristic of a poppet valve. *The Japan Society of Mechanical Engineers*, 1970.

[219] Maeda, T., Hayashi, K., Oouchi, M., Miyake, M., and Nakane, M. New type of poppet valve with 2 degrees of freedom. *International Fluid Power Workshop*, 1997.

[220] Maiti, R., Saha, R., and Watton, J. The static and dynamic characteristics of a pressure relief valve with a proportional solenoid-controlled pilot stage. *Proceedings of the Institution of Mechanical Engineers*, 1984.

[221] Mantilla, J., Falla, C., and Gómez, J. Simulación del flujo de gas en ductos de escape de motores de combustión interna. primera parte:aspectos teóricos. *Revista Ingeniería e Investigación vol. 29 nº 1*, 2009.

[222] Martin, G. Modélisation 0D−1D de la chaîne d'air des mci dédiée au contrôle. *Thèse*, 2010. 56

[223] McArdle, J. Internal characteristics and performance of an aerodynamically controlled, variable-discharge convergent nozzle. *National Advisory Committee for Aeronautics*, 1958.

[224] Medica, V., Carija, Z., and Franković, B. Control strategy for continuously variable pipes length of the intake manifold. *FISITA World Automotive Congress*, 2000.

[225] Merritt, H. Hydraulic control systems. *Wiley & Sons*, 1991.

[226] Mohammadi, A., Yaghoubi, M., and Rashidi, M. Analysis of local convective heat transfer in a spack ignition engine). *International Communications in Heat and Mass Transfer*, 2008.

[227] Moretti, R. Complicated one-dimensional flows. *Research Report*, 1971.

[228] Moretti, R. and DiPiano, M. An improved lambda-scheme for one-dimensional flows. *NASA Contractor Report 3712*, 1983.

[229] Mutoh, H., Kawakami, K., Hirata, Y., and Kawai, S. An approach to energy conservation in pneumatic systems with meter-out circuit. *Proceedings of the 7th JFPS International Symposium on Fluid Power*, 2008. 11

[230] Neice, S. A method for stabilizing shock waves in channel flow by means of a surge chamber. *National Advisory Committee for Aeronautics*, 1953.

[231] Neugebauer, A. Dove va la pneumatica? *Oleodinamica Pneumatica Lubrificazione*, 1998.

[232] Nguyen, N. Computational method for non-conservation form of 1-d unsteady euler equations for closed-loop transport systems. *American Institute of Aeronautics and Astronautics*, 2007.

[233] Niessner, H. Comparison of different numerical methods for calculating one-dimensional unsteady flows. *The Von Karman Institute of Fluids Dynamics*, 1981.

[234] Oneyama, N. Energy saving for pneumatic systems. *Energy Conservation Center*, 2003. 9

[235] Ortega, A., Azevedo, B., Pieres, L., and Nieckle, A. A numerical model about the dynamic behaviour of a pressure relief valve. *12th Brazilian Congress of Thermal Engineering and Sciences*, 2008.

[236] Ortega, A., Azevedo, B., Pieres, L., and Nieckle, A. Analysis of the discharge coefficient of a spring loaded pressure relief valves during its dynamics behavior. *20th International Congress of Mechanical Engineering*, 2009.

[237] Otis, D. The effect of air expansion on the work produced by an air cylinder. *Report no. ME-FP-911*, 1991. 8

[238] Otis, D. Reducing compressed air consumption by utilizing expansion energy during the actuation of a pneumatic cylinder. *National Fluid Power Association*, 1992. 8

[239] Pandolfi, M. Discontinuities in compressible flows italian contributions. *Notes on Numerical Fluid Mechanics*, 2009.

[240] Park, S., Kitagawa, A., and Kawashima, M. Water hydraulic high-speed solenoid valve - Part 1 development and static behaviour. *Proceedings of the Institution of Mechanical Engineers*, 2004.

[241] Parkkinen, J. and Zenger, K. A new efficiency index for analysing and minimizing energy consumption in pneumatic systems. *International Journal of Fluid Power*, 2008. 11

[242] Payri, F., Galindo, J., Serrano, J., and Arnau, F. Analysis of numerical methods to solve one-dimensional fluid-dynamic governing equations under impulsive flow in tapered ducts. *International Journal of Mechanical Sciences*, 2004.

[243] Pérez, J., Sanmiguel, E., and Viedma, A. Identificación del origien de las pérdidas energéticas en el flujo compresible en uniones de conductos mediante simulación numérica. *8º Congreso Iberoamericano de Ingeniería Mecánica*, 2004.

[244] Perotti, M. Speed-up of a dfem code for unsteady gas dynamics in pipes. *International Journal of Mechanical Sciences*, 1999.

[245] Persoons, T. Experimental flow dynamics in automotive exhaust systems with close-coupled catalyst. *Doctoral Dissertation*, 2006.

[246] Ponsoda, E., Romero, J., Serrano, J., and Arnau, J. A new iterative method for flow calculation in intake and exhaust systems of internal combustion engines. *Mathematical and Computer modelling*, 2003.

[247] Pourmovahed, A. Energy storage capacity of gas-charged hydraulic accumulators. *AIAA Thermophysics, Plasmadynamics and Lasers Conference*, 1988.

[248] Pourmovahed, A. and Otis, D. An experimental thermal time-constant correlation for hydraulic accumulators. *Transactions of the ASME*, 1990.

[249] Pu, J., Wang, J., Moore, P., and Wong, C. A new strategy for closed-loop control of servo-pneumatic systems with improved energy efficiency and system response. *The Fifth Scandinavian International Conference on Fluid Power*, 1997. 12

[250] Quaglia, G. Non-conventional energy-saving pneumatic actuator. *International Conference 11^{th} AFK*, 1994. 7

[251] Quaglia, G. and Castaldi, L. The design of pneumatic actuator with low energy consumption. *The 4^{th} Triennial International Symposium on Fluid control, fluid measurement, and visualization*, 1994. 7

[252] Quaglia, G. and Castaldi, L. The design of pneumatic actuator with low energy consumption. *The 4^{th} Triennial International Symposium on Fluid control, fluid measurement, and visualization*, 1994. 7

[253] Quaglia, G. and Castaldi, L. Compatto ed economico. *Progettare no. 179*, 1995. 7

[254] Quaglia, G. and Castaldi, L. Attuazione pneumatica con recupero energetico. *Progettare no. 176*, 1995. 7

[255] Quillman, B. Energy conservation in the industrial environment. *National Conference on Fluid Power Association*, 1978. 2

[256] Radcliffe, C. and Southward, S. A property of stick-slip friction models which promotes limit cycle generation. *American Control Conference*, 1990. 81

[257] Rahmat, M. and Sunar, N. Review on modelling an controller design in pneumatic actuator control system. *International Journal on Smart Sensing and Intelligent Systems*, 2011.

[258] Raithby, G. and Hollands, K. Natural Convection, *Chp 4. Handbook of Heat Transfer*, 1998.

[259] Rakova, E., Hepke, J., and Weber, J. Comparison of methods for the investigation on the energetic behaviour of pneumatic drives. *The 9^{th} International Fluid Power Conference*, 2014.

[260] Ray, A. Dynamic modelling and simulation of a relief valve. *Simulations Councils, Inc.*, 1978.

[261] Research-Councils, U. K. HSL - A collection of Fortran codes for large scale scientific computation (http://www.hsl.rl.ac.uk/). *HSL Archive*, 2011. xvii, 103

[262] Richer, E. and Hurmuzlu, Y. A high performance pneumatic force actuator system - Part 1 - Nonlinear mathematical model. *ASME Journal of Dynamic Systems Measurement and Control*, 2000. 94

[263] Rudinger, G. Nonsteady supercritical discharge through an orifice. *Journal of Basic Engineering*, 1961.

[264] Rymann, O. Valve device for hollow body blowing machines. *Eugen Seitz AG - European Patent no. PCT/CH2005/000591*, 2005. 23

[265] Rymann, O. Valve device for cavity blowing machines and method for injecting compressed air into a blowing volume. *Eugen Seitz AG - European Patent no. PCT/CH2005/000591*, 2007. 23

[266] Sai, M., Fujita, H., Kagawa, T., and Takeuchi, M. Research on assessment of air energy in pneumatic systems. *Hydraulic and Pneumatic Conference - Draft*, 2000. 11, 126

[267] Salacka, T. Review implementation and test of the qaz1d computational method with a view to wave rotor applications. *Doctoral Dissertation*, 1985.

[268] Sanville, F. The 7^{th} International Fluid Control Symposium. *Two-level Compressed Air Systems for Energy Saving*, pages 375–383, 1986. 4

[269] Sato, H., Takahashi, K., Ohtani, K., and Ikeo, S. Characteristics of the compressible flow between parallel disks. *Proceedings of the 6^{th} JFPS International Symposium on Fluid Power*, 2005.

[270] Sato, N. Method for recovery of blown air. *Yoshino Kogyosho Co Ltd - Japanese Patent JPH11207808*, 1998. 16

[271] Scandella, J. Air comprimé gare au gâchis! *L'Usine Nouvelle*, 2004.

[272] Schneider, E. Pneumatic circuit for rapidly transferring fluid under pressure from a work cylinder to a storage tank for subsequent use. *United States Patent no. US3400636*, 1966. 4

[273] Schweppe, J., Eichberger, L., Muster, D., Michaels, E., and Paskusz, G. Methods for the dynamic calibration of pressure transducers. *National Bureau of Standards Monograph 67*, 1963.

[274] Scopesi, M. Design and optimization of pneumatic devices for automation and automotive field. *Doctoral Dissertation*, 2011. 126

[275] Seifert, H. A mathematical model for simulation of processes in an internal combustion engine. *Acta Astronautica*, 1979.

[276] Senoo, M., Huping, Z., and Oneyama, N. Current conditions and issues of energy saving in pneumatic systems. *7th International Symposium on Fluid Control, Measurement and Visualization*, 2003. 10

[277] Serrano, J., Arnau, F., Piqueras, P., Onorati, A., and Montenegro, G. 1D gas dynamic modelling of mass convervation in engine duct systems with thermal contact discontinuities. *Mathematical and Computer modelling*, 2009.

[278] Serruys, M. L'Écoulement des fluides dans les moteurs à combustion interne. *Journal de S.I.A.*, 1957.

[279] Sesterhenn, J. A characteristic-type formulation of the navier-stokes equations for high order upwind schemes. *Computer and Fluids*, 2001.

[280] Shahani, A., Aryaei, A., Esmaili, H., Najar, M., and Mohammadi, S. Dynamic simulation of a high pressure regulator. *Journal of Computational & Applied Research in Mechanical Engineering*, 2011.

[281] Shapiro, A. The dynamics and thermodynamics of compressible fluid flow vol. I. *The Ronald Press Company*, 1953. 32

[282] Shapiro, A. The dynamics and thermodynamics of compressible fluid flow vol. II. *The Ronald Press Company*, 1954. 32

[283] Shen, X. and Goldfarb, M. Energy saving in pneumatic servo control utilizing interchamber cross-flow. *Journal of Dynamic Systems, Measurement and Control*, 2007. 12

[284] Shoucri, R. Application of the method of characteristics for the study of shock waves in models of blood flow in the aorta. *Cardiovasc Eng.*, 2007.

[285] Shu, P., Fleming, J., and Brown, J. Analysis of dynamic gas forces on reciprocating compressor valves. *International Compressor Engineering Conference*, 1984.

[286] Sidransky, F. and Smith, M. Nonsteady liquid and gas flow with heat addition and shock perturbations. *NASA Technical Note D-3684*, 1966.

[287] Siegrist, R. and Stillhard, B. Stretch blow forming method and blow forming press. *Procontrol Patent No. WO1996025285 A1*, 1991. 15

[288] Sod, G. A survey of several finite difference methods for systems of nonlinear hyperbolic conservation laws. *Journal of Computational Physics*, 1978.

[289] Southward, S., Radcliffe, C., and MacCluer, C. Robust non-linear stick-slip friction compensation. *Journal of Dynamics Systems Measurement and Control*, 1991. 81

[290] Spring, P. modelling and control of pressure-wave supercharged engine systems. *Doctoral Thesis*, 2006.

[291] Stanton, T. On the flow of gases at high speeds. *Proceedings of the Royal Society of London*, 1926.

[292] Stockar, S. Model-order reduction for nonlinear distributed parameter systems with application to internal combustion engine modelling and simulation. *Doctoral Dissertation*, 2013.

[293] Stoia-Djeska, M. and Mingireanu, F. A mathematical and numerical model for the analysis of hybrid rocket motors. *Incas Bulletin*, 2004.

[294] Stone, J. An investigation of discharge coefficients and steady state flow forces for poppet type valves. *Master Thesis*, 1955.

[295] Stosic, N. and Hanjalic, K. Computer simulation of two-stage reciprocating compressors. *International Compressor Engineering Conference*, 1978.

[296] Sullivan, D. Historical review of real-fluid isentropic flow models. *Transactions of the ASME*, 1981.

[297] Sunil, S. and Pandeyi, U. Mathematical modelling of pressure regulator for cryogenic applications. *Proceedings of the 37^{th} National & 4^{th} International Conference on Fluid Mechanics and Fluid Power*, 2010.

[298] Suzuki, K. and Urata, E. Dynamic characteristics of a direct pressure sensing water hydraulic relief valve. *Proceedings of the 6^{th} JFPS International Symposium on Fluid Power*, 2005.

[299] Suzuki, K. and Urata, E. Development of a direct pressure-sensing pressure reducing valve for water hydraulics. *Journal of Systems and Control Engineering*, 2008.

[300] Suzzani, R. L'accumulatore questo sconosciuto. *Oleodinamica Pneumatica Lubrificazione*, 1994.

[301] Szente, V. and Vad, J. A semi-empirical model for characterisation of flow coefficient for pneumatic solenoid valves. *Periodica Polytechnica Ser. Mech. Eng.*, 2003.

[302] Tang, Y., Lee, S., and Yang, J. A high-order pathline godunov scheme for unsteady one-dimensional equilibrium flows. *Computer Methods in Applied Mechanics and Engineering*, 1997.

[303] Tapio, V. and Mäkinen, E. 18^{th} International Conference on Hydraulics and Pneumatics. *Energy Conservation Center*, 2003. 12

[304] Taplin, J. and Anderson, J. Energy-conserving apparatus for a piston cylinder arrangement. *Rexnord Inc. - European Patent Office (GB2095759A)*, 1982. 6

[305] Terashima, K., Kawakami, Y., Arinaga, T., and Kawai, S. An approach for energy-saving of pneumatic cylinders by meter-in circuit. *Proceedings of FLUCOME*, 2000. 11

[306] Terenzi, A. Influence of real-fluid properties in modelling decompression wave interacting with ductile fracture propagation. *Oil & Gas Science and Technology*, 2005.

[307] Thomas, P. On the convection from disks at low Grashof numbers. *Fire Research Station Note no. 258/1956*, 1956.

[308] Tirkey, J., Gupta, H., and Shukla, S. Integrated gas dynamic and thermodynamic computational modelling of multicylinder 4-stroke spark ignition using gasoline as a fuel. *Thermal Science*, 2009.

[309] Tokashiki, L., Fujita, T., Kagawa, T., and Pan, W. Dynamic characteristics of pneumatic cylinders including pipes. *Proceedings of the 9^{th} Bath International Fluid Power Workshop*, 1996. 10, 40, 208

[310] Toro, E. NUMERICA: A library of source codes for teaching, research and applications. HYPER-EUL. methods for the Euler equations. *Wiley and Sons Ltd.*, 1999.

[311] Toro, E. NUMERICA: A library of source codes for teaching, research and applications. HYPER-LIN. methods for model hyperbolic equations. *Wiley and Sons Ltd.*, 1999.

[312] Toro, E. NUMERICA: A library of source codes for teaching, research and applications. HYPER-WAT. methods for the shallow water equations. *Wiley and Sons Ltd.*, 2000.

[313] Toro, E. Shock-capturing methods for free-surface shallow flows. *Wiley and Sons Ltd.*, 2001.

[314] Toro, E. Riemann solvers and numerical methods for fluid dynamics. A practical introduction. *Springer-Verlag*, 2009. 60

[315] Trangenstein, J. Numerical solution of hyperbolic conservation laws. *Cambridge University Press*, 2009.

[316] Trella, T. and Soedel, W. Effect of valve port gas inertia on valve dynamics - Part I: Simulation of a poppet valve. *International Compressor Engineering Conference*, 1974.

[317] Trujillo, M., O' Rourke, P., and Torres, D. Generalizing the thermodynamics state relationships in KIVA-3V. *Los Alamos-National Laboratory*, 2002.

[318] Turner, R., Addie, A., and Zimmerman, R. Charts for the analysis of one-dimensional steady compressible flow. *National Aeronautics and Space Administration TN - 1419*, 1948.

[319] Tyagi, M. and Sujith, R. Nonlinear distortion of traveling waves in variable-area ducts with base flow: a quasi-one-dimensional analysis. *J. Fluid Mech., Vol. 536*, 2005.

[320] van Leer, B., Thomas, J., Roe, P., and Newsome, R. A comparison of numerical flux formulas for the euler and navier-stokes equations. *American Institute of Aeronautics and Astronautics*, 1987.

[321] van Leersum, J. A numerical model of a high performance two-stroke engine. *Applied Numerical Mathematics 27,83-108*, 1998.

[322] van Niekerk, J. Effect of the tailpipe entry geometry on a two-stroke engine's performance prediction. *Master Thesis*, 2000.

[323] van Vuuren, C., Thiart, G., and Taylor, A. Computer simulation of internal combustion engine flow processes. *R & D Journal*, 2002.

[324] Varouxis, T. Air cylinder with self-contained pneumatic piston return. *United States Patent no. US3645170(A)*, 1969. 7

[325] Voth, K. and Stoiber, C. Blow molding machine comprising control valves, which are mounted on the blowing device and which control the blowing air. *Krones AG - European Patent US2003118686(A1)*, 2003. 23

[326] Wahlberg, P. Single acting pneumatic piston-cylinder unit. *European Patent Office - PCT/SE01/00589*, 1997. 6

[327] Wang, C. Transient flow analysis of a supersonic ludwieg-tube wind tunnel. *Master Thesis*, 1989.

[328] Wang, C. and Berry, G. Heat transfer in internal combustion engines. *The American Society of Mechanical Engineers*, 1985.

[329] Wang, J. and Gordon, T. Energy efficient tracking control of pneumatic cylinders. *50^{th} IEEE Conference on Decision and Control and European Control Conference*, 2011. 11

[330] Wang, J., Wang, J., and Liau, V. Energy efficient optimal control of pneumatic actuator systems. *Systems Science*, 2000. 11

[331] Warmbrod, J. A theoretical and study of unsteady in a ludwieg tube experimental flow processes wind tunnel. *National Aeronautics and Space Administration TN D-5469*, 1969.

[332] Warmbrod, J. and Struck, H. Application of the characteristics method in calculating the time dependent, one-dimensional, compressible flow in a tube wind tunnel. *National Aeronautics and Space Administration TM X-53769*, 1968.

[333] Warren, M. Open-end outflow boundary approximations for the solution of the equations of unsteady one-dimensional gas flow by the lax-wendroff method. *International Journal Heat & Fluid Flow*, 1984.

[334] Wayne, C. Recycling of blow air. *The Continental Group - Patent No.4488863*, 1984. 14

[335] Weaving, J. Discharge of exhaust gases in two-stroke enignes. *Proceedings of the Institution of Mechanical Engineers*, 1949.

[336] Weiss, R. Multiple utilization of working air. *Krupp Corpoplast Maschinenbau GmbH - Patent No. 5585066*, 1994. 15, 18

[337] Weiss, R. Multiple utilization of blow-mold air. *Krupp Corpoplast Maschinenbau GmbH - Patent No. 5648026*, 1994. 15

[338] Weiye, H. and Zhihang, Z. Resource regeneration energy saving and emission reducing system in blow moulding process. *GUANGZHOU XINQUAN Packing Container Co. Ltd. - Chinese Patent no. CN201423749Y*, 2009.

[339] Winterbone, D. and Nichols, J. A graphic description of the interaction of waves with various boundaries. *International Journal of Mechanical Sciences*, 1985.

[340] Winterbone, D. and Pearson, R. A solution of the wave equations using real gases. *International Journal of Mechanical Sciences*, 1992. 32

[341] Woods, W. and Allison, A. Effective flow area of piston controlled exhaust and inlet ports. *International Automotive Engineering Congress and Exposition Society of Automotive Engineers*, 1977.

[342] Woods, W. and Owen, D. Discharge from an autoclave system. *Fifth Australasian Conference on Hydraulics and Fluid Mechanics*, 1974.

[343] Yamaji, M. and Oneyama, N. Actuator exhaust recovery equipment. *SMC Corporation Ltd - Japanese Patent no. JPH02032882(Y2)*, 1981. 5

[344] Yan, S., Maolin, C., Weiqing, X., and Jie, L. Expansion energy used by pneumatic booster. *Chinese Journal of Mechanical Engineering*, 2012.

[345] Yang, J. and Chiu, K. Use of characteristics method with cubic interpolation for unsteady-flow computation. *International Journal for Numerical Methods in Fluids*, 1993.

[346] Yang, L., Wang, J., Mangan, S., Derby, J., and Lu, N. Mathematical model and energy efficiency analysis of a scroll-type air motor. *IAENG International Journal of Applied Mathematics*, 2008. 12

[347] Yang, X., Dou, C., Tian, C., and Hu, S. Dynamic behavior of control valve in variable displacement wobble plate compressor. *International Compressor Engineering Conference*, 2002.

[348] Yoshikawa, A. and Oneyama, N. Cylinder driving apparatus. *SMC Corporation Ltd - Japanese Patent JPH022964(Y2)*, 1980. 5

[349] Yu, S. and Chang, S. Treatments of stiff source terms in conservation laws by the method of space-time conservation element and solution element. *Aerospace Sciences Meeting & Exhibit*, 1997.

[350] Zevenhoven, R. Non ideal gases in diesel engine processes. *First Biennial Meeting and General Section Meeting of The Scandinavian-Nordic Section of the Combustion Institute*, 2001.

[351] Zhang, Q. Modelling the scavenging process in a two-stroke i.c. engine. *Master Thesis*, 1995.

[352] Zoppas, E. Method for recycling energy in a blow molding moulding machine for blow moulding containers. *San Benedetto Acqua Minerale - European Patent EP1905569 (A2)*, 2006. 19

[353] Zoppas, M., Pittari, G., Altoe, M., and Polentes, M. Method for recycling energy in a blow moulding machine for blow moulding containers. *SIPA - European Patent no. WO2009004472(A2)*, 2006. 22

[354] Zucrow, M. and Hoffman, J. Gas dynamics vol. I. *John Wiley and Sons, Inc.*, 1976. 48

[355] Zucrow, M. and Hoffman, J. Gas dynamics vol. II. *John Wiley and Sons, Inc.*, 1977. 48

[356] Zuk, J. Analysis of face deformation effects on gas film seal performance. *NASA Technical Memorandum X-68022*, 1972.

[357] Zuk, J. and Ludwig, L. Analysis of rotational effects on compressible viscous flow across shaft face seals. *NASA Technical Memorandum X-52991*, 1971.

[358] Zuk, J., Ludwig, L., and Johnson, L. Compressible flow across shaft face seals. *NASA Technical Memorandum X-52959*, 1971.

[359] Zuk, J., Ludwig, P., and Johnson, R. Quasi-one-dimensional compressible flow across face seals and narror slots. *NASA Technical Note D-6668*, 1972.

Declaration

I herewith declare that I have produced this paper without the prohibited assistance of third parties and without making use of aids other than those specified; notions taken over directly or indirectly from other sources have been identified as such. This paper has not previously been presented in identical or similar form to any other Spanish or foreign examination board.

The work was done under the guidance of Professor Esteban Codina Macià and Professor Pedro Javier Gámez Montero, at the Polytechnic University of Catalonia, Terrassa.

José Trujillo

In my capacity as supervisor of the candidate's thesis, I certify that the above statements are true to the best of my knowledge.

Esteban Codina Macià Pedro Javier Gámez Montero

Terrassa, 6^{th} of September 2015